UNIVERSITÀ DI PARMA

UNIVERSITA' DEGLI STUDI DI PARMA

DOTTORATO DI RICERCA IN

"Scienza e Tecnologia dei Materiali"

CICLO XXXII

Multiscale control of structure and functional properties in the Ni-Mn-Ga shape-memory compounds:

from epitaxial thin films to micro and nanostructures

Coordinatore:

Chiar.mo Prof. Enrico Dalcanale

Tutore:

Dott.ssa Franca Albertini

Dott.ssa Francesca Casoli

Dottorando: Milad Takhsha Ghahfarokhi

Anni 2016/2019

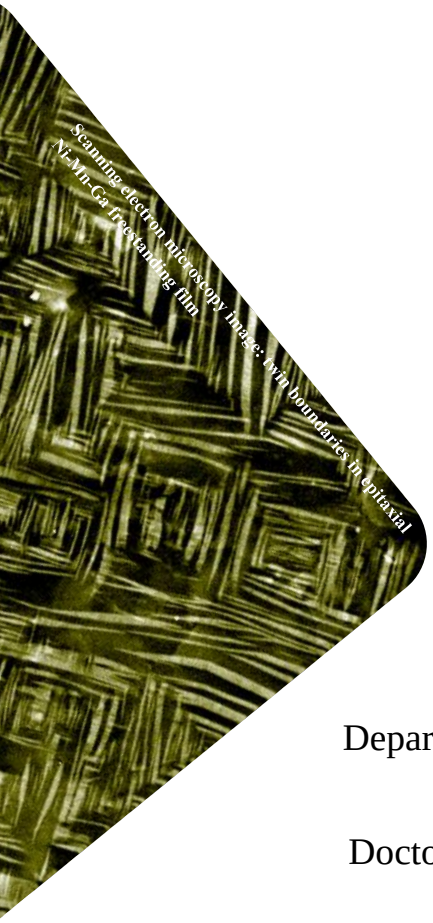

UNIVERSITÀ DI PARMA

Department of Chemistry, Life Sciences and Environmental Sustainability

Doctoral Dissertation in Materials Science and Technology

Cycle XXXII

Multiscale control of structure and functional properties in the Ni-Mn-Ga shape-memory compounds: from epitaxial thin films to micro and nanostructures

Milad Takhsha Ghahfarokhi

2016-2019

To my dear supervisors Franca & Francesca

Contents

Introduction

Imagine you are wearing magnifying microscope-glasses, looking at your surroundings. What would you see? Definitely, a new aspect of the world would appear to you, something quite different from our daily observations and expectation, something similar to what we have seen only in science fiction movies. A parallel world of small-scale creatures and objects, having fancy shapes and colors, moving around and doing tasks in a well-disciplined, efficient and intelligent manner. It also applies to how our body works, in most cases even more advanced than the capability of the current high technology. This sparks many questions in the minds of elites. Do we really need to spend such large mass of materials, huge energy sources and tremendous number of human sources to perform tasks? What consequences should we expect by investing on technologies requiring more materials, energy and human sources? Regardless of the environmental detrimental effects, should we consider the geopolitical aspects of the criticality of the material, energy and human sources when we stablish the horizon of the science and technology in our nations?

These are basically the questions led to the main motive for what is known as 'smart technology', in which the approach is to maximize the efficiency and intelligence as well as to minimize the required material, human and energy sources. A part of this approach is to invest on a type of materials called 'smart materials', which are a class of materials with extensive change of properties upon applied external stimuli. These materials are capable of converting different forms of energies as well as performing mechanical tasks in a partially or fully autonomous way. Among the smart materials piezoelectric, magnetostrictive materials and shape memory alloys (SMA) are of special interests due to the high efficiency and versatility. In the SMA, the external stimuli, i.e., stress, magnetic field and temperature gradient can lead to a reversible change of shape of the material, which can be exploited for a vast variety of applications. As a sub-class of SMA, there is a ternary Heusler compound, known as 'Ni_2MnGa', the most investigated and the representative of a group called ferromagnetic shape memory alloys (FSMA), in which there is a strong coupling between the magnetic and the structural degrees of freedom of the crystal cells. This unique coupling gives rise to a new generation of integrated actuating systems. In addition, due to the 'giant' thermo/magnetomechanical effects, these materials show giant caloric effects, which can be exploited into new generation of cooling devices.

The concept of smart materials gains special interest in small-scale devices (in the range of micro and nanometer), where the mechanical simplicity, compactness, intelligence, and efficiency of FSMA offer remarkable advantages for different application fields. Thin films can be integrated appropriately into the micro and nanodevices. In addition, Ni_2MnGa films can be considered as a model system for FSMA. By exploiting epitaxial growth on different substrates, suitable growth conditions (including the application of a mechanical stress), and geometrical parameters (e.g., thickness) high quality and suitably oriented epitaxial films can be obtained. They allow accurate studies of structure and magnetism at the different length scales. Finally, the special geometry of the

material in thin films, i.e., huge surface to thickness ratio, is expected to influence the mechanical, thermal and magnetic properties of FSMA, which in turn may give rise to novel functionalities.

Nevertheless, there are still some challenges concerning the full exploitation of these materials towards applications, among them are the technical obstacles related to the epitaxial growth of high-quality films as well as micro and nanofabrication. In addition, the knowledge about the effect of the reduction of size on the properties of FSMA are still quite limited. The complexity of the crystal structure, magnetic order and the dependence of the material characteristics to several intrinsic and extrinsic parameters makes the evaluation of the effect of size in FSMA a quite demanding task. Besides, one needs to take into account the complexity coming from the fabrication and the characterization sides as the size of the material is reduced.

FSMA undergo a diffusion-less thermodynamic phase transition between high-temperature cubic phase (austenitic phase) and low-temperature low-symmetry phase (martensitic phase). The stress caused by the symmetry breaking upon phase transition, imposes the formation of 3D zig-zag patterns in the low-temperature phase. The self-accommodation of these patterns (which are called twin variants) in a hierarchical fashion, enables unique characteristics of the material in the martensitic phase, e.g., the reversible change of shape. It is well known that some of the obstacles limiting the functionality of the material are linked to the hysteretic nature of this phase transition, which could in turn be related to several intrinsic and extrinsic characteristics of the material among which, is the self-accommodation of the twin variants in the martensitic phase. Nevertheless, there is few knowledge about the self-accommodation of the twin variants and its possible impact on the martensitic transition.

The focus of this thesis is to explore multifunctional properties of Ni-Mn-Ga Heusler films, micro and nanostructures, aiming at pushing the current knowledge about this type of smart materials forward. For this purpose, the exploration starts from continuous epitaxial films and proceeds with micro and nanostructures, fabricated by lithography techniques. The possibility of controlling martensitic configurations as well as the critical transition temperatures are investigated by a systematic evaluation of martensitic transition at various spatial length-scales under certain external stimuli, i.e., temperature, external magnetic field and mechanical stress.

In chapter 1, the extended background of SMA and the areas of applications, Ni-Mn-Ga crystallographic structures, magnetic characteristics, different mechanisms ruling the actuation and phase transition are discussed followed by a brief description of the overall challenges related to FSMA thin films. Chapter 2 is dedicated to the explanation of the experimental techniques including the details of the growth of the epitaxial Ni-Mn-Ga films, micro- and nano-fabrications as well as the several structural, magnetic and morphological characterization techniques. In chapter 3, the experimental results are reported, emphasizing on the effects of simple post-growth treatments for controlling the martensitic configurations of Ni-Mn-Ga films. Chapter 4 is dedicated to the direct observation of the evolution of the martensitic phase under different transformation conditions, emphasizing the role of the martensitic configuration and interfaces on the transition route. Finally, in chapter 5, by implementing the lithography-based micro and nanofabrication techniques, the effects of the lateral confinement on the martensitic morphology and the critical transition temperatures are systematically explored.

Chapter 1

State of art

1.1 Shape memory alloys

Shape memory alloys are a class of smart materials that undergo extensive change of properties such as shape, structure and magnetic order upon applying external stimuli, i.e., stress, magnetic field and temperature. Over the last decades, these types of materials have gained a considerable attention in several areas of technology. So far, they have been the subject of over 40,000 publications and 22,000 US patents [1]. In the following, the chronological background of SMA is briefly discussed and their application in four areas of technology i.e. bioengineering, aerospace, automotive and robotics are pointed out.

1.1.1 Chronological background

In 1932 for the first time, a temperature dependent reversible deformation was reported in Au-Cd by a Swedish chemist, Arne Olander. In his report, which is dedicated to the electrochemical investigation of the phase transition in Au-Cd alloys, he describes the elasticity of the Au-Cd alloys with 47.5 at. % of Cd as a rubber-like feature [2]. Later in 1938, Greninger and Mooradian reported the formation of 'parallel bands or markings' within the grains of the material upon quenching Cu-Zn and Cu-Sn alloys [3]. It took almost ten years before the principles of those observations were introduced based on shape memory effect and thermoelectricity by Kurdjumov and Khandros [4]. In the following years the principles were developed further and advanced by other scientist, e.g., Chang and Read [5] although the booming potential capabilities of these types of alloys was not recognized before 1962 [6]. In those years, in the Naval Ordnance Laboratory, William Buehler, Frederick Wang and co-workers were exploring the best candidates for the conic part of the missile nose that could withstand the extreme tensions, high temperatures and the fatigue; among the testing materials, there was a binary alloy of Nickel and Titanium. Inadvertently, they recognized that this alloy represents a significant shape recovery over a gradient of temperature, which was later shown to the colleagues during a scientific meeting by bending a piece of Ni-Ti bar and heating it up using a lighter. Upon heating, the alloy contracted simultaneously to its previous shape. The alloy which was later named Nitinol (a combination of the names of the constituting elements and the lab where it was first discovered), soon became a model system for SMA and huge number of labs around the world started to work on this unique feature. Only seven years after the first report, Nitinol was commercially utilized for the first time as the pipe couples in F-14 jet fighters [7]. This utilization was just an initial

step; over the next 20 years, a vast variety of other SMA were reported and specifically for Nitinol, the application widely expanded to other areas of technology such as automotive, bioengineering, aerospace and robotics [8] (sections 1.1.2 to 1.1.5). In the 90's the research and applications were further expanded to small scales, where shape memory integrated microdevices were introduced to the community [8] and up to now the researches for new materials, novel functionalities, modifying the features of the SMA and the commercialization are still on going. Nowadays, there are a vast variety of SMA, widely speared in technology from the scale of bulk to the micro-scales.

In 1960, two years before Nitinol was reported, people in another lab, in a totally different field of research, for the first time reported the ferromagnetic phase in Ni_2MnGa compound [9], which is a class of intermetallic magnetic materials called Heusler compounds (section 1.2) [10]. Initially, the unconventional ferromagnetic order in these compounds (section 1.2.1) was the point of interest. However, the research always benefits from the intersection of different areas of science. Ni_2MnGa was known as a ferromagnetic compound for over 30 years until in 1992, Chernenko *et al.* reported the thermoelastic effect of this compound as they described it as 'a new ferromagnetic ordered SMA' [11]. This was a launching stage for a novel functionality both for the SMA and for the Heusler compounds; the concept that ties the magnetic degrees of freedom to the structural degrees of freedom of the material. A few years later, in 1996, Ullakko *et. al.* reported the concept of magnetic shape memory effect (section 1.2.6.3) [12]. Since then, there have been a number of researches for getting deep into this effect and realizing the parameters influencing the effect. There have been also some investigations, introducing new materials showing these characteristics and realizing the novel functionalities (sections 1.2 and 1.3) rising from this thermo/magnetostructural coupling, e.g., magnetocaloric cooling [13] and FSMA-4D printing [14]. A schematic representation of the chronological background of the shape memory alloys is provided in **Figure 1.1**.

1.1.2 Automotive applications

The rising demands for automated, controllable and comfortable vehicles urge the car companies to invest on advanced technologies aimed at gradually substituting the conventional mechanical parts of the vehicles by electromechanical or electronic devices. The huge number of the sensors and actuators, integrated into the vehicles, open up a suitable platform for SMA to play a role. In addition to the high functionality with respect to the conventional alternatives, i.e., electric motors, piezoelectric and magnetostrictive materials [8], flexibility and compactness of the SMA (sections 1.2 and 1.3) enables the miniaturization of the sensors and actuators, which in turn decreases the cost of the manufacturing as well as the weight of the product. SMA could be also integrated into the vehicles as energy harvesters, reviving the waste forms of energies such as heat, converting them to productive energy sources, e.g., electrical and mechanical energies [15]. General Motors, one of the four major car companies in the world by more than 6.5 million vehicles per year, has started to utilize SMA as an actuator to vent the air in the trunk, facilitating the opening and closing of the trunk in Chevrolet Corvette model 2013 [16]. There are a number of other SMA enabled technologies in the forms of integrated thermo-magneto-mechanical sensors, actuators and vehicle energy engines. Some of them are shown in **Figure 1.2** [8].

A simplified example of a vehicle energy-engine is shown in **Figure 1.3**. Car exhaust is one of the parts of the vehicles, where the hot gaseous compounds, generated by the combustion of the fuel inside the engine are dissipated actively. Its tubal shape and long length provide a suitable surface

area for the heat exchange. As shown in the figure, the heat, generated by the engine can be safely converted to the mechanical energy by placing stretched shape memory cords (or bands), partially in touch with the part of the tube, where the hot gas passes and connecting the cords to a set of pulleys. In fact, the temperature gradient in the SMA causes the martensitic phase transition (section 1.2.1), which results in the contraction of the shape memory cords in the hot phase and the subsequent expansion in the cold phase, known as conventional shape memory effect (section 1.2.6.1). This cyclic contraction and expansion in the cords, gives rise to the rotation of pulleys [15].

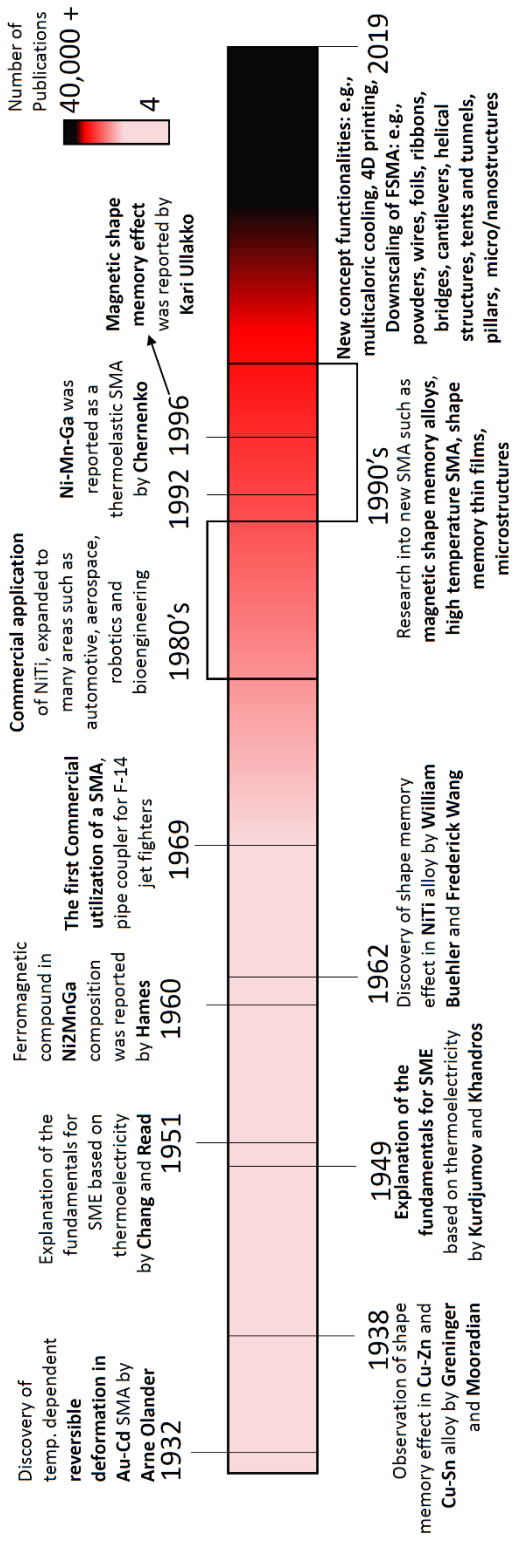

Figure 1.1: Schematic view of the chronological background of the SMA from the discovery to the application. The number of publications are shown by the intensity of the red color [1-9, 11-14, 17-22].

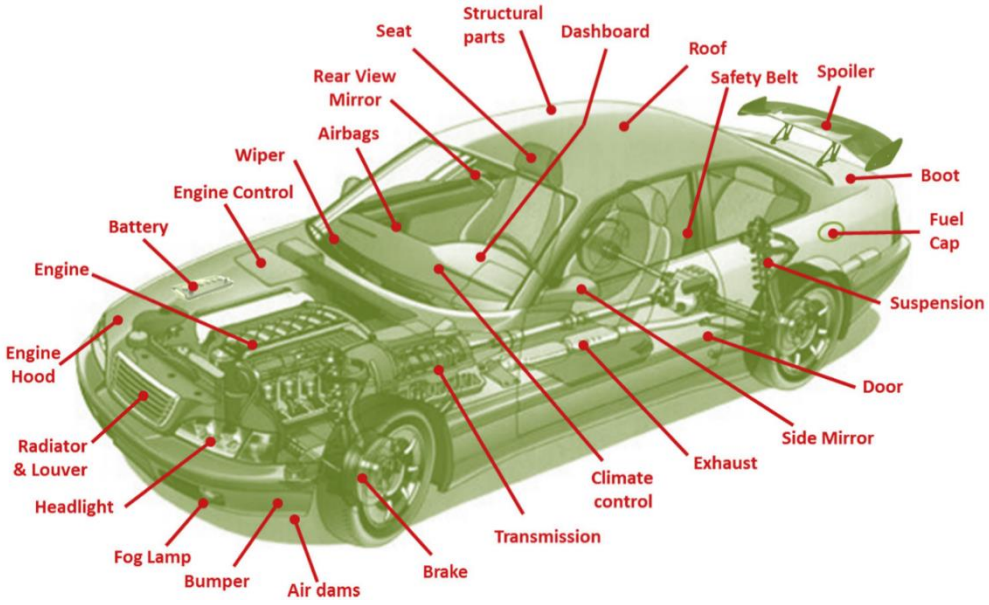

Figure 1.2: Schematic representation of a vehicle, showing the available and promising applications based on SMA in the automotive zone [8].

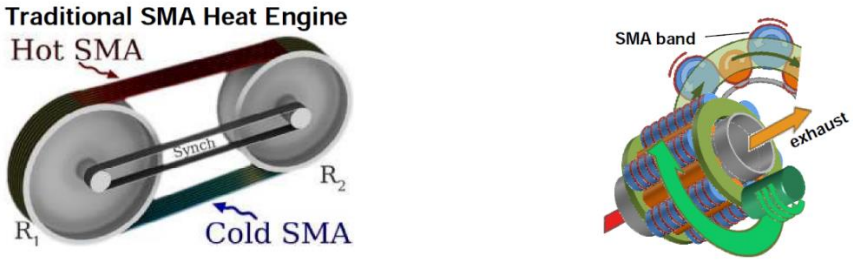

Figure 1.3: simplified example of a vehicle energy-engine [15].

1.1.3 Bioengineering applications

The compactness, flexibility and the superelastic characteristics (section 1.2.6.2) of SMA provide a suitable platform for the biomedical applications. After Nitinol received its proof of biocompatibility from the US food and drug administration in 1989, it entered the bioengineering market, and just in a period of 10 years, its application hugely widespread in biomedical devices and therapeutics, from implants to orthopedic surgery and cardiography [8]. Biocompatibility of Nitinol and its ability to be adapted to human bones and textiles as well as the stability in the human body temperature and the fluidic chemical matrix of the body have made it a unique flexible platform for the biomedical applications. It also found its way to be used as flexible eyeglasses-frames [23] and even in the dentistry [24]. Nowadays, the most prominent clinically available artery stents and dental braces are based on Nitinol. **Figure 1.4** show some of the current and potential biomedical applications of SMA [8].

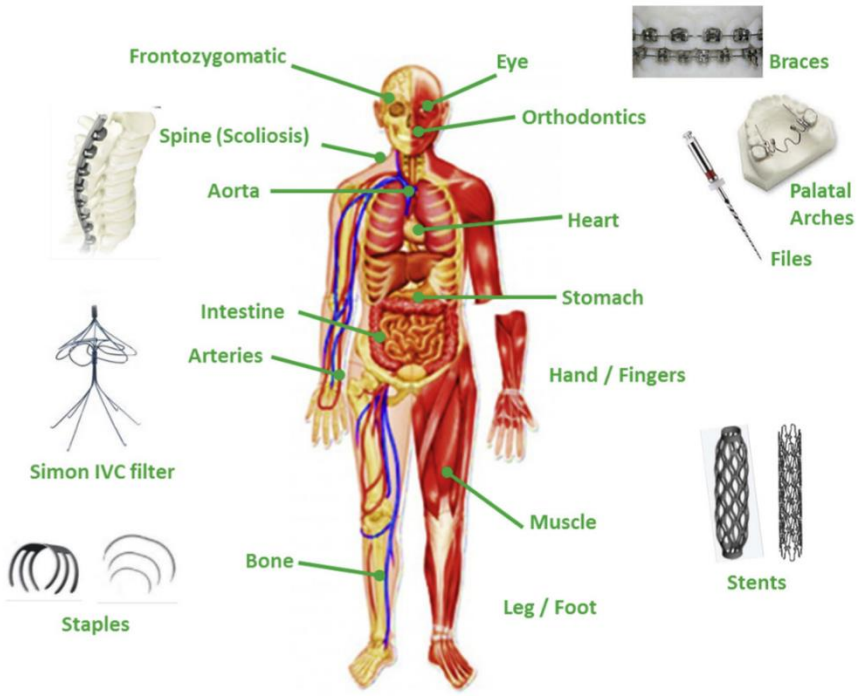

Figure 1.4: Schematic view of the current and potential biomedical applications of SMA [8].

SMA can be also integrated into implantable devices for biological purposes. Drug delivery capsules are one of the examples. As can be observed in **Figure 1.5**, a shape memory wire serves as an actuator opening and closing the capsule. The capsule has a container for the drug and a small space for the electrical circuit, connected to the shape memory wire. The entire capsule is covered by Silicon rubber, which protects the device and ensures the biocompatibility. The mechanism for the actuation is based on thermo-mechanical shape memory effect (section 1.2.6.1). The wire is heated through Joule-heating mechanism by passing pulses of current through the wire, remotely controlled by a transcutaneous transformer system. The contraction of the wire resulting from the phase transition opens the capsule and the drug is released into the target. For the presented prototype, minimum dose of the drug for each operation is 5 µl. These types of drug delivery systems are quite beneficial for the patients, who need to inject a certain dose of a drug multiple times per day. Using these SMA integrated implantable systems, the physical injection can be reduced by 200 times and can be limited to the times of reloading the container of the capsule [25].

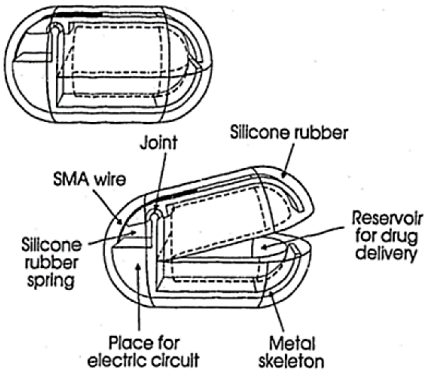

Figure 1.5: The scheme of SMA-based implantable drug delivery capsules [25].

1.1.4 Aerospace applications

As it was mentioned in section 1.1.1, the first utilization of SMA in a commercial application was in F-14 jet fighters. Since then, a number of companies started to invest on SMA and tried to improve the functionality of their products, taking the advantage of the SMA-enabled flexibility (section 1.2.6). In aerospace applications, in addition to the actuating feature, SMA have been also investigated for their significant filling and vibration damping characteristics [8]. A schematic representation for some of the available and promising applications of SMA in aerospace domain of technology is represented in **Figure 1.6** [8].

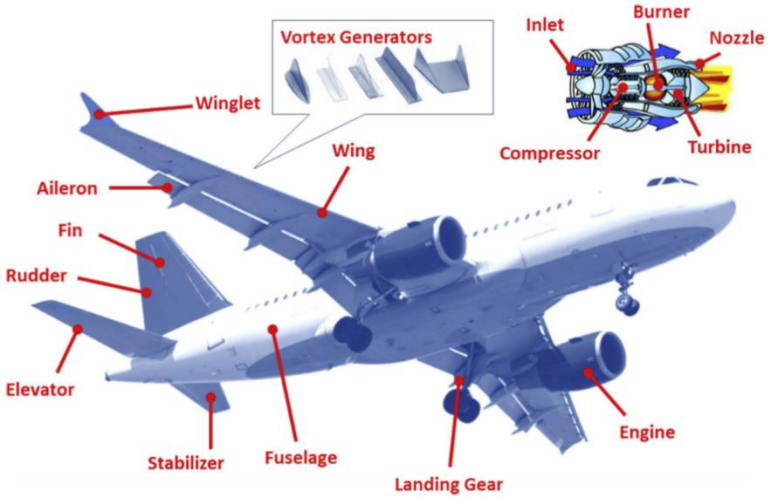

Figure 1.6: Schematic representation for some of the available and promising applications of SMA in aerospace area of technology [8].

The research centers of Boeing and NASA have been the pioneers for initiating the projects based on SMA. Boeing has been working on a project for implementing high-temperature SMA in the chevron of the jet engine and optimizing the design in order to reduce the vibration noise, as well as improving the control systems of the aircrafts during the take-off [26,27].

Recently, NASA has been working on a project called 'Reinventing the Wheel' with the aim of improving the functionality of wheels of the moon and mars rovers [28]. One of the aims of the project was to reduce the weight of the wheels as much as possible due to the limits of total available weight of the rovers permitted by the designs. Lighter wheels save some weight for the installation of more and heavier exploring and analyzing equipment. Lighter wheels also facilitate the speed of the transportation of the rovers. In addition to the lightweight, flexibility of the wheel was an important goal, as the space-rovers work in harsh thermal and mechanical stress conditions. Considering all the above-mentioned limitations, they have recently reconfigured the design and implemented SMA wire-chains for the tire of the wheels **Figure 1.7**, which are capable of working in extreme conditions, while keeping their characteristics, in this case superelasticity of SMA is the implemented characteristic (section 1.2.6.2).

Figure 1.7: SMA-based flexible tire of the Mars rover wheels, recently revealed by NASA [28].

1.1.5 Robotic applications

Similar to the previous areas of applications, SMA have been also explored for being utilized in robotics, where the performance, intelligence, controllability and the compactness are of the special interest. The SMA integrated robots can be categories by their forms of movement. Some of the examples are shown in **Figure 1.8** [8].

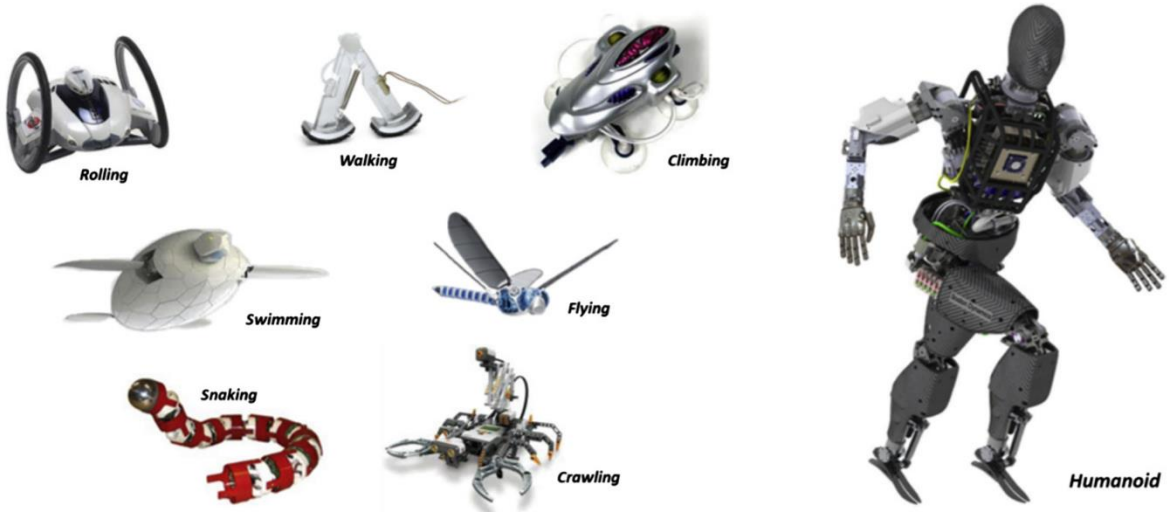

Figure 1.8: Schematic representation for some of the available and promising applications of SMA in robotic area of technology [8].

Size and shape affect the functionality of the SMA-based robotic systems. Recently, Kim *et al.* [29] from Harvard University have designed an artificial muscle fiber, made of Nitinol. The fibers, with 400 µm diameter and 0.5 m length, as shown in **Figure 1.9**, were annealed in a range of temperatures in order to stabilize a range of transition temperatures. Then the pitch of the spring-like fibers was inversed. By this action, a permanent pre-existing stress is created in the fibers, which facilitate the two-way actuation task (section 1.2.6.1). Then, the fibers are stitched together and integrated into a mesh form of tubal volume, containing segments with longitudinal as well as circumferential muscle fibers. To exploit the thermoelastic characteristics (section 1.2.6.1), the SMA muscle fibers are heated individually via the Joule heating mechanism. As can be observed in the figure, the individual heating of the segments gives rise to a 3D Oligochaeta-inspired actuation.

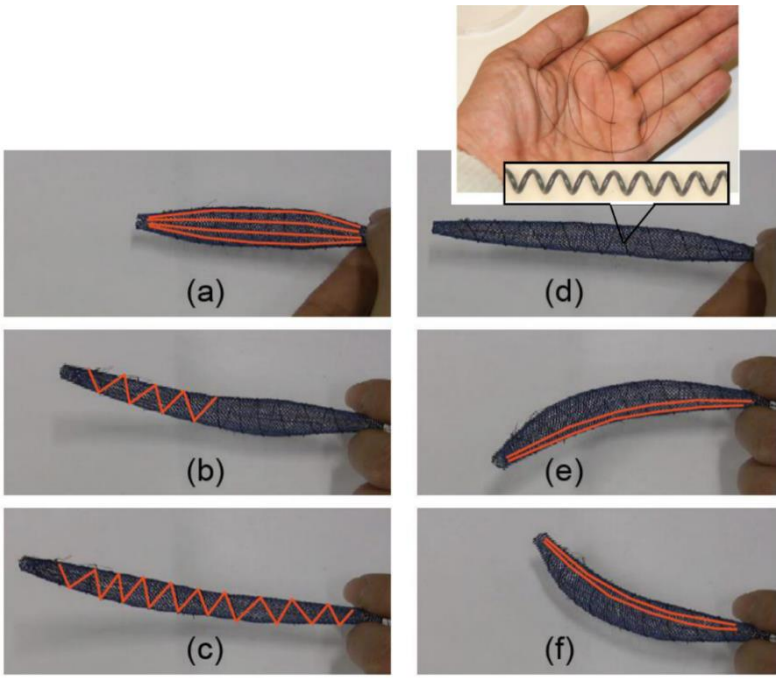

Figure 1.9: 3D Oligochaeta-inspired actuation, the activated muscle groups are shown in red: a) all the longitudinal segments are contracted, b) the circumferential segments are partially contracted, c) the circumferential segments are fully contracted, d) all segments are in the relaxed status, the inset shows the magnified image of the muscle fiber, e) the longitudinal segments in the bottom side of the structure are contacted, f) the longitudinal segments in the top side of the structure are contacted [29] (modified version of the original Figure is represented).

1.2 Ni_2MnGa

Stoichiometric Ni_2MnGa is a full Heusler compound having the nominal formula X_2YZ, where X and Y are typically among the d-block metals and Z is typically among the p-block elements [10]. Together with the stoichiometric Ni_2MnGa, there exist a large number of investigations in off-stoichiometric Ni_2MnGa (Ni-Mn-Ga) as well as doped compositions containing e.g. Fe, Co and Cu, aiming at tuning the transition temperatures and modifying the functionality of the material [30,31] (sections 1.2.2 and 1.2.3).

Ni-Mn-Ga is the first and most studied compound in FSMA however, later on, other Ni-Mn based Heusler compounds such as Ni-Mn-(Sn, In, Sb) have been also reported in the literature, having interesting properties such as inverse magnetocaloric effect [32]. The strong coupling between the magnetic degrees of freedom and the structural degrees of freedom in Ni-Mn-Ga expands the inter-connections between the characteristics of the material from thermo-mechanical in the conventional SMA to thermo-magneto-mechanical in FSMA. In the following, first the crystallographic structure of Ni_2MnGa is briefly introduced in the high temperature and low temperature phases, followed by the description of magnetic characteristics of the material. Second, the effects of composition on the martensitic crystal structure as well as the critical transition temperatures are introduced, followed by a brief discussion on the effects of the thermodynamically irreversible processes on the hysteretic martensitic phase transition. Third, different thermo-magnetic paths of the martensitic phase transition are introduced; and finally, the typical actuation mechanisms, reported for Ni-Mn-Ga are briefly discussed.

1.2.1 Structural and magnetic characteristics

The crystal structure of Ni_2MnGa at high temperature is determined as $L2_1$ structure with the space-group of Fm-3m, which consists of four face-centered cubic (fcc) sub-lattices. The lattice parameters for a stoichiometric stress free Ni_2MnGa is a = 0.582 nm. As it is shown in **Figure 1.10a**, the (0, 0, 0) and (1/2, 1/2, 1/2) positions are occupied by Ni atoms, (1/4, 1/4, 1/4) positions are occupied by Mn atoms and (3/4, 3/4, 3/4) fcc lattice-positions are occupied by Ga atoms [10].

As a thermoelastic material, Ni-Mn-Ga undergoes a reversible diffusionless, first-order phase transition between the high temperature cubic phase, whose characteristics have been mentioned above, and the low temperature low symmetry (e.g., tetragonal, monoclinic, orthorhombic) phase. The high-temperature phase is called austenitic and the low-temperature phase is called martensitic phase (**Figure 1.10b)**. Symmetry breaking occurs over the phase transition by the lattice strain as well as shuffling or shearing of certain planes of the crystal lattice, give rise to the distortion of the lattice parameters, which can be explained by Bain distortion model [33]. The distortion has also been reported to resemble Jahn-Teller effect in perovskites [34,35]. The distortion can result in tetragonal martensitic cells, which is shown in **Figure 1.10b**, or orthorhombic distorted cells where $a \neq b \neq c$ or even if the distortion accompanies with angular deformation, it could result into monoclinic cells with $a \neq b \neq c$ and $\beta \neq 90^{o}$. The cells are typically reported in a configuration setting, where the monoclinic cells are considered as pseudo-orthorhombic cells with a slight distortion in ɣ ($\gamma \neq 90^{o}$); this setting is called austenitic setting. The schematic representation of the relative orientations between the standard martensitic (dark red) and the austenitic setting (black) is reported in **Figure 1.10c**. The indices show the three axes of the martensitic cell in the two represented settings. The monoclinic cell non-right angle is β in the standard martensitic setting and ɣ in the austenitic setting. The austenitic setting (representing the cells as Pseudo-orthorhombic) provides a suitable compromise between the austenitic cell and martensitic cell by representing the axes of the martensitic monoclinic cell, matched with the axes of the cubic austenitic cell. Therefore, one can follow the evolution of the cells upon the martensitic phase transition nevertheless; this setting does not describe the monoclinic cells as precise as the actual monoclinic cells in the standard setting.

As a class of Heusler compounds, Ni_2MnGa also undergoes a magnetic second-order phase transition between the low temperature ferromagnetic and the high temperature paramagnetic phase [10]. The ferromagnetic order in Ni_2MnGa is mainly the result of indirect exchange interaction between the localized magnetic moments of the Manganese atoms. The interaction between the d-orbitals of Mn atoms and the d-orbitals of neighboring Ni atoms results in the formation of degenerated hybrid states. The p-orbitals in Ga atoms typically serve as the mediator for the exchange interaction between the Mn atoms (**Figure 1.10a**) [36,37]. The magnetostructural phase transition in Ni-Mn-Ga takes the advantage of the magnetostructural coupling of the cells over the martensitic phase transition. The easy magnetization direction of the martensitic cells in the two above described settings is ascribed as b’ = c (**Figure 1.10c)**.

In addition to the cell distortion though the Bain model, discussed above, it has been evidenced by high-resolution techniques [38-40] that over the martensitic phase transition in Ni-Mn based FSMA, the material could additionally undergo a periodic shuffling of the atoms (**Figure 1.10c**) along certain crystal orientations. This periodicity, which is believed to be due to the instability of the cubic austenitic cells over the phase transition, can be described as the presence of arrays of e.g., five-fold (5M) [41] or seven-fold (7M) [42] commensurate /incommensurate structures with the modulation

direction along specific orientation of the lattice planes. The simplified schematic view of the 5M and 7M structures are shown in **Figure 1.10d**. The modulation direction in 7M monoclinic structure for instance, is along the c' axis of cells in the standard martensitic setting (**Figure 1.10c**).

The origin of this periodicity is a subject of debate. There are two major models explaining this phenomenon, i.e., soft phonon model and the adaptive model. The first model describes the formation of the modulation as a result of softening, occurs in some of the phonon modes in the crystal lattice, giving rise to a short-range ordering of the austenitic cells as a function of reducing temperature [43]. The adaptive model considers the modulation as a long-range ordering of $L1_0$ tetragonal nanotwins [44]. The latter model is perfectly capable of describing the magnetic anisotropy as well as the mechanical properties of the material in the martensitic phase however; the experimentally evidenced presence of premartensitic phase as well as the incommensurate structures have been defined by the adoptive model with some uncertainty. In addition, in this model the conclusive explanation for the large-scale periodicity of the nanotwins is under debate. Gruner *et al.* [45] have recently reported a unified version of the two models using density functional theory calculation. They highlighted the formation of modulations by an initial contribution of phonon softening in the form of shuffling of lattice planes, which ends up with the formation of adaptive nanotwins. Very recently, Orlandi *et al.* [35] have investigated the evolution of the crystal structure of 5M Co-doped Ni-Mn-Ga over the martensitic phase transition by means of Neutron diffraction analysis. They have referred to the soft-phonon model by highlighting the primary role of modulation in the martensitic transition, which in turn induces the tetragonal distortion.

As we scale up, the next level of the martensitic architecture in Ni-Mn-Ga structure can be described as the mesoscopic elastic domains. During the martensitic phase transition, the symmetry breaking gives rise to a stress, which needs to be compensated by the martensitic cells. To accommodate the stress, the material forms invariant planes (habit-planes), which are the connections between austenitic and the martensitic cells. The habit-planes do not undergo distortion during the transition. Since the austenitic and the martensitic cells do not match perfectly, in order to fit the cells and form the habit planes, the martensitic cells of the material could undergo a slip dislocation process or the twinning process. The latter process is determined as an efficient way of compensating the stress. The twinned domains, which are called twin variants, are connected by atomically sharp boundaries called twin boundaries (**Figure 1.10e)** [44, 46-48]. The crystallographic details related to the twin boundaries including the types of twinning, symmetry operators and the twinning stress will be discussed in chapter 4. In the larger scale, colonies of twin boundaries with different crystallographic orientations in the martensitic phase differentiate by additional boundaries (**Figure 1.10f**). In polycrystalline martensitic materials, these boundaries can be an analogy for the grain boundaries [49] and in the single crystalline martensitic materials, they can be ascribed to the martensitic interfaces [50] (details are provided in chapter 4).

Very recently, Schwabe *et al.* [51] have proposed a model describing the hierarchical architecture of the Ni-Mn based Heusler compounds by highlighting the role of tetragonal distortion as the key parameter. The model includes five levels of martensitic building blocks starting from atomic scale to macroscale, which grow successively with the purpose of local energy minimization upon the martensitic transition.

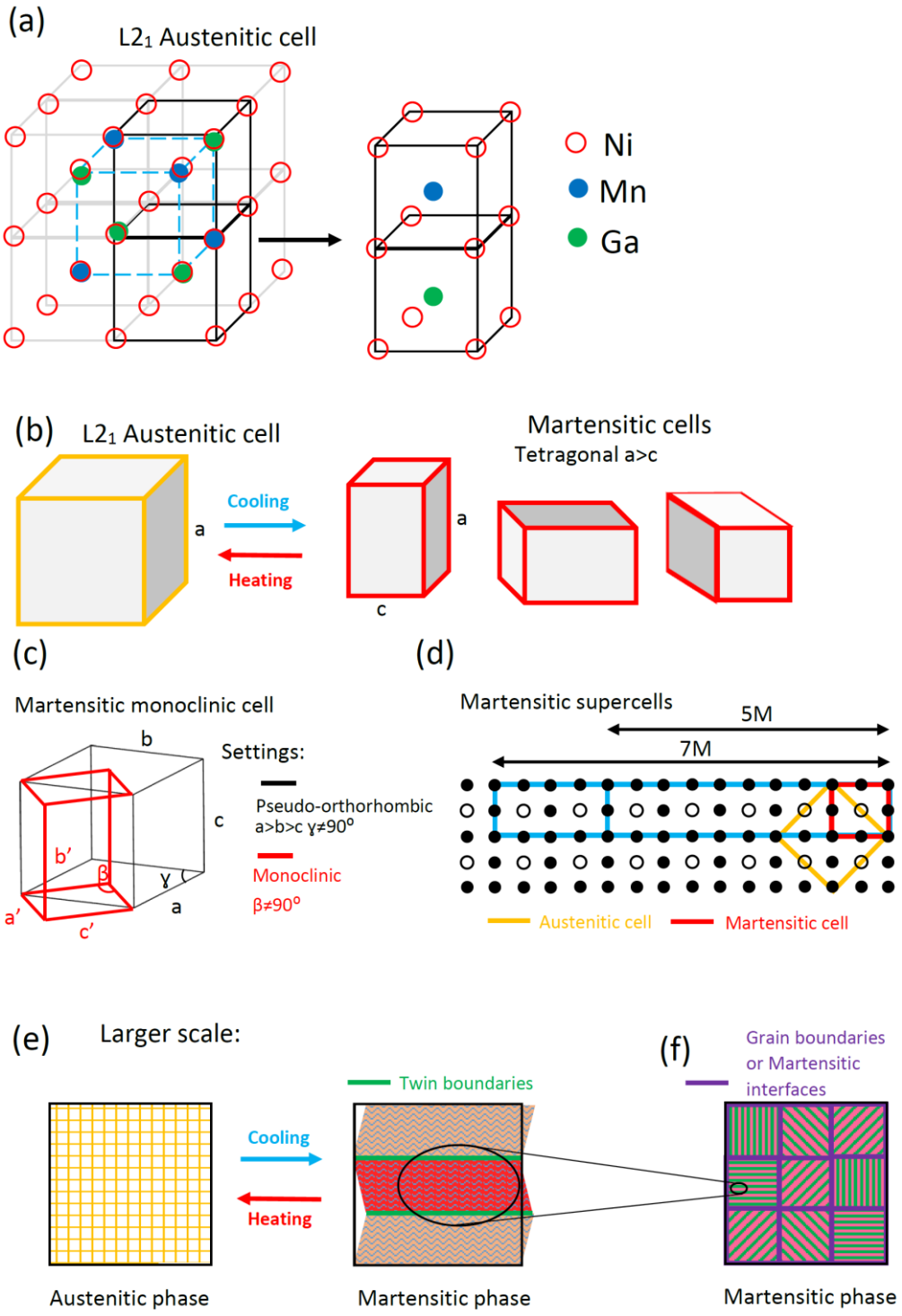

Figure 1.10: Ni_2MnGa structure: a) the austenitic crystal structure in the atomic level, Ni, Mn and Ga atoms are labeled. b) cell distortion upon the martensitic phase transition. c) schematic view of the relative orientations of the martensitic cell in the standard martensitic setting (red) and the austenitic setting (black); d) simplified representation of the martensitic superstructures (blue); e) simplified schematic view of the of hierarchical nature of the self-accommodation of the martensitic cells; yellow squares being the austenitic cells, tiny blue zig-zag features being the martensitic superstructures (modulation); green lines being the twin boundaries and f) purple lines being the martensitic interfaces or grain boundaries.

1.2.2 Composition vs. structure and modulation

During the martensitic transition, the electronic structure of Ni-Mn-Ga in the Fermi level is modified. This gives rise to a reconfiguration of the Fermi surface of the material, which can be observed as the phonon anomalies in the low temperature phase. Therefore, the number of the material's valence electrons per atom (e/a) could affect the crystallographic structure of the cells and the superstructures in the martensitic phase. There are a number of reports in the literature using the theoretical tools such as first principle calculations [52] as well as experimental investigations to figure out the dependence between the martensitic crystallographic structure and the composition of Ni-Mn-Ga. In a report by Richard *et al.* [53], which is shown in **Figure 1.11**, they investigated the structures of the martensitic cells for a set of Ni-Mn-Ga single crystal samples with a range of compositional difference. The plot shows the crystallographic structures of the martensitic cells as function of Mn and Ga contents. The inclined dashed line shows the position, where the Ni content is 50 at.%. The inclined solid lines indicate the measured martensitic transition temperatures. The points marked by the circle, rectangle and triangle vectors show the tetragonal, orthorhombic structure of the martensitic cells and the mixed structure of the two, respectively. As can be observed, when the content of the Ga increases at the expense of the content of Mn, the tetragonal structure is energetically stabilized.

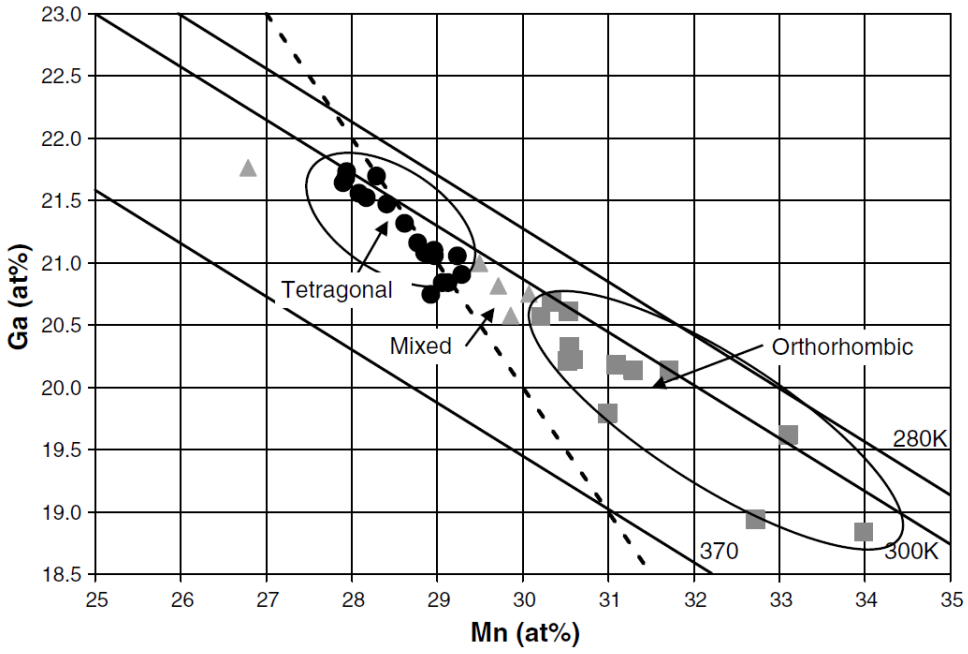

Figure 1.11: Compositional dependence of the structure of Ni-Mn-Ga martensitic cells measured for Ni-Mn-Ga single crystals [53].

The compositional dependence of the superstructures has been evaluated by ab initio calculations as a function of elemental contents for near-stoichiometric $Ni_{2+x}Mn_{1-x}Ga$ samples by Entel *et al.* [54]. **Figure 1.12** shows the sector of the phase diagram in the left-side of the figure including Ni-Mn-Ga compositions in the range of 7 to 8 of the valence electrons per atom (e/a). The dashed lines show the phase transition of the compositions, having the label e/a. In the phase diagram, a number of experimental data from Ni-Mn-Ga samples with different compositions have been inserted from previous works. The black squares represent the samples having the Curie temperature higher than martensitic transition temperature ($T_C > T_M$). The white squares represent the samples having $T_C <$

T_M. The black circles represent the samples having the Tc = T_M. The arrows show the calculated stabilized martensitic structure and modulations for different compositions of Ni-Mn-Ga in the phase diagram. The yellow circle in the center of the diagram shows the stoichiometric Ni-Mn-Ga, i.e., Ni_2MnGa (e/a = 7.5). The blue arrow shoes the e/a region, where typically the orthorhombic and monoclinic 5M and 7M structures are stabilized. The red arrow shows the e/a region, where typically the tetragonal NM structures are stabilized. The sector, shown in **Figure 1.12** is a part of the extended Ni-Mn-Ga phase diagram shown in the right side of **Figure 1.12** showing the position of the sector in yellow.

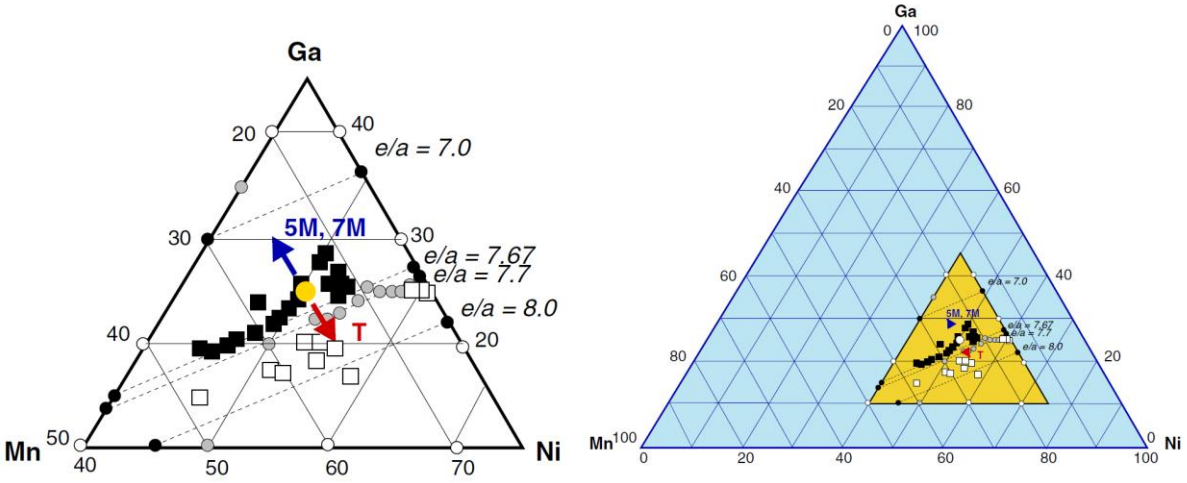

Figure 1.12: Compositional dependence of the superstructures for Ni-Mn-Ga martensitic cells, shown in the phase diagram [54].

1.2.3 Composition vs. magnetostructural phase transition

In addition to the structure of the cell, superstructures, twinning and interfaces, Ni-Mn-Ga composition could also significantly affect magnetocrystalline anisotropy, the transition critical temperatures and saturation magnetization, enabling a wide range of tunability of the material's basic properties. As mentioned in 1.2.1, the material undergoes a reversible structural first order and the magnetic second order phase transitions. One of the highly used techniques to measure the critical transition temperatures is to measure the magnetization of the samples over a certain range of temperatures in the presence of an external applied magnetic field. This technique enables tracking the magnetostructural phase transition. **Figure 1.13** shows an experimentally driven phase diagram of Ni- and Mn-rich Ni-Mn-Ga polycrystalline samples, reported by F. Albertini *et al.* [55], representing the critical transition temperatures as a function of composition. The diagram is accompanied by a number of schematic plots, showing the shapes of isofield magnetization curves for different contents of Ni as a function of temperature, where the critical transition temperatures can be extracted. The T_{AM} in the diagram is assigned for the temperature in which the cubic austenitic phase transforms to the low symmetry martensitic phase upon cooling (forward transition). The T_{MA} in the diagram is associated with the temperature in which the low symmetry martensitic phase transforms to the cubic austenitic phase upon heating (reverse transition). The T_{CA} is assigned for the Curie temperature of the austenitic phase in which the paramagnetic austenitic phase transforms to the ferromagnetic austenitic phase upon cooling and the vice versa upon heating. The T_{CM} is assigned

for the Curie temperature of the martensitic phase in which the paramagnetic martensitic phase transforms to the ferromagnetic martensitic phase upon cooling and the vice versa upon heating. As can be observed in the diagram, these critical transition temperatures raising from the first order structural and the second order magnetic phase transitions overlap in certain points, giving rise to a merged first-order and second-order phase transition for a certain range of Ni-Mn-Ga compositions. It is also observable that the martensitic transition temperatures ($T_{AM,}$ T_{MA}) show an opposite trend vs. the Ni content with respect to and the Curie temperatures ($T_{CM,}$ T_{CA}). In addition, a smoother dependence of the Curie temperatures is realized vs. the Ni content compared to the structural transition temperatures. The origin of the observed decrease of the transition Curie temperatures as the Ni content is increased can be explained by referring to the origin of the magnetism in this class of Heuslers, in which magnetism arises mostly from the Mn atoms. By increasing the content of Ni at the expense of the Mn, Ni atoms occupy the Mn positions in the structure, therefore (as mentioned in 1.2.1) the magnetic moment resulted by the exchange interaction between the Mn atoms is reduced. On the other hand, the raise of the structural transition temperatures upon increasing the Ni content can by related to the increases of the density of the valence electrons per atom (e/a). These trends can be determined by the first principle calculations and can be modeled using the concepts of phenomenology such as Ginzburg-Landau [56] nevertheless, a reasonable error and some misfits with respect to the experimental data is typically expected.

The schematic plots in the right side of the figure show the expected isofield magnetization curves of the samples with different content of Ni; the dashed lines are attributed to the cooling curves and the solid lines show the heating curves. The assigned numbers next to the plots indicate the different positions of the phase diagram, where such shapes of the isofield magnetization plots are expected, taking into account the content of Ni and the lines related to the critical transition temperatures on those positions. For instance, [0, 1) (the first plot on top) indicates the expected shape of the curves for a range of Ni content from 2 to 2.16. The parentheses show that the indicated upper limit of the range is not included. As can be realized from the plots, their shapes are determined basically by the magnetic status of the samples in the measured range of temperature, which can be followed through the shown phase diagram. As an example, for the first plot on top upon cooling the material undergoes respectively: the magnetic phase transition from paramagnetic to ferromagnetic, which is followed by a structural phase transition from austenite to martensite.

There exist two critical composition points, assigned as 1 and 2, in which the magnetic and the structural phase transition are merged. In other words, Ni-Mn-Ga samples having the Ni content range between the points 1 and 2 undergo a merged first and second order phase transition. Further content of Ni results in direct transition from the paramagnetic austenitic phase to ferromagnetic martensitic phase.

1.2.4 Martensitic phase transition and the origin of hysteresis

The first plot, shown in **Figure 1.13** on the top-right of the figure is reconstructed in **Figure 1.14** to explain the typical hysteretic and the smooth (non-singular) character of the martensitic phase transition in FSMA including Ni-Mn-Ga.

In contrast to the conventional thermodynamic phase transitions, which are based on the diffusion of the atoms, martensitic phase transition is a diffusion-less phase transition in which, the coordinated

shuffling of atoms in between the interatomic distances results in the cell distortion in martensitic phase (section 1.2.1). The transition can be divided into two steps, i.e. nucleation and growth. When the material is cooled down below the martensitic phase start temperature (T_{Ms}), the shear stress, caused by shuffling of atoms nucleate the phase boundaries.

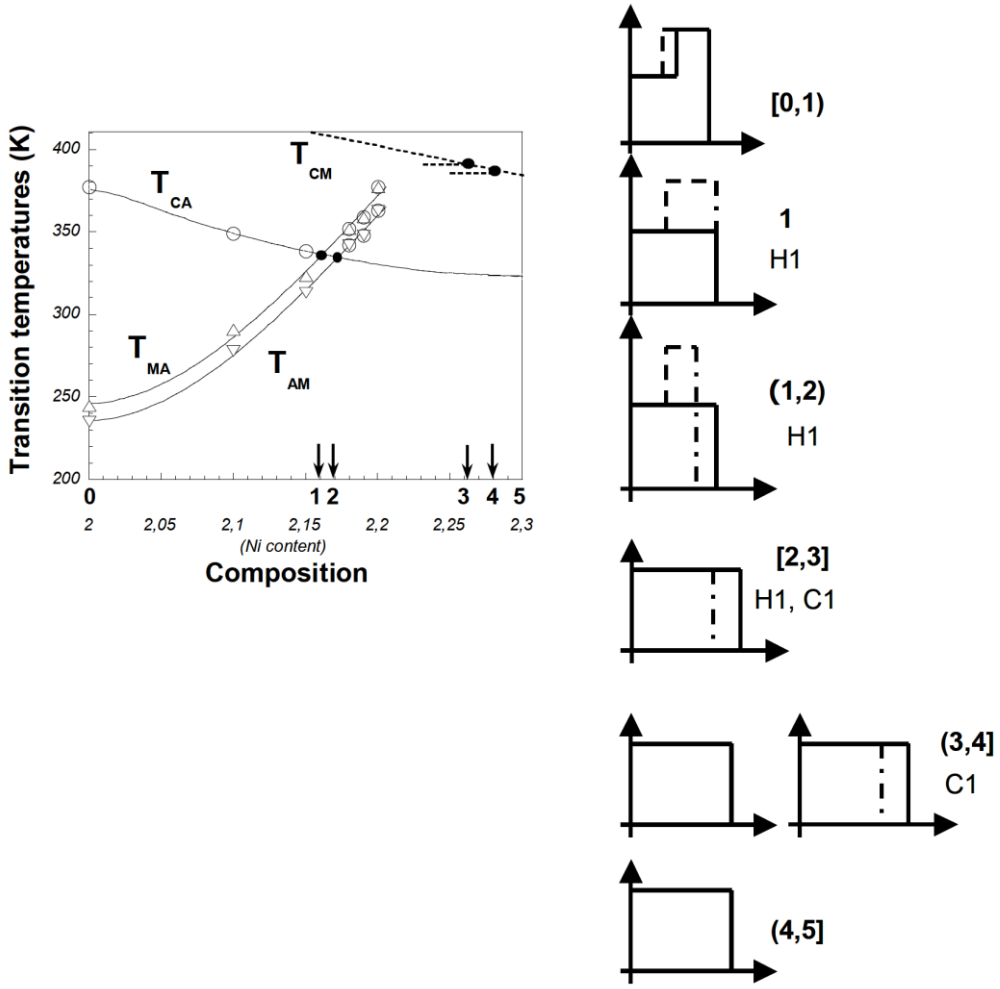

Figure 1.13: Experimentally driven phase diagram of Ni-rich Ni-Mn-Ga polycrystalline samples, showing the critical structural and magnetic transition temperatures as a function of Ni content (left), the corresponding expected isofield magnetization curves of Ni-Mn-Ga for different range of Ni content [55] (modified version of the original Figure is represented).

The transition proceeds with moving the phase boundaries, i.e., growth of the martensitic phase at the expense of the austenitic phase until the entire volume of the austenitic phase transforms to the martensitic phase; that temperature is called martensitic phase finish temperature (T_{Mf}). In the reverse transition upon heating, the austenitic high symmetry phase is nucleated at the austenitic phase start temperature (T_{As}) and grows until the entire high symmetry parent phase is recovered at the austenitic phase finish temperature (T_{Af}). In a thermodynamically ideal condition for a single variant single-crystal material, the transition is abrupt, meaning that the forward transition-start and -finish temperatures match and the only heat exchange is related to the thermodynamic latent heat (**Figure 1.14a**). Upon the reverse phase transition, the austenitic phase nucleates and grows at the same temperature as the forward transition. This unique temperature, shown in **Figure 1.14a** as T_0, is ascribed to the thermodynamic equilibrium transition temperature.

Figure 1.14a shows the phase transition in the presence of chemical Gibbs free energy term (ΔG_{ch}) (**Equation 1.1**). In such condition, the chemical free energy of the material is the only determiner of the phase transition and the heat exchange during the phase transition is equal to the latent heat of each phase. The transition occurs at the temperature, where the chemical Gibbs free energy (ΔG_{ch}) of the austenitic and martensitic phases are in equilibrium. The transition in such condition has a sharp and singular character. **Figure 1.14b** shows the martensitic transition in the presence of the frictional work (W_{fr}), which is related to a non-chemical, thermodynamically irreversible process of heat dissipation during the formation and moving of the phase boundaries. The frictional energy term is typically dissipated as heat upon the formation a well as moving of the phase boundaries during the transition. The frictional term resists the nucleation and the growth of the phase boundaries; therefore, the material requires an additional energy to overcome both the frictional resistance as well as chemical Gibbs free energy. By undercooling over the forward transition as well as a superheating over the reverse transition, the material gains additional energy as a result of increasing the gap between the free energy of the martensitic and the austenitic phase (**Figure 1.14d**). Hence, the forward and the reverse transitions occur sharply but with a delay with respect to the thermodynamically equilibrium transition temperature (T_0). **Figure 1.14c**, shows the more realistic condition that is typically observed in Ni-Mn-Ga samples. In this condition, the elastic energy term, shown in **Equation 1.1** is also involved, therefore; the total Gibbs free energy (ΔG_{tot}) can be determined as the summation of chemical free energy (ΔG_{ch}), frictional work (W_{fr}) and the elastic energy (ΔG_{el}). The latter term in a multi variant system (real system) is attributed mainly to any type of obstacles hindering the growth of the phase, e.g., grain boundaries, interfaces, interaction of the twin variants, precipitates and crystal imperfections. The elastic energy can also turn the singular temperature sharp transition to a smooth transition range giving rise to the transition start and finish temperatures [57]. It is worth noting that there are also other non-chemical energy terms, which can contribute to the phase transition, e.g., interfacial energy and surface energy however, their contribution is expected to be minor with respect to the elastic term as well as the frictional work in our system.

Equation 1.1:

$$\Delta G_{tot} = \Delta G_{ch} + (\Delta G_{el} + W_{fr})$$

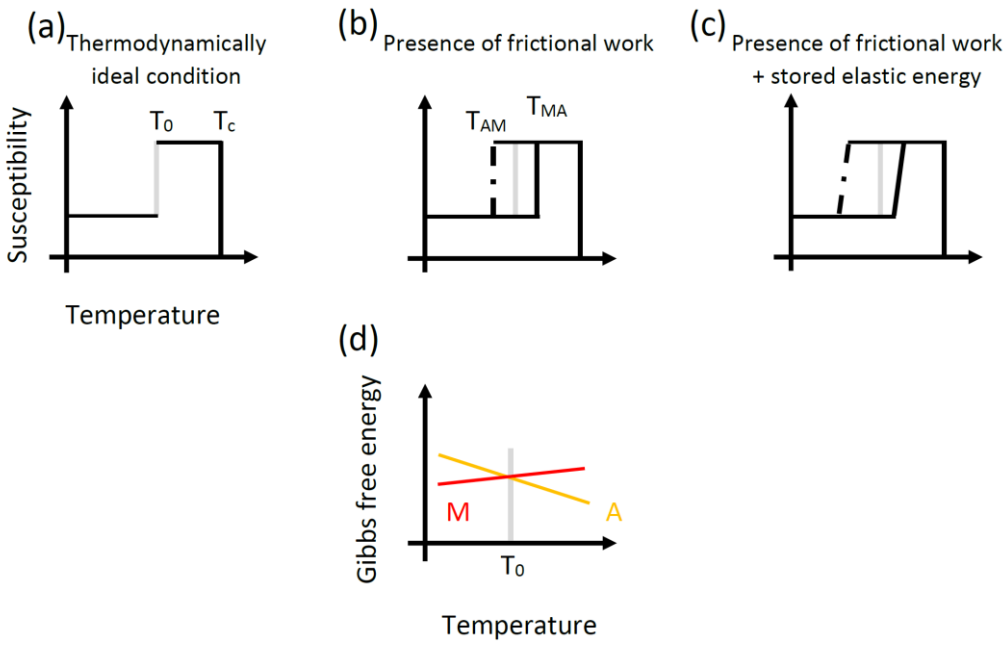

Figure 1.14: Martensitic transition from the thermodynamic point of view: a) phase transition in the absence of the non-chemical energies, b) transition in the presence of the frictional work, c) transition in the presence of the frictional work and elastic energy, c) simplified plot of the Gibbs free energy vs. temperature for the martensitic (red line) and the austenitic phase (yellow line).

There are some works in the literature reporting the physical origins of the effects, resulting in the observed hysteresis and the blunt martensitic transition. Recently Gutfleisch *et al.* [58] has categorized the possible origins of the hysteresis in FSMA into the intrinsic and the extrinsic parameters. According to the report, the two main aspects of the intrinsic parameters contributing to the hysteresis are the magnetism and the order parameters and among the extrinsic contributors, the parameters related to the kinetics of the transition as well as the characteristics of the material, related to the microstructure can be taken into account. The parameters are listed in **Figure 1.15**. These parameters are also expected to serve as the obstacles, affecting the width of the transition [59], although the extent of the contribution and the mechanisms of the influence of each parameter in the hysteresis as well as the width of the transition of the material are still unclear.

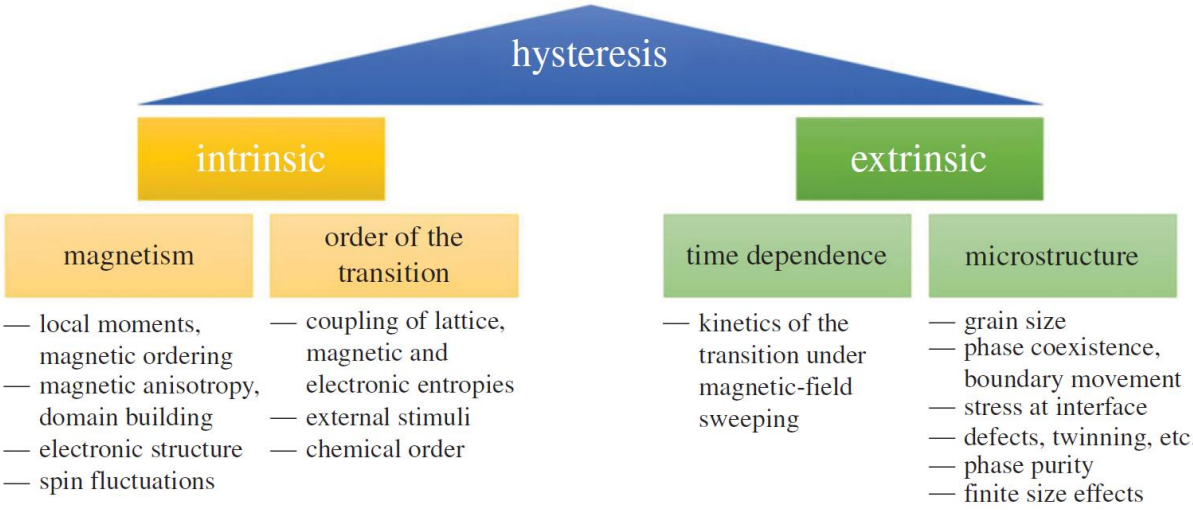

Figure 1.15: Possible physical origins of the hysteresis [58].

1.2.5 Phase transition vs. magnetic properties

In addition to the composition (section 1.2.3), the magnetic properties of Ni-Mn-Ga can influence the martensitic phase transition and in certain conditions, it could even be the driving force for the martensitic phase transition. Martensitic phase transition by an external magnetic field or assisted by an external magnetic field in Heusler compounds including Ni-Mn-Ga has been of great interest due its potential to be exploited in magnetic field controlled actuation [60] as well as magnetocaloric applications [13]. As it was mentioned in section 1.2.4, from the thermodynamic point of view, the free energy of the martensitic and the austenitic phase rule out the phase transition. When an external magnetic field is applied, the magnetic free energy terms are also added to the total Gibbs free energy equation (**Equation 1.2**).

Equation 1.2:

$$\Delta G_{tot} = \Delta G_{ch} + \left(\Delta G_{el} + W_{fr}\right) + (\Delta G_{MAE} + \Delta G_{mag})$$

ΔG_{mag} is referred to Zeeman energy which depends on the difference between the saturation magnetization of the austenitic phase and the martensitic phase for an applied magnetic field of $\mu_0 H$ (**Figure 1.16a**), being $G_{mag} = -M.\mu_0 H$. In Ni-Mn-Ga, the saturation magnetization in the martensitic phase is higher than in the austenitic phase; therefore, the martensitic phase is stabilized in the presence of an external magnetic field [60]. The other magnetic energy term ΔG_{MAE} represents the difference between the magnetocrystalline anisotropy energy of the two phases. In the martensitic phase, due to the lower symmetry, the anisotropy energy term is one order of magnitude higher than the austenitic cubic one and, in the approximation of a uniaxial system, it can be expressed by **Equation 1.3** (truncated at the second order), where θ is the angle between the magnetization vector and the easy-magnetization direction [61].

Equation 1.3:

$$G_{MAE} = Ku(Sin^2\theta)$$

A graphical description of Zeeman energy in the martensitic and austenitic phase and the anisotropy energy in the martensitic phase is provided in (**Figure 1.16 a, c**). The two energy densities are represented by the areas.

Based on the above discussion, a simplified temperature magnetic-filed phase diagram for Ni-Mn-Ga is shown in **Figure 1.16b**. The y-axis shows the strength of an external magnetic field and the x-axis is the temperature axis. The austenitic and the martensitic regions are shown in the diagram. The area isolated by the inclined dash-lines is referred to the region where both the phases co-exist due to the irreversible process of the transition (section 1.2.4). Three paths of transition are shown in the diagram by double-headed arrows. The grey arrow shows the typical temperature induced phase transition called (zerofield phase transition). The pink arrow shows an example for a magnetic field assisted temperature induced phase transition. In this path, a constant external magnetic field is applied to the system while the transition is induced by temperature. As can be observed, the dash-lines are inclined following the discussion in the previous paragraph. The martensitic transition shifts to higher temperatures as an external magnetic field is applied to the material. The brown arrow shows the condition in which the transition is induced by external magnetic field. In this path, starting from the austenitic phase, the temperature is kept constant (typically close to the transition temperature) and the magnetic terms of the total Gibbs free energy shown in **Equation 1.2** provide the free energy,

required for the martensitic phase transition. The detailed mechanism including the quantitative work output and the different energy compromises can be found in [60].

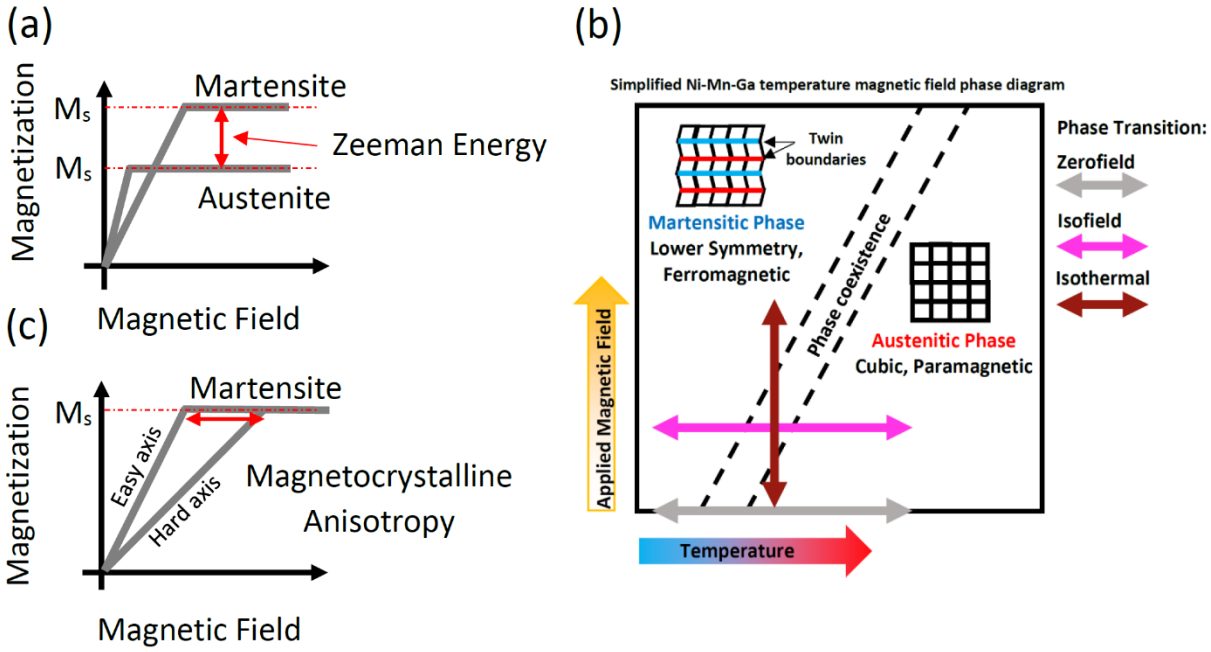

Figure 1.16: a) simplified representation of the Zeeman energy arising from the magnetization curves vs. applied magnetic field for the austenitic phase and the martensitic phase (M_s being the saturation magnetization), b) simplified temperature magnetic field phase diagram for Ni-Mn-Ga, showing three paths of the thermomagnetic phase transition, c) simplified representation of the magnetocrystalline anisotropy arising from the difference between the magnetization curves vs. the applied magnetic field along the magnetization easy axis and the magnetization hard axis of the martensitic cells.

1.2.6 Actuation mechanisms

So far, the key parameters of the phase transition in Ni-Mn-Ga have been introduced. However, phase transition does not necessarily result in a macroscopic mechanical deformation of the material. In fact, the entire complex twinning system described in 1.2.1 form to accommodate the stress induced by the symmetry breaking, preventing the macroscopic shape change. Therefore, for the material to undergo reversible mechanical deformation, there are some certain paths; the typical ones are described briefly below. It is important to note that, based on the desired application purposes, the paths could be also combined.

1.2.6.1 Shape memory effect

Shape memory effect is the most well-known characteristic of the SMA, so that the name of these types of materials ‘shape memory alloys’ has been adopted from this effect. The principle of the effect is based on thermoelastic phase transition. The symmetry breaking stress upon the phase transition from the high temperature phase to the low temperature phase is accommodated by the hierarchical architecture of the twin boundaries forming in the martensitic phase. The formation of the twins and their hierarchical self-accommodation is the most efficient mechanism to accommodate the elastic stress caused by the phase transition. Among the characteristics of the twins, there are the twinning

symmetry, energy, stress, and the twinning periodicity (chapter 4), which could be dependent on the cell misfit between the austenitic and the martensitic phase. In the process of shape memory effect, the twin boundaries, formed during the temperature induced phase transition, are mechanically moved through the specimen by an external mechanical stress. In this process, which is also called detwinning, i.e. some of the twin variants expand at the expense of the others. The collective consequence of the shuffling of twin boundaries is the macroscopic deformation of the material, which could be observed as the overall elongation or contraction of the specimen in specific directions depending on the direction of the applied stress and the orientations of the martensitic cells [62,63]. For this to happen, the applied stress needs to be higher than the twinning stress as shown in **Equation 1.4**.

Equation 1.4:

$$\varepsilon_0 \sigma_{ex} \geq \varepsilon_0 \sigma_{tw}$$

The external stress is defined as σ_{ex}, the twinning stress is determined by σ_{tw} and ε_0 is the martensitic distortion ($\varepsilon_0 = 1 - \frac{c}{a}$). The most typical form of shape memory effect can be explained as one-way shape memory effect (**Figure 1.17**), in which the material in the martensitic phase is deformed by an external stress; upon the heating, the specimen transforms to the austenitic phase and regains its previous shape. Upon the subsequent cooling, the material transforms to the twinned martensite. In this form of shape memory effect the deformation is irreversible, meaning that a permanent external stress is required for deforming the material in the martensitic phase, since the thermal cycles would not deform the material macroscopically [64].

Since a reversible actuation is typically beneficial for a large number of applications, people in the labs and in industry have developed some special designs or material post-growth treatments to turn the one-way shape memory effect to two-way shape memory effect, in which, after subsequent cooling, the material transforms back to its deformed status, i.e., detwinned martensitic phase (**Figure 1.17**). Some of the applications described in 1.1.2 to 1.1.5 mainly use the following techniques:

- Appling a permanent stress to the material, e.g., by stretching, so that upon cooling the material transforms back to the detwinned status (the heat-engine in section 1.1.2);
- Connecting multiple SMA with different phase transition temperatures, so that the force created by the contraction of one alloy upon the phase transition would expand the other and vice versa (the muscle fiber in section 1.1.5);
- Special designs in the spring fashion, so that reversing the pitch of the spring from clockwise to counter-clockwise applies a permanent stress to the material (the muscle fiber in section 1.1.5);

Basically, in Ni-Mn-Ga, similar principles of shape memory effect are applied. The only difference is that the martensitic phase in Ni-Mn-Ga is a ferromagnetic phase, while the austenitic phase is a paramagnetic phase.

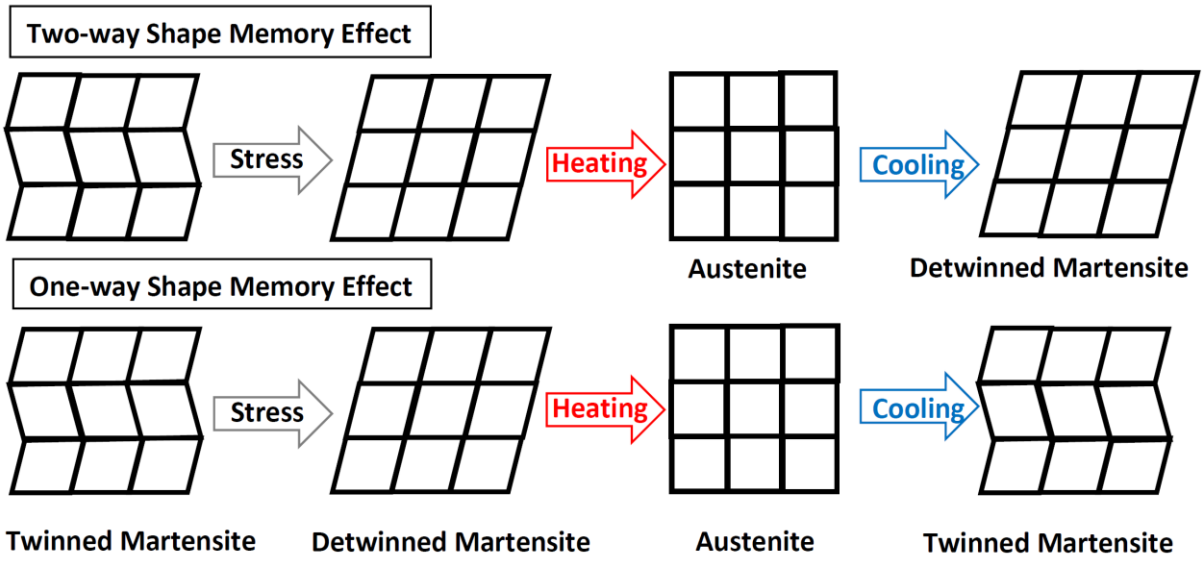

Figure 1.17: Simplified schematic view of the conventional shape memory effect.

1.2.6.2 Superelasticity

Superelasticity in SMA is based on the martensitic phase transition induced by an external mechanical stress (**Figure 1.18**). In fact, for Ni-Mn-Ga, it could be considered as an additional path for the ferroelastic phase transition, added to the temperature and magnetic field-induced phase transition paths described in 1.2.5. When the transition is induced or accompanied by an external stress, the energy term related to the external stress (ΔE_{mech}) is also added to the total Gibbs free energy (**Equation 1.5**).

Equation 1.5:

$$\Delta G_{tot} = \Delta G_{ch} + \left(\Delta G_{el} + W_{fr}\right) + \left(\Delta G_{MAE} + \Delta G_{mag}\right) - \Delta E_{mech}$$

Therefore, the chemical energy term, the elastic energy term, frictional work, magnetic energy terms as well as the energy related to the applied mechanical stress contribute to the phase transition. As for the energy term related to the external stress, it could be varied depending on whether it is a tensile or compressive stress, uniaxial or biaxial stress. The volume of the cells in the austenitic and the martensitic phases could also contribute to ΔE_{mech}.

For the phase transition induced or assisted by an external magnetic field or an external stress, the material does not necessarily undergo the detwinning process upon the phase transition [60,64]. In some cases, the energies provided by these external fields (mechanical or magnetic) influences the twinned martensitic phase by selecting some of the twin variants (or boundaries) out of the others at the proximity of the martensitic transition; typically the selection is related to the direction of these external fields [65,66]. Details are provided in chapter 3, chapter 4 and chapter 5. On the other hand, for the material to show the superelasticity effect (meaning the macroscopic deformation), it typically undergoes both the transition and detwinning process under the external mechanical stress (**Figure 1.18**).

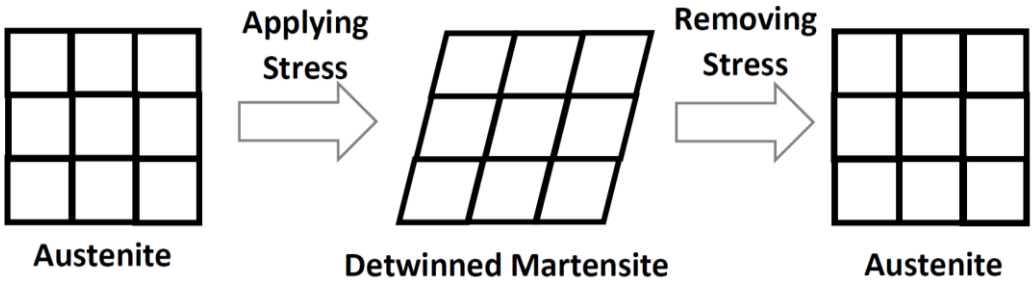

Figure 1.18: Simplified schematic view of the superelasticity in SMA.

Similar to the other actuation mechanisms, superelasticity has its own specified area of application. For instance, the new version of the Mars rover wheels developed by NASA (section 1.1.4), basically exploits the superelasticity of the NiTi. In 2006, Tao *et al.* [67] reported a design of a swimmer robot, in which Ni-Mn-Ga compound, serves as an actuator. The robot, which has been designed in the fish configure (**Figure 1.19**), exploits the superelasticity of Ni-Mn-Ga for the stress-induced actuation in the peduncle of the tail of the fish. SMA plates have been also placed as the tail fin, actuating via the superelasticity principles. In this design, which has been inspired by the swimming method of Atlantic Mackerel, 310 mm length of the robot fish swims by the assistance of the stressed induced martensitic phase transition of Ni-Mn-Ga induced by a DC motor in the 85 mm tail of the fish applying beating stress. By applying the voltage of 7 V, the tip to tip flexion of the actuator was measured as 85º at 4 HZ.

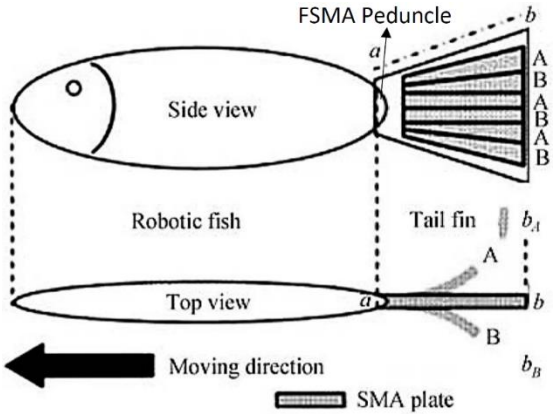

Figure 1.19: Schematic view of the robot-fish prototype, exploiting the superelasticity effect of Ni-Mn-Ga working as the tail peduncle [67] (modified version of the original Figure is represented).

1.2.6.3 Magnetic shape memory effect

In this path of actuation, the driving force for the deformation of the material is the external magnetic field, which elevate the speed of the twin boundary movement to the speed of sound. It provides the possibility of higher frequency actuation with respect to the conventional SMA actuation mechanisms, which are based on sluggish temperature induced phase transition. Obviously, this type of actuation is only applicable in FSMA and is the result of the strong magneto-structural coupling of the material. The principal of the magnetic shape memory effect is based on the reconfiguration of twinning blocks of the martensitic phase in the presence of an external magnetic field (**Figure 1.20**). The main energy terms involved in the mechanism of the actuation are the additional Zeeman energy

term due to the presence of an applied magnetic field, magnetocrystalline anisotropy energy of the martensitic variants (K_u) and the twinning stress (σ_{tw}). The magnetic shape memory effect occurs when K_u exceeds the energy required for moving the twin boundaries (**Equation 1.6**), where ε_0 is the martensitic distorsion.

Equation 1.6:

$$K_u \geq \varepsilon_0 \sigma_{tw}$$

As it is shown in the simplified scheme of the mechanism **Figure 1.20**, we consider the sketched arrangement of the twin variants on the left as the starting condition with the magnetization easy axis of the variants, shown by the arrows, rotated 90º with respect to each other. By applying an external magnetic field along the easy magnetization axis of one set of twin variants, the other set tends to align the magnetization direction of the cells along the external magnetic field to minimize the differential Zeeman energy (section 1.2.5) between the two sets of the twin variants in the external magnetic field. The alignment through switching of the magnetization direction of the cells is energy costly due to the high magnetocrystalline anisotropy energy of the martensitic cells. On the other hand, the energy required for the twin boundary motion is sufficiently low therefore, a coordinated movement of twin boundaries occurs in the material, aligning the magnetization easy axis of the cells along the direction of the external magnetic field [12, 68, 69]. The speed of the movement is close to the speed of the sound, which makes it quite faster than the conventional shape memory effect (will be discussed below). The process of the twin boundary motion is called detwinning and the result can be realized by macroscopic deformation of the material. In Ni-Mn-Ga 7M monoclinic martensite, the magnetization easy axis is the structurally the shortest axis of the martensitic cell (section 1.2.1) therefore, when the cells are aligned having their magnetization easy axis (shortest axis) along the direction of the external field, the collective result in that direction is the material shrinkage. This type of actuation is hugely dependent on the type of twinning and the microstructure of the material therefore, it has been observed so far only in single crystalline FSMA with low twinning stress of typically less than 2 MPa [70 and the references therein].

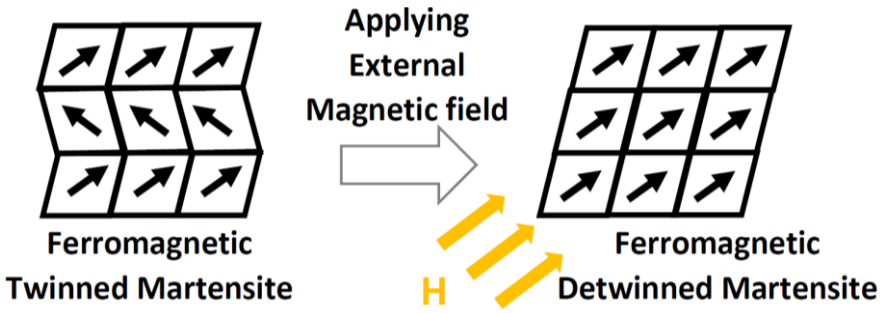

Figure 1.20: Simplified schematic view of the ferromagnetic shape memory effect in Ni-Mn-Ga.

This type of actuation has been implemented into some microscale porotypes. Recently, Saren *et al.* [71] have reported a single crystalline Ni-Mn-Ga fluidic pump, integrated into a microsystem for lab-on-a-chip application. By applying an external magnetic field, the crystal deforms and through that, the flow of a fluid can be regulated in tubal fluidic lines following the principles of the peristaltic pumps. The pump provides 0-2000 µL/min with resolution of down to 50 nL/min, which can be implemented both as a valve and a pump. The actuation stress results in a pumping pressure of more than 2 bar. The self-actuation of the system, which can be controlled by external magnetic field and

the simplicity of the mechanism enable its integration into small devices. **Figure 1.21** shows a scheme of the prototype, where the position of the Ni-Mn-Ga and the diametrically magnetized magnet on top, have been labeled.

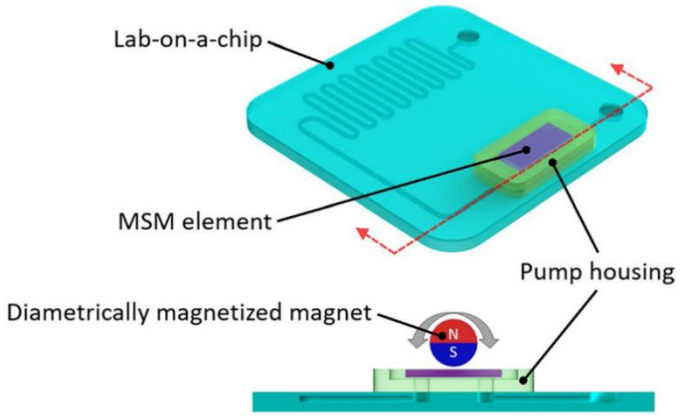

Figure 1.21: Fluidic micropump based on the magnetic shape memory actuation mechanism [71].

1.2.6.4 Thermomagnetic phase transition + shape memory effect

This type of actuation has been reported for Ni-Mn-Ga, exploiting the temperature-induced thermomagnetic phase transition combined with the stress-induced flexion of the material in the martensitic phase (**Figure 1.22**). The stress is applied via magnetic force, attracting the ferromagnetic Ni-Mn-Ga using a magnet.

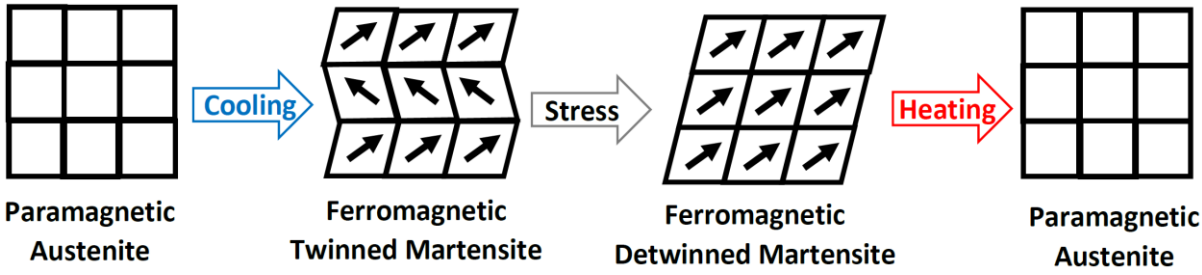

Figure 1.22: Simplified schematic view of the Ni-Mn-Ga actuation based on the thermomagnetic phase transition + shape memory effect.

A prototype for the above-mentioned path of actuation is shown in **Figure 1.23**. This prototype takes the advantage of the high-frequency and broad band-width actuation induced by thermomagnetic phase transition in FSMA thin films. Ni-Mn-Ga has been integrated into a system containing a sensitive optical setup. The Ni-Mn-Ga cantilever in the ferromagnetic phase at low temperature is attracted by the ferromagnetic force of a magnet positioned on the top of the cantilever, which induces deflection. The phase transition is induced by the Joule heating through the contacts to Ni-Mn-Ga cantilever, thus inducing the thermomagnetic phase transition (**Figure 1.23a**). Upon heating, the cantilever deflects back to its original position as it transforms to the high-temperature austenitic paramagnetic phase. This cyclic deflection of the cantilever is measured in real-time by an optical system (**Figure 1.23b**). The prototype scans the objects in the range of 60º angle, up to 30 m distance with an angular resolution of 0.5º. The cyclic deflection of Ni-Mn-Ga cantilever regulates

the deflection of a micromirror, mounted at the end of the cantilever, scanning the distances of the objects by measuring the running time in between a source of pulsed-laser and the objects [72].

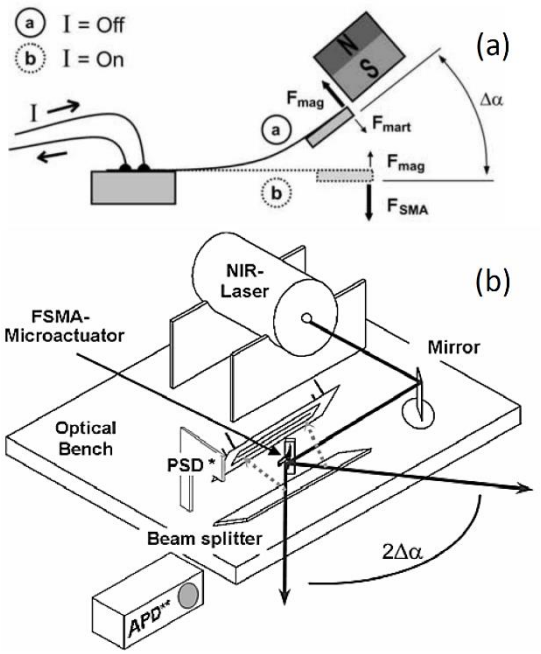

Figure 1.23: Microscanner prototype exploiting the thermomagnetic phase transition + shape memory effect (induced by magnetic force) a) schematic view of the actuating part, b) schematic view of the entire prototype [72].

In summary, the unique and multifunctional characteristics of FSMA such as Ni-Mn-Ga provide a flexible platform for a vast variety of applications. The connection between the three external stimuli, i.e., temperature (T), external stress (σ) as well as external magnetic field (H), shown in **Figure 1.24** as well as the coupling between the magnetic and structural degrees of freedom in Ni-Mn-Ga could lead to three types of phase transitions:

- Temperature induced phase transition
- External magnetic field-induced phase transition
- External stress-induced phase transition

In addition, two types of reorientation of twin variants in the martensitic phase could be observed:

- External magnetic field-induced reorientation of variants (or detwinning)
- External stress-induced reorientation of variants (or detwinning)

It is worth noting that a combination of the above mentioned phenomena can be also performed.

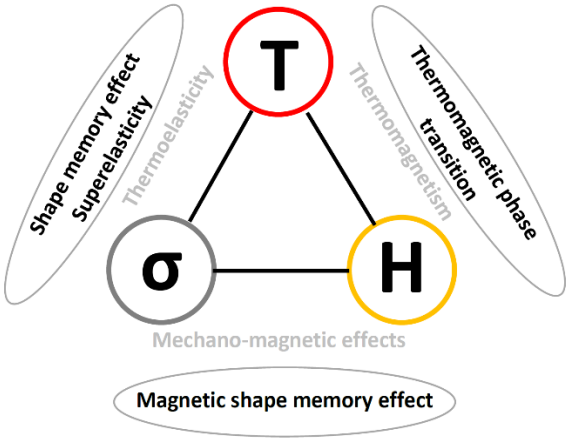

Figure 1.24: Multifunctional characteristics of FSMA such as Ni-Mn-Ga, interconnection between the three external stimuli, i.e., temperature (T), external stress (σ) as well as external magnetic field (H).

1.3 Ni-Mn-Ga thin films: downscaling vs. functionality

So far, the structural, magnetic characteristics and the interplay between the temperature, magnetic properties and the mechanical stress in Ni-Mn-Ga were briefly introduced. Although these characteristics give rise to the multifunctionality of the material, there are still some downsides to be improved. The actuators based on the conventional shape memory effect are bounded to the sluggish temperature-induced phase transition, which limits the frequency of the actuation typically to ~100 Hz (section 1.2.6.1) [73]. This could be considerably improved (up to 100 kHz) [74] via the magnetic shape memory effect enabled by FSMA such as Ni-Mn-Ga (section 1.2.6.3) however, the reorientation of twin variants induced by magnetic field requires very low twinning stress, which has been so far reported only for Ni-Mn-Ga single crystals [70,74 and the references there in].

Reducing the dimension of Ni-Mn-Ga to thin films at the first point could help the heat dissipation over the temperature induced phase transition, improving the actuation frequency by the temperature-induced phase transition, which is beneficial for the applications requiring cyclic thermal phase transition. In addition to the heat dissipation, Ni-Mn-Ga films can be considered a model system for FSMA. By exploiting epitaxial growth on different substrates, suitable growth conditions (including stress), and geometrical parameters (e.g., thickness) high quality and suitably oriented epitaxial films can be obtained. They allow accurate studies of structure and magnetism at the different length scales [75-77]. Despite their different martensitic configuration with respect to bulk materials, thin films provide a suitable platform to study the role of intrinsic and extrinsic properties in the martensitic transformation process and formulate models that can be extended to bulk materials [51,78]. Thin films can also be appropriately integrated into micro- and nano-devices and finally, due to the special geometry in thin films, novel functionalities are expected to arise.

In the following, first, some of the functionalities enabled by Ni-Mn-Ga epitaxial thin films are introduced; second, some of the promising functionalities for Ni-Mn-Ga epitaxial films are briefly discussed and finally, some of the challenges facing FSMA films including epitaxial Ni-Mn-Ga are pointed out.

1.3.1 Thin-film-enabled functionalities

In 2004, the first epitaxially grown Ni-Mn-Ga was reported by Dong *et al.* on GaAs substrate having ScErAs as underlayer [18]. Since then, there have a number of reports growing Ni-Mn-Ga epitaxial films and its Co-doped compositions on various substrates, e.g. MgO [79], Al_2O_3 [79], NaCl [80], YSZ [81] $SrTiO_3$ [82] and PMN-PT [83].

Upon the phase transition in Ni-Mn-Ga epitaxial thin films on (001) MgO, the twin boundaries (section 1.2.1) form, aligned with the six {110} planes of the cubic austenitic cells. In thin films compared to the bulk, because of the presence of the substrate, these planes are not equivalent, which gives rise to two different unique martensitic configurations in thin films called X-type and Y-type (**Figure 1.25a**, blue and red planes, respectively). The Y-type twin boundaries are normal to the substrate, typically nucleate and elongate along [100] MgO and [010] MgO whereas the X-type twin boundaries nucleate and elongate along [110] MgO and $[1\bar{1}0]$ MgO (**Figure 1.25b**, red and blue lines, respectively). The borders separating the colonies of the X-type and Y-type twin boundaries are assigned as the martensitic interfaces (section 1.2.1). For the sake of simplicity, only some of the possible interfaces are shown in **Figure 1.25b** nevertheless, X1-X2 and X3-X4 also form interfaces. The most characteristic difference between the interfaces and the twin boundaries is that the interfaces are not necessarily compatible and the atomically sharp twinning relation is not fulfilled (chapter 4).

Beyond the orientational difference, X-type and Y-type differ in the direction of the magnetization easy axis of the martensitic cells. The magnetization easy axis of the martensitic cells in X-type alternates in the plane and out of plane of the film while in Y-type it alternates in the plane of the film across the twin boundaries (**Figure 1.25c**). The yellow lines in the figure show the 180º magnetic domain walls and the arrows show the easy magnetization axes of the martensitic cells for each of the twin variants [76,84].

Niemann *et al.* [77] have recently reported a model for the formation of the twin boundaries in Ni-Mn-Ga epitaxial films, in which eight compatible variants form enclosed volumes of martensite in the form of diamonds. The diamonds could grow asymmetrically, which deforms the diamond to parallelograms. The midribs of diamonds serve as the twin boundaries (**Figure 1.26**). In order to translate the model into the scheme shown in **Figure 1.25**, the blue and red lines for X and Y can be considered as the large midribs of the X and Y diamonds, observable on the surface of the films.

The X/Y configuration-enabled magnetic flexibility discussed above for Ni-Mn-Ga epitaxial thin films could open up new prospective of applications for FSMA such as magnetic writing [85]. Recently, Ranzieri *et al.* [76] have investigated the X- and Y-type martensitic configurations in Ni-Mn-Ga epitaxial films. By tuning the thickness, choosing the Cr under-layer, applying mechanical stress during the growth and after the growth (**Figure 1.27**), they succeeded in manipulating the X- and Y-type martensitic configurations, reporting films having full X, full Y as well as combinations of X/Y in different portions and preferred orientations.

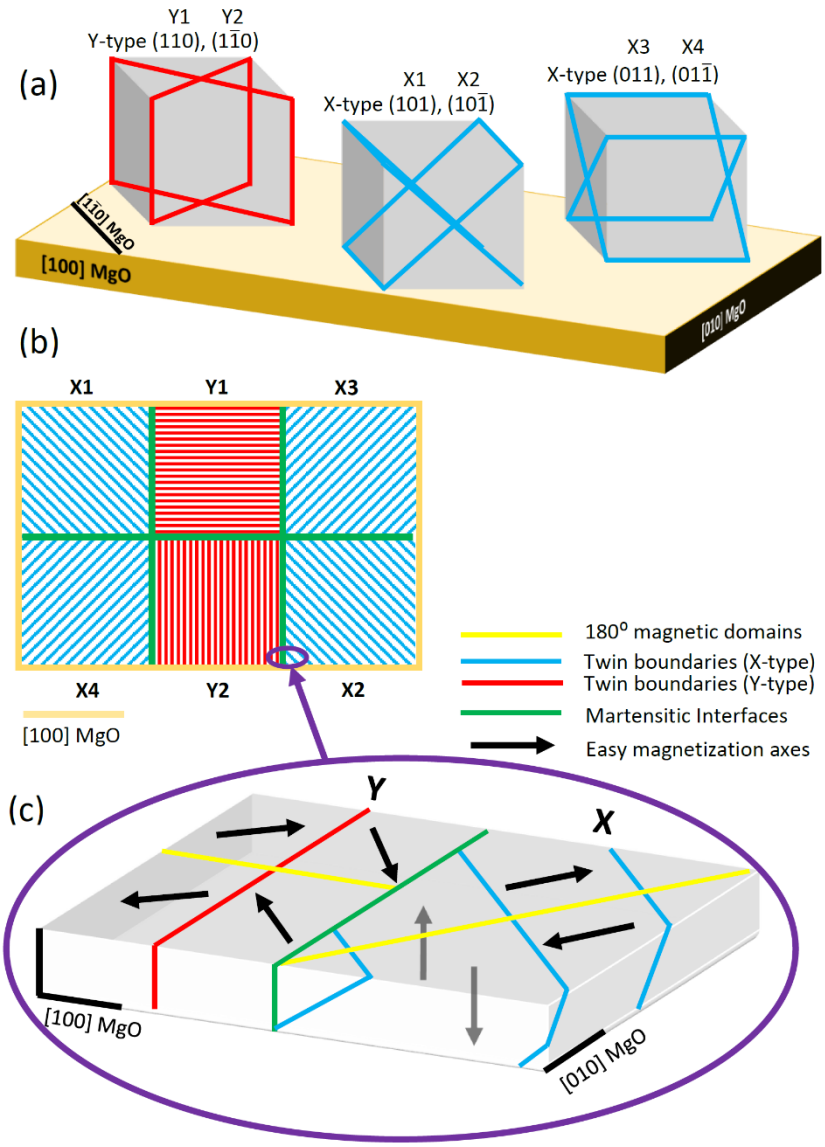

Figure 1.25: schematic representation of the martensitic configurations in Ni-Mn-Ga epitaxial films on (001) MgO: a) a category for the mesoscopic twinning possibilities originated from the six {110} planes of the austenitic cells (X in blue and Y in red); b) Simplified plan-view representation of the colonies of the twin boundaries (blue and red lines) originated from the six {110} planes of cubic cells, separated by the martensitic interfaces (green lines); c) 3D representation of the marked area in (b) showing a simplified example slice of the X- and Y-type twin boundaries (blue and red lines), martensitic interface (green line), 180º magnetic domain walls (yellow lines) and the direction of the easy magnetization axis of the martensitic cells (arrows) across the twin boundaries and the magnetic domain walls.

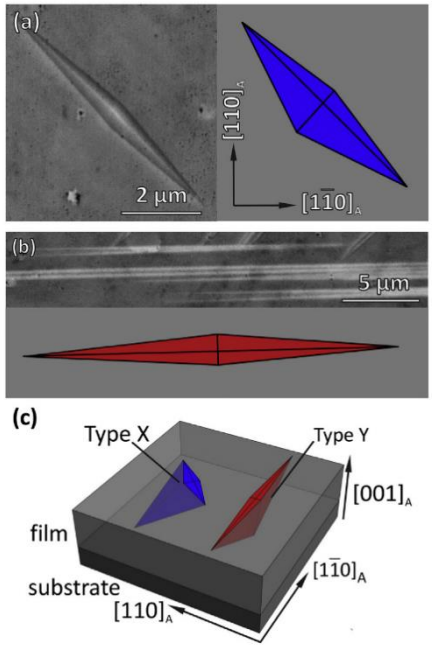

Figure 1.26: Diamond model for X- and Y-type twin boundaries a) X-type in plan view, b) Y-type in plan view, c) 3D representation of the X- and Y-type diamonds, $[110]_A$ = [100] MgO and $[1\bar{1}0]_A$ = [010] MgO [77].

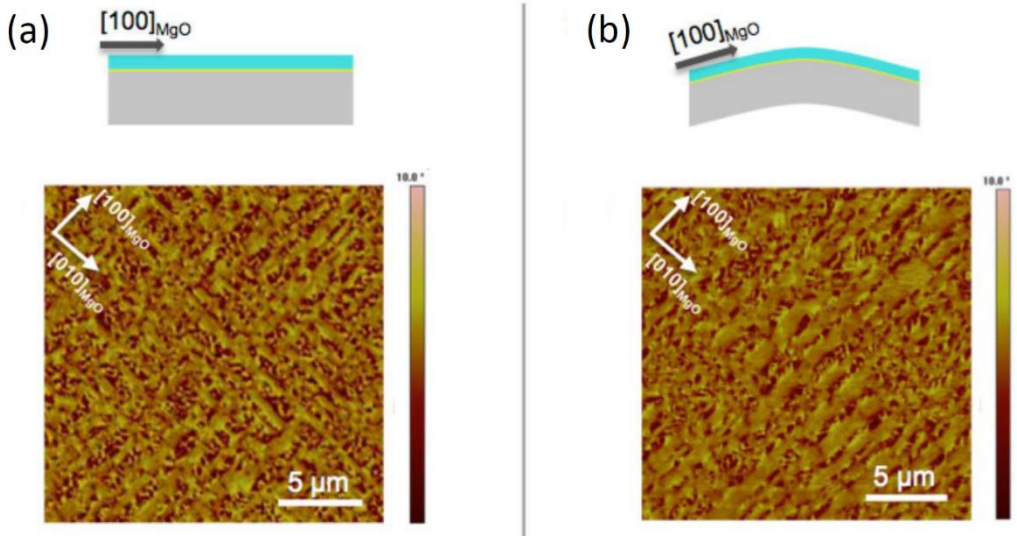

Figure 1.27: Post-growth three-point bending experiment a) MFM image of the as-prepared Ni-Mn-Ga film at room temperature, representing X/Y configurations, having orthogonal directions along [100] MgO and [010] MgO, b) after bending treatment, showing the reconfiguration of the X/Y twins; the portion of Y-type twins along [100] MgO has been increased at the expense of the Y-type twins along [010] MgO [76] (modified version of the original Figure is represented).

Beyond the magnetic flexibility, the well-defined and controllable martensitic configurations in epitaxial films provide a suitable platform for the fundamental research on the martensitic transition paths as well as the contributions of different external stimuli on the martensitic transition of FSMA. Thermal and magnetic hysteresis as well as the broadness of the martensitic transition are among the current major obstacles, preventing the full exploitation of FSMA towards the applications [58,59].

Epitaxial films enable visualizing and possibly quantifying the influence of extrinsic and intrinsic characteristics of the material on the aforementioned obstacles.

The geometry of thin films, having a huge lateral dimension to thickness ratio, gives rise to a unique feature upon the phase transition, called stray-field actuation, which was reported for the first time by Thomas *et al.* [86] in 2009 in epitaxial Ni-Mn-Ga freestanding films and further investigated by Campanini *et al.* in 2018 [22] in epitaxial Ni-Mn-Ga freestanding nanodisks (**Figure 1.28**). The principle of this effect stems from the influence of the magnetostatic energy of the ferromagnetic martensitic phase on the selection of the twin variants in the phase transition. To reduce the magnetic stray field of the system upon the martensitic phase transition in freestanding Ni-Mn-Ga thin films, the material tends to choose the configurations in which the magnetization easy axis of the martensitic cells lies in the plane of the film (e.g. Y-type). The easy magnetization axis of the martensitic monoclinic cells in the austenitic setting is the shortest axis of the cell (1.2.1) therefore, by choosing these variants, the total lateral size of the material reduces with respect to the austenitic parent phase. On the other hand, if the material is cooled down in the presence of an external magnetic field, normal to the film plane, the Zeeman energy contribution favors the formation of twin variants with the easy magnetization direction parallel to the external field (normal to the film plane). Having the shortest axis of the martensitic cells out of plane of the film, results in a lateral expansion of the material. For the nanodisks cooled down to the martensitic phase in the presence of $\mu_0 H \approx 2$ T, the relative areal expansion (with respect to the areal size of the disk in the austenitic phase) was measured to be around ~ 1 % and the for the nanodisks cooled in $\mu_0 H = 0$ T, the relative areal contraction was measured to be ~ -5.5 % (**Figure 1.28**). This unique geometry-enabled feature of the thin films proposes a preliminary step towards a novel thermomagnetic high-frequency actuation mechanism, which do not require the twin boundary motion therefore, could overcome the major issue of the twinning stress in the actuation mechanisms that are based on magnetic shape effect (1.2.6.3).

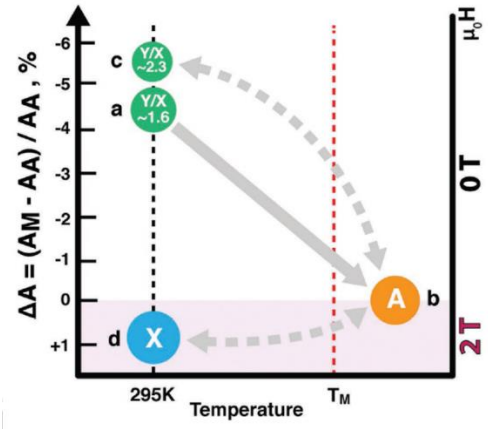

Figure 1.28: Stray-field based actuation of Ni-Mn-Ga epitaxial nanodisks [22].

Another unique feature arises from the huge surface to thickness ratio of the films is the enormous capability of the heat dissipation. Heat dissipation over a thermal cycle is among the major issues for the bulk conventional SMA as well as the FSMA. Although, there have been considerable progress for inducing and (or) assisting [60] the phase transition in FSMA by external magnetic field and mechanical stress, temperature has still kept its position as the most convenient and cost-effective path for the martensitic phase transition. In thin films due to the huge surface to thickness ratio, the heat dissipation occurs almost instantaneously. Gueltig *et al.* [87] in 2014 reported a prototype of a

microenergy-harvester, exploiting the actuation of a polyimide cantilever having Ni-Co-Mn-In FSMA polycrystalline film on its tip (**Figure 1.29**). The actuation is mainly based on the thermomagnetic phase transition. As a modification with respect to the previous actuator design (**Figure 1.23a**), heat is directly applied to a FSMA of 5 µm thickness on the tip of the cantilever. Taking the advantage of the heat dissipation of the film and the modification of the design, an actuation frequency of 200 Hz was reported.

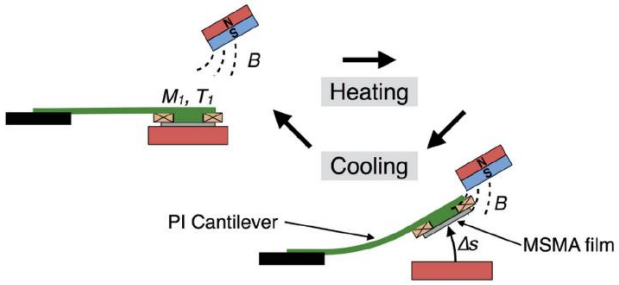

Figure 1.29: Energy harvesting prototype based on the thermomagnetic phase transition in FSMA films [87] (modified version of the original Figure is represented).

In 1999, Bhattacharya *et al.* [88] proposed a unique actuation model for martensitic materials. According to the model, for single crystalline SMA/FSMA films that are sufficiently thin, by partially releasing the film from the substrate along the interphases, phase transition could give rise to buckling of the released part, out the film plane. This was calculated using the 3D representation of the martensitic transformation theory by highlighting the role of interfacial energy in the total energy minimization as well as the floppiness of the thin films undergoing martensitic transition. According to their proposal, based on the geometry of the released parts, the architecture of the martensitic variants could be realized as geometrically defined 3D structures, called as tents or tunnels (**Figure 1.30a**), which was later explored by an experimental approach on CuAlNi (**Figure 1.30b**) [89] and Ni-Mn-Ga epitaxial films [18]. Although the proposed simultaneous actuation mechanism (as they called it 'the material is the machine') was an impressive finding, it has been followed quite poorly by the SMA and FSMA research communities in the following years [90-92], which is expected to be mainly due to the fabrication technical difficulties.

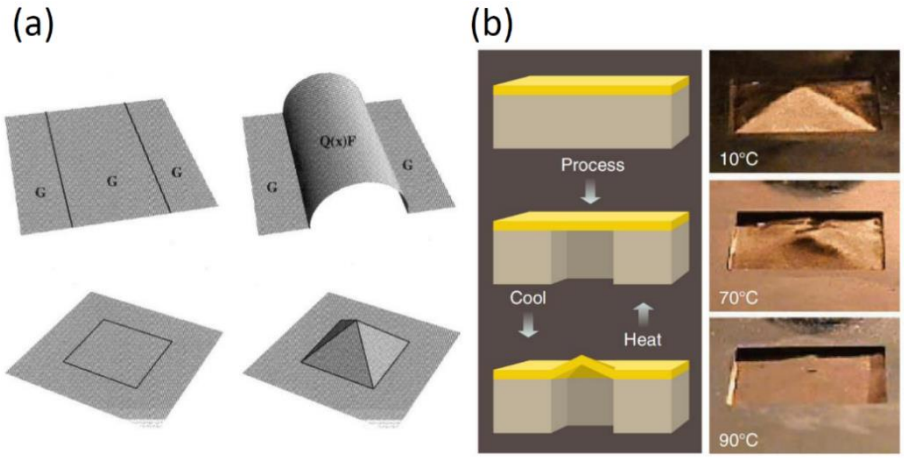

Figure 1.30: a) Tent and tunnel model for a simultaneous actuation in SMA/FSMA films [88], b) schematic representation of the experiment performed for CuAlNi [89].

1.3.2. New emerging functionalities

In this section, the perspective for the applications of FSMA micro and nanostructures is briefly discussed by highlighting some specific characteristics of Ni-Mn-Ga thin films, reported in the literature for freestanding micro and nanostructures, which can be exploited for fluidic and biological areas of applications.

Recently, Campanini *et al.* [22] have reported a new method of fabrication for preparing Ni-Mn-Ga nanodisks, starting from continuous epitaxial films (**Figure 1.31**). This method, which is based on nanosphere lithography technique, enables relatively large-scale fabrication of nanodisks with respect to the conventional lithography-based methods. The steps of the fabrication are shown in **Figure 1.31**. They reported a range of 150-650 nm for the diameter of the nanodisks. This range of diameter of disks, which can be selectively controlled by choosing appropriate polystyrene spheres and the time of the plasma etching in Ar^+ and O^- gas mixture, together with the capability of this technique, which can be applied using large wafers of Ni-Mn-Ga samples, proposes a relatively cost-effective technique for the fabrication of Ni-Mn-Ga freestanding nanodisks in relatively large-scales. The disks can be dispersed in appropriate solvents to form magnetic fluidic matrix.

Among the multifunctional characteristics of Ni-Mn-Ga epitaxial films discussed in 1.3.1, is the thermomagnetic phase transition. In the martensitic phase, the orientation of the magnetic easy axis of the martensitic cells can be selected to be in the plane of the film (Y-type) or alternating in-plane and out of plane of the film (X-type) using microstructure engineering. Selective orientation of the martensitic cells gives rise to the selective magnetic anisotropy of the material, which can be switched off and on by temperature induced thermomagnetic phase transition. Nanodisks directly obtained by suitably engineered epitaxial thin films in a fluidic matrix, could potentially lead to a multifunctional smart fluidic system with capabilities beyond the conventional oxide-based ferrofluids. Some of the expected characteristics of the possible fluidic matrix based on Ni-Mn-Ga nanodisks are listed below:

- High magnetic moment in the martensitic phase;

(with respect to the conventional fluids based on magnetic oxides);

- Switchable magnetic phase, activated by thermal cycling;

(transition temperature can be tuned);

- Smart control of the collective orientations of the disks in the fluid;

(by the orientation and the strength of the external magnetic field)).

In 2017, Vemulkar *et al.* [93] reported the self-assembly of the magnetic multilayer microdisks (D = 2 μm) with perpendicular magnetic anisotropy, in the presence of uniaxial external magnetic field in a fluidic environment (**Figure 1.32a-d**). As shown in the figure, by switching-on the external field, the randomly oriented disks mechanically rotate and gather side-by-side, forming magnetically assembled chains of disks. As the strength of the external magnetic field increases, the disks turn to a new assembly of head-to-head connected disks in a coin-pile fashion (**Figure 1.32d**). These smart magnetic fluids have the potential to be exploited for a vast variety of the applications including bioengineering. Nevertheless, coating the disks with a biocompatible material would be required.

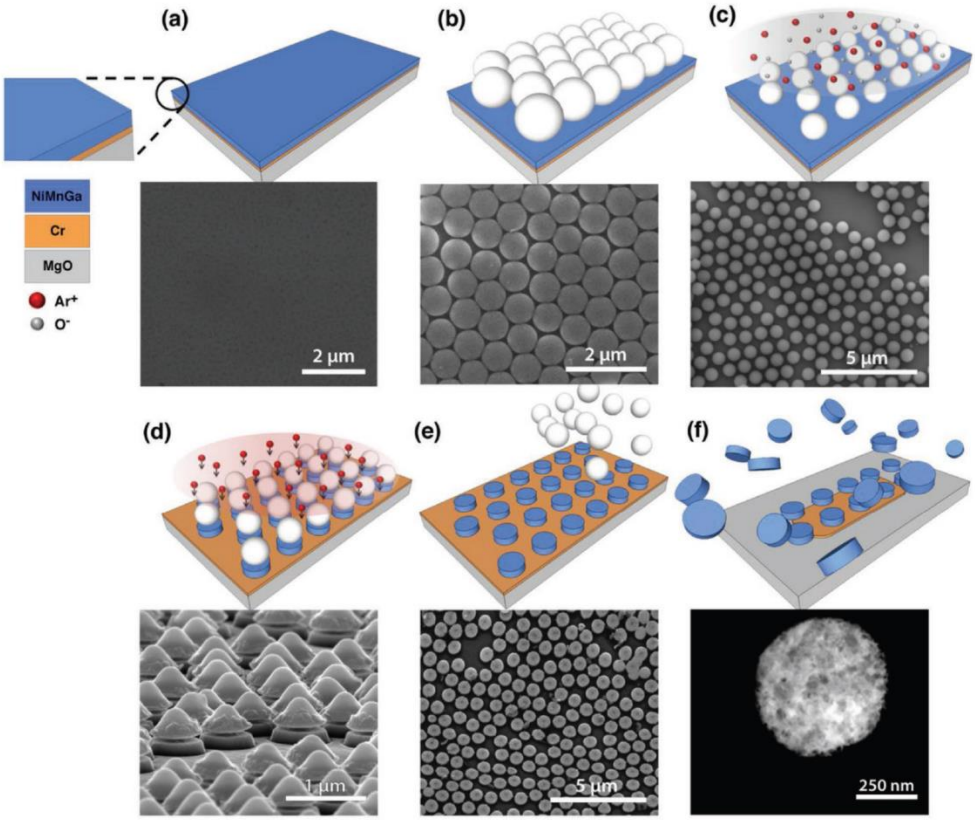

Figure 1.31: Fabrication steps for Ni-Mn-Ga epitaxial nanodisks, a) Ni-Mn-Ga continuous film, grown on Cr under-layer in turn on (001) MgO, b) monolayer coating of the polystyrene spheres on the continuous film, c) plasma etching in Ar+ and O− gas mixture for reducing the diameter of the spheres, d) Argon etching removes-off the uncovered Ni-Mn-Ga film, e) removing the polystyrene spheres using ultrasonic bath in acetone, f) peeling-off the Ni-Mn-Ga nanodisks by selective Cr chemical wet-etching.

In another work by Mansell *et al.* [94], they reported the mechanical rotation of the magnetic microdisks under external rotating magnetic field. Depending on the direction of the magnetization easy axis of the disks, under an external rotating magnetic field, the disks can rotate whether around the axis normal or parallel to the disk plane (**Figure 1.32e**). They have exploited this mechanical rotation of the disk under an external magnetic field for successively destroying human U87 brain tumor cells in an in-vitro approach.

As a complimentary approach for cancer therapy, thermomagnetic phase transition of Ni-Mn-Ga nanodisks provide the potential to be exploited for FSMA-based self-regulating agents for Hyperthermia [95]. Nevertheless, a biocompatible coating would be required. In addition, their cost and the efficiency would need to be accurately assed with respect to the already reported self-regulating Hyperthermia agents in the literature.

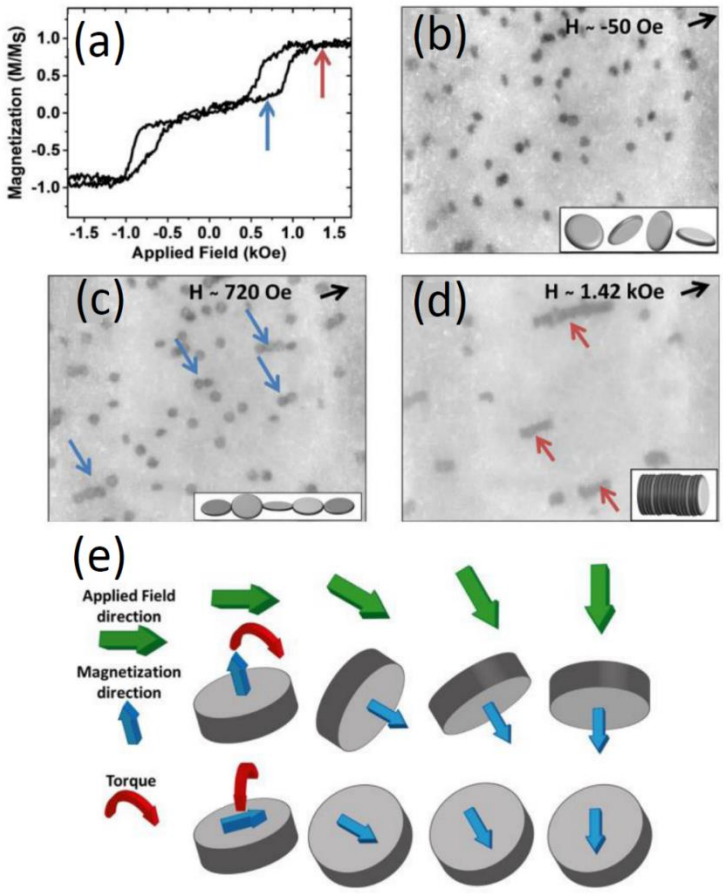

Figure 1.32: a) Magnetization loop vs. applied magnetic field measured by vibrating sample magnetometer (VSM) for an aqueous suspension of the CoFeB 2-µm-diameter microdisks, b-d) optical microscope images (~52 µm × ~68 µm) of the aqueous suspension of the microdisks in different strength of uniaxial magnetic field; direction of the field is shown by the black arrows [93] (modified version of the original Figure is represented) . e) schematic representation of the different magnetically induced torque of the microdisks over applying rotating magnetic field. The disk presenting perpendicular magnetization direction is CoFeB and the disk showing in-plane magnetization direction is a Py disk with magnetic vortex configuration [94].

Another fascinating feature of FSMA films is a reversible macroscopic twisting, observed in Ni-Mn-Ga films upon the martensitic phase transition, specifically in the fabricated freestanding structures with large lateral aspect ratio. This behavior has been also observed in Ni-Mn-Ga foils [96,97], giving rise to a macroscopic length change, induced by twisting over the martensitic transition. Recently, Ganor *et al.* [98] has investigated this phenomenon in the martensitic materials including Ni-Mn-Ga by a theoretical and an experimental approach. They explained the observed twisting effect to be due to the configuration of the ferroelastic domains in the martensitic phase, which are in a zig-zag fashion to satisfy the magnetic, kinematic and the crystallographic compatibility of the twin variants, minimizing the total energy of the system. This could give rise to the formation of rotation or (and) axial strain within the material which is combined with the floppiness of the thin films and could result in a large macroscopic deformation of the structure (**Figure 1.33b,c**). This simultaneous temperature (or magnetic field) induced bending or twisting of the FSMA, which has been so far observed in Ni-Mn-Ga films and foils can be an initial step towards FSMA-integrated smart actuator microrobots with versatile purposes including microinjection for bioengineering applications. A type of microinjection has been inspired by an injection process in Escherichia virus T4 (**Figure 1.33a**). This virus attaches to the host's cells (typically Escherichia coli

bacteria) through its tail- fibers, injecting its DNA through a process in its protein tail, which is similar to the martensitic transition. The contraction of the tail induced by structural transition pushes the DNA of the virus mechanically into the host cell [99].

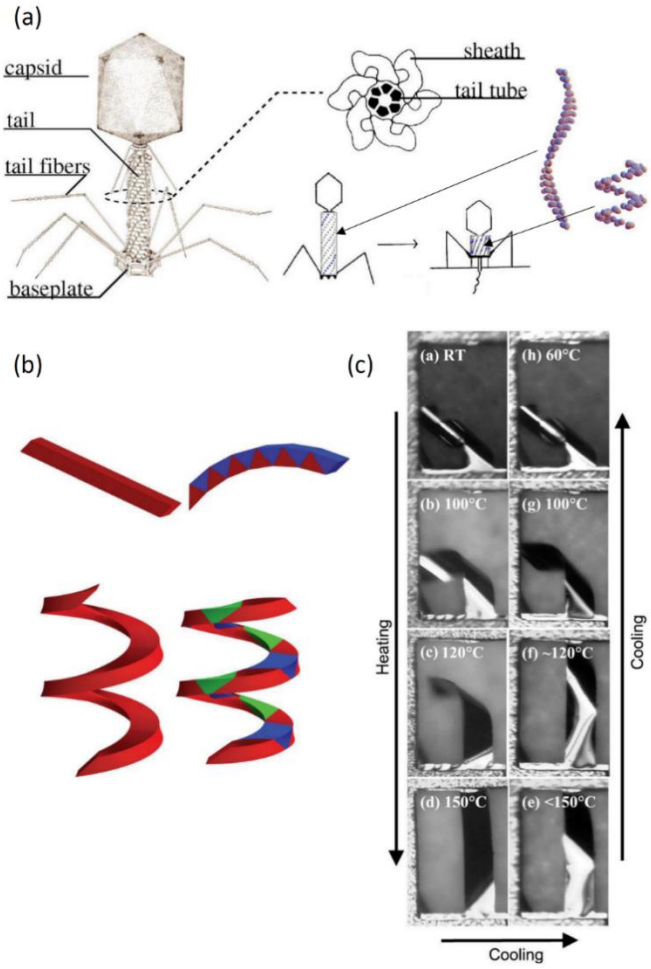

Figure 1.33: a) Schematic view of Escherichia virus T4, different parts of the virus are labeled including its tail, which undergo a structural transition changing the length of the tail [99] (modified version of the original Figure is represented), b) bending and twisting as a result of the martensitic transition, red-color refers to austenite or martensitic single variant status, green and blue refers to the martensitic twin variants [98]. c) Optical microscope images of freestanding 90 nm-thick Ni-Mn-Ga epitaxial bridge (400 µm long × 100 µm wide) undergoing twisting contraction upon the martensitic transition [18].

1.3.3 Challenges

In this section, the following challenges of FSMA thin films including Ni-Mn-Ga are briefly discussed:

i. Technical challenges:
   a) Epitaxial growth;
   b) Detaching films from the substrates;
   c) Micro and nanofabrication;
ii. Lack of explicit knowledge about the effect of lateral size on the properties of FSMA;
iii. Lack of extensive knowledge about the hierarchical nature of the twins and its possible impact on the martensitic transition;
iv. High twinning stress as well as fine twinning structure, which is likely to hinder the magnetic shape memory effect in FSMA thin films.

Generally, growing high quality, homogenous FSMA films with the desired composition and structural order, which undergo sharp phase transition, showing low thermal hysteresis, is a demanding task. FSMA are typically ternary compounds; in case of adding dopants, they could turn into quaternary compounds or even more. Optimizing the growth conditions to have all the elements be deposited homogenously through the entire substrate, showing the desired structural order and having the desired composition is challenging. For growing epitaxial films, in addition to the above-mentioned difficulties, choosing the proper substrate, having the minimum lattice mismatch with respect to the crystal cells of the FSMA film is a factor of concern. The growth conditions giving rise to the epitaxial growth is also an important factor to be considered. Since the growth is typically performed at high temperatures, even small amount of impurities, oxidation or intermixing of elements can jeopardize the epitaxial relation between the substrate and the film or at least could deteriorate the quality of the growth. Adhesivity is another factor of the growth to be considered. Adhesivity of the films to the substrate is crucial and needs to be assed when choosing the substrate for the growth. In case of need, adhesive under-layers could be grown on the substrate prior to the growth of the films although, the under-layer should be selected wisely, since any kind of intermixing of elements at high temperatures, or a large misfit between the substrate, under-layer and FSMA film could also jeopardize the epitaxial growth (section 2.1).

Apart from the difficulties in the growth process, detaching the films from the substrate in the process of micro and nanofabrication is also among the challenges. Specifically, for Ni-Mn-Ga and its Co doped compositions, there have been recently a number of successful attempts for growing the epitaxial films on dissolvable substrates such as (001) NaCl [80] or Cr under-layer [100], which can be selectively removed by chemical etching (section 2.2.3). In addition to those, in the literature, there exist a few repots of detaching Ni-Mn-Ga films and other components directly from MgO [101,102], which were proven to be moderately beneficial in case of growing Ni-Mn-Ga directly on MgO substrates.

The method of the micro and nanofabrication of FSMA needs to be selected appropriately based on the characteristics of each technique and the desired properties of FSMA. The so far reported micro and nanofabrication methods in the literature for downscaling FSMA (such as lithography as well as focused ion beam techniques) starting from continuous single crystalline bulk, thin films (or patterned substrates) are among the most selective, accurate, high-resolution and flexible methods of fabrication, giving rise to micro and nanostructures with well-defined properties [22, 103-105]. On

the other hand, the other reported top-down or bottom-up micro and nanofabrication techniques (such as chemical methods [106], milling [107], melt spinning [108], etc.) might show lower selectivity and controllability of the fabrication though, they enable low-cost fabrication of FSMA micro and nanostructures in much higher quantity.

Heusler-based FSMA including Ni-Mn-Ga are complex systems. This complexity can be realized from the crystal structure, self-accommodation of the martensitic twin variants, and the magnetic orders of the material. Additionally, the dependence of the material characteristics on several intrinsic and extrinsic parameters, e.g., a slight variation of the composition, chemical order, internal stress and structural defects (section 1.2.1 to 1.2.5), makes the evaluation of the effect of size in FSMA a quite demanding task. In addition to the complexity coming from the material side, one needs to consider the technical issues rising from the fabrication and the characterization sides as the size of the material is reduced (chapter 2). So far, there have been only few systematic investigations in the literature exploring the effects of the lateral confinement on the properties of Heusler-based FSMA, e.g. in references [105,109,110], which deserves further investigation.

It is well known that some of obstacles, i.e., thermal and magnetic hysteresis, broadness of the transition (section 1.2.4) and the twinning stress (chapter 4), preventing the full exploitation of FSMA properties towards the applications are linked to e.g. crystal structure, internal stress and structural defects. The two latter parameters are strongly dependent to the configuration of the twin variants in the martensitic phase, which covers a long range from nano- to macroscale. In the literature however, there are only few works focused on the crystallographic structures and the martensitic configurations of epitaxial Ni-Mn-Ga and Co-doped thin films through experiments and models (section 1.3.1). Nevertheless, the knowledge about the multiscale hierarchical self-accommodation of the twin variants in the martensitic phase and its possible links to the transition route is still limited, mainly due to lack of direct multiscale observation.

In FSMA thin films such as epitaxially grown Ni-Mn-Ga, due to the presence of the rigid substrate as well as the specific geometry (huge surface to thickness ratio), the internal stress is expected to be considerably higher with respect to the bulk counterparts, imposing a large elastic stress to the film upon the martensitic transition. According to the theory of the elastic equilibrium for epitaxial films, formation of elastic domains is energetically required to compensate the elastic stress caused by the symmetry reduction during the martensitic phase transition and to minimize the total energy of the system [111,112]. Although not yet explicitly quantified for thin films, this unique condition with respect to the bulk samples imposes the formation of finer twin boundaries in thin films. In 2014, Lou *et al.* [113] measured the elastic properties and the twinning stress of the mesoscopic twin boundaries in Ni-Mn-Ga epitaxial films on (001) MgO using atomic force acoustic microscopy measurements.

By using contact-resonance spectra, they obtained the local elastic modulus, stiffness and damping of a 1 µm-thick substrate-constraint Ni-Mn-Ga film. They also determined a large twinning stress of 0.5 GPa for the substrate-constraint films. Interestingly, the direct measurements of the tensile stress-induced detwinning process in Ni-Mn-Ga freestanding films also show a huge twinning stress of around 23 MPa at room temperature (**Figure 1.34a**) [114], which can be reduced to around 15 MPa as a function of temperature (**Figure 1.34b**) [115] however, it is still much higher than typical twinning stress in the bulk single crystalline counterparts [116]. This could increase the actuation stress, leading to a higher work output in Ni-Mn-Ga films compared to bulk, which is an advantage, provided that the actuation mechanism is based on a mechanical stress or a temperature variation. It is well known that the upper limit of the stress induced by an external magnetic field in FSMA so far

has been reported to be around 2 MPa [70,74,116 and the references there in]. Comparing this stress with the required stress reported for detwinning the boundaries in Ni-Mn-Ga thin films (discussed above) turns the magnetic shape memory effect (1.2.6.3) in thin films very unlikely to happen. In addition, a recently published theoretical work [117] proposes an increase in the stress required for the twin boundary motion in Ni-Mn-Ga structures having high density of twin boundaries (e.g. thin films). The effect of the density of the twin boundaries has been explained to be due to the high interaction between the twin boundaries and the magnetic domain walls, giving rise to the formation of high density of magnetoelastic defects, which serve as obstacles in the process of the twin boundary motion.

The occurrence of magnetic shape memory effect in thin films is highly debated in the literature. A model was proposed in 2008, suggesting a reversible magnetic shape memory effect with zero shape change in substrate constrained Ni-Mn-Ga epitaxial thin films [118]. Contrarily, some other experimental and theoretical reports published later do not propose the magnetic shape memory effect in thin films. The major works that have reported experimental evidences for the occurrence of the magnetic shape memory effect in FSMA thin films can be classified into two categories:

1. The reports, suggesting the magnetic shape memory effect by referring to the typically reversible anomalous jumps in the magnetization curves of the films over applied magnetic field in the martensitic phase [76, 81, 82, 115, 118-122];
2. The reports, suggesting the magnetic shape memory effect by referring to the direct observation of the change of the shape in freestanding films in the presence of an external magnetic field **Figure 1.34c,d** [18, 122].

Recently, Laptev *et al.* [123] has reported a model derived by micromagnetic simulations, in which they have proposed a pure magnetic origin for the observed anomalous jumps in the magnetization curves of the films. They have referred the anomalous jumps to the magnetization switching in the twin variants in the presence of an external magnetic field. As for visualizing the shape change of freestanding films using optical microscope, it has to be considered that the length-scale of the twin boundaries and magnetic domains in thin films are well below the spatial resolution of the optical microscope. Therefore, the collective change of the shape of the films, may be possibly described as the magnetic-torque induced bending [124] or the conventional shape memory effect induced by magnetic force in the presence of the an external magnetic field [125,126] (section 1.2.6.4).

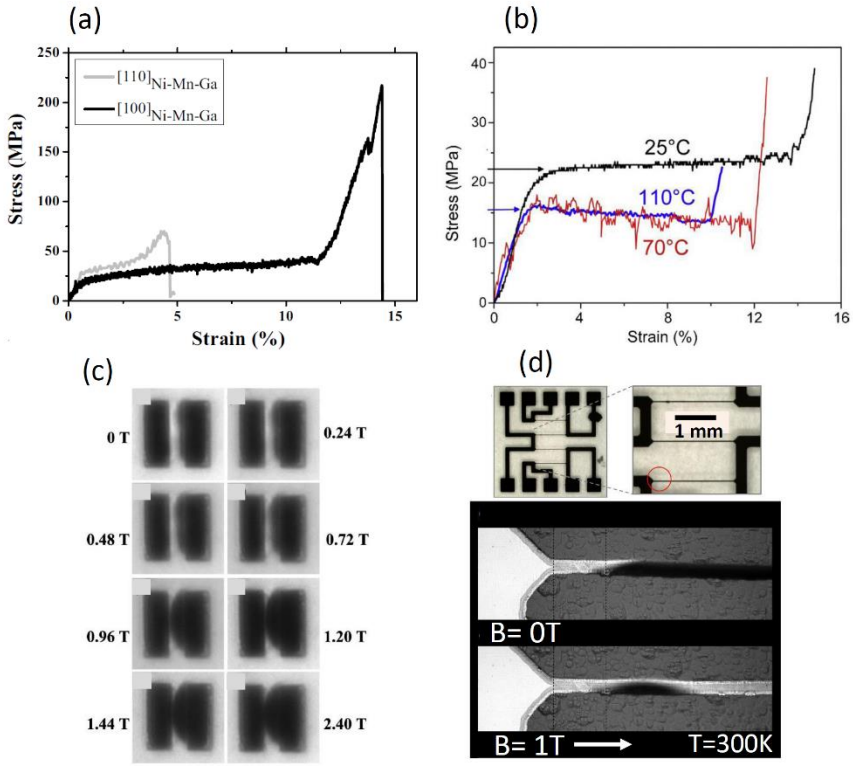

Figure 1.34: a) Stress-strain curves measured for a 1µm-thick freestanding Ni-Mn-Ga epitaxial film in the martensitic phase, applying tensile stress along $[110]_{Ni\text{-}Mn\text{-}Ga}$ = [100] MgO and $[100]_{Ni\text{-}Mn\text{-}Ga}$ = [110] MgO at room temperature [114]. b) Stress-strain curves measured for a 2µm-thick freestanding Ni-Mn-Ga epitaxial film in the martensitic phase, applying tensile stress along $[100]_{Ni\text{-}Mn\text{-}Ga}$ = [110] MgO at 25ºC, 70ºC and 110ºC [115]. c) deformation of a 90 nm-thick freestanding Ni-Mn-Ga lithography fabricated bridge in the martensitic phase, measured by optical microscope imaging (100 µm long × 25 µm wide) in presence of an external magnetic field perpendicular to the film plane [18](modified version of the original Figure is represented). d) deformation of a 500 nm-thick freestanding Ni-Mn-Ga lithography fabricated bridge in the martensitic phase, measured by optical microscope imaging in presence of an external magnetic field along the length of the bridge [122] (modified version of the original Figure is represented).

References:

1. Sellitto, A. & Riccio, A. *Materials* **12**, 708 (2019).
2. Ölander, A. *J. Am. Chem. Soc.* **54**, 3819 (1932).
3. Greninger, A.B. & Mooradian, V.G. *Trans. AIME* **128**, 337 (1938).
4. Kurdjumov, G.V. & Khandros, L.G. *Dokl. Akad. Nauk SSSR* **66**, 211 (1949).
5. Chang, L.C. & Read, T.A. *JOM* **3,** 47 (1951).
6. Buehler, W.J. *et al. J. Appl. Phys.* **34**, 1475 (1963).
7. Kauffman, G.B. & Mayo, I. *Chem. Educat.* **2**, 1 (1997).
8. Jani, J. *et al. Mater. Des. (1980-2015)* **56**, 1078 (2014).
9. Hames, F.A. *J. Appl. Phys.* **31**, S370 (1960).
10. Galanakis, I. Theory of Heusler and full-Heusler compounds (Springer, Chambridge, 2016).
11. Chernenko, V.A. & Kokorin, V.V. *Proceedings of ESOMAT* (California, U.S.A., 1992).
12. Ullakko, K. *et al. Appl. Phys. Lett.* **69**, 1966 (1996).
13. Planes, A. *et al. J. Phys. Condens. Matter.* **21**, 233201 (2009).
14. Caputo, M. P. *et al. Addit. Manuf.* **21**, 579 (2018).
15. Browne, A. L. *et al. Smart materials, structures and NDT in Aerospace Conference* (Montreal, Canada, 2011).
16. Motors, G. Chevrolet debuts lightweight 'smart material' on Corporate, https://media.gm.com/media/us/en/gm/home.detail.html/content/Pages/news/us/en/2013/Feb/0212-corvette.html (Accessed: February 12, 2013)
17. Dunand, D.C. & Müllner, P. *Adv. Mater.* **23**, 216 (2011).
18. Dong, J.W. *et al. J. Appl. Phys.* **95**, 2593 (2004).
19. Schmitt, M. *et al. Microelectron. Eng.* **98**, 536 (2012).
20. Eichhorn, T. *et al. Acta Mater.* **59**, 5067 (2011).
21. Jenkins, C.A. *et al. Appl. Phys. Lett.* **93**, 234101 (2008).
22. Campanini, M. *et al. Small* **14**, 1803027 (2018).
23. Zider, R.B. & Krumme, J.F. U.S. Patent No. 4,772,112 (Washington DC: U.S.A. 1988).
24. Torrisi, L. *Bio-Med. Mater. Eng.* **9**, 39 (1999).
25. Reynaerts, D. *et al. Sensor Actuat. A-Phys.* **61**, 455 (1997).
26. Hartl, D.J. *et al. Smart Mater. Struct.* **19**, 015021 (2009).
27. Hartl, D.J. *et al. Smart Mater. Struct.* **19**, 015020 (2009).
28. Smith Kilkenny, N. Reinventing the Wheel, https://www.nasa.gov/specials/wheels/ (Accessed: October 26, 2017).
29. Kim, S. *et al. IEEE/RSJ, Proceeding of IROS*, (St Louis, U.S.A. 2009).
30. Khovailo, V.V. *et al. Mater. Trans.* **44**, 2509 (2003).
31. Khan, M. *et al. J. Appl. Phys.* **97**, 10M304 (2005).
32. Krenke, T. *et al. Nat. Mater.* **4**, 450 (2005).
33. Bain, E.C. & Dunkirk, N.Y. *Trans. AIME* **70**, 25 (1924).
34. Brown, P.J. *et al. J. Phys. Condens. Matter* **11**, 4715 (1999).
35. Orlandi, F. *et al. Phys. Rev. B* **101**, 094105 (2020).
36. Lázpita, P. *et al. New J. Phys.*, **13**, 033039 (2011).
37. Kübler, J. *et al. Phys. Rev. B* **28**, 1745 (1983).
38. Webster, P.J. *et al. Philos. Mag. B* **49**, 295 (1984).
39. Brown, P.J. *et al. J. Phys.: Condens. Matter* **14**, 10159 (2002).
40. Pons, J. *et al. J. Appl. Phys.* **97**, 083516 (2005).

41. Righi, L. *et al. Acta Mater.* **55**, 5237 (2007).
42. Righi, L. *et al. Acta Mater.* **56**, 4529 (2008).
43. Zheludev, A. *et al. Phys. Rev. B* **51**, 11310 (1995).
44. Khachaturyan, A.G. *et al. Phys. Rev. B* **43**, 10832 (1991).
45. Gruner, M.E. *et al. Sci. Rep.* **8**, 8489 (2018).
46. Müllner, P. & King, A.H. *Acta Mater.* **58**, 5242 (2010).
47. Christian, J.W., & Mahajan, S. *Prog. Mater. Sci.* **39**, 1 (1995).
48. Pitteri, M. & Zanzotto, G. Continuum models for phase transitions and twinning in crystals (CRC Press, Boca Raton, 2002).
49. Malik, A. *et al. Modell. Simul. Mater. Sci. Eng.* **21**, 085003 (2013).
50. Chulist, R. *et al. Int. J. Plast.* **114**, 63 (2019).
51. Schwabe, S. *et al. arXiv preprint arXiv:*2004.09768, https://arxiv.org/abs/2004.09768 (Accessed: April 21, 2020)
52. Entel, P. *et al. J. Alloys Compd.* **577**, S107 (2013).
53. Richard, M. *et al. Scr. Mater.* **54**, 1797 (2006).
54. Entel, P. *et al. J. Phys. D Appl. Phys.* **39**, 865 (2006).
55. Albertini, F. *et al. Mater. Sci. Forum* **583**, 169 (2008).
56. Entel, P. *et al. J. Phys. D: Appl. Phys.* **39**, 865 (2006).
57. Wollants, P. *et al. Prog. Mater. Sci.* **37**, 227 (1993).
58. Gutfleisch, O. *et al. Philos. Trans. R. Soc., A* **374**, 20150308 (2016).
59. Cugini, F. *et al. Philos. Trans. R. Soc., A* **374**, 20150306 (2016).
60. Karaca, H.E. *et al. Acta Mater.* **55**, 4253 (2007).
61. Tickle, R. & James, R.D. *J. Magn. Magn. Mater.* **195**, 627 (1999).
62. Mihálcz, I. *Period. Polytech., Mech. Eng.* **45**, 75 (2001).
63. Ma, J. *et al. Int. Mater. Rev.* **55**, 257 (2010).
64. Mihálcz, I. *Period. Polytech., Mech. Eng.* **45**, 75 (2001).
65. Eichhorn, T. *et al. Acta Mater.* **59**, 5067 (2011).
66. Davis, P.H. *et al. J. Appl. Phys.* **123**, 215102 (2018).
67. Tao, T. *et al. Int. J. Control Autom.* **3**, 366 (2006).
68. Murray, S.J. *et al. J. Appl. Phys.* **89**, 1295 (2001).
69. O'Handley, R. C. *J. Appl. Phys.* **83**, 3263 (1998).
70. Straka, L. *et al. Acta Mater.* **59**, 7450 (2011).
71. Saren, A. *et al. Microfluid. Nanofluid.* **22**, 38 (2018).
72. Brugger, D. *et al. Int. J. Appl. Electrom.* **23**, 107 (2006).
73. Krulevitch, P. *et al. J. Microelectromech. Syst.* **5**, 270 (1996).
74. Musiienko, D. *et al. Scr. Mater.* **162**, 482 (2019).
75. Ranzieri, P. *et al. Acta Mater.* **61**, 263 (2013).
76. Ranzieri, P. *et al. Adv. Mater.* **27**, 4760 (2015).
77. Niemann, R. *et al. Acta Mater.* **132**, 327 (2017).
78. Li, Z.B. *et al. IUCrJ* **6**, 909 (2019).
79. Jakob, G. *et al. Phys. Rev. B* **76**, 174407 (2007).
80. Heczko, O. *et al. Appl. Phys. Lett.* **94**, 152513 (2009).
81. Zhang, Y. *et al. Smart Mater. Struct.* **18**, 025019 (2009).
82. Heczko, O. *et al. Appl. Phys. Lett.* **92**, 072502 (2008).
83. Schleicher, B. *et al. J. Appl. Phys.* **118**, 053906 (2015).

84. Diestel, A. *et al. J. Phys.: Condens. Matter* **25**, 266002 (2013).
85. Watson, C.S. *et al. Adv. Funct. Mater.* **23**, 3995 (2013).
86. Thomas, M. *et al. Adv. Mater.* **21**, 3708 (2009).
87. Gueltig, M. *et al. Advanced Energy Materials* **4**, 1400751 (2014).
88. Bhattacharya, K. *et al. Mater. Sci. Eng., A* **273**, 685 (1999).
89. Bhattacharya, K., & James, R.D. *Science* **307**, 53 (2005).
90. Liakhova, J. *et al. Ferroelectrics* 342, 73 (2006).
91. Luskin, M. & Zhang, T. *Comput. Methods Appl. Mech. and Engrg.* **196**, 3759 (2007).
92. Lei, C.H. *et al. Mech. Mater.* **134**, 9 (2019).
93. Vemulkar, T. *et al. Appl. Phys. Lett.* **110**, 042402 (2017).
94. Mansell, R. *et al. .Sci. Rep* **7**, 1 (2017).
95. Yang, Y. *et al. Adv. Funct. Mater.* **25**, 812 (2015).
96. Suzuki, M. *et al. Mater. Trans.* **43**, 861 (2002).
97. Ohtsuka, M. & Itagaki, K. *Int. J. Appl. Electrom.* **12**, 49 (2000).
98. Ganor, Y. *et al. Philos. Trans. R. Soc., A* **374**, 20150208 (2016).
99. Falk, W. & James, R.D. *Phys. Rev. E* **73**, 011917 (2006).
100. Backen, A. *et al. Acta Mater* **58**, 3415 (2010).
101. Edler, T. & Mayr, S.G. *Adv. Mater.* **22**, 4969 (2010).
102. Liu, Z. *et al. J. Am. Chem. Soc.* **127**, 6 (2005).
103. Khelfaoui, F. *et al. Eur. Phys. J-Spec. Top.* **158**, 167 (2008).
104. Schmitt, M. *et al. Microelectron. Eng.* **98**, 536 (2012).
105. Lambrecht, F. *et al. Shap. Mem. Superelasticity* **2**, 347 (2016).
106. Nehla, P. *et al. J. Alloys Compd.* **776**, 379 (2019).
107. Tian, B. *et al*. *Intermetallics* **16** 1279 (2008).
108. Gómez-Polo, C. *et al. J. Appl. Phys.* **107**, 123908 (2010).
109. Ozdemir, N. *et al. Acta Mater.* **60**, 5670 (2012).
110. Gottschall, T. *et al. Adv. Funct. Mater.* **27**, 1606735 (2017).
111. Roitburd, A.L. *Phys. Status Solidi A* **37**, 329 (1976).
112. Pompe, W. *et al. J. Appl. Phys.* **74**, 6012 (1993).
113. Luo, Y. *et al. New J. Phys.* **16**, 013034 (2014).
114. Yeduru, S.R., *et al. Phys. Procedia* **10**, 162 (2010).
115. Yeduru, S.R. *et al. J. Alloys Compd.* **577**, S353 (2013).
116. Khelfaoui, F. *et al.* EDP. Sciences, *Proceedings of ESOMAT* (Prague, Czech Republic 2009).
117. Veligatla, M. *et al. Acta Mater.* **193**, 221 (2020).
118. Thomas, M. *et al. New J. Phys.* **10**, 023040 (2008).
119. Buschbeck, J. *et al. Acta Mater.* **57**, 2516.
120. Ren, X. *et al. Chin. Phys. B* **23**, 068103 (2014).
121. Ren, X. *et al. Chin. Phys. B* **22**, 107502 (2013).
122. Eichhorn, T. Microstructure of epitaxial thin films of the ferromagnetic shape memory alloy Ni_2MnGa, Ph.D dissertation, Johannes Gutenberg University Mainz (2011).
123. Ohtsuka, M. *et al. Mater. Sci. Eng. A* **378**, 377 (2004).
124. Ohtsuka, M. *et al. J. M. M. M.*, **310**, 2782 (2007).
125. Laptev, A. *et al. Appl. Phys. Lett.* **109**, 132405 (2016).
126. Zheng, P. *et al. J. Alloys Compd* **624**, 226 (2015).

Chapter 2

Experimental

In this chapter, the experimental techniques are briefly introduced. The techniques include sample preparation, micro and nanofabrication, and the different types of characterization techniques. The characterizations include a number of techniques, which were performed to investigate the structure, morphology and magnetic characteristics of the samples in different length-scales ranging from nanometer to tens of microns. The part of the work including sample preparation, magnetic characterizations, topography and magnetic imaging as well as the transmission electron microscopy analysis and the lamella preparation were performed at IMEM-CNR, Parma, Italy. A part of the X-ray diffraction measurements as well as the scanning electron microscopy imaging were performed at University of Parma and at INRIM, Turin, respectively. The part of the work including micro and nanofabrication and the characterizations related to the micro and nanostructures were performed as a part of a 7-month internship at CEITEC, Brno University of Technology, Czech Republic. The in situ temperature and magnetic field dependent imaging as well as the magnetic measurements in high external magnetic fields were performed in collaboration with the Functional Materials, Technical University of Darmstadt, Germany.

2.1 Sputtering technique

Radio-frequency (RF) sputtering was used as the deposition technique for growing over 100 Ni-Mn-Ga epitaxial films with the thickness range of 10-200 nm directly on (001) MgO and on Cr / (001) MgO. Sputtering is a cost effective and highly reproducible technique for the preparation of polycrystalline and single-crystalline thin films in both the lab-scale and industrial-scale. Sputtering principles are based on the voltage potential difference between a target (a block of material from which the material is deposited) and a substrate (typically single crystalline, polycrystalline or amorphous material on top of which the target-material is deposited) in vacuum. In between the target and the substrate, reduced pressure (e.g., 0.1-100 Pa) of an inert gas is introduced and simultaneously ionized due to the discharge. The created high-energy positive ions hit the target (having a negative voltage) and thermally excite the atoms of the material. When the kinetic energy of the hitting ions exceeds the binding energy of the atoms of the material, the atoms leave the target and deposit on the surface of the substrate. A simplified schematic representation of the sputtering process is shown in **Figure 2.1**.

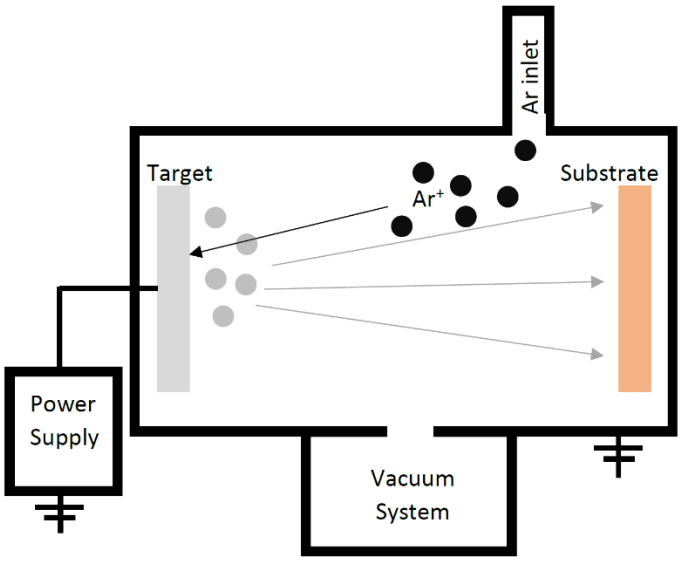

Figure 2.1: Simplified schematic representation of the sputtering process.

RF sputtering is a modified version of the basic direct current (DC) sputtering described above. In RF sputtering technique in contrast to DC sputtering, the sign of the electric potential of the target switches in a rapid, oscillatory fashion; therefore, the possible accumulation of the charges in the target can be significantly avoided. This could be an advantage specifically for the deposition of electrically insulating targets. In addition, RF sputtering provides efficient discharge, which enables the deposition in lower pressure of the inert gas, which reduces the risk of possible contamination during the growth of thin films [1].

In the apparatus used in this study, the RF power supply operates at 13.56 MHz. The maximum power is transferred to the target through the matching network controller and the vacuum in the deposition chamber is obtained by a cryopump providing a base vacuum of between 2×10^{-6} to 4×10^{-6} Pa. The sample is loaded to the deposition chamber via a load-lock chamber. The epitaxial growth requires the deposition on top of the substrate at elevated temperatures. For this purpose, the apparatus is capable of heating the substrate to high temperatures, which can be measured by a thermocouple located in the backside of the substrate-holder and additionally on top of the substrate via a feedthrough thermocouple. With a temperature of 873 K on the backside of the substrate-holder, the typical temperature on top of an MgO single-crystal substrate with 0.25 mm thickness is ~623 K. The substrate is mounted vertically on a cylindrical carousel. The carousel oscillates back and forth in front of the target with the feedback control of 1/4096º. Oscillating deposition mode improves the homogeneity of the deposition and the thickness of the film on the substrate. The temperature of the target is retained at around room temperature by cooling water circulation via a Copper backing plate bonded to the backside of the target. The apparatus provides three positions for mounting three different targets.

The deposition rate depends on several parameters including the deposition yield of the atoms of the target. Deposition yield is the number of atoms leaving the target per the number of ions hitting the target [2]. In addition, the target power, the inert gas pressure and type of the inert gas are also important factors, determining the deposition rate. Some of these parameters influence the deposition rate directly while some of them indirectly, i.e., through changing the yield. Pure Ar (99.999 %) was selected in our depositions due to its comparable atomic mass to the target atoms. The Ar pressure of

1.5 Pa was regulated by a flux-meter. The deposition rate is calibrated periodically by depositing the target material on a Si substrate at fixed target power, Ar flux and number of oscillations at 300 K. The film thickness is then measured by a profiler and the deposition rate is calculated subsequently. **Table 2.1** represents an overview of the growth conditions of the samples, which will be used in chapters 3, 4 and 5.

Table 2.1: overview of the growth conditions of the samples used in chapters 3-5.

Chapter	Sample	T_{growth} (K)	Dep. rate (nm/sec)	Ar p. (Pa)	Thickness (nm)	Cr under-layer	Post-annealing (at 623 K, 3.6 ksec)
3, 4	#1, E	623	0.1	1.5	200	-	□
3, 4	#1P, #1, C	″	″	″	″	″	■
3	#2	573	0.1	1.5	200	-	□
3,4	#2P	″	″	″	″	″	■
3	#3	523	0.1	1.5	200	-	□
3	#3P	″	″	″	″	″	■
4	#2	623	0.1	1.5	200	50 nm	□
4	A	628	0.1	1.5	200	-	■
4	B	612	0.1	1.5	200	-	■
4	D	609	0.1	1.5	200	-	□
4	F	613	0.1	1.5	200	-	□
4	G	628	0.1	1.5	200	-	□
4, 5	H, micro	619	0.1	1.5	200	-	□
4	I	605	0.1	1.5	200	-	□
5	nano	623	0.1	1.5	75	-	□

2.2 Micro and nanofabrication

In this section, the typical methods of the lithography techniques, i.e., photolithography and electron beam lithography as well as the typical etching techniques are briefly discussed. The methods were optimized based on Ni-Mn-Ga epitaxial thin films in order to fabricate micro and nanostructures and investigate some of the characteristics of these class of Heusler compounds including martensitic morphology and the critical transition temperatures vs. the lateral size, shape and orientation. The fabrication procedures including coatings and bakings were performed by a SUSS-RCD8 spin coater. The photo-exposures were performed using a SUSS-MA8 mask-aligner (Hg lamp 1000 W, UV400 350–450 nm); the electron beam exposure was performed by a Scanning Electron Microscope/E-beam writer TESCAN MIRA3 and the dry etching procedures were performed via an Oxford PlasmaPro 80 Instrument, located at CEITEC, Brno University of Technology.

2.2.1 Photolithography

Photolithography is among the typical top-down techniques for downscaling the materials having ~1 µm nominal spatial resolution, which can be also improved to sub-micron spatial resolution by using deep ultraviolet light sources. Photolithography enables patterning "well defined" microstructures, creating desired shapes, sizes, arrays, or even complex designs. The principle of the technique is based on imprinting designed structures on the soft, photosensitive, typically polymeric

thin layers (photoresist), which are coated on top of the material, typically thin films. These photosensitive layers are able to protect the underneath material during the next step of the fabrication, i.e. the etching process. At the end of the process, the protective layer is removed and underneath are the fabricated structures, which are the imprint of the designed structures. Like the other micro and nanofabrication technologies, the photolithography procedures need to be selected and optimized based on various factors such as the material characteristics, designed structures, the required lateral resolution and the scale of the fabrication. For the epitaxial Ni-Mn-Ga films, the resist coating procedure is shown in **Figure 2.2**, summarizing the first steps of the fabrication. The steps are as follows:

1. Prebaking the clean 5×5 mm films at 393 K for 300 s in air to remove the moisture, increasing the adhesion of the next step coating;
2. Inserting a droplet of the resist on top of the film by a micropipette,
3. Spin coating of the resist (4000 rpm, for 60 s), coating conditions are based on the types of the resists, determining the thickness of the resist layer;
4. Soft baking in air in order to evaporate the solvent. The time and temperature depend on the type of the resist.

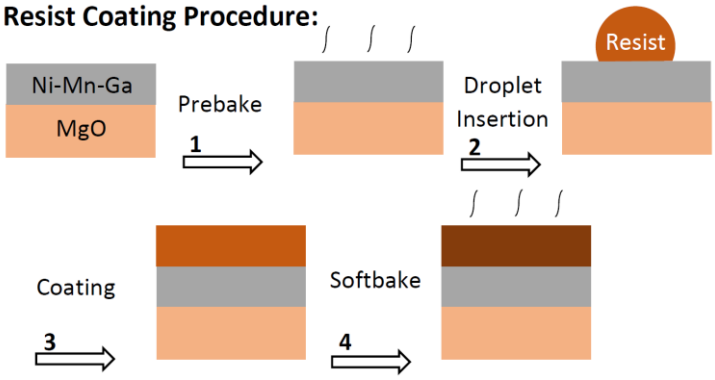

Figure 2.2: Resist coating procedure.

On the next step, the coated films are exposed to a certain wavelength and dosage of light, which is chosen based on the type of the resist. A photo-mask, typically made of Cr-coated quartz, containing the designed structures is placed in the proximity of contact with the coated films; therefore, the light can reach the films only through the designed structures, prohibiting the exposure of the whole surface of the samples. The exposure modifies the property of the resist, based on its type. For the positive resists, the exposed region becomes more soluble in the standard developers, which are typically alkali solutions, while the negative resists after exposure undergo crosslinking, hence, become hardly soluble in the standard developers [3]. A brief representation of the procedures based on the type of resists is provided in **Figure 2.3**:

1. Resist coating procedure as discussed above,
2. Exposure in the presence of the photo-mask; exposure dose is specified based on the type of resist;

For positive resists:

3. Developing in the standard solution for a specified time;

For negative resists:

3’. Crosslinking bake, which is an after exposure baking, depends on the characteristics of the resists;

4’. Developing the resist in the standard solution for a specified time.

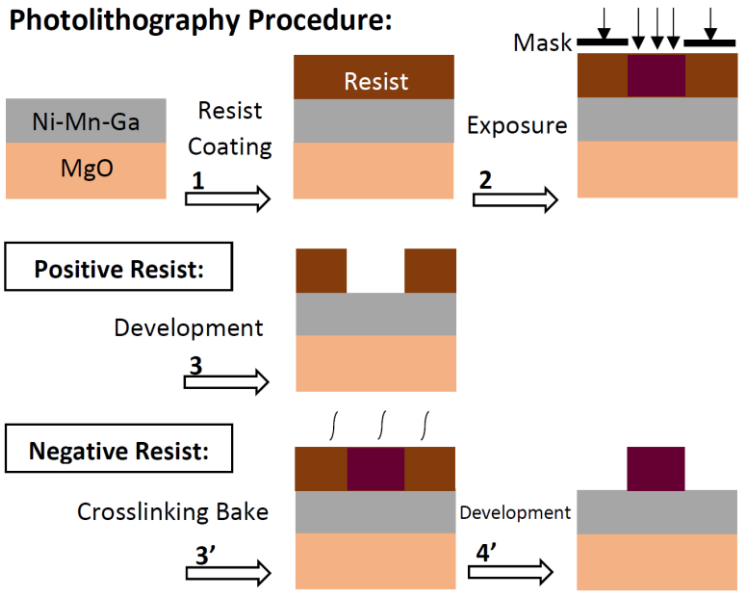

Figure 2.3: Typical photolithography procedure, comparing the positive and negative resists.

For fabricating the Ni-Mn-Ga microstructures with lateral size of 3-100 µm, after attempting different types of positive and negative resists, the following procedure proved the best results. Among the parameters, which were taken into account are the resist/Ni-Mn-Ga thickness ratio, adhesivity of the resist on Ni-Mn-Ga, resolution of the resist (capability of the resist to give well defined/small structures), etching rate of the resist under optimized Ar-ion plasma condition and the ease of the resist removal after the etching step. A summary of the optimized fabrication procedure is shown in **Figure 2.4**:

1. Coating the 200 and 75 nm thick Ni-Mn-Ga films by AR-N4340 resist (4000 rpm, for 60 s gives rise to the nominal thickness of 1.5 µm), following the standard procedure;
2. Exposure at 150 $mJ.cm^{-2}$, crosslinking bake and development following the standard procedure;
3. Ar ion etching; Ar = 0.8×10^{-6} $m^3.s^{-1}$, ΔV = 550 v, T = 300 K, t = 1.26 ksec for 75 nm NiMnGa films (grown on 20nm Cr underlayer) and t = 1.68 ksec. for 200 nm films, He backside cooling pressure ≈ 0.6 kPa (section 2.2.3);
4. Resist removal in hot acetone in an ultrasonic bath;
5. Annealing at 623 K for 3600 sec. and p = 10^{-6} Pa, in order to remove the stress possibly imposed to the sample during the lithography and etching process.

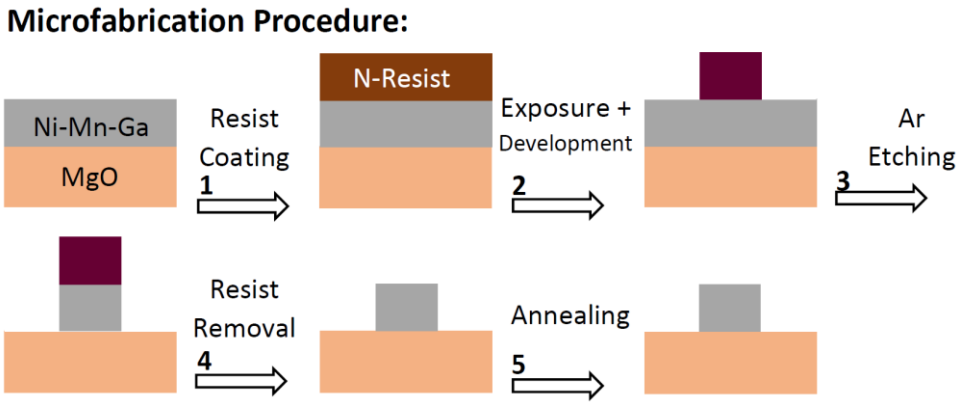

Figure 2.4: Summarized view of the optimized process used to fabricate Ni-Mn-Ga microstructures.

2.2.2 Electron beam lithography

To fabricate the submicron structures, the lithography technique is needed to be selected accordingly. Obviously, the photolithography resolution used above is not proper for submicron structures. For this purpose, electron beam lithography (EBL) was implemented. EBL uses electron beam to write the designed structures into a resist. Compared to the photolithography, discussed above, using the electrons pushes the nominal resolution of the lithography process below 10 nm. In addition, the electron beam directly moves on top of the resist, exposing the designed regions. Therefore, there is no need for the photo-mask. This enables the rapid modification of complex designs. However, compared to the above-discussed technique, EBL is more time consuming, specifically if a large surface area is supposed to be exposed [3].

The other difference with respect to the previous technique, which causes issues when the size of the structures reduces to submicron, appears in the step of the resist removal. Typically, due to the ion bombardment during the Ar etching (details are provided in section 2.2.3), the polymeric resists (in our case, novolac resist) change their properties and become stiff, therefore it would be demanding to remove them off the Ni-Mn-Ga film. Even after trying the standard resist removal procedures, some residuals of the resist typically remain on top of the structures specifically on the edges. This issue gets more critical as the size of the structures reduces. Adding a buffer layer prevents the direct contact between the resist and Ni-Mn-Ga. The buffer layer should be sufficiently adhesive to Ni-Mn-Ga, easy to etch using plasma etching and can be removed selectively, by chemical wet etching after the Ar etching process.

In order to select the proper buffer layer, a number of candidates (e.g. Cu, SiO_2 and Cr) were tested and some of them excluded. Specifically, in the case of SiO_2, it was observed that during the chemical etching, which is performed using buffered oxide etchant (BOE), this chemical solution interacts with Ni-Mn-Ga, creating nanometric holes in the material. After considering all the aspects of the restrictions, Cr was selected as the best candidate. Chromium is well known as an adhesive layer, can be etched rapidly by Chlorine reactive ion etching (RIE) and finally could be selectively etched off the Ni-Mn-Ga by the commercially available Cr-etchant. A Leica EM ACE600 coater was used to deposit the Cr buffer layer on top of Ni-Mn-Ga films.

Moreover, the type and thickness of the resist were needed to be carefully selected based on the resolution of the resist and the etching rate in Ar ions. As it will be shown in 2.2.3, the plasma etching process could give rise to some side-effects such as deposition of sidewalls, which is directly related to the thickness of the Ni-Mn-Ga and the resist, or the appearance of undercutting or mask erosion due to the active species in RIE. All of these processes need to be minimized by choosing the appropriate type and thickness of the resist, buffer layer and the etching conditions. The exposure dose depends on the type and the thickness of the resist and needs to be optimized as well, because if the structures are overexposed, after the development, they appear deformed and thicker than initially designed and if they are underexposed, the structures are washed away during the development step. The optimized procedure for 75 nm Ni-Mn-Ga films, which enabled the fabrication of nanostructures with the lateral size of 150-800 nm, is shown in **Figure 2.5**:

1. Cr sputter coating (50 nm);
2. Coating the films by AR-N7520.07 resist (4000 rpm, for 60 s, giving rise to the nominal thickness of 100 nm), following the standard procedure; **Figure 2.2**;
3. Exposure (600 $\mu C.cm^{-2}$, HV = 30 kV, BI = 7) and development;
4. RIE etching; $Cl_2 = 0.8\times10^{-6}\ m^3.s^{-1}$, $O_2 = 0.5\times10^{-7}\ m^3.s^{-1}$, $\Delta V = 125\pm1$ v, T = 263 K, t = 120 sec, He backside cooling pressure ≈ 0.6 kPa (section 2.2.3);
5. Ar ion etching; $Ar = 0.8\times10^{-6}\ m^3.s^{-1}$, $\Delta V = 550$ v, T = 263 K, t = 900 sec, He backside cooling pressure ≈ 0.6 kPa (section 2.2.3);
6. Resist removal by Cr wet etching at room temperature (120 sec soaking the sample in commercially available Cr-etchant), followed by rinsing in deionized water as well as ultrasonic cleaning in acetone and isopropanol;
7. Annealing at 623 K for 3600 sec. and $p = 10^{-6}$ Pa, in order to remove the stress possibly imposed to the sample during the lithography and etching process.

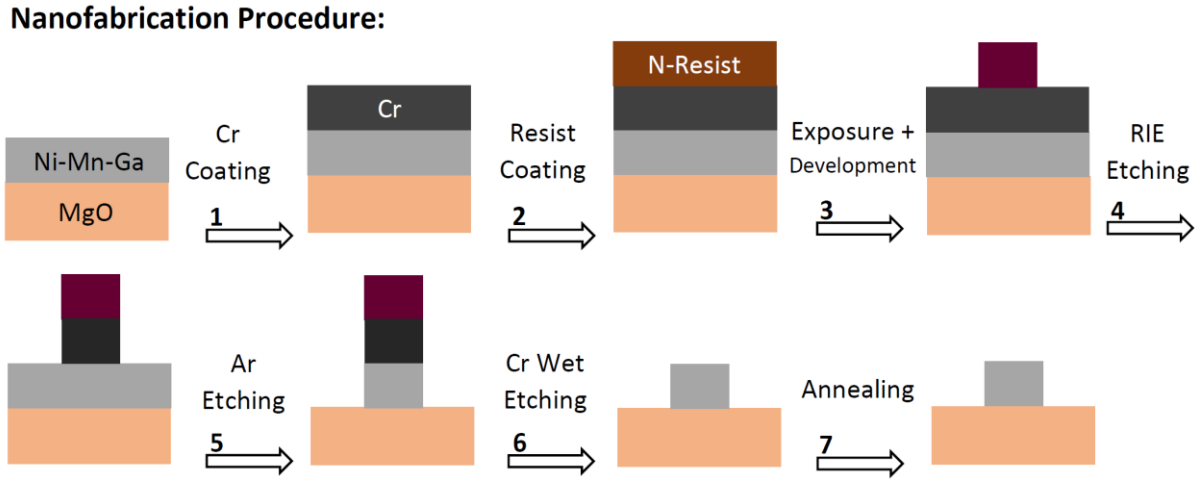

Figure 2.5: Summarized view of the optimized process used to fabricate Ni-Mn-Ga nanostructures.

2.2.3 Etching techniques

As mentioned above, after writing the designed structures on top of the continuous Ni-Mn-Ga films, the micro and nanofabrication proceed with the etching. Generally, the etching can be categorized into wet and dry. Within the wet etching process, different concentrations and mixtures of base, acid or buffered chemical solutions serve as the etchants, removing the regions of the continuous film that are not covered by the resist.

In addition, in case of multilayers or Ni-Mn-Ga films having buffer layers such as Cr or SiO_2, some of these chemical solutions, i.e. Cr-etchant and BOE could selectively etch the buffer layer while preserving the Ni-Mn-Ga film. If the buffer layer is in between the substrate and the film, etching process detaches the film from the substrate, giving rise to freestanding Ni-Mn-Ga films and in case the buffer layer is in between the resist and Ni-Mn-Ga film, it could promote the resist removal process, which is specifically beneficial for the nanofabrication (as discussed above).

In the dry etching process instead, high-energy ions, neutral species and radicals serve as the etchants. This process is based on the ionization of gaseous agents in vacuum, creating a plasma by applying RF power. The type of the ionized gas or the mixture of gases are chosen with respect to the type of material that is supposed to be removed. Etching in this technique is sufficiently selective and controllable by choosing the type and the pressure of inserted gases as well as the etching conditions such as temperature, time, pressure and RF power [4]. In this work, the micro and nanostructures were fabricated using Ar ions and RIE, while the wet etching process was only used to promote the resist removal step in the fabrication of the nanostructures. In the following, the parameters, conditions and selected gases are briefly discussed.

The main plasma etching process for the fabrication of the Ni-Mn-Ga micro and nanostructures was performed using Ar ions. A simplified scheme of the plasma etching apparatus is shown in **Figure 2.6**. The power source system is a competitively coupled plasma (CCP) and the RF generator operates at 13.56 MHz. As the Ar gas enters the main chamber from the gas inlet, it is ionized in-between the top and the bottom electrodes, creating the Ar plasma. The sample chuck is located on the bottom electrode, which is connected to a He backside cooling stage. Helium gas increases the thermal contact between the substrate and the cooling stage, preventing the raise of temperature during the etching process. The inserted gas pressure is controlled by the control valve and the vacuum is controlled by a throttle connected to a turbo molecular pump. The principle of the Ar^+ etching is based on the physical bombardment of the sample, sputtering off the uncovered material. Since the etching rate of the resist is typically lower than the target material, the resist can protect the imprinted structures underneath during the etching procedure. Before starting the Ar etching, a short Oxygen plasma etching is always beneficial. It removes the possible residuals of the undeveloped resist.

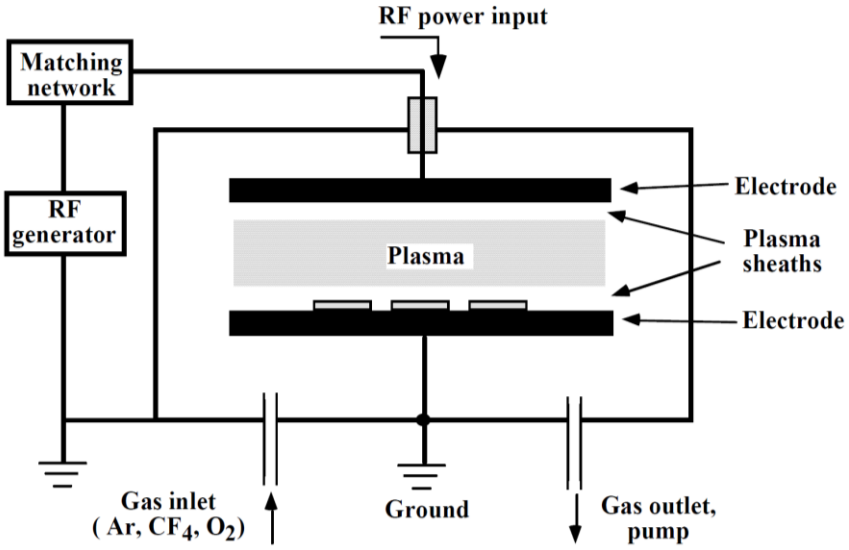

Figure 2.6: Simplified scheme of the plasma etching apparatus [4].

In order to accelerate the sputter etching of the Cr buffer layer as mentioned above, the EBL nanopatterned structures were subjected to chemically reactive ion etching (RIE). In this process, the etching is performed by gaseous active chemicals, selected based on the type of the material, which is supposed to be etched away. The gaseous chemicals are inserted through the gas inlet. Since in this case, Cr buffer layer is the top layer to be etched off, Chlorine was selected as the reactive agent, which is well known for fast and selective etching of metals.

In contrast to Ar plasma etching, which is anisotropic (**Figure 2.7**), dependent on the orientation of the crystal planes, defects and the position of the sample with respect to the ions, the etching process related to the reactive species is isotropic (i.e., equal etching in every directions), although quite selective to the type of the material. Chemically active species also enhance the physical etching of the Ar ions by removing the byproducts and inhibiters. Similar to other steps of micro and nanofabrication, dry etching also needs to be diligently optimized based on the type of the material to be etched, thickness of the film, lateral sizes of the lithography fabricated patterns and aspect ratio of the patterns. A simplified schematic representation of the plasma etching process is shown in **Figure 2.7**, summarizing the etching process of the ions and chemically active species, as well as the possible processes, byproducts and side effects occurring during the plasma etching [4].

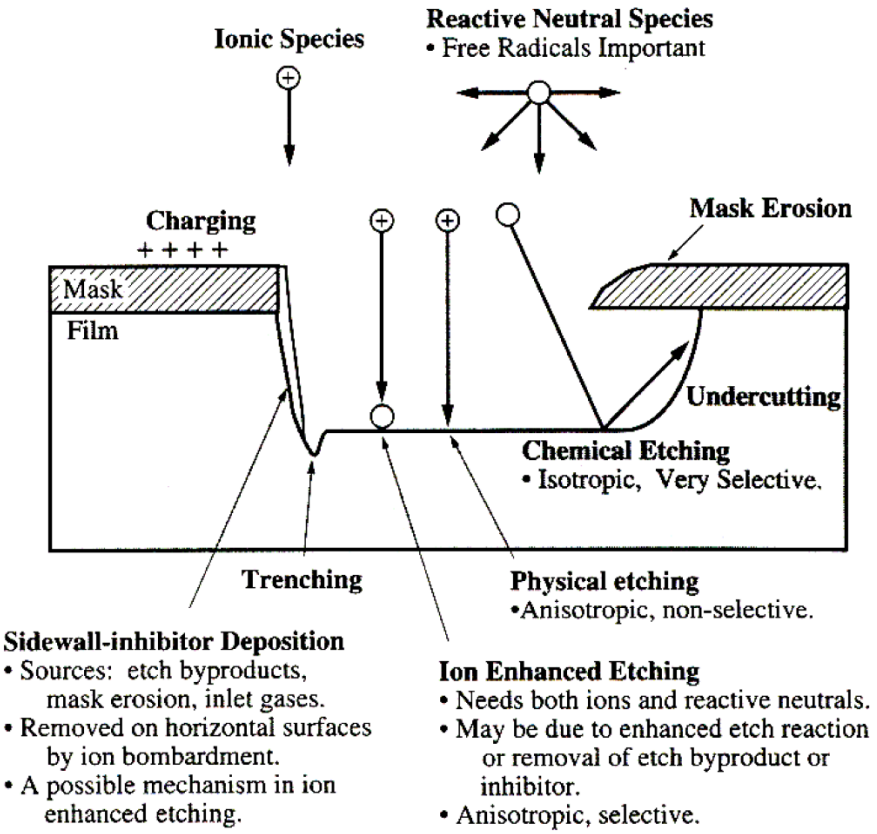

Figure 2.7: Representation of the summarized plasma etching process [4].

2.3 Characterization

2.3.1 Polarized light microscopy

Polarized light imaging via an EVICO Micromagnetic Kerr microscope (CEITEC, Brno University of technology) provided the large-scale visualization of the colonies of differently oriented twin boundaries in epitaxial Ni-Mn-Ga thin films at room temperature. A simplified schematic representation of different part of the instrument is shown in **Figure 2.8**. The light generated by the LED lamps is passed through a slit and a polarizer, where it is converted to a linear polarized light, illuminating the sample. The reflected light from the surface of the sample passes through the compensators and the analyzer. Finally, the light reaches the charge-coupled device (CCD) camera, where the laterally resolved image from the objective lens is recorded [5]. The colonies of the differently oriented twin boundaries can be visualized by subtracting the images acquired by setting the compensator to ±2° from the extinction condition (90º crossed polarizer-analyzer configuration). The principal is based on the different change of the polarization of the incident light, upon reflecting from differently orientated colonies of twin boundaries, which gives rise to the observed dark and bright gray contrasts [6].

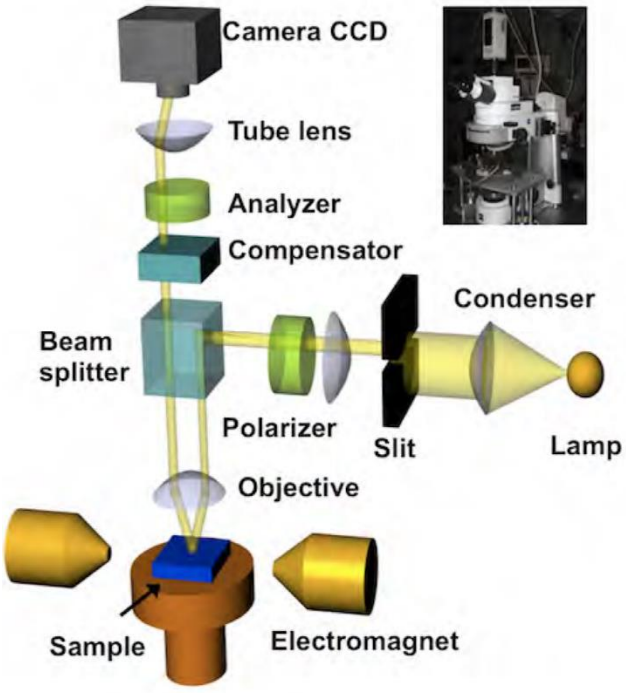

Figure 2.8: Schematic representation of different parts of the Kerr microscope [5].

2.3.2 Scanning electron microscopy

Scanning electron microscopy (SEM) is a versatile technique providing the possibility of a number of characterizations as well as the sample manipulation. A basic scheme of the instrument is shown in **Figure 2.9**. In this technique, the electrons are generated by the electron cathode (or gun). The electrons are then aligned and focused by a set of magnetic lenses to the spot size of around 5 nm. The deflection coils in the column are responsible for scanning the sample by deflecting the primary electron beam. The primary beam hits the sample and penetrates into it based on the sample characteristics, energy of the beam and the angle between the sample and the beam. The signals resulting from the interaction between the primary beam and the sample are then detected and the data is generated [7].

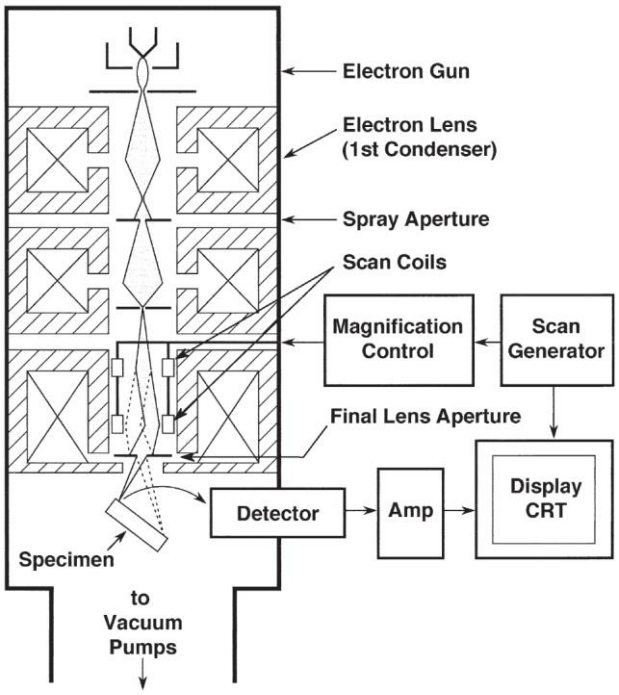

Figure 2.9: Basic scheme of SEM, representing different parts of the instrument [7].

The major sample-electron interactions typically give rise to the secondary electrons (SE), backscattered elections (BSE) and the X-rays (X). The first two are typically detected by specific detectors, used to generate the SEM images. The X-rays however, are typically detected by the electron dispersive X-ray spectroscopy (EDS) detectors, determining the elemental composition characteristics of the samples. SE electrons are the result of the inelastic interaction between the primary beam and the material, meaning that the primary electrons lose a part of their energy to create the SE electrons. In contrast, BSE electrons are the result of the elastic interaction between the sample and the incident beam. Since the SE electrons have a reduced energy with respect to BSE, only the ones which are emitted from the material close to the surface have the sufficient energy to reach the detector [8]. This makes the SE electrons providing mostly the characteristics of the sample surface such as topography, unlike BSE, which in Ni-Mn-Ga films, could also provide the characteristics related to the orientation of the twin boundaries with respect to the substrate. A scheme for the emission depth of SE, BSE and X-rays is shown in **Figure 2.10**. As can be observed, the X-rays determining the elemental composition of the samples are emitted from the bulk of the material and as the electron beam penetrates into the sample, the divergence of the interaction increases.

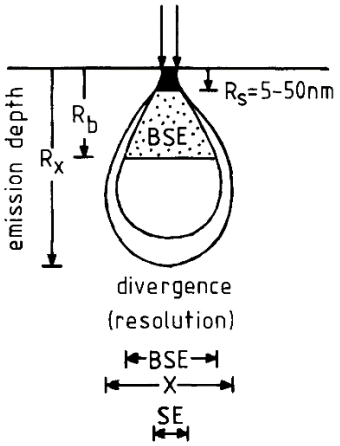

Figure 2.10: Scheme of the emission depth of SE, BSE and X-rays [8].

One of the advantages of the scanning electron microscopy imaging that was taken for visualizing X- and Y-type twinning configurations in Ni-Mn-Ga epitaxial films can be described as the channeling effect. This effect is based on the interactions between the high-energy incident electron beam and the crystalline structure of the material. By choosing suitable relative orientations between the electrons and the sample, the crystallographic information, e.g., grain boundaries and twinned structures can be detected and appear as different contrasts in the SEM image or even in certain conditions, some patterns can be detected, related to the crystallographic structure of the samples. The latter is known as an independent SEM-enabled technique called electron-backscattered diffraction.

Channeling effect enables the orientational characterization of the twin boundaries by BSE-imaging. It exploits the interaction between the incident electrons and the arrangement of the atoms in the lattice (both orientational arrangement and packing). **Figure 2.11** shows schematically the principle of the channeling effect. The grey vectors show the primary electrons hitting the crystal structure of the sample from different directions. The electrons that directly hit the atoms or planes of packed-atoms are typically scattered close to the surface of the sample (called channel closed) and are detected by the SEM detectors, which in turn increase the intensity of the backscattered electrons reaching the detector, causing that part of the sample to appear bright grey in the image. In contrast, when the electrons hit the lattice in the channel or gap between the atomic planes, they can penetrate into the structure to a relatively higher depth before they are scattered (called channel open). The energy of scattered electrons coming from higher depth of the sample is typically lower than energy of those scattered from the surface of the sample. Therefore, the intensity of the electrons reaching the detector from the depth of the sample is lower and they form a dark contrast in the BSE-images. This effect is prominent for back scattered electrons (BSE) due to their higher energy with respect to secondary electrons (SE).

Different twinning configurations with respect to the substrate, i.e., X- and Y-type were visualized by BSE-imaging based on the channeling effect. Nevertheless, the scheme shown in **Figure 2.11** can be considered as a simplified representation, showing the principles of the effect and cannot be directly applied to the complex twinned systems such as in Ni-Mn-Ga films. As can be observed, the figure shows the variation of the angle of the primary electron beam while in the case of Ni-Mn-Ga films the microstructural orientations of X- and Y-type twinning configurations are the variables and the angle of the primary electrons is fixed.

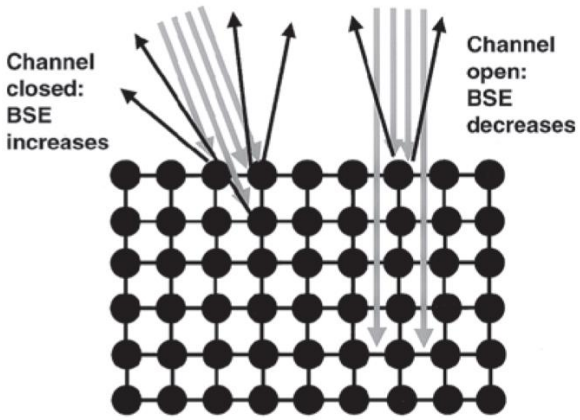

Figure 2.11: The principle of the channeling effect for the electrons hitting the crystal, generating BSE [7].

The SEM images and the EDS analysis were performed at room temperature using the following instruments:

- SEM, FEI Inspect – F equipped with EDS analytical detector, (INRIM, Turin)
- Zeiss Auriga Compact SEM, (IMEM-CNR, Parma);
- FEI-VERIOS 460L equipped with EDS analytical detector, (CEITEC, Brno University of Technology).

Since the SEM imaging is based on electrons, conductivity of the sample plays an important role on the quality of the images. It requires an appropriate mounting of the Ni-Mn-Ga films on the SEM standard stubs using the conventional double-sided Cu tapes, creating a few bridges from the stub to the top side of the samples. The conductivity would become a real challenge for imaging the micro and nanostructures, where small isolated volumes of Ni-Mn-Ga structures are surrounded by the insulating MgO substrate. This makes the high-resolution imaging quite demanding. To overcome this obstacle, the fabricated structures were grounded individually (some examples are shown in **Figure 2.12**) by TPT HB 16 wire bonder. The optimum imaging parameters are as follows HV: 20 kV, Current: 0.2 nA, Dwell time: 300 µs.

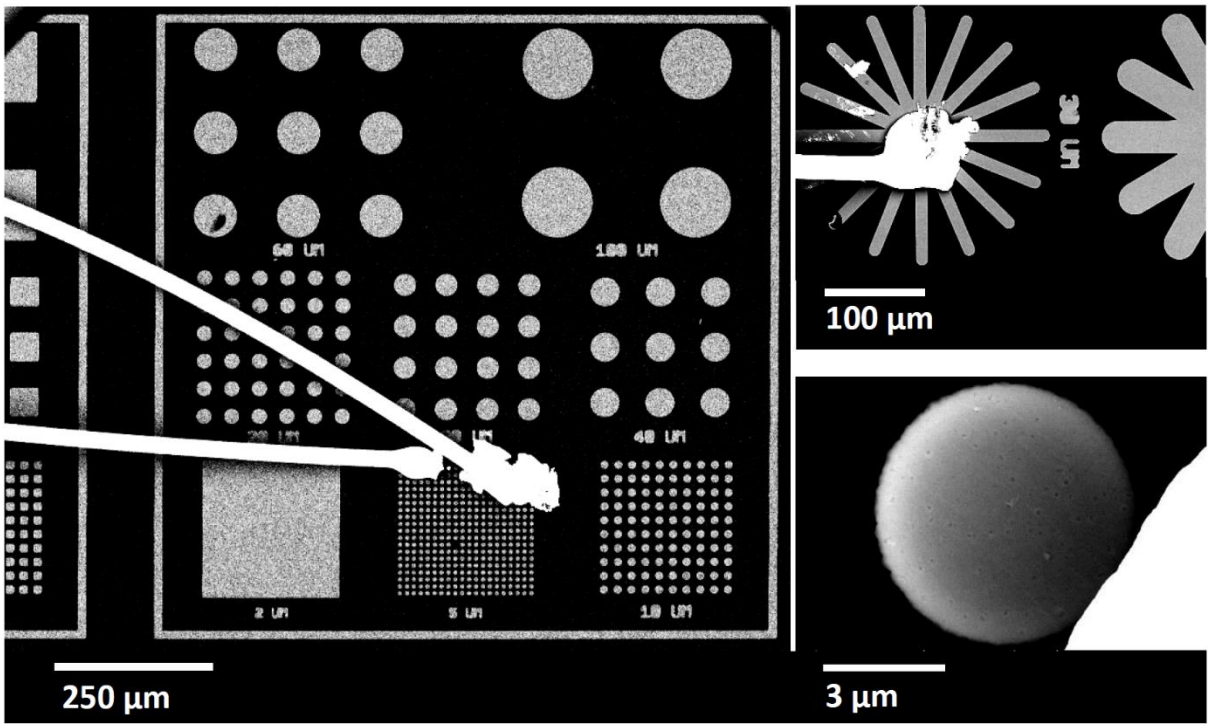

Figure 2.12: Promoting the conductivity of the Ni-Mn-Ga microstructures for BSE imaging by grounding the structures using bonding technique.

2.3.3 Transmission electron microscopy

Transmission electron microscopy (TEM) is a highly accurate and versatile technique, enabling the structural, compositional, magnetic and morphological characterizations of materials from atomic to micrometer scale. The key point of this versatility lies in the presence of high-energy electrons passing through the specimen. Since the electrons present the wave nature and the particle nature simultaneously, they provide both the diffraction and imaging related characterizations as well as analytical characterizations, such as EDS. In addition, due to their intrinsic charge, the electrons are deflected by the Lorentz force upon passing through thin magnetic samples, enabling the magnetic characterization of magnetic samples. The short wavelength of the electrons, which is in the picometre range at the working accelerating voltages (200 kV), enables the lateral resolution of as low as fractions of nanometer, which are not reachable by other conventional techniques [9].

Different TEM techniques were performed with a JEOL 2200FS microscope (at IMEM-CNR, Parma) working at 200 kV including High angle angular dark field scanning transmission electron microscopy (HAAFD), high resolution transmission electron microscopy (HR-TEM), Fast Fourier Transform patterns (FFT), selected area electron diffraction (SAED) and electron holography.

The TEM analysis of Ni-Mn-Ga films were performed in the cross-sectional view on the TEM lamellas prepared by focused ion beam (FIB) lift-off technique and on plan-view specimens prepared by chemical etching technique. For the cross-sectional investigation, the TEM lamellas were prepared by a Zeiss Auriga Compact SEM equipped with FIB.

2.3.4 Atomic and magnetic force microscopy

Atomic force microscopy (AFM) and magnetic force microscopy (MFM) are among the scanning probe microscopy techniques. AFM enables the morphology investigation of samples with height resolution in the range of fractions of nanometer and the lateral resolution of a few nanometers depending on the chosen probe tip. MFM provides a detailed view of the magnetic stray field of the magnetic samples thanks to the interaction between the magnetic tip and the perpendicular stray-field gradient of the magnetic materials [10]. The principles of the technique are based on the atomic force interaction (in case of AFM) or the magnetic force interaction (in case of MFM) between the atoms of the tip and the sample. These interactions cause different amplitudes and gradients of deflections while the tip is scanning the sample. The tip is attached to a cantilever, typically made of Silicon oxide or Silicon nitride; therefore, the deflection is directly transferred to the cantilever. In the backside of the cantilever, the deflection is detected by a highly sensitive optical system, in which a laser source is focused on the cantilever and its reflection is detected by photodiodes (**Figure 2.13**) [10]. The AFM images were chaptered in tapping mode. Tapping and contact modes are the most popular AFM modes for surface exploration. The contact mode is realized as the fundamental procedure of the AFM. The tip is placed at the proximity of the surface of the sample, scanning the surface. The deflection of the cantilever is detected by an optical setup including a laser source and a photodetector, which is then plotted as the force curves vs. the position of the tip. The force of the tip in each position is used to generate the topography images. The disadvantage of this mode is the presence of the high lateral-force between the tip and the sample, which can basically damage the sample or the tip during the scan. In the contact mode, the tip could also adsorb the loose parts, dirt or dust from the surface of the sample, which might in turn influences the measurement. The issue with the lateral force can be solved if the tip touches the surface of the sample only for a short time. In other words, the tip oscillates on top of the surface of the sample during the scanning. In this mode of scan, which is called tapping mode, the deflection is based on the change in the modulation of the amplitude of the oscillation in the lock-in condition. In contrast to the relatively simple detection of the force curves in the contact mode, mentioned above, the detection is much more complicated in the tapping mode and is related to the average results of many interactions between the oscillating tip and the surface of the sample, including van der Waals and Coulomb interactions.

In order to characterize the Ni-Mn-Ga films, AFM and MFM images were captured by:

- Dimension 3100 microscope equipped with Nanoscope Veeco controller equipped with a heating stage (IMEM-CNR, Parma);
- Scanning Probe Microscope Bruker Dimension Icon SPM, (CEITEC, Brno University of Technology);
- Quantum design (QD) physical property measurement system (PPMS) 14-AFM/MFM (Functional Materials, Technical University of Darmstadt).

The images were taken in the interleave mode using MESP-V2 magnetic tips (nominal radius: 35 nm), having Co-Cr reflective magnetic coating. In this case, two-pass scanning mode was conducted, i.e., the first pass, collects the data related to the short range interaction of the topography of the surface, while the second pass scans with a constant height from the surface of the sample, to avoid the short range topography interactions. The second pass collects the data related to the long-range magnetic stray field gradient of the sample. A simplified schematic representation of the AFM and MFM imaging for a Ni-Mn-Ga epitaxial film is shown is **Figure 2.13**. When the magnetized

oscillating tip scans a magnetic sample, the attractive or repulsive interactions between the tip and the long-range stray field gradient of the sample shift the resonance curve of the oscillating tip to lower or higher frequencies, respectively, which is converted to dark and bright contrasts in an MFM image.

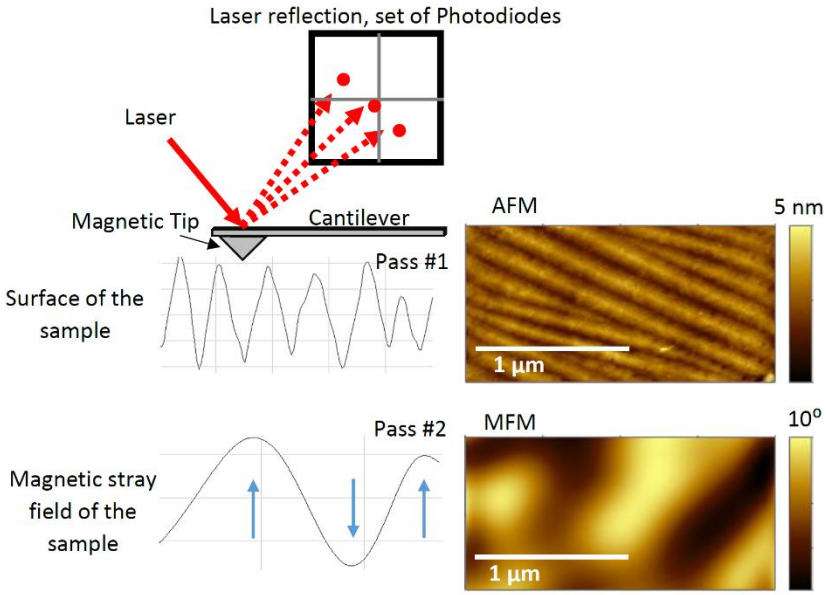

Figure 2.13: Simplified schematic representation of the AFM and MFM imaging technique for a Ni-Mn-Ga epitaxial film.

2.3.5 X-ray analysis

The X-ray diffraction analysis was performed on the Ni-Mn-Ga films to characterize the structure of the samples at the high temperature austenitic phase and the low temperature martensitic phase, as well as to obtain the lattice parameter values (section 1.2.1). Moreover, for the thinner samples (75 nm) the X-rays reflectivity measurements were additionally used to determine the exact thickness of the films.

The structural characterization was performed by means of X-ray diffraction (XRD) through the following diffractometers:

- Thermo ARL X'tra diffractometer with Cu-Kα radiation (λ = 1.5406 Å) equipped with an environmental chamber (SCVSA, University of Parma);
- High-brightness source diffractometer (Rigaku Smartlab 9kW) with Cu-Kα radiation (λ = 1.5406 Å), equipped with a high-temperature chamber (CEITEC, Brno University of Technology).

The principle of the structural characterization via X-rays is based on the interaction between the X-ray beam and those lattice planes of the crystal structure which fulfill the Bragg's law [11]. The positions of the diffraction peaks as a result of the constructive interference between the X-ray beam and the crystal planes are unique for different crystal structures and orientations. As it will be discussed in details in the following chapters, different scan modes and configurations were performed for better visualization of the Ni-Mn-Ga crystal structure in the austenitic and martensitic

phases. They include line scans, wide-angle diffraction and reciprocal space mapping for in-plane and out-of-plane configurations.

Figure 2.14 shows the geometry of the experiment for acquiring reciprocal space maps (RSM) in an out-of-plane **Figure 2.14a** and in-plane configuration **Figure 2.14b**, giving access to the Ni-Mn-Ga lattice planes that are epitaxially grown on (001) MgO. For the out-of-plane RSM measurements, a double-bounce (022) Ge monochromator and a 5° soller slit in the incident and diffractive optics were employed, respectively. RSM datasets are acquired performing coupled 2θ/ω scans for different orientations of ω between the X-ray source and the sample (**Figure 2.14a**). For the in-plane RSM measurements **Figure 2.14b**, the monochromator was removed in order to maximize the diffracted intensity and 0.5° soller slits were employed instead in both incident and diffractive optics to ensure a good $2\theta_\chi$ angular resolution. In-plane RSM datasets are acquired at grazing incidence ($\omega \approx 0.7°$) and performing coupled $2\theta_\chi/\varphi$ scans for different azimuthal orientations φ of the sample (in-plane angle between the x-ray source and vertical lattice planes of the film). For the temperature dependent measurements, the samples were placed in a high-temperature chamber using a N_2 gas environment and a hemispherical graphite dome for an improved temperature homogeneity.

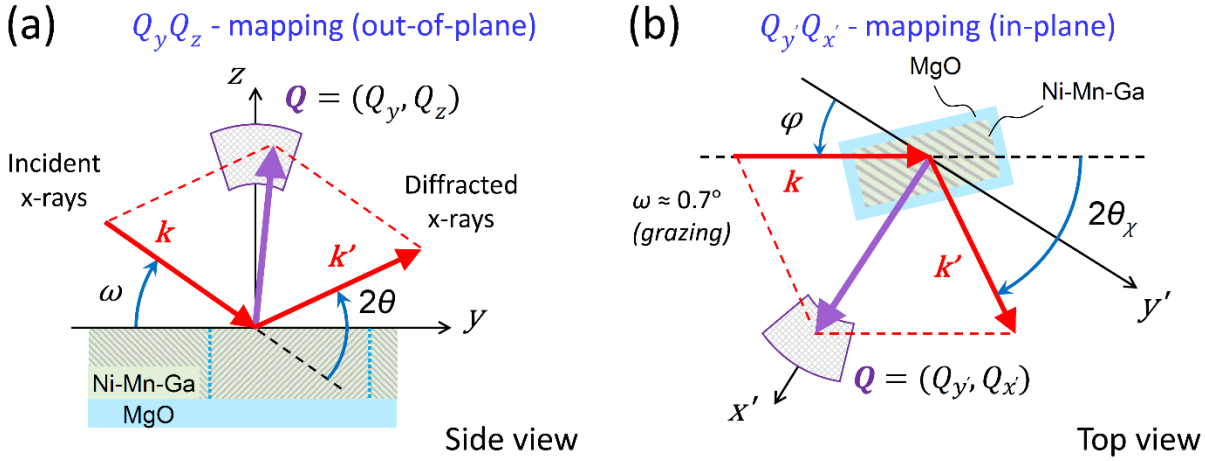

Figure 2.14: Geometry of the experiment for acquiring reciprocal space maps (RSM) in an out-of-plane (a) and in-plane configuration (b), giving access to the Ni-Mn-Ga lattice planes that are epitaxially grown on (001) MgO.

In addition to the structural characterization, X-rays can provide an accurate measure of the thickness of the thin film samples as well (for typically up to ~100 nm thickness). The technique, which is called X-ray Reflectivity (XRR), is a grazing angle scan based on interference of the X-rays reflected from the surface of the film and the reflected X-rays from the film-substrate interface. For a sample, aligned with respect to the incident beam, upon the θ-2θ scan, below the critical angle (θ_c), the entire reflected beam originates from the surface of the sample. For the angles higher than θ_c, a part of the beam that reaches the detector is reflected from the interface between the film and the substrate, as it is shown in **Figure 2.15**, generating Kiessig fringes and Fresnel reflectivity. The periodicity of the Kiessig fringes as well as well their variation of the intensity are related to the thickness of interfaces, i.e. the thickness of Ni-Mn-Ga films [12].

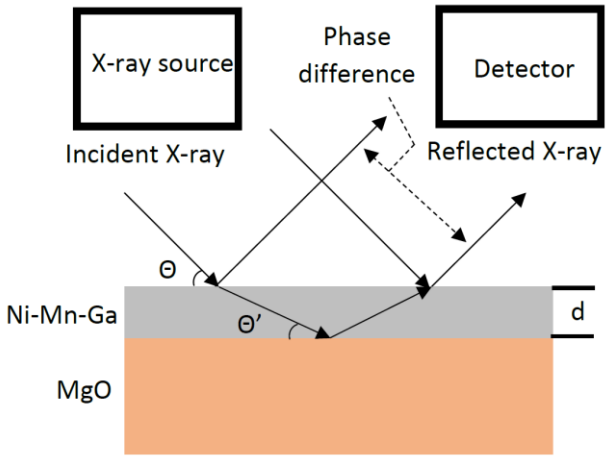

Figure 2.15: Schematic representation of the principles of the thickness measurement using X-ray reflectivity.

2.3.6 Electrical transport measurements

Four probe electrical transport measurements vs. temperature were performed to directly measure and compare the critical transition temperatures and the thermal hysteresis of the Ni-Mn-Ga micro and nanostructures, taking the advantage of the change in the electrical resistance of the material through both the first order and the second order phase transitions [13,14]. The measurements were performed by a Cryogenic-free VERSALAB electrical transport measurement system from Quantum Design in a temperature range of 200-400 K ($dT/dt = 8$ mK.s^{-1}). Micro and nanostructures with stripe geometry were fabrication and connected to lithographically fabricated pads. The pads were bonded individually to the electrodes using a TPT HB 16 wire-bonder. The scheme of the designed pads are provided in **Figure 2.16**, showing the pad of the microstripes (**Figure 2.16 a**) and the pads designed for the nanostripes (**Figure 2.16 b**).

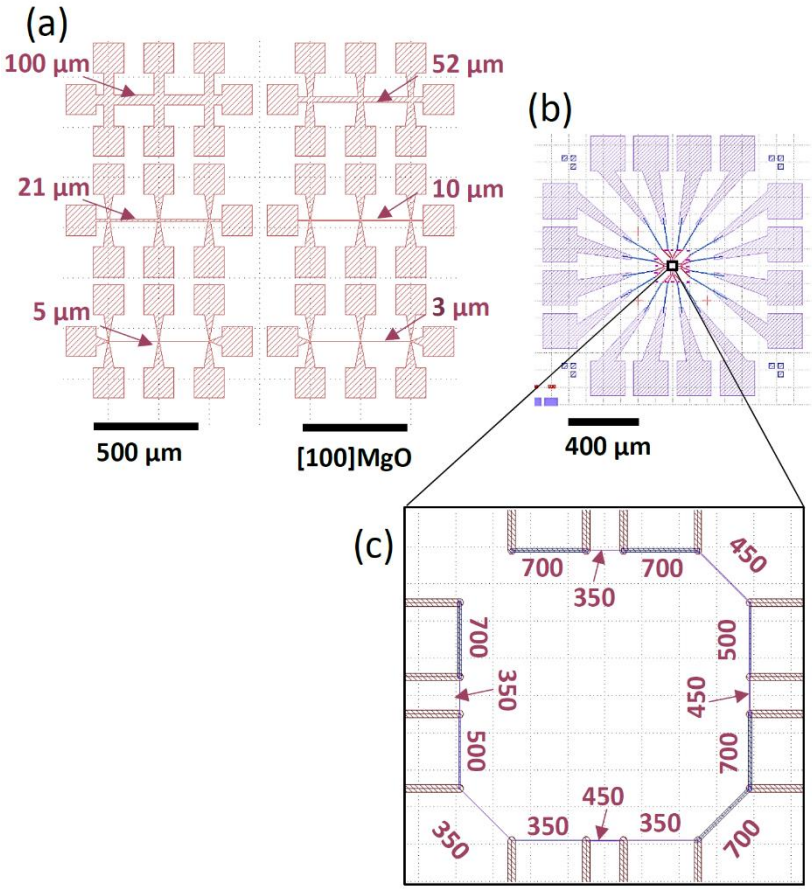

Figure 2.16: Scheme of the designed pads: a) for microstripes, b) nanostripes, c) the magnified image of the marked region in (b). The numbers represent the actual width of the stripes in micron for microstripes and in nanometer for nanostripes, measured by AFM.

2.3.7 Vibrating sample magnetometry

Vibrating sample magnetometery (VSM) is a magnetic characterization technique for the accurate quantification of the magnetic moment of magnetic materials upon applying external magnetic fields. As schematized in **Figure 2.17**, the principle of the technique is based on applying a magnetic field to the sample, positioned inside the detector coil. The sample is forced to oscillate (vibrate) inside the detector coil along its axis. The oscillating magnetization creates a time dependent magnetic flux variation across the coil, thus inducing an electromotive force on it. This effect is detected as a voltage variation in the coil, the variation is proportional to the magnetic moment of the magnetic material [15]. For a 4×4 mm Ni-Mn-Ga sample, a QD PPMS 14-VSM was used in order to measure the magnetization curves vs. applied magnetic field ($\mu_0 H$ = -1 to 14 T normal to the film plane, $d\mu_0 H/dt$ = 1 $mT.s^{-1}$, T = 323 K). In addition, the magnetization curves of the sample vs. temperature (350 to 260 to 350 K, dT/dt = 8 $mK.s^{-1}$) were measured in the presence of the applied magnetic fields of 0.1, 0.8 and 14 T, which were applied normal to the film plane as shown in **Figure 2.17**.

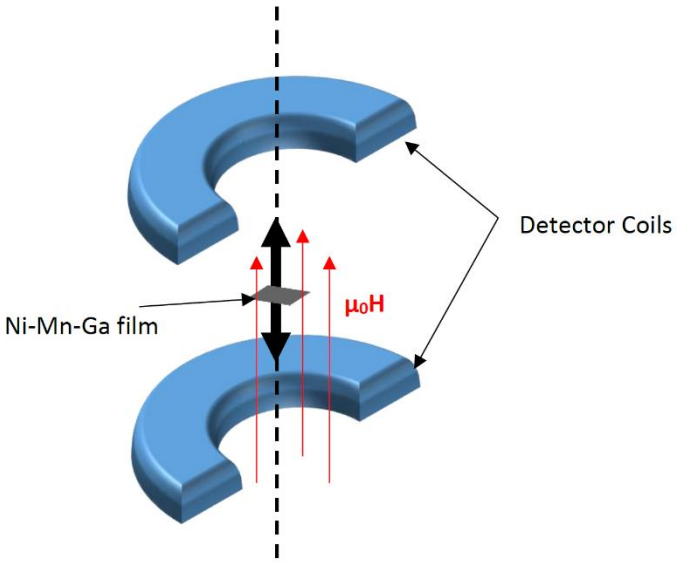

Figure 2.17: Simplified representation of the VSM technique for measuring the magnetization of Ni-Mn-Ga thin films.

2.3.8 Superconducting quantum interference device magnetometry

The superconducting quantum interference device (SQUID) magnetometer is a sensitive technique for detection of the magnetic flux. It contains a superconducting pickup coil operating at liquid Helium temperature, capable of detecting very small magnetic signals. As it is shown in **Figure 2.18**, the principle of the technique is based on moving the sample inside the superconducting pickup coil. The magnetic flux of the sample is detected by the coil windings, which are connected to the SQUID sensor. The entire circuit transfers the signal to the SQUID controller, where the magnetic flux is converted to voltage and plotted as a function of the position of the sample. The voltage is proportional to the magnetization of the sample. The external magnetic field is applied by a superconducting magnet parallel to the moving direction of the sample [16]. As shown in the figure, the thin film samples can be mounted inside a drinking straw in different positions, working as a sample holder in order to have the applied magnetic field along the desired orientations of the film. A Quantum Design SQUID magnetometer (installed at IMEM-CNR, Parma) was used to measure the transition critical temperatures and the thermal hysteresis of the continuous Ni-Mn-Ga films for 200-400 K temperature range ($\mu_0 H$ = 2 mT along <100> MgO, dT/dt = 8 mK.s^{-1}).

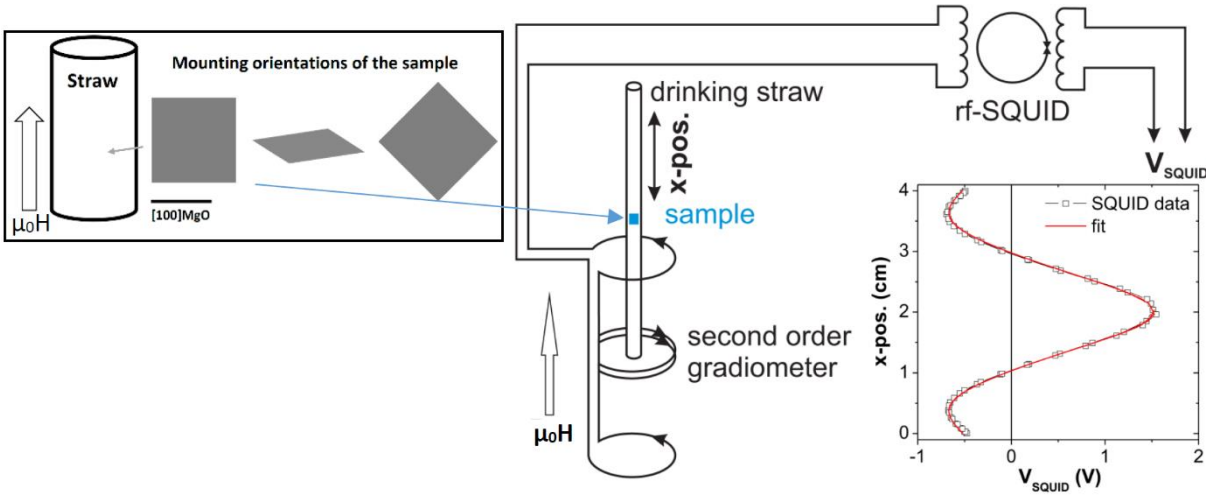

Figure 2.18: Simplified representation of the SQUID magnetometer technique for measuring the magnetization of Ni-Mn-Ga thin films ([16], the image was modified).

References

1. Chapman, B. Glow Discharge Processes (John Wiley & Sons, New York, 1980).
2. Matsunami, N. *et al. Atom. Data nucl. Data* **31**, 1 (1984).
3. Guozhong, C. Nanostructures and nanomaterials: synthesis, properties and applications (Imperial college press, London, 2004).
4. Plummer, J.D. *et al.* Silicon VLSI technology: fundamentals, practice and modeling (Pearson Education, London, 2009).
5. Idigoras, O. *et al. Nanofabrication* **1**, 23 (2014).
6. Lai, Y. W. *et al. Appl. Phys. Lett.* **90**, 192504 (2007).
7. Goldstein, J.I. *et al.* Scanning electron microscopy and X-ray microanalysis (Springer, New York, 2017).
8. Lloyd, G.E. *Mineral. Mag.* **51**, 3 (1987).
9. Williams, D.B., & Carter, C.B. Transmission Electron Microscopy: A Textbook for Materials Science (Plenum Press, New York, 1996).
10. Wiesendanger, R. Scanning probe microscopy and spectroscopy: methods and applications (Cambridge university press, Cambridge, 1994).
11. Warren, B.E. X-ray Diffraction (Dover Publications, New York, 1990).
12. Parratt, L.G. *Physical review* **95**, 359, (1954).
13. Srivastava, V.K. *et al. Applied physics letters* **89**, 222107 (2006).
14. Alexandrakis, V. *et al. Scripta Mater.* **156**, 101 (2018).
15. Foner, S. *Rev. Sci. Instrum.* **30**, 548 (1959).
16. Buchner, M., *et al. J. Appl. Phys.* **124** 161101 (2018).

Chapter 3

Martensite-enabled magnetic flexibility: the effects of post-growth treatments in magnetic-shape-memory Heusler thin films

3.1 Introduction

Magnetic-shape-memory Heusler materials have the capability of shape recovery through a diffusion-less thermodynamic structural martensitic phase transformation between high-temperature austenitic and low-temperature martensitic phase. Across the martensitic transition, the material encounters coordinated movement of atoms, which produces stress in the system. This gives rise to a remarkable change of microstructure: twin variants nucleate and organize in a hierarchical architecture (section 1.2.1). Typically, in epitaxial Ni-Mn-Ga films on (001) MgO, two different martensitic microstructures, called X-type and Y-type, can form and they may coexist in the same film depending on the substrate or under-layer, composition and growth conditions [1,2 and references therein]. In Y-type microstructure, the twin boundaries grow perpendicular to the substrate surface, while in X-type the twin boundaries grow at 45° to the substrate surface. The easy-magnetization axis of the martensitic cells lies alternately in-plane and out-of-plane in X-type twin variants, while it alternates between two different in-plane directions in Y-type microstructure [1,3,4] (section 1.3). Controlling twin variants' orientation and their organization in X and Y microstructures is crucial for optimizing the multifunctional properties and could also better enable a number of thermo/magnetomechanical applications beyond magnetic refrigeration and energy harvesting, e.g. actuation [5,6], magnetic field writing [7,8] and magnetic anisotropy dependent biological applications [9].

So far, there have been few attempts for overall manipulation of microstructure in epitaxial Ni-Mn-Ga films. Jenkins et al. reported the magnetic rearrangement of twin boundaries in epitaxial Ni-Mn-Ga cantilever released from the substrate [10]. Eichhorn et al. reported partial alignment of twin boundaries in freestanding epitaxial Ni-Mn-Ga bridges using magnetic field cooling [11]. In 2015, a detailed study on the correlation between structure, microstructure and magnetic properties of substrate constrained Ni-Mn-Ga films grown on Cr/ (001) MgO was reported, showing the preferential alignment of the Y-type variants along a specific direction [1] (section 1.3.1). More recently, Campanini *et al.* [5] reported thermo-magnetic actuation of freestanding Ni-Mn-Ga nanodisks based on X-type and Y-type twin variants' selection (section 1.3.1). In addition, there have been some works on local tuning of magnetism both for Ni-Mn-Ga bulk single crystals [7,8] and local manipulation of epitaxial films using nanoindentation [12].

In this chapter, the manipulation of the microstructure and magnetic configuration of Ni-Mn-Ga films directly grown on (001) MgO is shown by tuning the twin boundaries from all X-type to mixed

X/Y. Starting from films of different morphology obtained by changing growth temperature, suitable post-growth treatments are applied, i.e., post-annealing, magnetic field cooling and a local mechanical stress.

It is clearly demonstrated how different simple post-growth treatments open up the possibility to tailor the martensitic configuration of magnetic-shape-memory thin films and consequently obtain the magnetic configuration best suited to the required purpose. This remarkable "magnetic flexibility", enabled by the martensitic configuration and the strong spin-lattice coupling of these materials, makes magnetic-shape-memory alloys a unique class among magnetic materials for the easy manipulation of magnetic configuration at different length scales. The presented results in this chapter has been published in reference [13].

3.2 The effects of growth temperature and post-annealing

Ni-Mn-Ga films were grown epitaxially on (001) MgO (**Table 2.1** in section 2.1). The effects of growth temperature (T_g) were investigated by growing three different samples at decreasing T_g (from 623 K to 523 K, **Table 3.1**). The grown films show Ni-rich, Ga-rich compositions (**Table 3.1**), differently from the sputtering target ($Ni_{49.3}Mn_{27.8}Ga_{22.9}$), due to the different sputtering yields of Ni, Mn, and Ga [14] (section 2.1). Considering the uncertainty of energy dispersive X-ray spectroscopy (EDS) technique on these samples, the composition does not substantially change neither with growth temperature nor with post-annealing. Post-annealing for the as-grown samples was performed for 3600 sec at 623 K in 10^{-3} mPa (**Table 3.1**).

Table 3.1: Growth temperatures, compositions, critical temperatures and thermal hysteresis (Hyst.), deduced from the isofield ($\mu_0 H$ = 2 mT along [100] MgO) magnetization curve as a function of temperature on films with thickness = 200 nm and deposition rate = 0.1 nm.sec^{-1} ([a](Uncertainty~5 K); [b](Uncertainty~1 at%)). The average transition width is shown as (ΔT_{Avg}) [13]. The transition temperatures were obtained using inflection method.

Sample (#)	**1**	**2**	**3**	**1P**	**2P**	**3P**
Growth Temp. (K)[a)]	623	573	523	Sample #1 After Annealing	Sample #2 After Annealing	Sample #3 After Annealing
Ni (at. %)[b)]	52.5	52.4	52.0	52.7	52.6	52.3
Mn (at. %)[b)]	20.7	20.6	21.8	19.9	20.6	22.9
Ga (at. %)[b)]	26.8	27.0	26.2	27.4	26.8	24.8
T_C (K)	340	344	-	338	340	350
T_M (K)	328	326	-	322	317	307
T_A (K)	333	330	-	328	325	311
Hyst. (K)	5	4	-	6	8	4
ΔT_{Avg} (K)	3	18	-	2	4	11

Thermomagnetic analysis gives the first clear evidence on how the growth temperature affects the martensitic transformation. The analysis were performed by SQUID magnetometer in the presence of 2 mT in-plane magnetic field along [100] MgO (section 2.3.8). The results are reported in **Figure 3.1a**. The film grown at 623 K shows on heating a sharp transition from the ferromagnetic martensitic phase to the ferromagnetic austenitic phase, which soon becomes paramagnetic. This is coherent with our previous results: 623 K was chosen as the optimum growth temperature to obtain the epitaxial austenitic phase at high temperature and a martensitic phase with high structural quality stable at room temperature (RT) [1,15]. The critical temperatures are 328 K for the martensitic transition (T_M), 333 K for the austenitic transition (T_A) and 340 K for the Curie transition temperature (T_C). The hysteresis of the martensitic transition is around 5 K. When the growth temperature is decreased (samples #2 and #3), the martensitic transition is less and less evident and broadens, while the Curie transition shifts towards high temperature (sample #3). Magnetization, here measured at 2 mT, is also reduced. These characteristics can be due to compositional inhomogeneity, reduced crystalline quality and structural disorder caused by reduced growth temperature.

Figure 3.1b shows that the post-annealing at 623 K improves the quantity and quality of martensitic phase present in the films grown at lower temperatures, i.e., #2 and #3, increasing the magnetization variation at the martensitic transformation and reducing its broadening. The most evident effect of post-annealing on the film grown at the optimum temperature, i.e. #1, is a small shift of the martensitic transformation towards low temperatures. A higher magnetization was measured for samples #2P and #3P with respect to sample #1P, due to a higher fraction of the film with easy-magnetization direction in the film plane (discussed below).

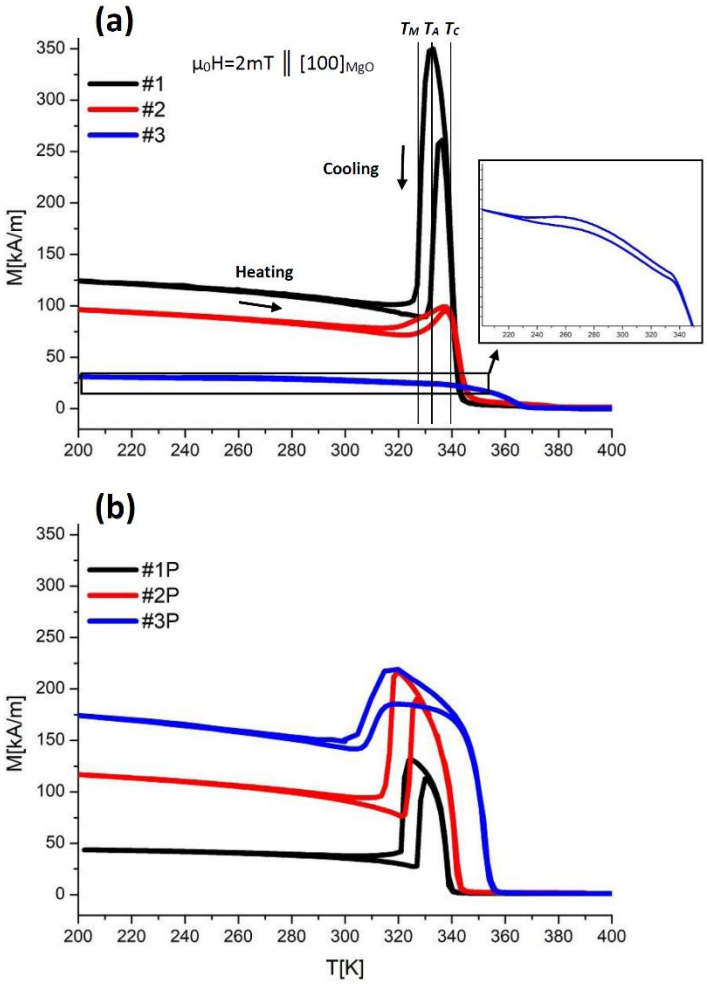

Figure 3.1: The isofield (μ_0H = 2 mT along [100] MgO) magnetization curves as a function of temperature for the as-prepared samples a)#1, #2, #3 and the corresponding post-annealed samples b) #1P, #2P, #3P. Different samples are represented in different colors. Arrows show the heating and the cooling curves. As an example, the martensitic transformation, austenitic transformation and Curie temperature are labeled for sample #1. Magnified graph of #3 is represented as inset. The critical temperatures, i.e. T_M, T_A and T_C have been obtained using inflection method [13].

The evolution of the structure as a function of temperature was measured using X-ray diffraction (XRD), performed by a Thermo ARL X'tra diffractometer equipped with a solid-state Si(Li) Peltier detector and an environmental chamber (section 2.3.5). High temperature XRD for samples #1, #1P, #2, #2P and #3P shows similar epitaxial cubic austenitic structure with {*00l*} family of crystallographic planes representing the cell parameter normal to the plane of the film (**Figure 3.2a**). Sample #3, grown at the lowest temperature, shows a different behavior as described further below. As the temperature is reduced, the films encounter martensitic transformation to 7M monoclinic incommensurate structure [16]. The structural quality, in agreement with the thermomagnetic analysis, worsens with decreasing the growth temperature. The martensitic structure is hereby described within the austenitic reference, where the *c* axis corresponds to the unique axis (and to the easy-magnetization direction) and the modulation direction lies on one of the two *a*-*b* plane diagonals (section 1.2.1). **Figure 3.2b-g** shows 58-70° ϑ-2ϑ scans of the samples in the martensitic state. The figures are parts of wide range (28-70°) scans, which were cut and magnified to improve the legibility. As can be observed, only the {*0k0*} family of planes of the martensitic cells are detectable by a conventional ϑ-2ϑ scan [1,15]. By tilting the diffraction vector from the substrate normal to approximately 2°, {*0k0*} planes exit the diffraction condition while {*h00*} as well as {*00l*} diffraction

peaks appear. This is due to the misorientation of the martensitic cells, i.e., a slight rotation around the *b* axis to reduce the coherency strain in the phase boundaries [17]. The misorientation is apparent in our diffraction dataset when the *b* axis is in the plane of the film (X-type). Hence, the $(040)_M$ can be majorly refed to the out of plane *b* axis in Y-type regions and the $(400)_M$ as well as $(004)_M$ peaks to the crystal planes of the cells in X-type regions (details can be found in ref. [1]). According to this explanation, the relative low intensity of $(040)_M$ in **Figure 3.2b** and **Figure 3.2c** for high temperature grown samples can be attributed to the absence of Y-type twin variants in these two samples. Consistently, comparing the diffraction patterns of samples #2 (**Figure 3.2d**) and #2P (**Figure 3.2e**), it is possible to appreciate that the $(040)_M$ reflection in sample #2 has a broader profile and a lower relative intensity with respect to the other martensitic $(400)_M$ $(004)_M$ peaks. These features can be justified by the improved crystallinity as well as by the presence of a relatively larger amount of Y-type twin variants in the annealed #2P sample. This was confirmed by Scanning Electron Microscope (SEM) and Magnetic Force Microscope (MFM) measurements (discussed below). **Figure 3.2f** shows the X-ray analysis for sample #3, which was grown at 523K. The figure does not show the expected martensitic offset peaks neither at room temperature (RT) nor below RT. Instead, a broad peak is observed in normal scan, which can be attributed to a fundamental (004) bcc-like reflection peak originating from a disordered phase where the structural transformation has been hindered. After annealing (sample #3P), the microstructure partially recovers, as testified by the diffraction patterns (**Figure 3.2g**).

Different colonies of twin boundaries were recognized by Backscattered Electron (BSE) SEM images thanks to the electron channeling effect, which provides selective interaction of incident electrons with different crystal orientations (section 2.3.2). It gives an overview of the microstructures, showing different contrasts for different crystallographic orientations of twinning configurations (**Figure 3.3**). **Figure 3.3a** shows large-scale view of the colonies of twin boundaries for sample #1, which are oriented along [110] and $[1\bar{1}0]$ directions of the MgO substrate, as expected for X-type twins [1]. Dark and bright zones are referred to different twin boundaries nucleated from different austenitic {110} cubic planes [18] (section 1.3.1). In the as-grown sample the size of the colonies is in the range of tens of microns, while after post-annealing (sample #1P) it extends to a few hundred microns (**Figure 3.3b**).

Sample #2, which was grown at reduced growth temperature compared to sample #1, shows a striking difference in the BSE image (**Figure 3.3c**). It is the appearance of bright needle-shape contrast zones, oriented along [100] and [010] MgO in the matrix of dark X-type contrast zones: these are Y-type regions. In addition, the surface roughness, as measured by atomic force microscopy (AFM, insets in **Figure 3.3**), increases from 0.5 nm to 1.2 nm by reducing growth temperature from T_g = 623 K to 573 K. The post-annealing has a strong effect on the microstructure of the film grown at 573 K (sample #2P, **Figure 3.3d**). Not only the relative length-scale of the twinning configurations increases compared to the as-grown sample, but also the Y-type regions expand at the expense of X-type.

After further reducing the growth temperature to 523 K, no twin variant contrast can be observed in the BSE image (sample #3, **Figure 3.3e**). Surface roughness is also further increased to 2.7 nm. This is in agreement with the X-ray and thermomagnetic analyses (**Figure 3.2f and Figure 3.1a**, which evidenced that the dominant structural disorder in sample #3 hinders the martensitic transformation). Despite the absence of twin variants in the as-grown state, after post-annealing the martensitic microstructure is recovered. **Figure 3.3f** in fact shows the contrasts typical of the X and Y zones. Y-type configuration is dominant and run along the edges of the MgO substrate, though the length-scale of the Y-type colonies are lower than in sample #2P giving rise to a basket-like morphology.

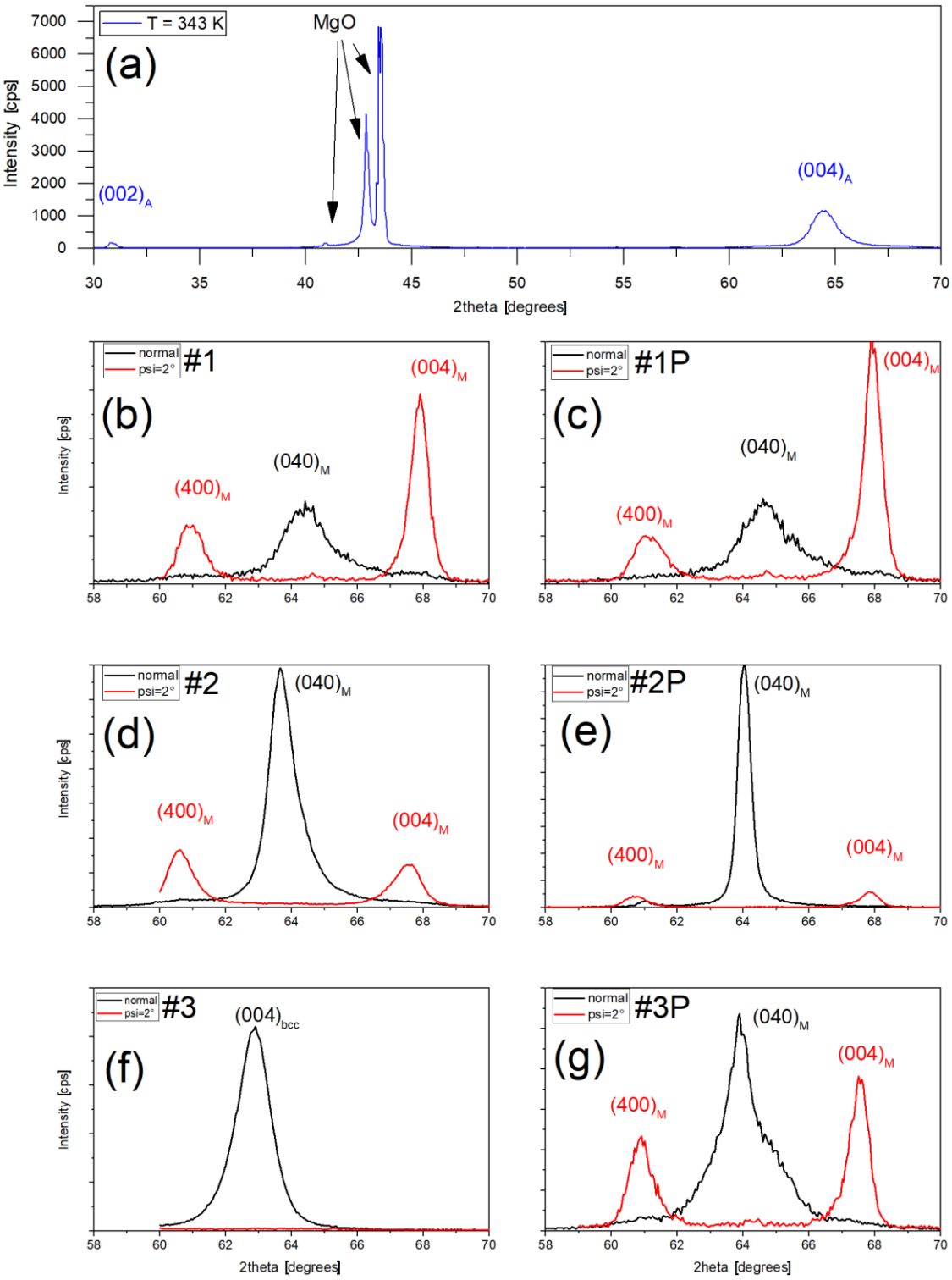

Figure 3.2: X-ray diffraction for the as-prepared and post-annealed samples, a) #1, 2theta = 30-70 at 343 K showing the epitaxial {*00l*} family of austenite peaks, b) #1, c) #1P, d) #2, e) #2P, f) #3 and g)#3P, 2theta = 58-70 at 300 K. The term psi = 2° refers to asymmetric theta-2theta scan, diffraction vector ~2° offset from the substrate normal (modified version of the original Figure is represented) [13].

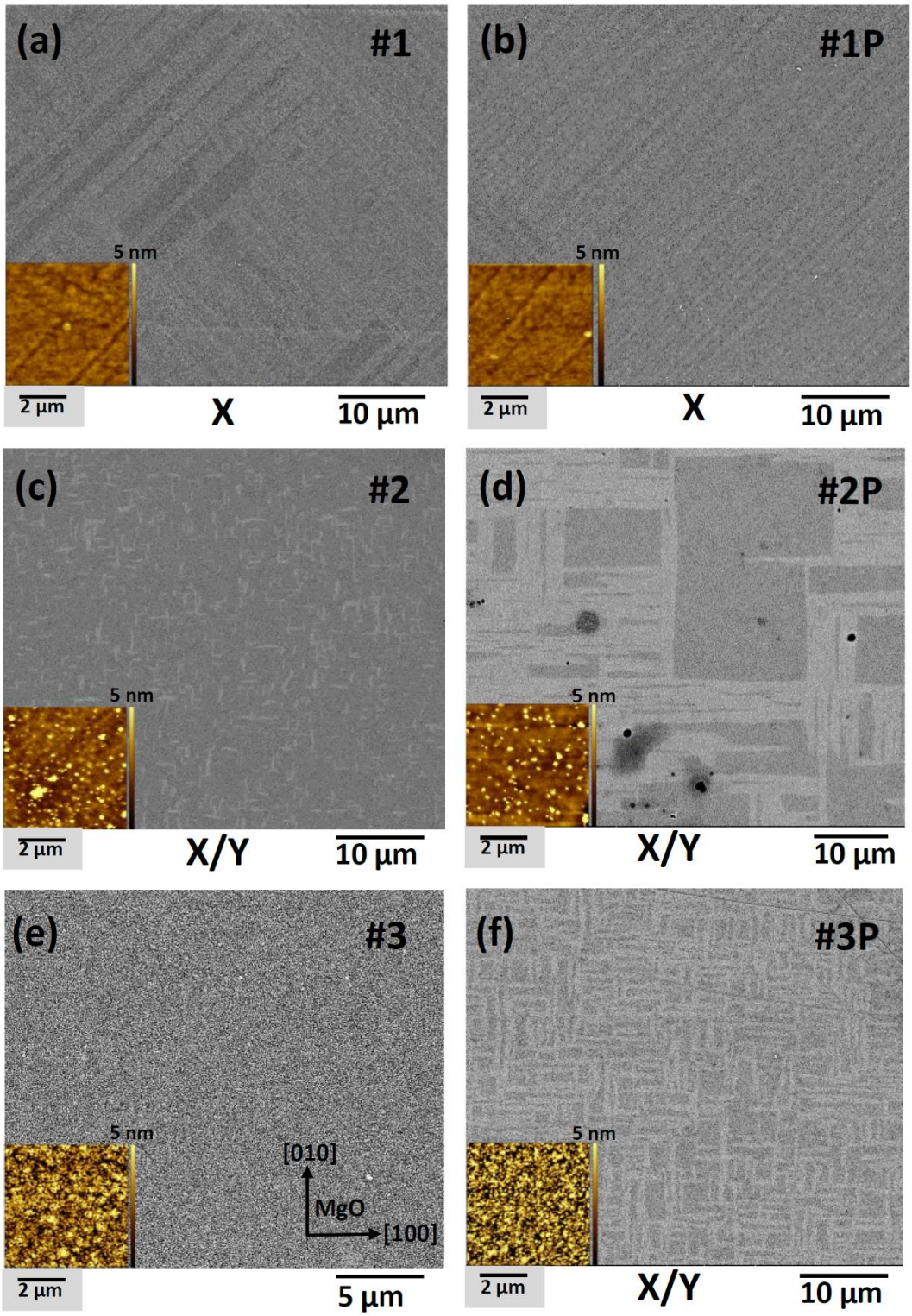

Figure 3.3: Large-scale BSE images at room temperature showing X-type and Y-type contrasts for the as-prepared and post-annealed samples, insets illustrate the topography images showing the roughness increasing as the growth temperature decreases a) #1, b) #1P, c) #2, d) #2P, e) #3 and f) #3P. The edges of the images are parallel to [100] MgO and [010] MgO [13].

Magnetic Force Microscopy (MFM) images, captured for the as-grown and annealed samples at RT are reported in **Figure 3.4a-f**. Sample #1 shows the typical out of plane magnetic domain patterns (dark and bright contrasts) of X-type zones. This is due to the perpendicular anisotropy contribution

originating from the twin variants with out-of-plane *c* axis [1]. With decreasing growth temperature, the magnetic domain stripes of sample #1 (**Figure 3.4a**) break down into maze-like patterns with dark/bright contrast of lower intensity (**Figure 3.4b,c**). Areas with no magnetic contrast are also visible. The presence of MFM contrast in sample #3 could be due to the perpendicular anisotropy originating from a strain in the film or from the minority martensitic phase stable at RT (in this sample the transformation is almost completely hindered). The magnetic domain configuration reflects the structure and microstructure evidenced by XRD and SEM, with a decreased structural quality at low growth temperature and appearance of Y-zones, which are characterized by easy-magnetization *c*-axes in the film plane.

A clear notable modification is observed for the MFM patterns of the annealed samples (**Figure 3.4d-f**). Sample #1P (**Figure 3.4d**) shows very regular stripe domains extending to length-scales of the order of tens of microns, reflecting the large-scale X-type colonies, measured by SEM. Sample #2P (**Figure 3.4e**) clearly shows that stripe domain areas (X-type twin variants) are separated by no signal areas. The latter corresponds to Y-type zones, which have in-plane magnetic easy-axis and, as evidenced by the other characterization techniques, are promoted by post-annealing. The coherence of the perpendicular magnetic stripes in the X zones reflects the general improvement of the structure quality after post-annealing. Finally, **Figure 3.4f** shows isolated areas containing a mixture of out-of-plane and in-plane magnetic domains, which are quite larger than the domain islands in #3, and correspond to the X/Y microstructure evidenced by SEM (**Figure 3.3f**).

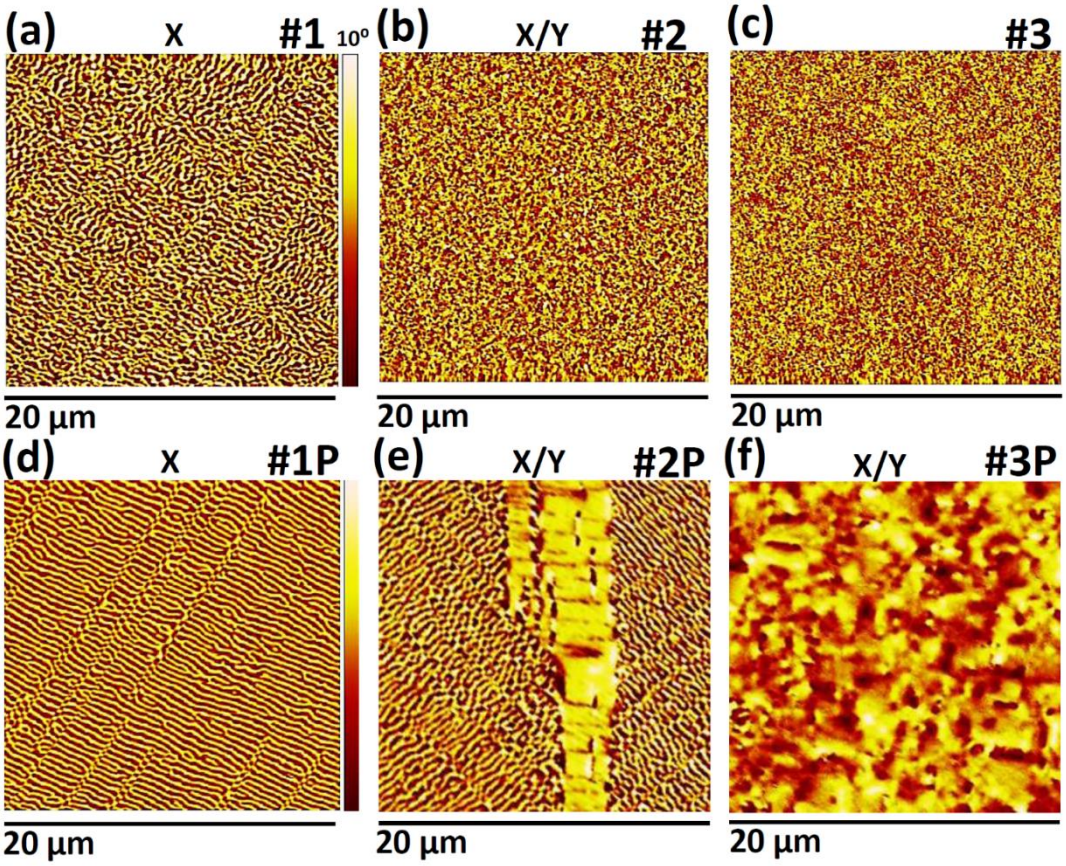

Figure 3.4: MFM images at room temperature showing stray field magnetic domain contrasts for the as-prepared and post-annealed samples, a) #1, b) #2 , c) #3, d) #1P, e) #2P and f) #3P. The edges of the images are parallel to [100] MgO and [010] MgO [13].

Transmission electron microscopy (TEM) plan-view measurements were performed at RT on samples #1 and #2 to study the martensitic structure (section 2.3.3). The image in **Figure 3.5a** shows HAADF plan-view of X-type twin variants in #1. Since thickness and elemental composition are constant throughout the specimen, the contrasts in the HAADF image can be ascribed to different crystallographic orientations of twin variants or to martensitic structural modulation.
Stripe contrast pattern is observed, with stripes along the [110] and [$1\bar{1}0$] directions of MgO substrate and stripe-width in the range from a few hundreds of nanometres to approximately 20 nm. This contrast is associated with twin variants with different crystallographic orientations.
Martensitic fine contrast modulation parallel to the [100] and [010] directions of MgO is also visibly observed in the regions where the modulation vector lies in the plane of the film, meaning that the easy-magnetization direction is oriented along the out-of-plane direction. **Figure 3.5b** shows a typical HRTEM image. The associated FFT in the inset clearly shows the satellite spots typical of 7M modulated structure with the modulation vector perpendicular to the observation direction.
The HAADF and HRTEM analyses confirmed the co-existence of X- and Y-type twin variants in sample #2. The HAADF image in **Figure 3.5c** shows both stripe contrast patterns oriented at 45° and 90° with respect to the substrate edges. A HRTEM image in a region containing both the X and Y variants is shown in **Fgure 3.5d**. The FFTs taken in two adjacent regions present the typical pattern of X- and Y-type variants. It is worth noting that, differently from the pattern shown in **Figure 3.5b**, the X-type variant observed here has the magnetization vector in-plane, i.e., the modulation vector inclined to the film plane.

In this class of materials, the martensitic transformation occurs in two steps, starting with nucleation of phase boundaries, where the austenitic and martensitic phases are connected and proceeding with the growth of one phase at the expense of the other. Any approach, which reduces the lattice misfit or volume change between the two phases, decreases the energy barrier of the transformation. In the transformation the defects play the role of nucleation points, since the energy barrier is considerably reduced close to imperfections due to the local elastic field [12,19]. This has been reported to facilitate structural transformation and reduce the hysteresis in magnetocaloric and shape-memory compounds by using ion irradiation or growing precipitates [20,21].

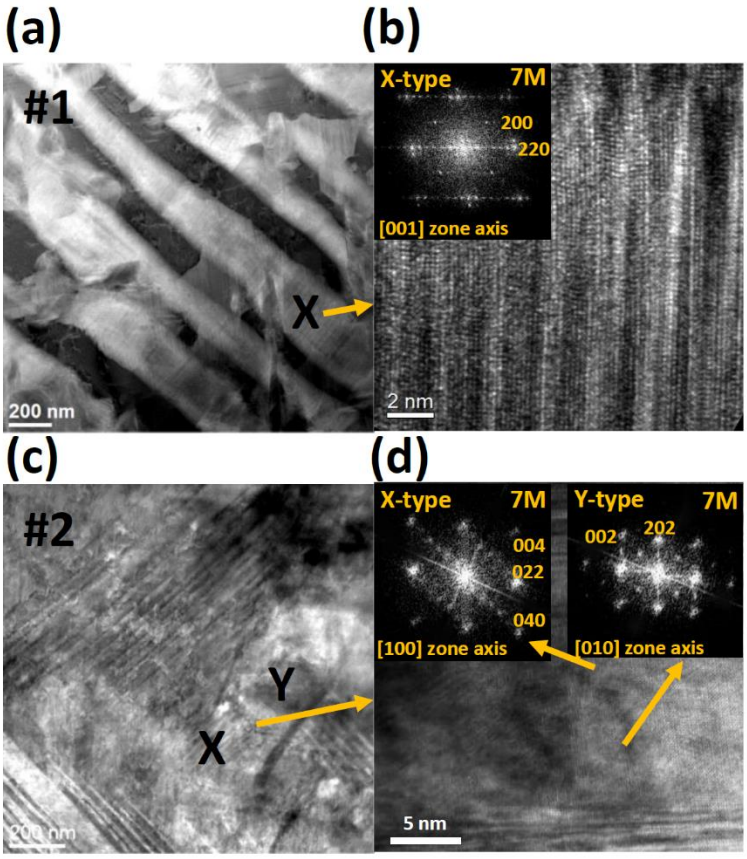

Figure 3.5: TEM analysis for samples #1 and #2. Sample #1: a) HAADF-STEM, b) HRTEM taken in the zone marked by the arrow in panel (a) and the corresponding FFT. Sample #2: c) HAADF-STEM image, d) HRTEM of X-and Y-type adjacent regions taken in the zone marked by the arrow in panel (c) and related FFTs. The edges of the images are parallel to [100] MgO and [010] MgO [13].

For the described films, by reducing the growth temperature from sample #1 to #3, the diffusion energy of Ni, Mn, and Ga atoms reduces, therefore atoms with lower energy form nanometric inclusions, epitaxial defects and inhomogeneities, as also observed by Sharma et al. for thicker films [22]. Consequently, the roughness of the films increases by a factor of six from #1 to #3. These epitaxial imperfections in sample #2 might play the role of nucleation points by applying a large number of local elastic fields to the film. As the martensitic phase nucleates from a large number of points, the length scale of twin boundary colonies decreases compared to sample #1. As for sample #3, besides inclusions and microstructural defects, atomic disorder plays a primary role in inhibiting the martensitic transformation. After annealing, defects and imperfections reduce [23] and ordering occurs due to heat diffusion along both the surface and volume of the films, therefore the nucleation sites decrease and the growth of the martensitic phase increases, which enlarges the length scale of twin boundary colonies (#1P, #2P). For sample #3P, partial recovery of the structure through annealing promotes the transformation, though the length scale of twin boundary colonies is the lowest (compared to #1P and #2P). It was also observed that the samples grown at lower temperature select mixture of X-type and Y-type microstructures. Since the other effective variables (thickness and substrate) are not varied, it is suggested that in samples #2, #2P and #3P Y-type configuration is energetically favored close to the local elastic field of the imperfections.

In summary, decreasing growth temperature introduces defects and disorder in the austenitic phase and changes the martensitic transformation path by giving rise to different twinning configurations, from full X-type to mixed X/Y-type. Instead, post-annealing reduces the defects in the epitaxial films

and alters the transformation route. Taking advantage of both effects, one can tailor the twinning configuration: from full X-type to mixed X/Y-type with controlled patterns.

3.3 The effect of magnetic field cooling

Magnetic field cooling was performed on sample #2P. The sample was heated up to 338 K in ambient atmosphere and zero magnetic field and cooled down to room temperature in an external magnetic field of 0.5 T along the [100] and [010] MgO crystal (one experiment for each field direction). In each experiment, the sample was characterized after the field-cooling and a further thermal cycle in zero magnetic field (up to 393 K with a heating rate of 0.1 $K.s^{-1}$ and back to RT with a cooling rate of 0.3 $K.s^{-1}$). The MFM measurements were performed ex-situ at RT on an area of approximately 50×50 µm. Results are shown in **Figure 3.6**.

The MFM image of the virgin sample (**Figure 3.6a**) shows the areas corresponding to the two types of twinning configurations. The major area (approximately 84% of the whole scanned area) corresponds to X-type variants, with the twin boundaries along [$1\bar{1}0$] MgO direction (inclined white lines). Y-type zones are evident in the right side portion of the image, which are oriented along [010] direction of MgO and correspond to ~4% of the surface, and at the bottom, which are oriented along [100] MgO direction and occupy 12% of the scanned area (horizontal white lines). The sample was heated up to 338 K and cooled down to RT in the presence of a 0.5 T field along [010] MgO, as sketched in the figure. The experiment was followed by a thermal cycle (up to 393 K and back to RT in $\mu_0 H = 0$) in order to measure the sample in the demagnetized state. The resulting MFM image (**Figure 3.6b**) evidences the propagation of Y-type zones at the expense of X-type zones, along both [100] MgO and [010] MgO. This modification is stable after further thermal cycling, possibly due to the advantage in magnetostatic energy of Y-type microstructure compared to X-type microstructure, while the latter is favored by the epitaxial constraint. A coherent and complete interpretation of this experimental evidence would require a theoretical modelling able to take into account the complexity of this system in terms of elastic and magnetic terms and of their temperature evolution across the transformation.

Comparing **Figure 3.6a** and **Figure 3.6b**, it could be estimated that the surface area occupied by X-type configuration was reduced from ~84% to ~38% and conclude that the majority of Y-type twin boundaries after in-field cooling was oriented along the direction of the applied magnetic field, i.e., [010] direction of MgO. This was calculated as $(S_{Y[010]} \times S^{-1}_{Y[tot]}) \times 100 \approx 58\%$, where $S_{Y[010]}$ corresponds to the surface area occupied by Y-type twin boundaries along the [010] direction and $S_{Y[tot]}$ to the total surface area occupied by Y-type twin boundaries. The experiment was followed by another field-cooling step (applying 0.5 T along [100] direction of MgO), followed by a thermal cycle (up to 393 K and back to RT in $\mu_0 H=0$). As observed in **Figure 3.6c**, after this further field cooling almost the whole surface area shows the Y-type twinning configuration; approximately 78% of the total surface area was occupied by Y-type boundaries aligned along the direction of the applied magnetic field ([100] direction of MgO substrate).

The experiments described above demonstrate how the twinning configuration of magnetic-shape-memory thin films can be modified by applying an external magnetic field while crossing the martensitic transition on cooling. Thanks to the additional Zeeman energy term and the strong spin-lattice coupling, the twin variants with easy-magnetization direction parallel to the applied field are energetically favored and grow at the expense of the competing twin variants [1,4]. In **Figure 3.6**, the field was applied in the plane of MgO substrate therefore the nucleation of Y-type twins is

energetically favored (having the easy-magnetization direction of the twin variants in the plane of the film). The direction of twin boundaries and magnetic domains in X- and Y-type areas are sketched in **Figure 3.6d**, as it was previously deduced by electron holography and MFM analyses [1,4]. The figure also illustrates the overall direction of magnetization in adjacent magnetic domains in the Y-type regions (blue arrows).

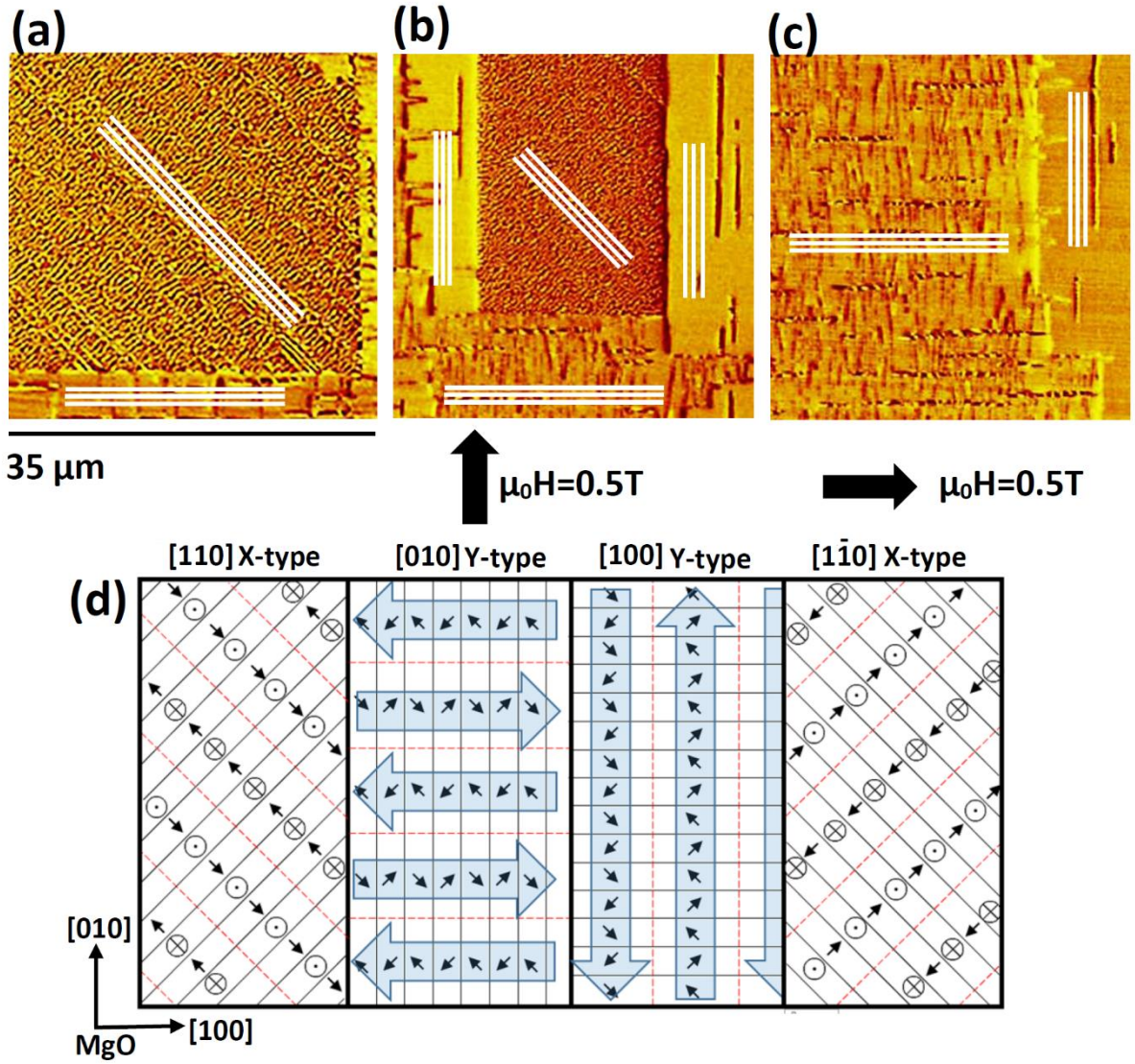

Figure 3.6: MFM images at room temperature showing the manipulation of twinning configurations by substituting X-type and Y-type through magnetic field cooling of sample #2P. The evolution of twin variants can be followed through the white lines: a) starting sample. b) cooled from 338K in the presence of in-plane magnetic field $\mu_0 H$ = 0.5 T along [010] MgO followed by cooling from 393K in $\mu_0 H$ = 0. c) cooled from 338K in the presence of in-plane magnetic field $\mu_0 H$ = 0.5 T along [100] MgO followed by cooling from 393K in $\mu_0 H$ = 0. d) Schematic representation of magnetic domains and twin boundaries in X- and Y-type, directions of black arrows show the easy magnetization direction, black lines represent twin boundaries, dash lines show 180° magnetic domain walls and the superimposed blue arrows illustrate the directions of resultant magnetic vectors in Y-type twin boundaries [13].

In **Figure 3.7**, a magnetic field cooling experiment followed by a heating + cooling cycle in zero external field is reported for a different area of the sample #2P with respect to **Figure 3.6**. This

experiment confirms that the observed microstructural change is reminiscent of the previous field-cooling treatment, as it remains also after a successive heating + cooling cycle in zero applied field.

The salient results of this new experiment are reported in **Figure 3.7**. The sample was imaged by MFM in the virgin state (**Figure 3.7a,d**), after cooling it in 0.5 T from 393 K to RT (**Figure 3.7b,e**), and after successive thermal cycling from 393 K to RT (**Figure. 3.7c,f**). The field was applied along [010] MgO. Image size is 50×25 μm in **Figure. 3.7a-c** and 25×12.5 μm in **Figure. 3.7d-f**, which are the magnified images of **Figure 3.7a,c**. **Figures 3.7b,c,e and f** have been tilted to align the MFM scan direction to the MgO edges. White crosses have been inserted in the images to have a fixed reference.

Different Y-type areas are present in the investigated region, appearing as light stripes in the central part of the 50×25 μm scans. Despite the fact that 50 μm lateral scale does not allow us a detailed view of the magnetic domains and the domain walls, it offers the possibility to clearly visualize the Y-zone extension in an area with a small fraction of Y-type twins. The experiment demonstrates that the increase in the Y-type area occurs after the in-field cooling treatment and is maintained also after the successive thermal cycle. Typically, in our films mixed X/Y microstructures are quite stable after thermal cycling across the martensitic transition: Y zones tend to form every time in the same position after successive cycles. In this case, it was verified that the fraction of Y-type twins can be increased by applying in-plane magnetic field of 0.5 T across the martensitic transformation. The magnetic field application favors the twinning configuration with easy-magnetization direction along the external magnetic field direction. This modification is stable after further thermal cycling, possibly due to the advantage in magnetostatic energy of Y-type configuration compared to X-type configuration, while the latter is favored by the epitaxial constraint. A coherent and complete interpretation of this experimental evidence would require a theoretical modelling able to take into account the complexity of this system in terms of elastic and magnetic terms and of their temperature evolution across the transition.

In summary, even if the equivalent stress of the applied magnetic field is of moderate intensity (around two order of magnitude lower than the typical residual stress reported for epitaxial Ni-Mn-Ga thin films grown on MgO), its application during the temperature induced martensitic transformation is effective in changing the microstructural patterns. The present experiments definitely show that for Ni-Mn-Ga films with X- and Y-type mixed microstructure, the martensitic transformation path is very sensitive to small variations in the boundary conditions and can be easily influenced. A prevalent Y-type microstructure can be obtained for in-plane applied magnetic fields.

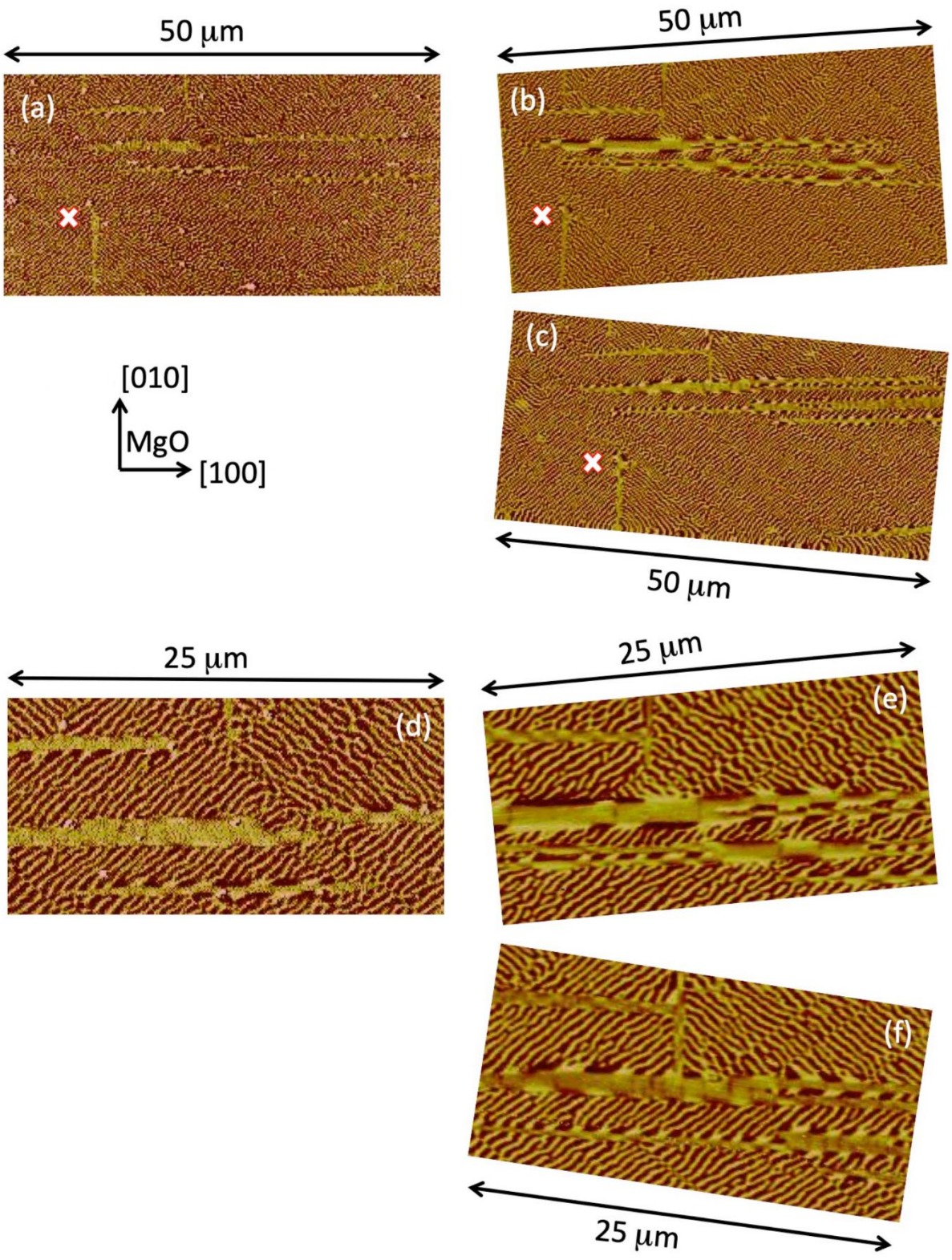

Figure 3.7: MFM images of a portion of sample #2P. a),d) virgin state; b),e) after cooling it in 0.5 T from 393 K to RT; c),f) after successive thermal cycling from 393 K to RT. The magnetic field was applied along the [010] MgO direction. Image size is 50×25 μm in (a), (b), (c) and 25×12.5 μm in (d), (e), (f). The images (d), (e), (f) are the magnified images of (a), (b), (c). The images (b), (c), (e) and (f) have been tilted to align the MFM scan direction to the MgO edges. White crosses have been inserted in the images to have a fixed reference [13].

3.4 The effect of local mechanical stress

Local mechanical stress was performed on sample #1P. The stress was applied at RT using a stainless steel sharp tool (nominal thickness 228 μm) covered by lens-cleaning paper, oriented perpendicular to the substrate surface and straining the surface along [010] MgO or [110] MgO direction. Unless otherwise noted, the stress was followed by a thermal cycle (up to 393 K with a heating rate of 0.1 $K.s^{-1}$ and back to RT with a cooling rate of 0.3 $K.s^{-1}$).

A sketch of the microstructure for the stressed sample has been reported in **Figure 3.8a** and **Figure 3.8b**, showing a number of stripes along [010] MgO. The length of the stripes was measured by AFM as tens of microns, the width in the range of 0.4-2 μm, while the height in the range 4-50 nm. The MFM and its corresponding topography height-section image (**Figure 3.8c** and **Figure 3.8d**) measured at RT show stripe-like Y-type martensitic configurations appearing along [010] MgO direction.

The stressed sample was further investigated by several TEM techniques including electron holography. The induced Y-type region shown in the SEM image in **Figure 3.8e** was investigated by cross-section TEM analysis. Typical Y-type configuration perpendicular to the interface are visible in the dislocation lines, as shown in the HAADF image in **Figure 3.8f**. The HRTEM images with corresponding FFTs taken in- and out of the stress-induced area clearly demonstrate that the *c* axis is out of the plane for the observed X-type region (**Figure 3.8g**) while *b* axis is out of plane of the film in Y-type region (**Figure 3.8h**). No detachment of the film from the substrate was observed.

The correlation between the twinning structure and the magnetic configuration has been directly visualized by means of in-line electron holography experiments that provide the direct evidence of the magnetic patterns inside the twinned regions. **Figure 3.8i** shows the magnetic induction color map obtained by electron holography in X-type region. The direction of the easy-magnetization axis pointing alternatively out-of-plane and in-plane at each variant is indicated by arrows. The cross-section geometry does not allow us to visualize the magnetic contrast from Y-type configuration, having the easy-magnetization axis always in plane of the film (section 1.3.1).

The twinning relation of the variants was also determined in the stressed region. As can be observed through the HRTEM image (**Figure 3.8j**), the continuity of the atomic planes does not change across the twin boundary, therefore, the twin boundary can be assigned as type-II [1] (details can be found in section 4.1).

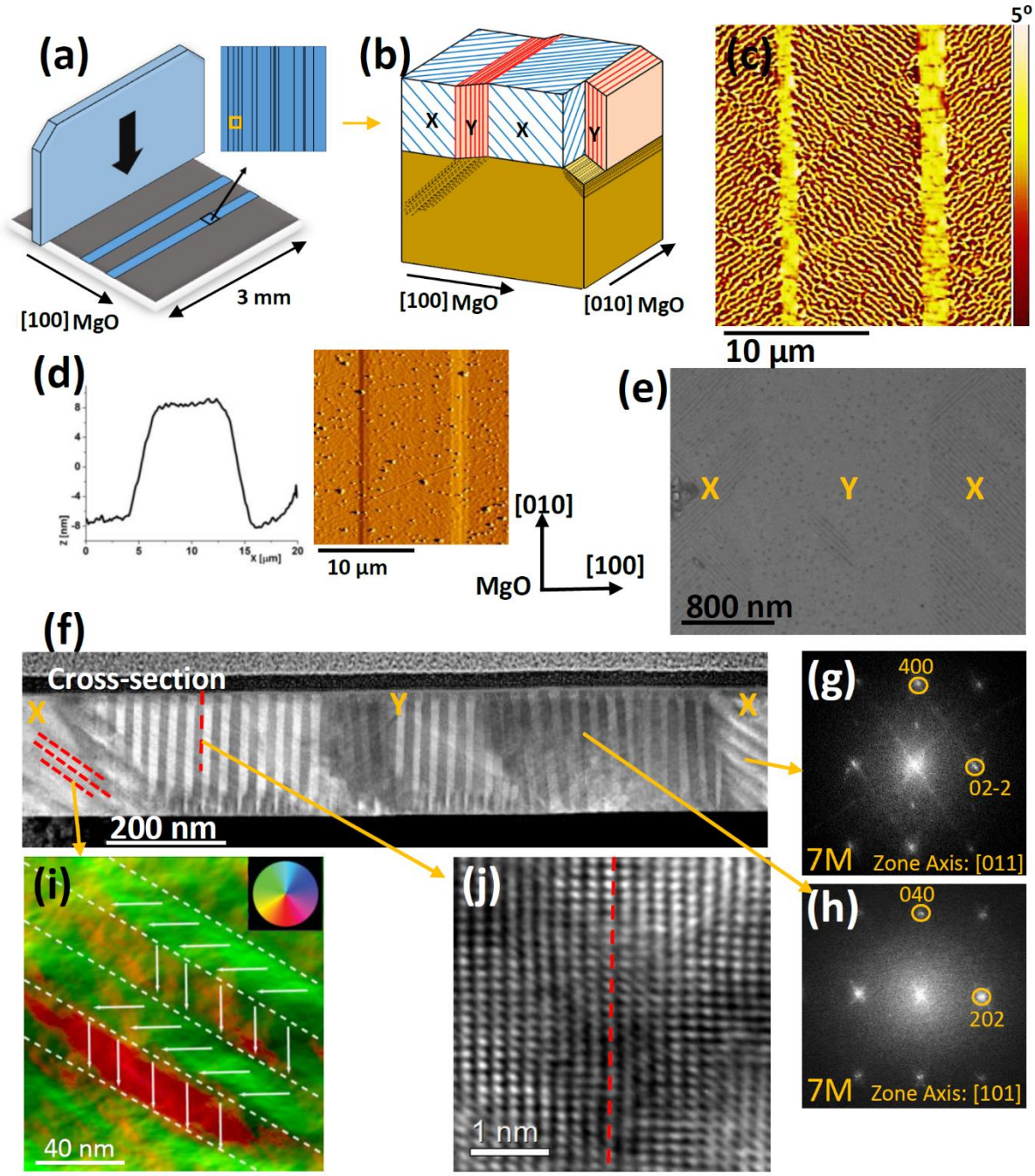

Figure 3.8: Local control of twinning configurations of sample #1P by mechanical stress: a) schematic representation of the applied stress along [010] MgO and the corresponding arrays of dislocations for 3×3 mm sample. b) 3D representation of the assigned region, showing the dislocated arrays of planes in MgO and the related Ni-Mn-Ga martensitic configurations on top. c) MFM image of the stressed area at RT and d) its corresponding topography and the height section. e) plan-view SEM image of the stressed area. f) cross-section HAADF-STEM analysis of the twin boundaries and g, h) corresponding FFT analysis pointed by arrows. i) magnetic induction color map, obtained by electron holography for X-type region in cross-section, colors represent the magnetization directions and color saturation indicates the magnetization intensity. j) HRTEM image of the marked twin boundary in (f) [13].

In attempting to understand the mechanism generating the Y-type configuration after the stress application, the surface deformation around the regions subjected to mechanical stress was investigated for both the film and an MgO reference substrate. The direction of the stress was also alternated from [010] MgO to [110] MgO.

The BSE and AFM images of the stressed regions (**Figure 3.9** and **Figure 3.10**) show the typical arrays of dislocations along [010] MgO, as observed in the stress-treated MgO substrate. The applied stress values (not directly measured in our experiment) were estimated to be >20 MPa, by comparing our topographic results on MgO reference substrate with the experimental and simulated results reported in references [24,25]. Based on the results reported for micro-indentation tests in (001) MgO surface [24,25], the dislocations along the [100] and (or) [010] directions correspond to slip-line dislocations emerging at the free surface, which are visible in topography as they produce emerging deformations perpendicular to the surface.

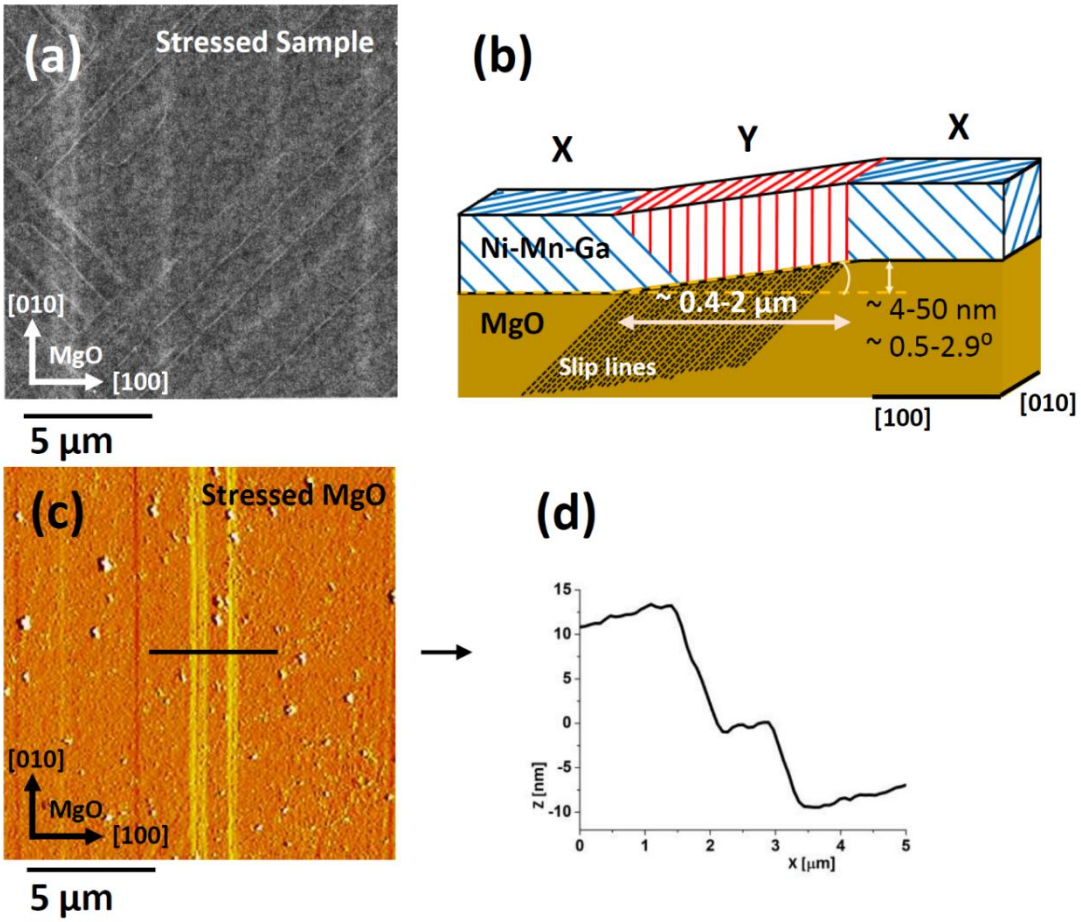

Figure 3.9: Origin of the stress-induced Y-type twinning configuration. a) BSE image for the stressed area of the sample (#1P) b) Cross-sectional 3D scheme of the slip lines showing the approximate width, slope and the related surface relief measured via AFM imaging and averaged for different stressed induced regions, c) AFM image of the stress treated MgO reference substrate and d) its corresponding surface relief along the black line [13].

Figure 3.9a represents the BSE image of the stressed region in sample #1P, showing the vertical stripes corresponding to the arrays of slip lines along [010] MgO [24,25]. For better visualization of the phenomenon, a cross-sectional scheme of these slip lines is shown in **Figure 3.9b**: the geometric arrangement of the slip lines with the corresponding deformations measured by AFM (width, emerging height and slope of the surface relief) as well as the position of the X-type and Y-type twin boundaries are shown. Evidently, Y-type configuration are parallel to the direction of the propagation of the slip lines on the surface. On the contrary, the slip lines propagate on the surface of MgO at ~45° to the direction of the X-type configuration. This could make the growth of X-type configuration more energy costly compared to Y-type. To better clarify the origin of the surface relief in the stressed sample, the topography of a reference (001) MgO substrate subjected to an equal stress was

investigated as well (**Figure 3.9c and Figure 3.9d**). By comparing the results obtained for the stressed sample (**Figure 3.8d** and **Figure 3.9a**) and the results obtained for the stressed substrate (**Figure 3.9c,d**), it can be concluded that the arrays of dislocations and the corresponding surface relief observed in the stressed region in sample #1P are due to the deformation of the underlying MgO.

The two possible martensitic configurations (X- and Y-type) for epitaxial Ni-Mn-Ga films on (001) MgO have a precise geometry with respect to the substrate. Since the direction of slip lines on the surface of the film (i.e. along [010] MgO) matches the orientation of Y-type twin boundaries, the nucleation of Y-type in the stressed regions is geometrically and possibly energetically favored. This interpretation is supported by the diamond model proposed for the formation of the martensitic mesoscopic configurations of Ni-Mn-Ga epitaxial thin films, based on the well oriented nucleation and growth of the enclosed volumes of martensitic nuclei [3] (section 1.3.1). The in-plane and spatial orientation of the nuclei of the two different martensitic configurations (X- and Y-type) are different. In the case of Y-type, the diamond-like nuclei have high aspect ratio between the two axes, and the long axis is aligned along [010] MgO or [100] MgO. A simplified cross-section sketch is reported in **Figure 3.9b**, showing the possible relation between the dislocations and Y-type configuration.

It was found that the height and slope of the slip lines are important factors for the local inducement of Y-type twinning configuration (**Figure 3.10**). Evidently, the X-type martensitic configuration remains unchanged up to ~4nm surface reliefs (slope ~ 0.5°), while for the surface reliefs up to ~23nm (slope ~ 2.0°) the typical X-type magnetic stray field, observable in MFM images is disrupted after applying the stress followed by a thermal cycle (**Figure 3.10d-f**). These regions with disrupted magnetic stray field were confirmed to have converted to Y-type twin boundaries (**Figure 3.8**). For higher values of surface relief, the typical magnetic stray field, observable in MFM images for X-type configuration disrupts right after applying the stress at room temperature (**Figure 3.10a-c**). This disruption could be due to detwinning of the X-type twins, plastic deformation of the material or switching of X-type to Y-type at room temperature in those regions as a result of the applied mechanical stress. Cross-sectional TEM analysis are required to confirm the status of the Ni-Mn-Ga film in the latter case although, it is more likely that the material undergoes detwinning process under the applied mechanical stress in the latter case.

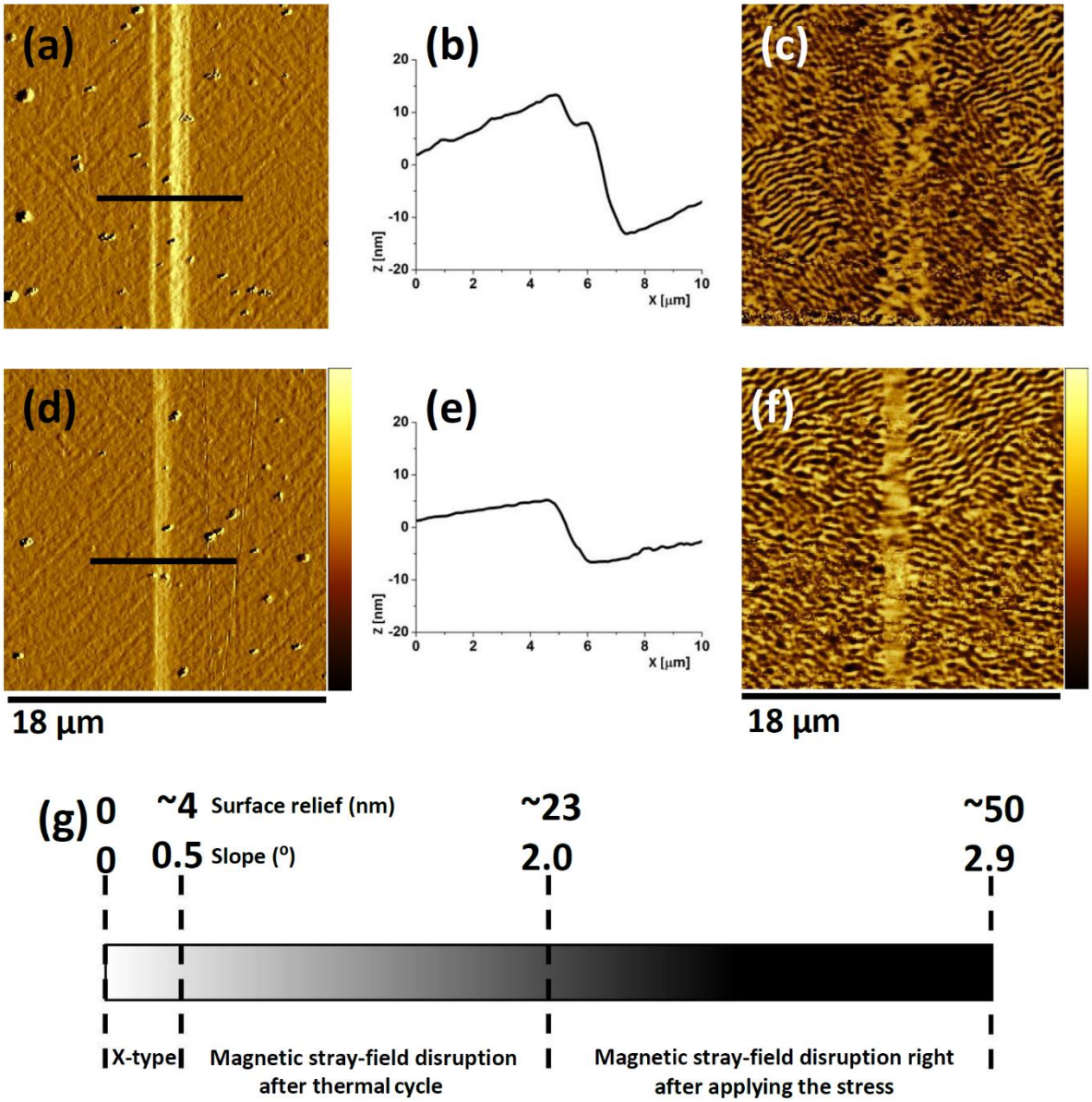

Figure 3.10: Stress induced martensitic configuration for different stressed regions in sample #1P. Area with ~25 nm surface relief after applying stress a) topography, b) height section and c) MFM. Area with ~15 nm surface relief after applying stress and a subsequent thermal cycle: d) topography, e) height section and f) MFM. (g) an approximate scheme for the magnetic stray field disruption as a function of surface relief, measured by AFM/MFM at room temperature (modified version of the original Figure is represented) [13].

Applying the mechanical stress perpendicular to the film along [110] MgO (**Figure 3.11a-c**) shows the appearance of the arrays of dislocations in the form of interrelated crosses. The applied stress in this case has two components along the substrate crystal directions, which give rise to the horizontal slip lines along [100] MgO and the vertical slip lines along [010] MgO. **Figure 3.11a** shows schematically the direction of the applied stress and the resultant slip lines. These slip line crosses which are also known as rosette arms [24,25], introduce a unique feature for the stressed sample by inducing Y-type twin boundaries along both [100] MgO and [010] MgO, providing a further proof of the role of MgO substrate in our mechanical-stress-assisted martensitic configuration engineering.

A number of tiny zig-zag patterns were observed as well, correlated to out-of-plane magnetic domains that apparently correspond to tiny X-type stripes entering Y-type regions. To visualize the patterns, a part of the stress induced Y-type, represented in **Figure 3.11c** has been magnified and shown in **Figure 3.11d** with the related AFM image in **Figure 3.11e**. Tiny twin variants entering the neighboring variants, known as "comb-like microstructure", were previously observed in Ni-Mn-Ga bulk single-crystals by electron backscattered diffraction [26]. Such a microstructure could also be the origin of the out-of-plane tiny stripes of magnetic domains inside Y-type regions, visualized in epitaxial Ni-Mn-Ga films by MFM imaging [4].

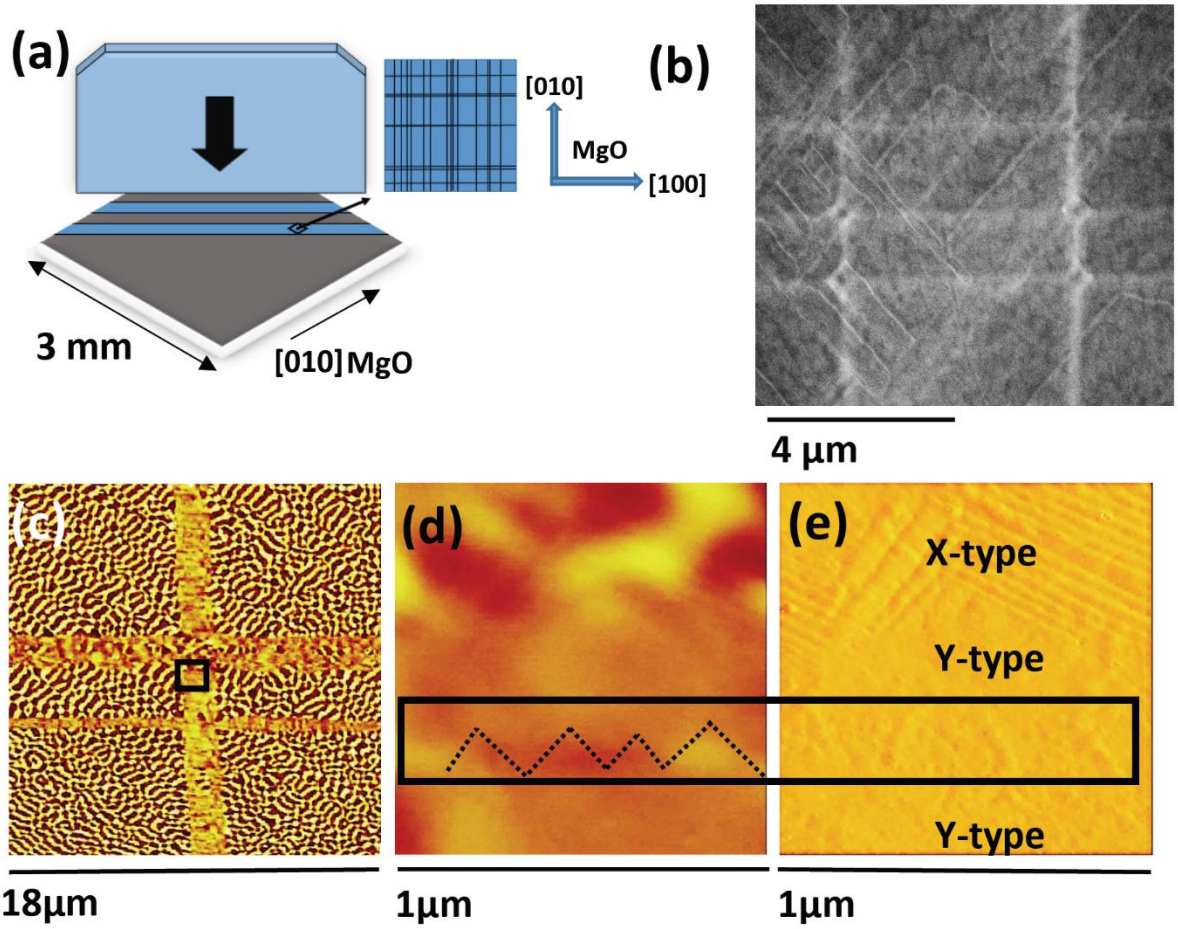

Figure 3.11: Mechanical stress along [110] MgO: a) schematic representation of the stress applied to the film along [110] MgO, b) BSE image of the stressed area showing the arrays of dislocations, which arrange in the form of interrelated crosses, c) MFM image at RT, d) magnified image of the selected region in (c), e) its related AFM topography image showing the tiny zig-zag structure [13].

In summary, it was demonstrated that the application of stress as a post-growth treatment, locally transforms X-type into Y-type twinning configuration along the selected directions of the substrate. These findings, represents a first step towards the easy manipulation of microstructural and magnetic patterns in magnetic shape memory thin films by the application of local stress as a post-growth treatment.

3.5 Conclusions

In conclusion, we have shown how different simple post-growth treatments (i.e. post-annealing, magnetic field cooling and the application of a local mechanical stress) open up the possibility to tailor the twinning configuration of magnetic-shape-memory epitaxial thin films. Taking the advantage of growth temperature and post-annealing treatment, twinning configurations can be easily tuned from full X-type to mixed X/Y-type with different geometrical distribution, in which controlling the defects and disorder affecting the martensitic transformation path play an important role. Mixed X/Y-type configuration can be modified by applying an external magnetic field while crossing the martensitic transformation, exploiting the additional Zeeman energy term. In this case, with the field applied in the film plane, a predominant Y-type configuration can be obtained. The application of post-growth stress is suitable for locally transforming X-type to Y-type configuration along the MgO crystal direction.

References

1. Ranzieri, P. *et al. Adv. Mater.* **27**, 4760 (2015).
2. Tillier, J. *et al. Acta Mater.* **59**, 75 (2011).
3. Niemann, R. *et al. Acta Mater.* **132**, 327 (2017).
4. Diestel, A. *et al. J. Phys-Condens Mat.* **25**, 266002 (2013).
5. Campanini, M. *et al. Small* **14**, 1803027 (2018).
6. Kohl, M. *et al. Appl. Phys. Lett.* **104**, 043111 (2014).
7. Watson, C.S. *et al. Adv. Funct. Mater.* **23** 3995 (2013).
8. Davis, P.H. *et al. J. Appl. Phys.* **123**, 215102 (2018).
9. Mansell, R. *et al. Sci. Rep.* **7**, 4257 (2017).
10. Jenkins, C.A. *et al. Appl. Phys. Lett.* **93**, 234101 (2008).
11. Eichhorn, T. *et al. Acta Mater.* **59**, 5067 (2011).
12. Niemann, R. *et al. APL Mater.* **4**, 064101 (2016).
13. Takhsha Ghahfarokhi, M. *et al. Acta Mater.* **187**, 135 (2020).
14. Matsunami, N. *et al. At. Data Nucl. Data Tables* **31**, 1 (1984).
15. Ranzieri, P. *et al. Acta Mater.* **61**, 263 (2013).
16. Righi, L. *et al. Mater. Sci. Forum* **684** 105 (2011).
17. Chulist, R. *et al. Int. J. Plasticity* **114**, 63 (2019**)**.
18. Yang, B. *et al. Adv. Eng. Mater.* **20**, 1700171 (2018).
19. Khachaturyan, A.G. Theory of structural transformations in solids, Courier Corporation; (Dover Publications INC.: Mineola, USA, 2008).
20. Trassinelli, M. *et al. Appl. Phys. Lett.* 104 081906 (2014).
21. Zhou, N. *et al. Acta Mater.* **58**, 6685 (2010).
22. Sharma, A. *et al. Philos. Mag.* **98**, 819 (2018).
23. Machain, P. *et al. Philos. Mag.* **95**, 2527 (2015).
24. Amodeo, J. *et al. Crystals* **8**, 240 (2018).
25. Amodeo, J. *et al. Acta Mater.* **59**, 2291 (2011).
26. Chulist, R. *et al. Acta Mater.* **61**, 1913 (2013).

Chapter 4

Following the martensitic configuration footprints in the transition route of Ni-Mn-Ga magnetic shape memory films

4.1 Introduction

As already discussed in chapters 1 and 3, epitaxial Ni-Mn-Ga films form interrelated 3D hierarchical pattern of twin boundaries in the martensitic phase to compensate the stress caused by the symmetry reduction during the martensitic phase transition from the cubic austenitic phase to the lower symmetry martensitic phase. The symmetry operator(s) for the twin boundaries connecting twin variants, is (are) rotation or (and) mirror [1-3]. The hierarchical nature of the self-accommodation occurring at the transition covers a broad range from nanoscale to macroscale [4] (section 1.2.1).

For most of the applications mentioned in chapter1, the material cyclically undergoes one of the following phenomena (section 1.2):

i) Martensitic phase transition induced by magnetic field, stress or temperature;
ii) Magnetic field or stress induced reorientation of the twin variants in the martensitic phase.

It is well known that there are some obstacles stemming from both the intrinsic and the extrinsic characteristics preventing the full exploitation of the material towards the applications. Among the obstacles are the thermal and magnetic hysteresis [5], broadness of the transition [6] and the twinning stress [7], which are affected by several parameters, e.g., the composition, chemical order, crystal structure, geometrical compatibility of the martensite and austenite [8], dynamics of the transition [9], internal stress and structural defects. The two latter parameters are strongly linked to the configuration of the twin variants in the martensitic phase (section 1.2.1).

Therefore, in order to find possible solutions to overcome the aforementioned obstacles, it is necessary to gain a comprehensive view of the configuration of the twin variants at the different length scales and its evolution upon martensitic phase transition in different conditions. In the literature, there are few works focused on the crystallographic structures and the martensitic configurations of epitaxial Ni-Mn-Ga and Co-doped Ni-Mn-Ga thin films through experiments and models [10-15]. However, the knowledge about the multiscale hierarchical self-accommodation of the twin variants in the martensitic phase and its possible links to the transition route is still limited, mainly due to lack of direct multiscale observation (section 1.3.3).

In this chapter, first, we directly visualize the crystallography of seven-fold modulated (7M) Ni-Mn-Ga epitaxial films, the symmetry relations between the twin boundaries and the interfaces between the colonies of different twin boundaries in the martensitic phase by means of different transmission electron microscopy (TEM) techniques from atomic- to micro-scale. This enables us to characterize the twin boundaries in a large-scale range. Our direct observations through TEM techniques in cross-sectional view are combined with atomic force microscopy (AFM) topography imaging vs. temperature. We propose a route for the martensitic forward and reverse transitions of the films, highlighting the major role played by the different martensitic interfaces. The obtained results have been published in reference [16]. Second, we evaluate the linkage between the density of the martensitic interfaces, martensitic transition width, thermal hysteresis as well as the effects of post-annealing by means of morphological analysis and low-field magnetization curves vs. temperature. Third, we directly visualize the evolution of the twin boundaries in different transition conditions, thanks to an advanced in situ magnetic field and temperature dependent imaging.

4.2 Insight into the role of twin boundaries and interfaces

4.2.1 Basic concepts on the crystallography of the twin boundaries

As it was briefly discussed in chapter 1, section 3.1 as well as chapter 3, section 1, in epitaxial Ni-Mn-Ga films compared to the bulk single crystal, the six {110} planes of the cubic austenitic cells are not equivalent. The two planes, which are normal to the substrate plane are closely aligned to the martensitic configuration called Y-type, where the magnetic easy axis alternates in the plane of the film. The four remaining {110} planes of the austenitic cells, which are 45º inclined with respect to the substrate, are along the martensitic configuration called X-type (**Figure 4.1**). For these configurations, the easy magnetization axis of the martensitic cell alternates in and out of the plane of the film (**Figure 4.1c**). As shown in **Figure 4.1b**, the six orientations of twin boundaries in X- and Y-type regions are conjugated in three pairs, i.e., Y1-Y2, X1-X2, X3-X4 and give rise to a typical microstructure, characterized by twin boundaries oriented at 45° or at 90° with respect to the substrate plane.

From the crystallographic point of view, X- and Y-type twin boundaries separate regions following strict twinning relations (**Figure 4.1d**). The twinning operators are mirror or (and) rotation. Therefore, based on theoretical models within the continuum theory of martensite, we introduce three atomically sharp crystallographic twin boundaries, which are observed in our seven modulated monoclinic epitaxial films:

1) Type I twin boundary, where the a and c axes of the monoclinic cells alternate through a mirror plane (K1 is the twinning plane, left panels in **Figure 4.3**e and **Figure 4.5**d);

2) Type II twin boundary, in which the a and c axes of the monoclinic cells alternate by a 180º rotation (around the η1 axis, middle panel in **Figure 4.3e** and right panel in **Figure 4.5d**);

3) Modulation twin boundaries (MTB), where only the modulation direction (MD) of the martensitic cells alternates across the boundary (right panel in **Figure 4.3e**). In this type of boundary, both twinning operators are satisfied [1-3].

Among the twinning systems, type I and type II and their related twinning stress are of special interest, since they alternate the easy magnetization axis in the martensitic cells. In the literature for Ni-Mn-Ga bulk single crystals, the twinning stress of type II twin boundaries has been reported to be up to around twenty times lower than type I counterpart, i.e., type II twin boundaries are considered highly mobile upon applying an external magnetic field [7,17,18]. Hence, in order to achieve giant magnetic field induced strain, type II twin boundaries are evidently desired.

Yang et al. in 2015 reported a combination of type I and type II twin boundaries for both X-type and Y-type configurations in 7M Ni-Mn-Ga epitaxial films [13]. In 2017, Niemann et al. reported a model for the X- and Y-type configurations, where combinations of eight compatible martensitic variants nucleate diamond-like enclosed volumes of martensite. The diamonds grow until they meet each other or (and) the substrate. The midribs of the diamonds serve as the twin boundaries (type I, type II and modulation) [14].

In addition to the above twinning systems, there exist interfaces separating colonies of X- or Y-type twin boundaries in larger scale, for which the exact atomically sharp twinning relations are not necessarily fulfilled. These interfaces can be sorted into conjugation interfaces and non-conjugation interfaces, depending on whether they separate colonies of conjugated or non-conjugated planes (**Figure 4.1d**) [19-21].

Simplified schematic representations of the twin boundaries nucleated from different {110} planes and the interfaces connecting the colonies of the twin boundaries are provided in **Figure 4.1d**. The scheme shows the twin boundaries as the inclined and vertical red lines (X and Y, respectively). The pink line corresponds to a ridge and the yellow line corresponds to a valley [15], both can be categorized as conjugation interfaces. The green lines are assigned to the non-conjugation interfaces [19-21].

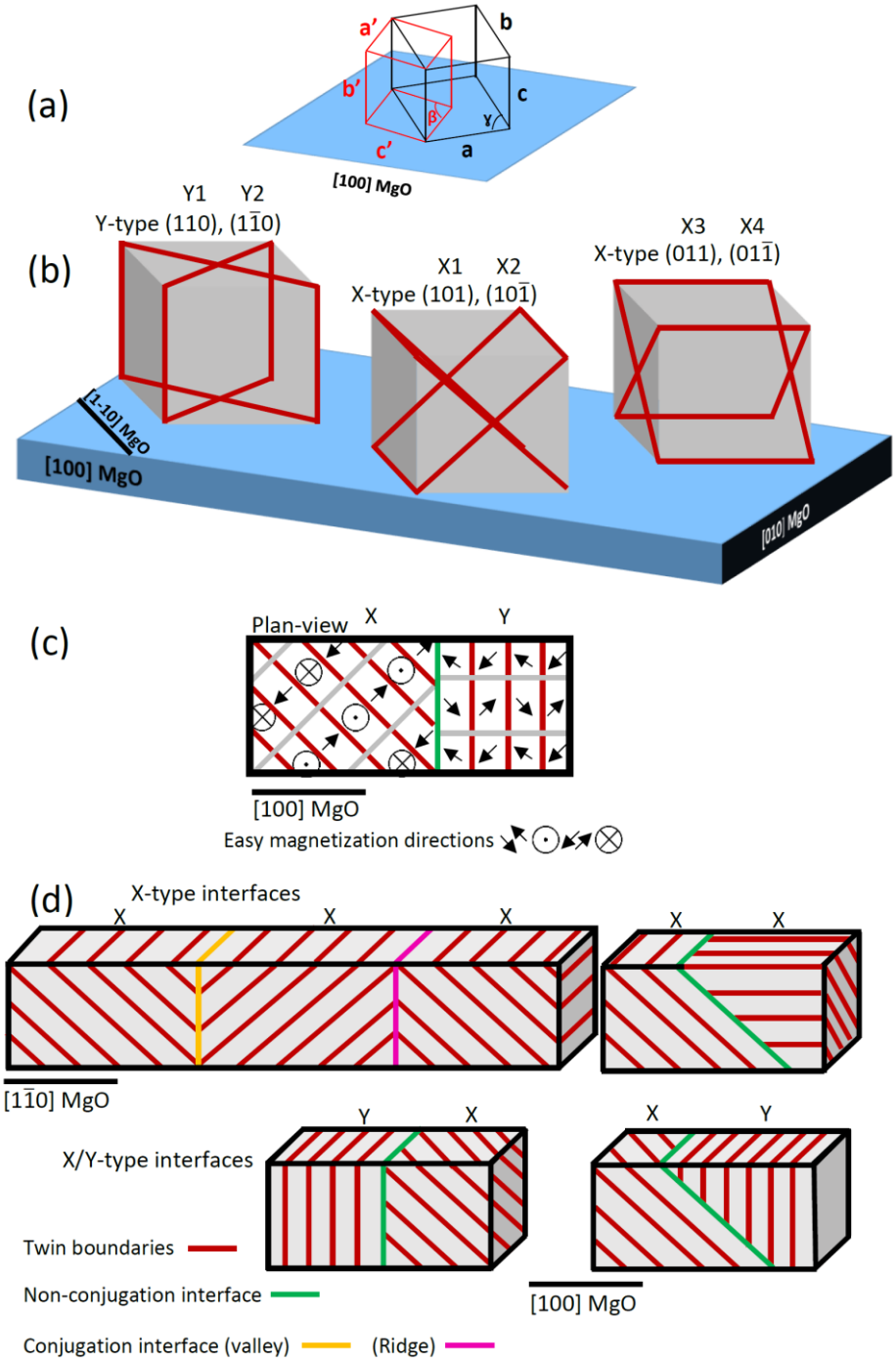

Figure 4.1: a) Schematic representation of the relative orientations between the standard martensitic (red) and the austenitic setting (black) with respect to the MgO substrate directions. The indices show the three axes of the martensitic cell in the two represented settings. The martensitic seven modulation direction is along c', while it is along one of the [110] directions in the austenitic setting. The easy magnetization direction in the two settings is b' = c. The monoclinic non-right angle is β in the monoclinic setting and ɣ in the austenitic setting. b) Schematic representation of the six {110} cubic planes in the Ni-Mn-Ga austenitic cell that are aligned with the twin boundaries in X-type and Y-type martensitic twin boundaries. c) Plan view of the X- and Y-type twin boundaries, showing the orientation of the magnetic easy axis in both the configurations. d) Schematic representation of the martensitic interfaces in X-type and Y-type connecting the colonies of the twin boundaries nucleated from different austenitic planes [16].

4.2.2 Symmetry of the twin boundaries

Two samples were selected for this investigation.The first sample (#1) was grown directly on (001) MgO followed by post-annealing (3600 s at 623 K in 10^{-3} mPa) and local mechanical stress, which locally induced the Y-type configuration (sample #1P in section 3.4). The second sample (#2) was grown on 50 nm Cr uderlayer in turn grown on (001) MgO substrate (details of the growth conditions can be found in **Table 2.1**). The composition measurements were performed using energy dispersive X-ray spectroscopy (EDS), giving the results $Ni_{52.7}Mn_{19.9}Ga_{27.4}$, $Ni_{53.0}Mn_{20.3}Ga_{26.7}$, for sample #1 and #2, respectively (uncertainty 1.0%). Atomic and magnetic force microscopy images of the as-grown samples are represented in (**Figure 4.2**) showing the X-type martensitic configuration [15].

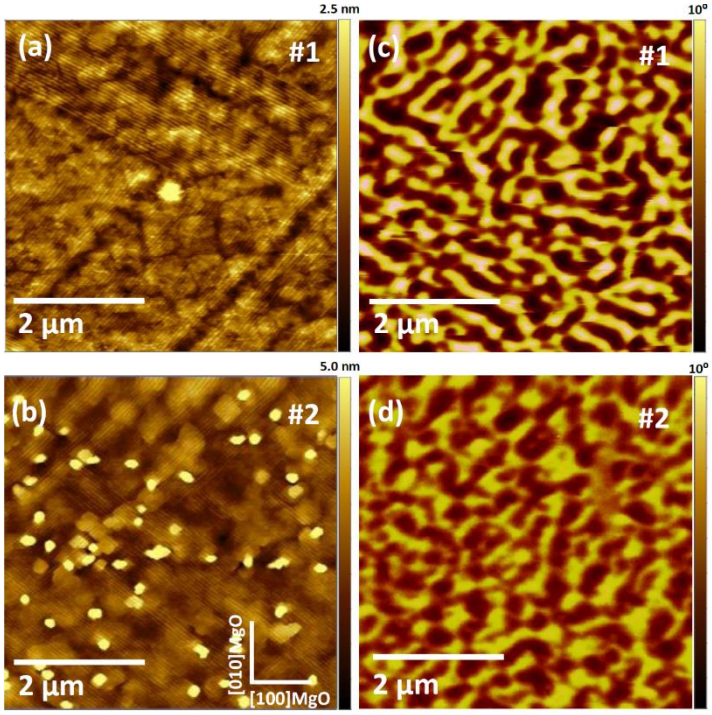

Figure 4.2: a),b) atomic force microscopy images and c),d) magnetic force microscopy images at room temperature showing the typical X-type configuration for the as-grown sample #1 and #2 [16].

The epitaxial crystallographic relations of the MgO substrate, Cr underlayer (for sample #2) and Ni-Mn-Ga cells were determined by TEM analysis as (001)[100]Ni-Mn-Ga//(001)[110]MgO for sample #1 and (001)[100]Ni-Mn-Ga//(001)[100]Cr//(001)[110]MgO for sample #2. The crystal symmetry of the martensitic cells was characterized as 7M monoclinic structure. The crystallographic coordinates describing the martensitic cell are provided in **Figure 4.1a**. In order to keep the coherency and simplify the description, the martensitic cells will be described only in the austenitic setting (i.e. a, b and c, c is the shortest axis and the magnetization easy axis).
The cell parameters of the martensitic cells were measured by TEM and X-ray diffraction for sample #1 as a = 0.608 nm, b = 0.578 nm, c = 0.552 nm, ɣ = 91.5º and for sample #2 as a = 0.609 nm, b = 0.577 nm, c = 0.552 nm, ɣ = 91.5º.

To avoid the superposition of the twin boundaries across the TEM lamella, the cross-section samples were prepared along [100] MgO (for observing Y-type in sample #1) and $[1\bar{1}0]$ MgO (for investigating X-type in sample #2).

Figure 4.3 shows the results obtained for sample #1, presenting the coexistence of X-type and the stress induced Y-type configurations (**Figure 4.3a**). The extensive characterization can be found in section 3.4. The strategy we used to evaluate the type of twin boundaries in Y-type configuration is based on the change of the modulation direction across the boundaries observed by HAADF and HR-TEM (**Figure 4.3c,d** and **Figure 4.4**). This enables us to identify the types of twin boundaries in a large scale. The diffraction pattern taken from the [101] zone axis of the Y-type region is shown in **Figure 4.3b**. The b axis of the cells lies out of plane of the film and the a and c axes alternate in the plane of the film (c axis being the shortest axis and the easy magnetization axis), which is the typical pattern for the Y-type twinning configuration in 7M monoclinic martensitic phase. The HAADF image of the whole lamella is shown in **Figure 4.3c**. The three marked square areas are magnified and represented in **Figure 4.3d**. As can be observed, inside each variant there are tiny contrast variations with certain directions, which correspond to the 7M contrast modulation of the martensitic phase.

Depending on the change of the modulation direction across the Y-type boundaries, three types of twin boundaries can be identified, which have been marked with red, blue and purple lines. The direction of the modulation only changes across the red and purple boundaries. For the middle HAADF image of **Figure 4.3d** as an example, the directions of the contrast variations across the boundaries are shown by double-headed arrows. Higher resolution version of the right image in **Figure 4.3d** can be found in **Figure 4.4a**. In addition, the schematic explanation of the observed changes is provided in **Figure 4.3e**. If we consider the martensitic monoclinic cell in the austenitic setting, the direction of the modulation always lies in the plane of the a and b axes (**Figure 4.2a**). For the top left scheme, shown in **Figure 4.3e**, the K1 mirror plane (type I) serves as the twin boundary alternating the orientation of the martensitic cell, while for the middle top image the η1 axis (type II) serves as the twin boundary by rotating the cell of about 180º. As for the top right scheme, only the modulation direction (MD) of the cell alternates across the twinning plane. In all the three schemes double-headed arrows show the MD across the twin boundaries. In **Figure 4.3e** in the bottom, the schemes show the relative (with respect to the top schemes) projection of these MD across the twin boundaries in the plane of the lamella (FIB-cut along [100] MgO), proving the types of twin boundaries in the Y-type configuration in the prepared lamella. We scanned the whole Y-type region to find the distribution of the types of twinning. Only the twin boundaries marked with red and purple in **Figure 4.3b** were found to have type I and modulation symmetry relations. The rest of the twin boundaries evidently show type II twin boundary. It is worth mentioning that close to the substrate interface (~50 nm), we observed a pronounced branching of the twins showing type I boundaries, which are represented in **Figure 4.4**. This represents an experimental evidence for the model proposed as the diamond model of the nucleation and growth of the martensitic nuclei in Y-type configuration [14].

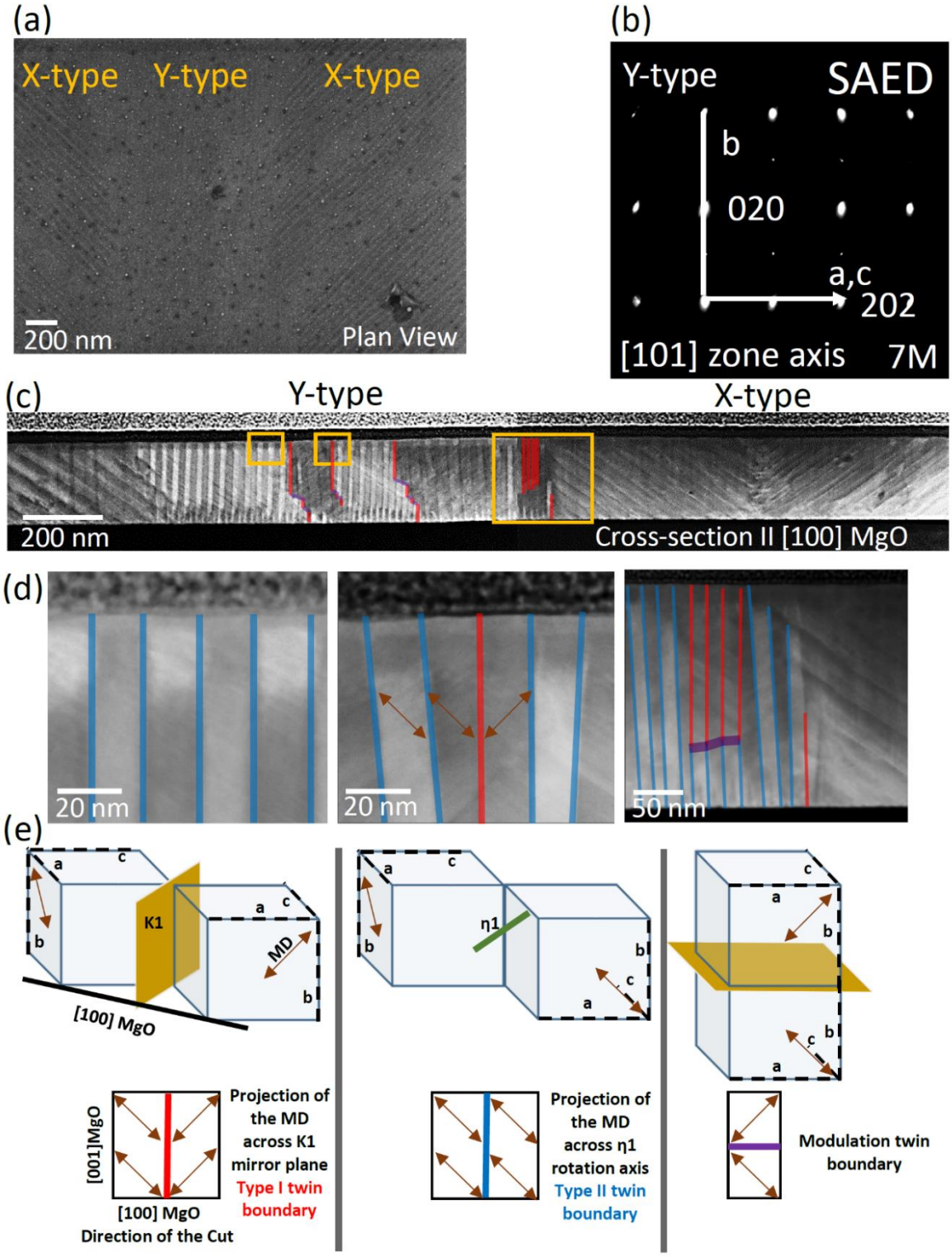

Figure 4.3: a) SEM secondary electron image of sample #1 showing the coexistence of X-type and Y-type configurations. b) SAED pattern of the Y-type region showing the martensitic cell parameters in the Y-type configuration, which have been fitted to 7M monoclinic cell and the orientation of each axis. c) large-scale cross-section HAADF image of the sample, d) magnified HAADF images of the marked areas in (b) showing the types of twins (red for type I, blue for type II and purple for modulation twin boundaries). The modulation directions are shown by double-headed arrows, e) top: schematic representations of the martensitic cell axes and the modulation direction in Y-type across type I, type II and modulation boundaries (austenitic setting); bottom: the corresponding projection of the modulation direction in the plane of the lamella (FIB-cut along [100] MgO) [16].

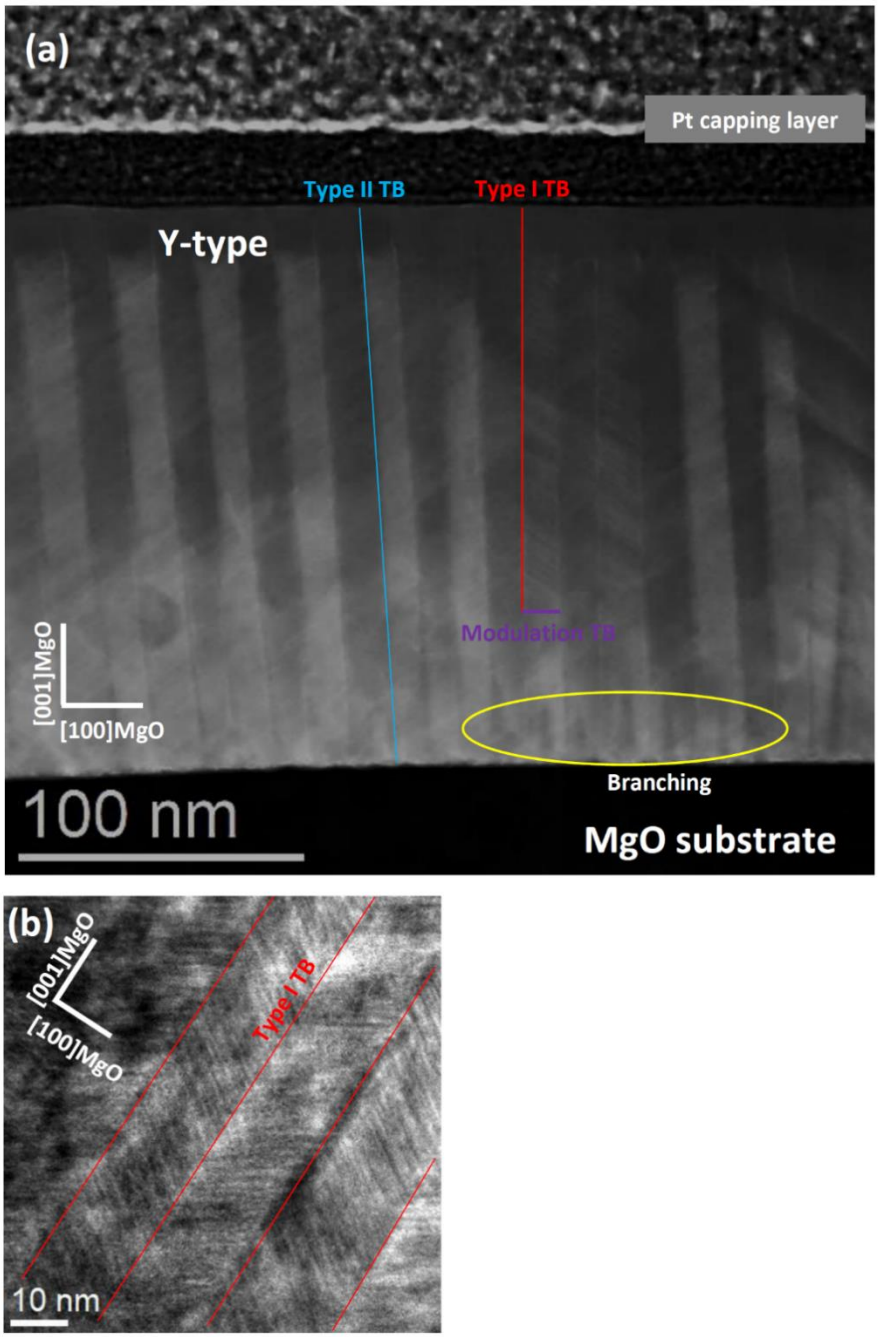

Figure 4.4: Type of twin boundaries in the Y-type configuration of the lamella prepared from sample #1: a) HAADF image of the lamella, examples of different types of twins are highlighted. In addition, the observed branching of the Y-type twins close to the MgO interface is highlighted, b) HR-TEM of an example of the type I twin boundaries alternating the modulation direction of the cells across the boundaries near the substrate [16].

Figure 4.5a shows the HAADF image of the lamella prepared from sample #2, alternating stripes with bright and dark contrasts, around 45º and -45º tilted with respect to the substrate, which are typical of X-type configuration.

Besides X-type twin boundaries (marked with blue lines), some conjugation interfaces connecting the colonies of differently inclined twin boundaries at the valley and ridges are marked with yellow and pink, respectively.

For the X-type configuration, due to the orientation of the twin boundaries, as it is shown in **Figure 4.5d**, the projections of the resultant MDs for both the mirror and rotation symmetry operators in the plane of the lamella (FIB-cut along [1$\bar{1}$0] MgO) are equal. In this case, the presence of the type II twinning system for a cross section along [1$\bar{1}$0] MgO is proposed in ref [14].

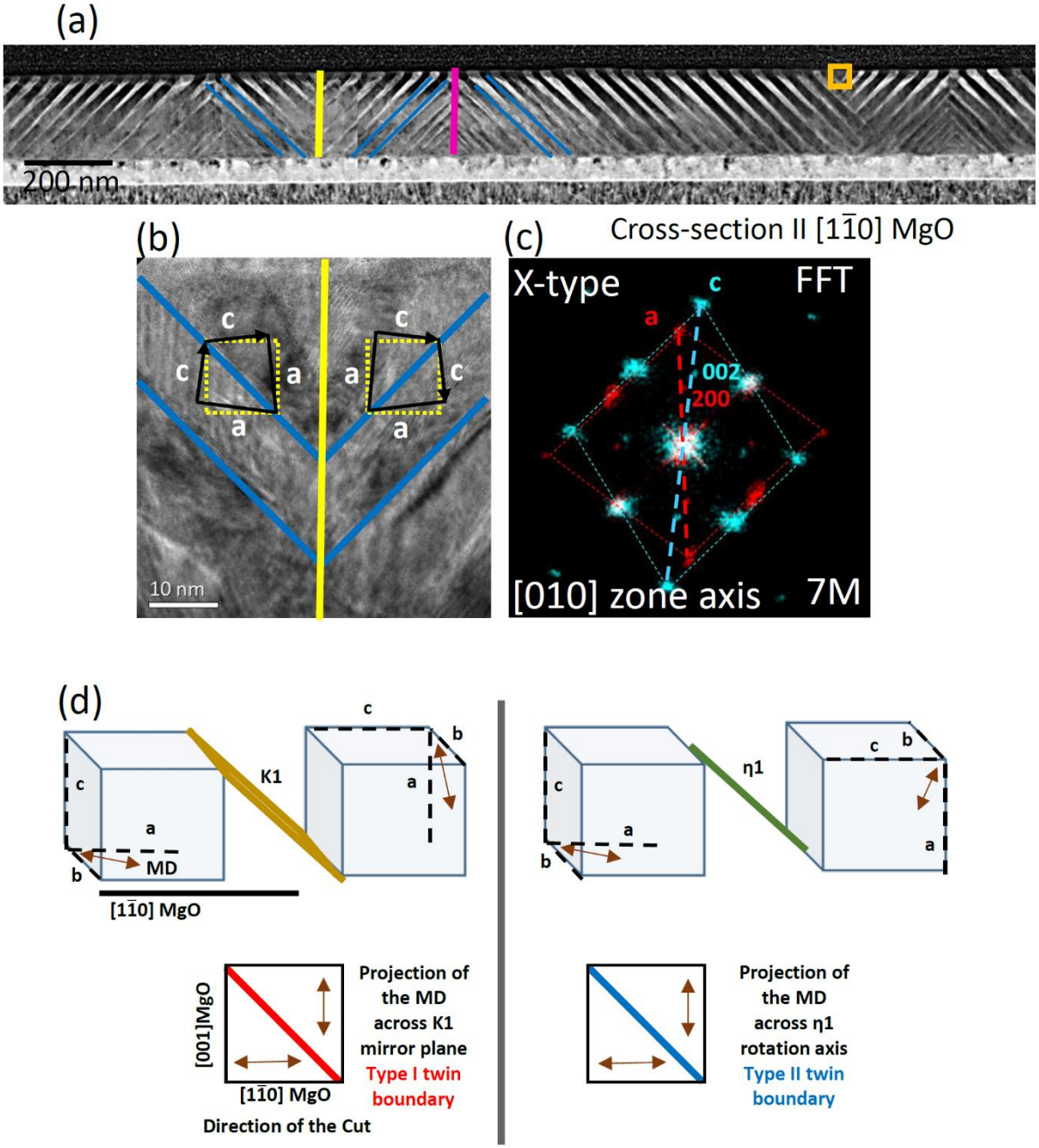

Figure 4.5 a) Large-scale HAADF image of sample #2, the twin boundaries and the conjugation interfaces are marked by blue, pink and yellow lines. b) HR-TEM of the marked area in (a) showing the symmetry of the martensitic cells across the twin boundary and the conjugation interface, c) FFT pattern taken at the twin boundary (shown in (b), the left) showing the a and the c axes (black lines) alternating across the twin boundary. The yellow dashed lines aligned along the edges of MgO are guides for eyes to evidence the observed cell misorientation. Cell parameters are fitted to the 7M monoclinic cell. d) top: schematic representation of the martensitic cell axis and the modulation direction in X-type across type I, type II boundaries (austenitic setting), bottom: the corresponding projection of the modulation direction in the plane of the lamella (FIB-cut along [1$\bar{1}$0] MgO) [16].

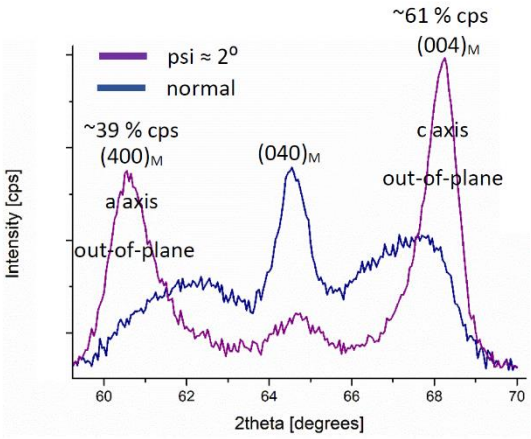

Figure 4.6: Out-of-plane configuration X-ray diffraction of sample #2 at 223 K, the dark blue shows the $(040)_M$ epitaxial peak in a normal theta-2theta scan for 2theta = 58-70º and the purple peaks were obtained in an asymmetric scan (diffraction vector ~2º offset from the normal to the substrate). The (400) and (004) martensitic peaks measured in the asymmetric scan are assigned to the a and c-axis of the martensitic cells oriented out-of-plane of the film, respectively. The relative intensity counts of the two peaks is reported in the figure. Considering the possible errors of the measurement and the calculations, the values are in reasonable agreement with the relative intensity counts calculated from the STEM image of the lamella #2 for a-axis and c-axis out-of-plane of the film (34% a-axis and 66% c-axis). As it was explained above, the peaks related to the out-of-plane a-axis and c-axis typically appear with slight misorientation with respect to the substrate normal due to the slight (CW or CCW) rotation of the martensitic cells around the b axis upon the formation [16].

4.2.3 Evolution of the interfaces

Figure 4.7a shows the HAADF image of conjugation interfaces separating colonies of differently inclined twin boundaries. The conjugation interfaces highlighted in the HAADF image can be directly correlated to the plan view topography imaged by AFM showing the ridges and valleys (**Figure 4.7b,d**) [15]. As it is shown in the MFM image (**Figure 4.7c**), across the conjugation interfaces, the easy magnetization axis of the martensitic variants inverts its direction. This leads to discontinuity of the out-of-plane magnetic stray field measured by MFM. In order to schematize this effect in the atomic scale we inserted arrows in **Figure 4.5b** to evidence both the crystallographic orientations and the magnetization directions (i.e., c axis) across the conjugation interface.

Figure 4.7a also shows a variation of the spatial twinning periodicity throughout the film (Λ range $\approx$ 10-30 nm). Looking at the ridges, it is evident that for the twin boundaries that intersect at the ridges Λ reduces close the substrate, while the opposite trend is observed for the valleys, i.e., for the twin boundaries that intersect at the valleys Λ decreases close the surface. These twin boundaries with low twinning periodicity in the ridge positions (pink lines) do not reach the surface and in the valley position (yellow line) they do not reach the Cr under-layer; evidently, because they meet each other before growing through the whole thickness of the film, therefore their further growth is hindered. In addition, more symmetric conjugation interfaces are observed in the lamella at the ridges rather than at the valleys (**Figure 4.5a**). Symmetric conjugation typically appears when the two sides of the conjugation system meet at the registry [21]. In the present case (i.e. Ni-Ni-Ga film), it could occur when the twins nucleate at the same point (or grow equally towards each other). All these observations are coherent with in-situ AFM topography measurements vs. temperature, and can be explained by a transition route, in which the nucleation of the twin boundaries initiates from the ridges and proceeds until they meet at the valleys, non-conjugation interfaces or they reach the substrate (**Figure 4.7a**), as will be discussed in details below.

The other type of martensitic interface, which was shown schematically in **Figure 4.2d**, is the non-conjugation interface. An example of this type of interface is shown in the topography plan view (**Figure 4.7e**) and HAADF cross-section (**Figure 4.7f**), representing a blurred region on the right side of the image and a region with well distinguishable twin boundaries on the left separated by an inclined green line. In the blurred region, the twin boundaries are parallel to the lamella. The observed blurredness is due to the superposition of the twin boundaries. The relative orientations of the twin boundaries are highlighted by the blue lines, while the ridge and valley by pink and yellow lines, respectively.

In the martensitic forward and reverse transitions, the interfaces play an important role. In thermoelastic materials, the martensitic forward transition starts with the formation of the phase boundaries and proceeds with moving the phase boundaries, propagating the martensitic phase at the expense of the austenitic phase. The nucleation of the lower symmetry phase is energy costly, which needs to be compensated. To reduce the energy cost, the transition initiates by a heterogeneous nucleation of the low symmetry phase from the most vulnerable regions (e.g. defects, impurities, scratches, etc.). On the other hand, in the reverse transition (martensite to austenite) the material transforms back to the high symmetry austenitic phase [22]. Residuals of untransformed austenitic phase inside the martensitic phase have been suggested to serve as the starting points for the reverse transition. In the literature, the above-described martensitic interfaces are generally suggested to be the regions maintaining the residuals of the untransformed austenitic phase [23].

In order to clarify this point, we explored the X-Y interfaces (**Figure 4.3**) and X-X interfaces (**Figure 4.5**, both conjugation and non-conjugation) by HR-TEM. No trace of the austenitic phase was found at room temperature by FFT and SAED analysis.

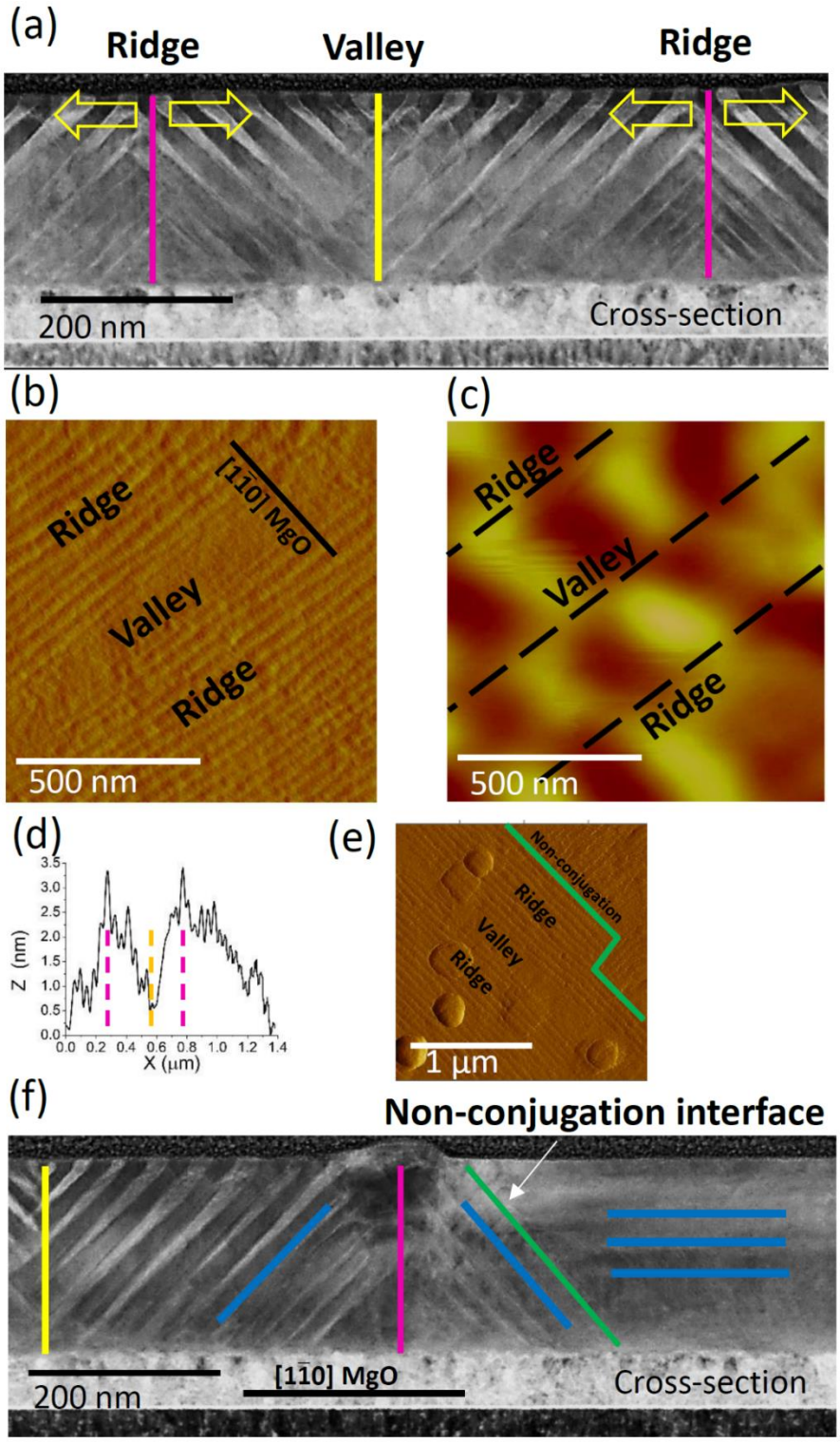

Figure 4.7: a) HAADF image of the sample #2 showing the ridges and valleys created by the conjugation interfaces (pink and yellow lines), b,c) AFM/MFM images of the sample #2 at RT showing the conjugation interfaces in plan-view (b), and the related disconnections in the magnetic domains (c). d) height profile of the topography (b) across the boundaries showing the position of the two ridges and the valley, e) topography image, illustrating the conjugation and non-conjugation interfaces (green lines) in plan-view. f) HAADF image of sample #2 showing the non-conjugation interface (green line) in the cross-section view, the geometry of the twins (blue lines) and the conjugation interfaces (pink and yellow) [16].

To deepen the phenomenology of the transition, we measured the evolution of the interfaces (conjugation and non-conjugation) upon phase transition by in-situ topography imaging vs. temperature (**Figure 4.8**). Sample #2 was cooled down from 345 K to 300 K and subsequently heated up to 345 K, capturing the topography images in different stages of the forward and reverse transition. **Figure 4.8a** shows the status of the sample at 328 K (austenitic phase). As the temperature is decreased to 321 K (**Figure 4.8b**), the X-type twin boundaries nucleate in isolated regions (ridges, some of them are highlighted), which then continue to nucleate and grow towards each other. The highlighted areas in **Figure 4.8c** show the valleys and the non-conjugation interfaces, which are not yet transformed. Upon further decreasing temperature to 315 K (**Figure 4.8d**), the scanned area fully transforms to the martensitic phase. One can trace the positions of the ridges, valleys and the non-conjugation interfaces. Upon subsequent heating (to 326 K, **Figure 4.8e**), the reverse transition takes place, starting from the positions of the valleys and the non-conjugation interfaces. **Figure 4.8f** shows that the ridges degrade at the final stages of the reverse transition. In order to better visualize the positions of the interfaces, the height profile of the marked areas in **Figure 4.8a,d** are shown in **Figure 4.8g**. As it is shown in **Figure 4.8g**, evidently a kind of nanometric surface relief pre-exist close to the martensitic transition. Identifying the origin of these corrugations requires further investigation. One could take into account the possibilities e.g. short-range ordering [24], thermomagnetomechanical history of the sample [25], or precursory of the interfaces as a transition progress [20]. Finally, one can follow the imaging temperatures on the low field magnetic curves over temperature for the same sample, reported in **Figure 4.8h**, which was measured by superconducting quantum interference device (SQUID) magnetometer.

With these results, we propose that the nucleation of the martensitic phase in sample #2 starts from the positions of the ridges on the surface of the sample. The twin boundaries continue to nucleate and grow towards each other and towards the substrate, until they meet at the valleys and the non-conjugation interfaces. For the reverse transition however, the non-conjugation interfaces and the valleys transform to the austenitic phase at the initial stages of the transition and ridges are the last to transform. In the light of our experiments, we highlight the primary role played by the interfaces in the transition route; we can exclude that it has to be related to residuals of the austenitic phase.

Ni-Mn-Ga cells on the surface of the film provide an additional degree of freedom compared to the cells at the interface with the substrate, which impose huge pinning constraint [26]. The surface of the film serves as the interface for the heat exchange, facilitating the transition [27]. Hence, upon the forward transition, it is likely that the heat exchange favors the nucleation of the martensitic phase primarily on the surface at the ridges having convex shape.

In addition, these coarse corrugations break the elastic homogeneity of the material, facilitating the heterogeneous nucleation of the martensitic phase. Upon the nucleation of the martensitic twin boundaries and their subsequent growth in the austenitic matrix, the created elastic strain typically dissipates in the form of heat and acoustic waves and partially stores in the material in the form of stored elastic energy. This energy is related to the irreversible steps of the transition, e.g., the obstacles stopping the growth, therefore it is thermodynamically irreversible [28]. The stored elastic energy works in a spring fashion by partially storing the strain during the forward transition. Over the reverse transition, the stored energy is released back serving as a driving force; hence, it could be mechanically reversible.

For a multi variant system, where the self-accommodation of the twin variants takes place by the coalescence of differently oriented equivalent boundaries, the dissipation and storage of the elastic strain typically occurs locally upon the nucleation as well as at pinning obstacles [28]. This makes conjugation and non-conjugation interfaces critical regions of the sample (**Figure 4.7**).

The size of twin boundaries is expected to be directly proportional to the dissipated energy over the martensitic transition [29]. Thus the stored elastic energy is expected to be inversely proportional the size of the twin boundaries. The low-twinning-periodicity boundaries in **Figure 4.7a,f**, which do not grow across the whole thickness of the film, are expected to have a larger portion of stored elastic energy.

The stored elastic energy also regulates the sequence of the transition of the twin boundaries: in **Figure 4.8** the first twin boundaries that appear at the forward transition are the last boundaries to disappear at the reverse transition, which is in agreement with the model proposed in references [28] and [30] for the thermoelastic martensites. In fact, the boundaries that appear first over the forward transition are typically the largest, which dissipate the largest energy in the form of heat and acoustic waves and store the lowest elastic energy. On the contrary, the boundaries that appear as the last over the forward transition are typically the smallest, which dissipate the lowest energy in the form of heat and acoustic waves and store the highest portion of elastic energy. These smaller boundaries annihilate first over the reverse transition (compare **Figure 4.7** and **Figure 4.8**).

Recently, the transition temperature of a 400 nm epitaxial Ni-Mn-Ga film was investigated by a nanolocalized scanning thermal microscopy, reporting a considerable temperature gradient (~20 K) for the reverse phase transition of different regions of the sample [31]. Based on the route provided in this study, the reported temperature gradient is likely to be linked also to the transition temperature difference for the martensitic interfaces (i.e., ridges and valleys).

In a system where the transition involves the nucleation and growth of a ferromagnetic phase in a paramagnetic matrix, such as our Ni-Mn-Ga thin film, surface topography and spatial distribution of nucleation sites may have an important influence on the magnetostatic energy. A quantitative evaluation in the specific case would require an accurate modeling, such as proposed for bulk La-Fe-Si [32], a system for which the preferential nucleation of the ferromagnetic phase at the convex areas has been experimentally demonstrated [27].

In summary, our investigation provides a direct evidence of the major role played by the martensitic interfaces on the forward and the reverse transition in epitaxial Ni-Mn-Ga films (**Figure 4.8**). We propose that the forward transition initiates heterogeneously from the position of the conjugation interfaces, i.e., ridges on the surface of the film. The twin boundaries continue to nucleate and grow until they meet at the conjugation interfaces, i.e., valleys and the non-conjugation interfaces, where the growth is hindered. In these regions, the elastic strain created during the transition is partially stored. The stored energy in these regions serves as the driving force for the reverse transition by initiating the nucleation of the austenitic phase.

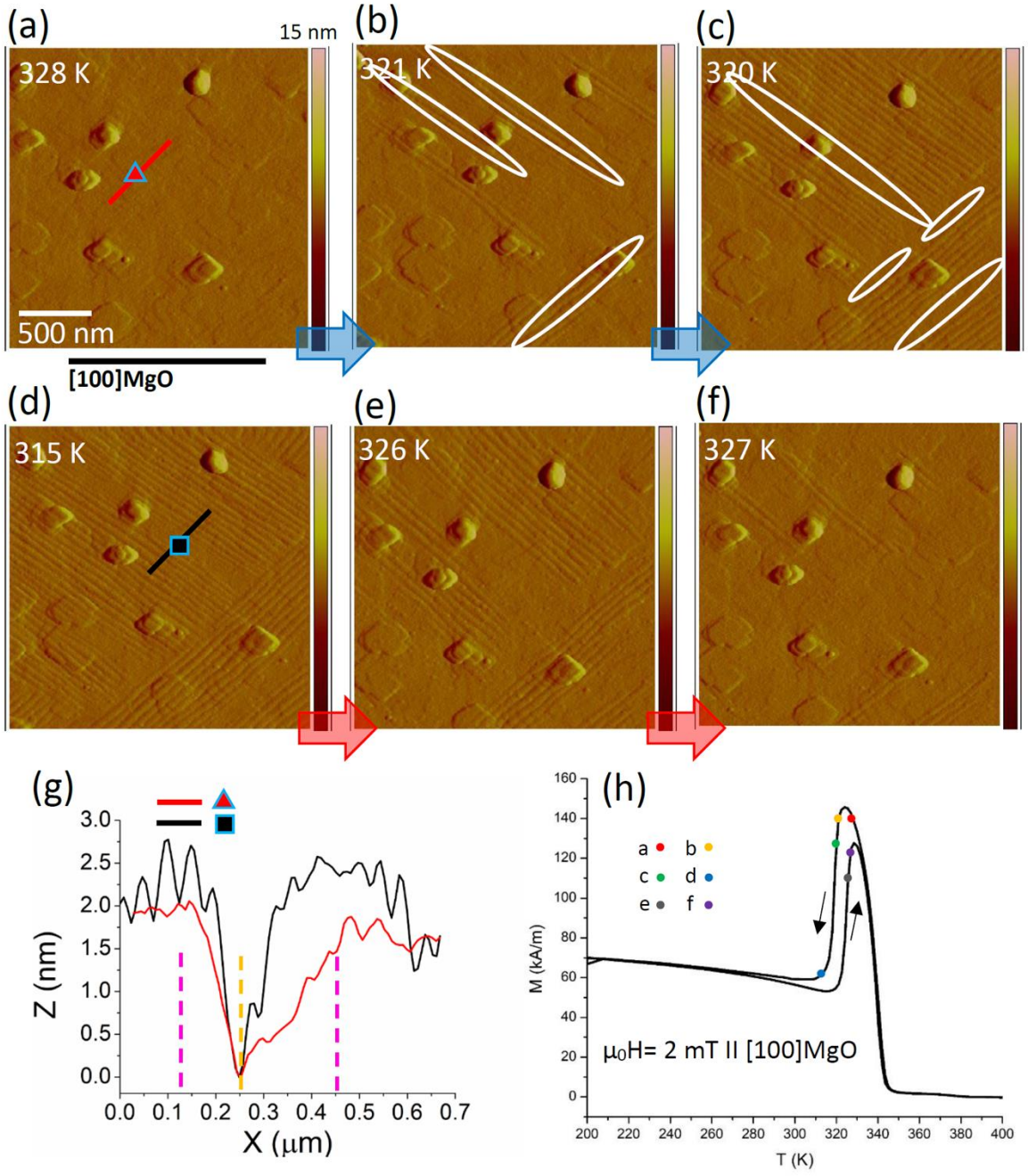

Figure 4.8: Tracing the formation and annihilation of the interfaces in sample #2 by means of in situ topography imaging vs. temperature (345 K - 293 K – 345 K): a) 328K, the film is in the austenitic phase. b) 321 K, nucleation of the martensitic phase starting from the ridges (conjugation interfaces), some are highlighted. c) 320 K, twin boundaries continue to nucleate and grow until they meet each other, the highlighted valleys and non-conjugation interfaces have not transformed yet. d) 315 K, the film is in the martensitic phase, the valleys and the non-conjugation interfaces have transformed as well. e) 326 K, the material transforms back to the austenitic phase starting from the valleys and the non-conjugation interfaces. f) 327 K, only the ridges are still untransformed. g) height profile of the marked area (the two ridges and the valley are assigned by the pink and yellow dash-lines, respectively). h) The isofield ($\mu_0 H$ = 2 mT along [100] MgO) magnetization curve as a function of temperature for the sample with schematic correspondence between the imaging temperatures and the transition curve [16].

4.3 Martensitic transition width and thermal hysteresis

The martensitic morphology and the critical transition temperatures of nine samples (A-I) were evaluated having similar thickness (200 nm), grown epitaxially on (001) MgO following the growth conditions as shown in **Table 2.1**. The samples show the martensitic phase at room temperature having X-type twinning configuration, except for sample B, with dominant X-type and minority Y-type configuration. The composition of the samples was measured by energy dispersive X-ray spectroscopy as $Ni_{52.5\pm1}Mn_{20.7\pm1}Ga_{26.8\pm1}$ (at. %). We scanned areas of 5×5 and 20×20 μm^2 of the samples by the topography imaging. We can confirm that the reported images in **Figure 4.9** are representative for the morphology of the martensitic X-type configuration of the investigated samples. The images were refined by Laplacian-Gaussian edge detector algorithm, height-sensor color map, as well as the azimuth filters. The tools are available in the open-source Gwyddion program (available at http://gwyddion.net/). Then the approximate density of the martensitic interfaces was calculated for each sample manually, by calculating the total perimeter of the border between differently oriented colonies of X-type twin boundaries per scanned area, i.e. the density of the non-conjugation interfaces, using open source ImageJ program (available at https://imagej.net/). In addition, the total length of the valleys (a type of conjugation interface, **Figure 4.2**) per scanned area was calculated for each of the samples. Finally, the summation of the values of the valleys and the non-conjugated interfaces were reported as the martensitic interface density of each sample (η). We were unable to calculate the density of the ridges due to resolution limitations. η was plotted vs. the average transition width ($\Delta T_{average}$), which is defined as the average temperature difference between the forward and reverse transition temperatures (**Figure 4.10**). The transition temperatures were obtained using inflection method. Additionally, η was plotted vs. the thermal hysteresis of the samples. Since higher magnification images provide proper resolution to distinguish the morphology of the X-type configuration of the samples, only 5×5 μm^2 images are reported in **Figure 4.9**.

In **Figure 4.9**, we have provided the representation of the morphology of the samples as well as the low-field magnetization curves vs. temperature. **Figure 4.9a** represents the annealed samples. As can be observed, the filtered topography images show the homogenous large-scale colony of X-type twin boundaries oriented along [110] MgO. The length-scale of the colony exceeds the scan window therefore, other colonies of the twin boundaries, i.e. X-type along $[1\bar{1}0]$ MgO can't be observed. After filtering the image with the azimuth filter, the orientation of the twin boundaries is confirmed; the entire scan window appears in green, which is the color code for the twin boundaries along [110] MgO. The height-sensor filter visualizes the position of the valleys in blue. We applied the azimuth and the height-sensor filters to all the samples; though only the filtered images of sample A are shown in **Figure 4.9a** as an example. On the right side of **Figure 4.9a** the martensitic transition curves show quite sharp transitions for samples A-C. **Figure 4.9b** shows the same above-mentioned measurements for sample D-F. The morphology images show the homogenous X-type twin boundaries. In these three samples the length-scale of the colonies of twin boundaries is not as large as the annealed samples (samples A-C), therefore, both the colonies of the X-type twin boundaries along [110] and $[1\bar{1}0]$ MgO are detectable in the scan window. The transition curves also show relatively sharp transition for the samples. Finally, **Figure 4.9c** shows the topography and the transition curves of samples G-H. The morphology of these samples shows a few epitaxial imperfections possibly due to slight growth temperature variation (**Table 2.1**) or slight inevitable variations of other growth variables [33]. It also shows quite finer length-scale of X-type twin boundaries with respect to samples A-F, which turns these samples appear in basket-like morphology, as also confirmed by the images (**Figure 4.9c**). Since the length-scale of the twin boundaries is reduced for these samples, the density of the intersection regions (section 4.2.1), i.e., the martensitic interfaces, is evidently higher than samples A-F. The azimuth and the height-sensor filtered images of sample H are shown in the

figure as an example. The transition curves also show relatively smooth transition for samples G-I, i.e. the martensitic transition accomplishes in relatively larger temperature range, also resulting in a kind of transition tails.

So far, we have shown and compared the morphology as well as the martensitic transition curves of samples A-I, qualitatively. **Figure 4.10** represents the plots showing the quantitative values for the density of the martensitic interface (η), average width of the martensitic transition ($\Delta T_{average}$) and the thermal hysteresis of the samples. The values are also provided in **Table 4.1**. **Figure 4.10a** shows the plot of the average width of the martensitic transition vs. the density of the martensitic interface. It shows a consistent increase of $\Delta T_{average}$ as η is increased. The fitting line is shown as well. The three annealed samples, i.e. A-C, highlighted ellipse, have the lowest density of the martensitic interface ($\approx 0.5\ \mu m^{-1}$) and their average width of the martensitic transition are also among the lowest values. The lowest $\Delta T_{average}$ belongs to sample C: it is $\Delta T_{average} \approx 1.8$ K. The thermal hysteresis for the annealed samples (A-C, highlighted by the ellipse) is relatively higher with respect the rest of the samples (**Figure 4.10b**).

On the other hand, Samples D-I show lower thermal hysteresis values (i.e. in the range 4.6 K to 5.4 K) and only a minor change of the thermal hysteresis as a function of η. In **Figure 4.10c** the thermal hysteresis of the samples has been plotted vs. the average width of the martensitic transition. Noticeably, the thermal hysteresis of samples D-I is almost independent of $\Delta T_{average}$.

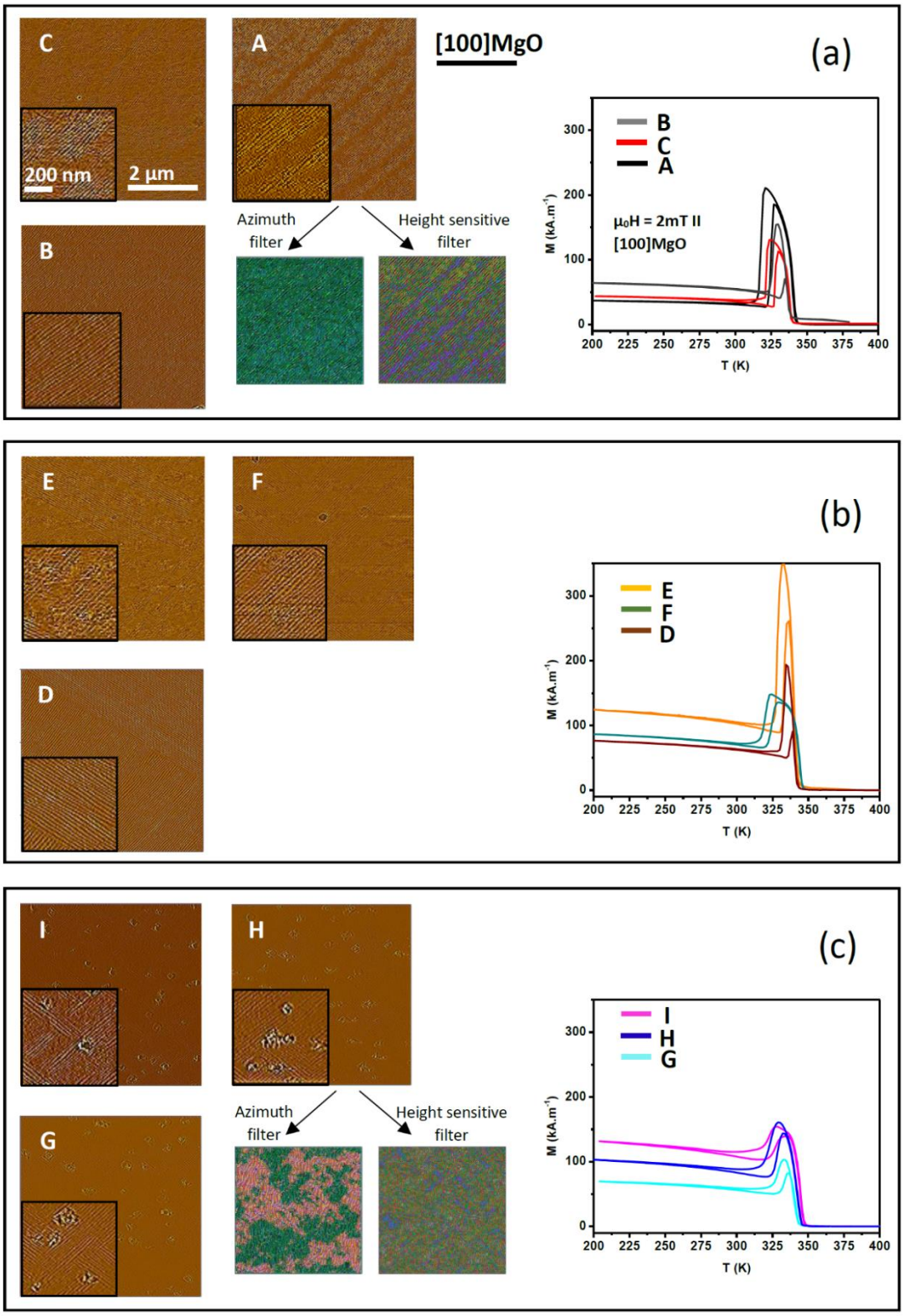

Figure 4.9: Representation of the morphological status and the isofield ($\mu_0 H$ = 2 mT along [100] MgO) magnetization curves as a function of temperature for a) samples A-C (post-annealed samples), b) samples D-F, c) samples G-I; the represented topography images were filtered by the Laplacian-Gaussian algorithm edge detector filter, showing the X-type twin boundaries along [110] MgO and [1$\bar{1}$0] MgO; the azimuth and the height-sensor filtered images are also shown for sample A and H, as an example; the azimuth filter highlights the colony of the X-type twin boundaries along [110] MgO and [1$\bar{1}$0] MgO and the height –sensor filter highlights the position of the valleys.

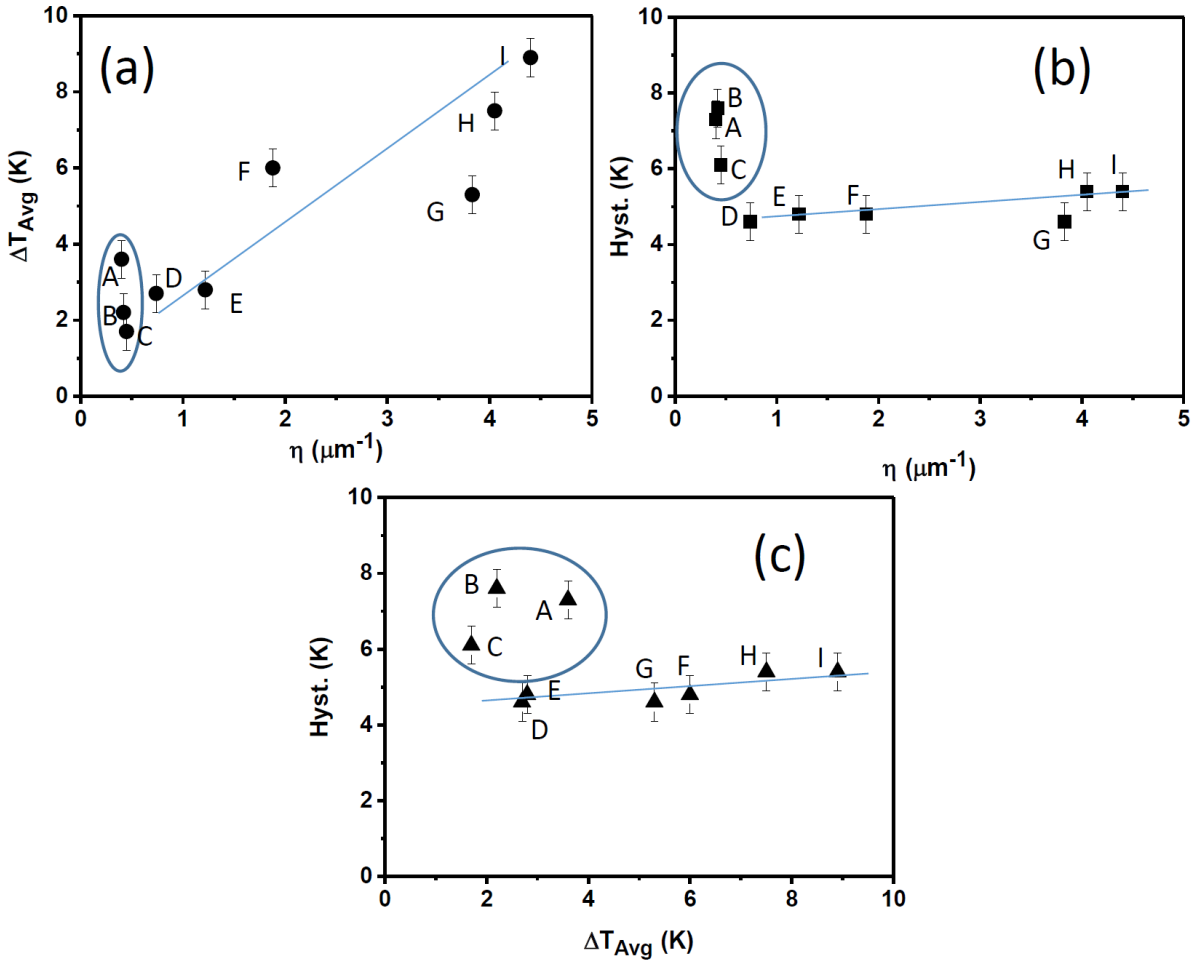

Figure 4.10: Quantitative representation of the relations between the densities of the martensitic interfaces (η), average transition width (ΔT_{Avg}) and the thermal hysteresis (Hyst.) for samples A-I (A-C are post-annealed samples); a) ΔT_{Avg} vs. η, b) Hyst. vs. η and c) Hyst. vs. $\Delta T_{Avg.}$

Table 4.1: Morphological characteristics and the transition critical temperatures of samples A-I, η is the density of the martensitic interfaces, ΔT_{Avg} is the average transition width measured for the cooling the heating curves, Hyst. represents the difference between the transition temperature in the cooling and the heating curves, T_c is the Curie temperature of the samples and R_q is the average roughness of the samples measured by AFM. The transition values were obtained using inflection method.

#	η (μm^{-1})	ΔT_{Avg} (K)	Hyst. (K)	T_C (K)	Rq (nm)
A	0.40	3.6	7.3	339.1	0.80
B	0.42	2.2	7.6	336.6	0.73
C	0.45	1.7	6.1	337.4	0.69
D	0.74	2.7	4.6	339.1	0.64
E	1.22	2.8	4.8	340.1	0.67
F	1.88	6.0	4.8	343.1	1.04
G	3.83	5.3	4.6	340.9	2.73
H	4.05	7.5	5.4	342.3	2.66
I	4.40	8.9	5.4	343.6	2.04

The sharpness of the transition in compositionally homogenous, structurally ordered epitaxial thin films as in our case, can be directly related to the stored elastic energy (section 1.2.4). Stored elastic energy is the residual elastic strain in the material, typically in the position of the pinning obstacles [28], where the growth of the twin boundaries is hindered, e.g., grain boundaries or in our films martensitic interfaces (section 4.2), regulating the transition. As proposed in section 4.2.3, the conjugation and non-conjugation martensitic interfaces can be considered as the critical areas of the samples. **Figure 4.10a** provides an experimental evidence for the direct (approximately linear) relation between the densities of the martensitic interfaces of the samples and the average transition width.

Storing partial amount of the transition elastic strain in the structure of the martensitic phase works as a resistance to the process of the forward transition, which can be realized by the value of the average transition width. The resistance imposes the transition to occur in a range of temperatures instead of a singular temperature and by that, the material gains certain amount of energy due to further cooling, to accomplish the transition. This sorted strain is recovered over the reverse transition facilitating the nucleation and the growth of the parent phase (1.2.4).

Our investigation clearly shows that annealing plays a key role on the transition regime of the samples: i.e. the annealed samples (A-C) have the lowest density of the martensitic interfaces, the sharpest martensitic transitions among the investigated samples but the highest thermal hysteresis. To explain this behavior, both the thermodynamic as and the kinetics of the transition need to be taken into account. As it was discussed in Chapter 3.2, annealing reduces the number of defects, imperfections and in general the number of disordered areas in the material and increases the microstructural ordering. This gives rise to the reduction of the martensitic nucleation points; therefore, from the kinetics' point of view, more undercooling is required to overcome the nucleation barrier of the martensitic phase transition, which results in the larger thermal hysteresis. There are promising routes dealing with the kinetics of the transition by reducing the nucleation barrier such as adding artificial defects [34,35] and precipitates [36] or possibly tuning the grain boundary dimensions in polycrystalline samples (**Figure 1.10f**). A reduced number of obstacles as a result of annealing on the other hand promotes the sharpness of the transition: the twin boundaries, after the nucleation, can grow larger until they meet each other. Larger-scale twin structures are expected to dissipate (relax) a larger portion of the transformation elastic strain in the forms of heat and acoustic waves and store a smaller portion of it. This phenomenon results in a sharper transition in the annealed samples.

In addition, other approaches, aimed at reducing the nucleation energy barrier have been reported in the literature. For instance, in the process called minor-loops, the material is maintained in the growth step of the transition by cooling and heating only in between the martensitic finish temperature (T_{Mf}) and the austenitic finish temperature (T_{Af}) [37]. Taking the advantage of this approach the nucleation energy barrier could be skipped to some extent. In contrast, inspired by another approach, which has not been experimentally tested yet [38], the material could be maintained in the nucleation step of the transition. In this approach, which requires a material e.g. FSMA, full of nanometric homogenous defects, the material is only cooled down to the temperatures close the martensitic start temperature ($>T_{Ms}$). Depending on the magnetic order of the austenitic and martensitic phase, the phase can be transformed by applying external magnetic field. Taking advantage of the reduced nucleation energy barrier of the defects and the magnetic field induced local strain, the defects transform to the martensitic phase at the temperatures $>T_{Ms}$ and because of the volumetric dominance

of the defects in the material, the major volume of the sample is transformed by transforming the defects. This approach is expected to be fully reversible, non-hysteretic and considerably sharp. Nevertheless, further theoretical and experimental studies are required to unveil all the contributing thermodynamic, kinetic, and thermoelastic parameters influencing this phenomenon.

In **Figure 4.11**, we have provided a schematic representation of the effect of annealing on the morphology and the critical transition temperatures. The martensitic transition curves of samples A (in black) and H (in blue) are superimposed as the examples for the annealed and the as-grown samples, respectively. The morphology of the two samples are also sketched in the figure and the transition width, thermal hysteresis as well as the density of the martensitic interfaces of the two samples are reported in the right-side of the figure. The plots show an evident inverse relation between the thermal hysteresis and the width of the transition as function of annealing. Nevertheless, a desired system for typical applications with cyclic phase transition requires the smallest possible transition width and the smallest possible thermal hysteresis.

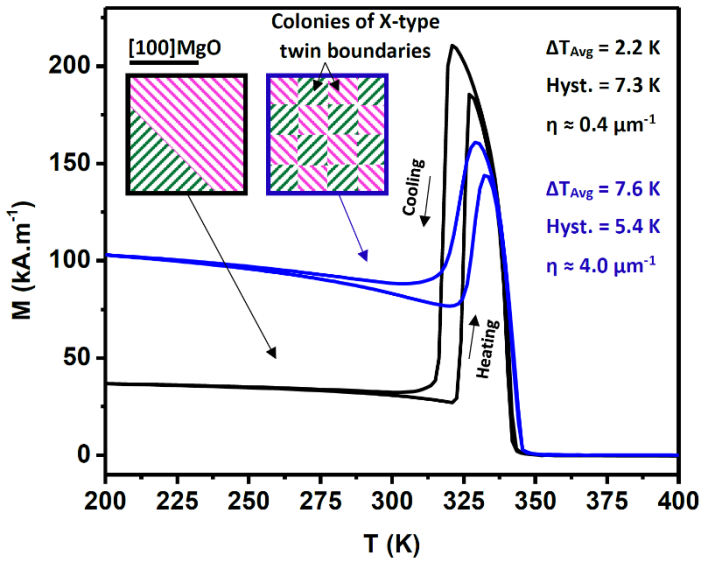

Figure 4.11: Effects of post-annealing (at 623 K, 3.6 ks) on the martensitic morphology, transition width and thermal hysteresis. The isofield ($\mu_0 H$ = 2 mT along [100] MgO) magnetization curves as a function of temperature of sample A in black and sample H in blue. The sketches show the simplified configuration of the X-type twins related to each of the samples; the pink and green textures are the X-type twin boundaries along [1$\bar{1}$0] MgO and [110] MgO, respectively. The boundaries between pink and green are assigned as the non-conjugation interfaces; the average transition temperature width (ΔT_{Avg}), thermal hysteresis (Hyst.) and the approximate density of the martensitic interfaces (η) of the two sample are provided for comparison reason.

Interestingly, according to the measurements shown in **Figure 4.10a,b,c**, for samples D-I, the width of the transition is directly related to η, while the thermal hysteresis of the samples shows only a minor change vs. η. Surface roughness of the samples (D-I), reported in **Table 4.1**, also shows a correlation with η. This desirable decoupling between thermal hysteresis and transition width has been obtained through controlling the density of the martensitic interfaces. The reported phenomenon suggests the possibility to control the transition width while keeping the thermal hysteresis almost unchanged via martensitic morphology engineering.

4.4 A journey across martensitic transition

As it was introduced in section 1.2.5, martensitic phase transition in the presence of magnetic field stabilizes the ferromagnetic phase [39,40], therefore, the martensitic transition temperature shifts to higher temperatures, which typically results in the inclined phase borders in the diagram shown by dashed lines in **Figure 1.16b**. Although in a thermodynamically ideal condition, the martensitic phase transition is expected to be fully reversible and steep, in the presence of the irreversible energy terms (**Equation 1.1**) the transition shows a hysteretic and relatively gradual character, which gives rise to the area in the diagram labeled as phase coexistence.

In **Figure 1.16b** , three paths of phase transitions were introduced, which will be investigated below. Briefly, in a zerofield phase transition (grey double-headed arrow), the transition is induced only by varying the temperature while in an isofield phase transition (pink double-headed arrow), the transition is induced by varying temperature in the presence of constant external magnetic field. In the latter case, the transition temperatures of Ni-Mn-Ga are expected to shift to higher temperatures [39,40]. The third path of phase transition is the isothermal transition. In this case, the temperature is kept constant in the austenitic phase (typically close to the martensitic forward transition temperature) and the phase is transformed by applying external magnetic field. As it was mentioned, the twin variants and boundaries symbolized in **Figure 1.16b**, cover a long rage of nano- to macroscale, coalescing in the form of self-accommodation of X- and Y-type twinning configurations (section 1.3.1).

Sample #2P of chapter 3 was selected for this experiment. The austenitic fraction was measured by analyzing the MFM images via contrast threshold subtraction using the open-source ImageJ program and the values were used to construct the phase transition curves for each of the measured transition paths. Additionally, the isofield magnetic curves over temperature and isothermal magnetic curves vs. magnetic field were measured for the sample as well.

4.4.1 Zerofield phase transition

The results of the zerofield martensitic phase transition is provided in **Figure 4.12**, which consists of the MFM images over cooling and heating (**Figure 4.12a-f**), the phase transition curves deduced from the MFM images and, finally, the phase transition curves measured for the entire sample by SQUID magnetometer in the presence of 2 mT magnetic field along [100] MgO.

Figure 4.12a shows the magnetic stray field of the material, detected by the MFM imaging technique at 320 K, which evidently is the starting point of the forward phase transition (M_F). At this temperature, the major part of the scanned area (20×20 μm) is in the austenitic phase (labeled as A). There exist only a few tiny needle-shape bright contrasts along the [010] MgO, i.e., Y-type twin boundaries, some of them are labeled. The reason why the formation of Y-type twin boundaries with in-plane magnetization is detectable in the MFM images could be due to the fact that Y-type boundaries are surrounded by the austenitic phase having different magnetic properties. This could give rise to the observed slightly brighter contrast for Y-type. We also considered two scratches shown in the image as a reference in order to spot the same area for all the scans. All the images were taken in the same area. We assume that the presence of the reference scratches does not dominate the

transition characteristics of the whole scanned window due to the reduced mechanical coupling of different regions of the material in thin films compared to the bulk.

As the temperature is reduced to 318 K in **Figure 4.12b**, more Y-type twins nucleate and grow along [010] MgO. In addition to Y-type at 318K, a few contrasts appear in the image, elongated along [$1\bar{1}0$] MgO. They are related to X-type twin boundaries; one of them is labeled in **Figure 4.12b**. Further reducing the temperature, further nucleation, growth and coalescence of the Y-type and X-type twin boundaries occurs and, as can be observed in **Figure 4.12c**, the austenitic phase is limited to small windows. At 300 K, the material is fully martensitic (**Figure 4.12d**). X-type twin boundaries with the typical alternation of out-of-plane magnetic stray field contrasts can be observed, together with Y-type twin boundaries, giving rise to the background contrast. The vertical out-of-plane contrasts elongated along [010] MgO are small colonies of X-type twin boundaries, forming at the last stages of the transition, filling the gap between Y-type twins. There are also a few tiny dark contrasts elongated along [100] MgO inside the background contrast (Y-type). These are possibly tiny X-type twins entering Y-type colonies (section 3.4, **Figure 3.11**). As the film is heated up to 322 K, the reverse phase transition (M_R) takes place: the martensitic phase gradually annihilates. The annihilation can be realized in **Figure 4.12e** by the appearance of tiny contrasts along [100] MgO and [010] MgO inside the area attributed to Y-type twin boundaries. The small colonies of X-type also annihilate in the initial stages of the reverse transition. Unlike the M_F and the initial stages of the M_R, where the evolution of Y-type is evidently prior to the evolution of X-type, in the late stages of the M_R the both the martensitic configurations annihilate equally as highlighted in **Figure 4.12f**. The complete in situ MFM imaging including 27 images, showing the evolution of twin boundaries through the cooling- heating cycle is provided in the end of the chapter as **Figure 4.15**.

Figure 4.12g shows the martensitic transition curves, constructed from the in situ MFM imaging showing the martensitic transition temperature (T_M) in M_F, austenitic transition temperature (T_A) in M_R and the thermal hysteresis (Hyst.), i.e., the temperature gap between the T_M and T_A curves. The curves were constructed by measuring the austenitic fraction of the scanned area vs. temperature (grey line). The evolution of twin boundaries vs. temperature were also determined for the X-type (blue curves) and Y-type (red curves), separately, and fitted into the grey curves for comparison. Therefore, a brief look can show us the contribution of each of the martensitic configurations (X and Y) in different stages of the martensitic transition. Evidently, as it was also detectable in the MFM images (**Figure 4.12a-f**), in M_F, the Y-type twin boundaries nucleate sooner and grow in a shorter temperature range compared to X-type, while in M_R, Y-type twin boundaries start to annihilate sooner in the initial stages of the reverse transition. In the late stages of the reverse transition however, both configurations annihilate equally. This behavior can be also observed from the measured values of the critical transition temperatures and the hysteresis, shown in the figure. The T_M for the X-type was measured to be 318 K, while this value for Y-type was measured as 316 K. The Hyst. was also measured to be 7 K for Y-type and 9 K for X-type. The T_A for X-type though, was measured to be equal to Y-type (325 K).

In order to confirm the transition temperatures measured via the in situ MFM imaging, we also measured the magnetization curves vs. temperature of the sample in the presence of $\mu_0 = 2$ mT along [100] MgO **Figure 4.12f**. The forward and reverse transitions are labeled in the figure. The critical temperatures were measured using inflection method; the following symbols are assigned to the critical temperatures: star to T_M, square to T_A and triangle to the Cure temperature ($T_C = 340$ K). The

martensitic transition temperatures are in full agreement with the values measured in the constructed curves (**Figure 4.12g**).

We showed that the nucleation of Y-type twin boundaries occurs prior to X-type over the martensitic transition, which is impressive, unique and evidently is the most prominent effect for all the investigated three paths of the transition (the other two paths are reported below). This discrepancy can be explained through two possible scenarios:

The first explanation highlights the effect of compressive strain in stabilizing the martensitic phase of the Y-type configuration. It has been reported that in the same growth condition, 75-nm-thick epitaxial Ni-Mn-Ga films, grown on 50 nm Cr under-layer/(001) MgO substrate typically transform to the martensitic phase forming Y-type configuration. In contrast, the same films, directly grown on (001) MgO transform to the martensitic phase forming X-type configuration. The lattice mismatch between Ni-Mn-Ga austenitic cell and Cr cell gives rise to a biaxial compressive misfit strain of around 1%. While the lattice mismatch between Ni-Mn-Ga austenitic cell and MgO cell gives rise to a biaxial tensile misfit strain of around 2.2% [41]. Therefore, Y-type and X-type could be respectively considered as indicators for bi-axial in-plane compressive as well as tensile stress in epitaxial Ni-Mn-Ga films. According to thermodynamic equilibrium of the elastic domains in epitaxial layers [42,43], in the competition between substrate/film misfit strain as well as the martensitic interface strain, thickness of the film plays a crucial role. For thin films having low thicknesses, the major contribution to the total energy of the system comes from the substrate/film misfit strain. However, when the film exceeds a critical thickness (experimentally evaluated for epitaxial Ni-Mn-Ga thin films on (001) MgO to be in between 75-100 nm [41]), the contribution of the martensitic interface becomes significant and the evaluation of different sources of strain contributions to the total energy of the system becomes more complex. For thick films, the system may reach an equilibrium by an inhomogeneous distribution of compressive and tensile strain in the specimen, choosing all the possible elastic domain orientations as in the case of our 200-nm Ni-Mn-Ga film, keeping Y-type and X-type as indicators for bi-axial in-plane compressive as well as tensile stress, respectively. In addition, martensitic transition in Ni-Mn-Ga results in a negative change of the cell-volumes therefore; a compressive stress is typically expected to stabilize the martensitic phase by shifting the transition to higher temperatures [44]. Hence, the Y-type martensitic configuration nucleates prior to X-type, since the Y-type region is under compressive strain.

The second scenario highlights a possibility of lower nucleation energy barrier for Y-type configurations. Looking at the theory of the elastic equilibrium for epitaxial films, formation of elastic domains is energetically required to compensate the elastic strain caused by the symmetry reduction during the martensitic phase transition and to minimize the total energy of the system [42,43]. There are a number of terms and variables contributing to the elastic equilibrium of the system for choosing the twinning planes in the martensitic phase. In the multidomain case, where both the configurations of the martensitic phase (X and Y) are energetically permitted, as reported in this study, the formation of the twin boundaries along the {110} planes of the cubic parent phase, which are normal to the substrate is probably less energy costly than the {110} planes which are 45º inclined to the substrate. Nevertheless, inclusive theoretical studies are required to confirm and quantify these formation energies.

In addition to the nucleation, it was evidenced that the Y-type twin boundaries grow larger and in a shorter range of temperature (i.e. sharper growth) with respect to the X-type twin boundaries. To explain this, we refer to the diamond model of the X and Y-type twin boundaries [14]. According to this model, X and Y configurations nucleate and grow in the form of 3D parallelograms (i.e. deformed diamonds) having their midribs as the twin boundaries, i.e., short, medium and long midribs of the 3D structure. For Y-type twins, the position of the 3D parallelogram is such that the medium midrib

is placed across the thickness of the film and the other two midribs lie in the plane of the film, while for X-type, the long midrib is placed across the thickness of the film and the other two midribs lie approximately in the plane of the film. In other words, upon the nucleation, Y-type diamonds can grow much larger before they reach the substrate. The substrate can be considered among the obstacles hindering the growth of the 3D parallelograms. For the X-type however, the 3D parallelograms touch the substrate sooner through their long midrib. Since the substrate represents an obstacle, in order to transform the same volume of the material, relatively more nuclei are required in X-type compared to Y-type. Nucleation of new twin boundaries is energy costly mainly due to the increase in interface energy. This energy can be compensated through further under cooling. The gap between X and Y transition temperature is mainly observable in M_F.

It was also observed that throughout the cooling, the small colonies of the X-type twin boundaries (one of them is highlighted in **Figure 4.12e**), appear in between the Y-type twin boundaries at the last stages of the forward transition. Over the reverse transition, however, they annihilate at the early stages. This can be explained by the effect of the stored elastic energy [27] (section 4.2.3). The same scenario is expected to be the case for the tiny line contrasts along [100] MgO and [010] MgO (one of them is highlighted in **Figure 4.12e**). Although the resolution of images does not allow us to conclude, we expect that these lines are the positions of the martensitic Y-Y and X-Y interfaces (**Figure 4.1d**). They transform at the last stages of M_F to the martensitic phase and transform back the austenitic phase at the initial stages of M_R (section 4.2.3).

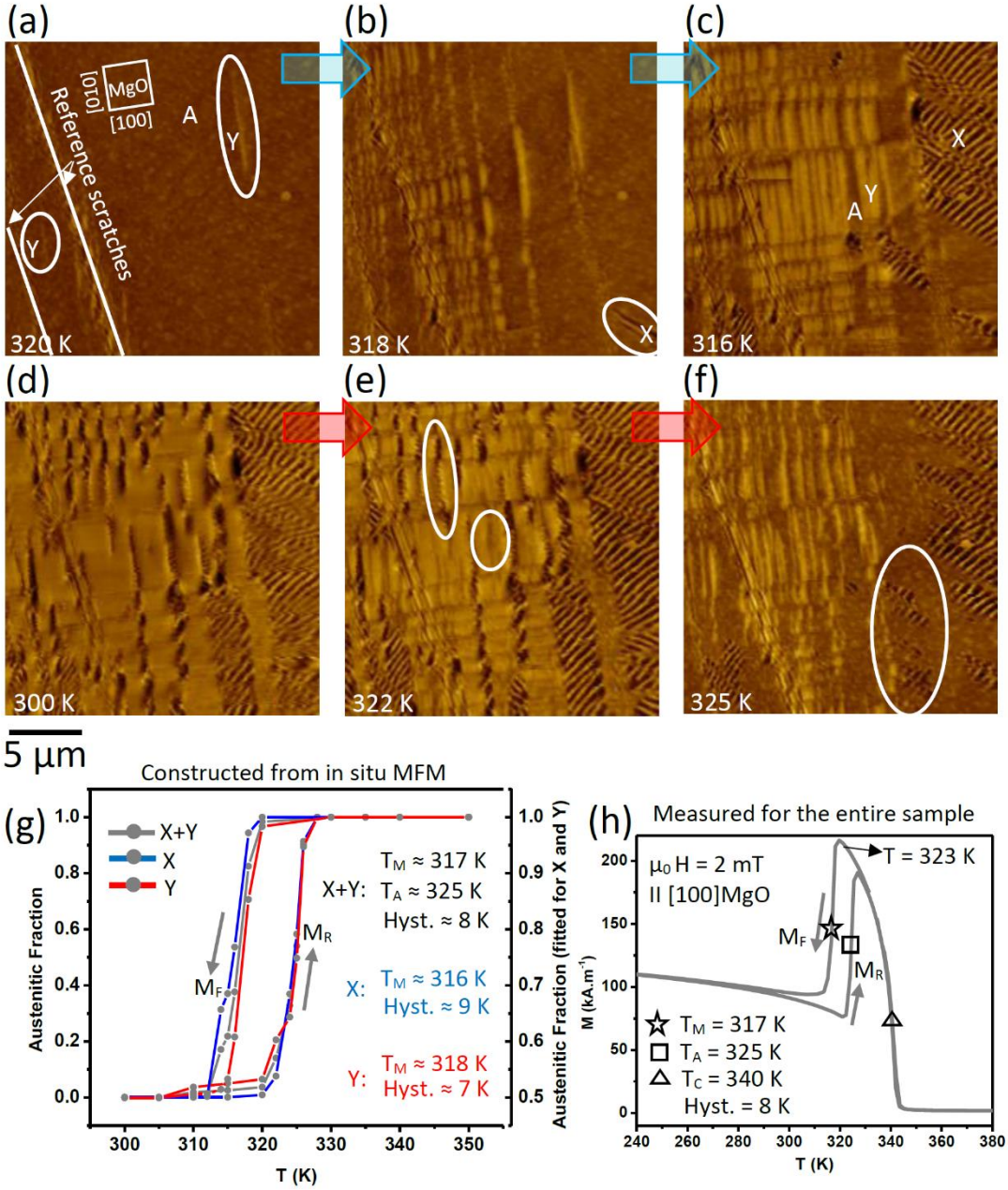

Figure 4.12: Zerofield phase transition: a-f) in situ magnetic force microscopy (MFM) images captured on cooling (a-c) and on heating (d-f), showing the formation, coalescence and annihilation of the X- and Y-type twin boundaries; the position of the reference scratch is highlighted. Direction of the MgO substrate as a reference and the temperatures, at which the images were captured are reported. Some of the X- and Y-type regions as well as the austenitic areas (A) are also highlighted. g) the hysteresis curves of the phase transition constructed from the MFM images, showing the martensitic forward (M_F) and reverse (M_R) transitions separately for X-type (blue lines), Y-type (red lines) and the sum of X and Y (total transition, grey line)), the related critical temperatures and the hysteresis of each are also reported. h) isofield ($\mu_0 H = 2$ mT along [100] MgO) magnetization curve as a function of temperature measured for the same sample, the martensitic transition temperature (T_M), austenitic transition temperature (T_A), Curie temperature (T_c) and the thermal hysteresis are reported. The transition temperatures were obtained using the inflection method.

4.4.2 Isofield phase transition

The results of the isofield martensitic phase transition are provided in **Figure 4.13**. The figure consists of the MFM images over cooling in the presence of 0.8 T magnetic field along [001] MgO (**Figure 4.13a-c**), the phase transition curves constructed from the MFM images (**Figure 4.13d,e**) and the magnetization curves vs. temperature in the presence of 0.1 T, 0.8 T and 14 T magnetic field along [001] MgO.

Figure 4.13a illustrates the starting point of the martensitic transition, showing the nucleation of the Y-type twin boundaries in the austenitic matrix; some of them are highlighted. By decreasing the temperature to 318 K (**Figure 4.13b**), X-type twin boundaries also appear, while Y-type twin boundaries continue to nucleate and grow. Cooling to 316 K (**Figure 4.13c**) turns the austenitic matrix to small windows, which finally transforms to the martensitic phase upon further cooling. The complete in situ MFM imaging including 14 images, showing the evolution of twin boundaries through the isofield cooling is provided in the end of the chapter as **Figure 4.16**.

Figure 4.13d,e were constructed from the in situ imaging, comparing the forward transition curves of the zerofield (in grey) and isofield (in pink). Looking at **Figure 4.13d**, it is clear that cooling the film in the presence of 0.8 T magnetic field along [001] MgO mostly affects the initial stages of the phase transition, i.e. the nucleation step. The shift of the curve in the nucleation step is ~2 K. However, following the growth step, the curve almost merges with the zerofield curve. In order to compare the contribution of X-type and Y-type twin boundaries to the observed shift, we constructed the transition curves of X (in blue) and Y (in red) configurations separately in zerofield (solid grey circle) and isofield (solid pink square) paths. Evidentially, most of the contribution to the applied magnetic field upon cooling is attributed to Y-type twin boundaries, which is observable by the gap between the two red curves in **Figure 4.13e**. To compare the above results to the behavior of the entire sample, the magnetization curves were measured vs. temperature in the presence of 0.1 T, 0.8 T and 14 T magnetic field along [001] MgO (**Figure 4.13f**). The T_M are highlighted in the figure. It shows a shift of ~0.5 K per Tesla. Further prove of the measured value of the shift of the transition in the presence of the applied magnetic field is provided by the isothermal phase transition curves.

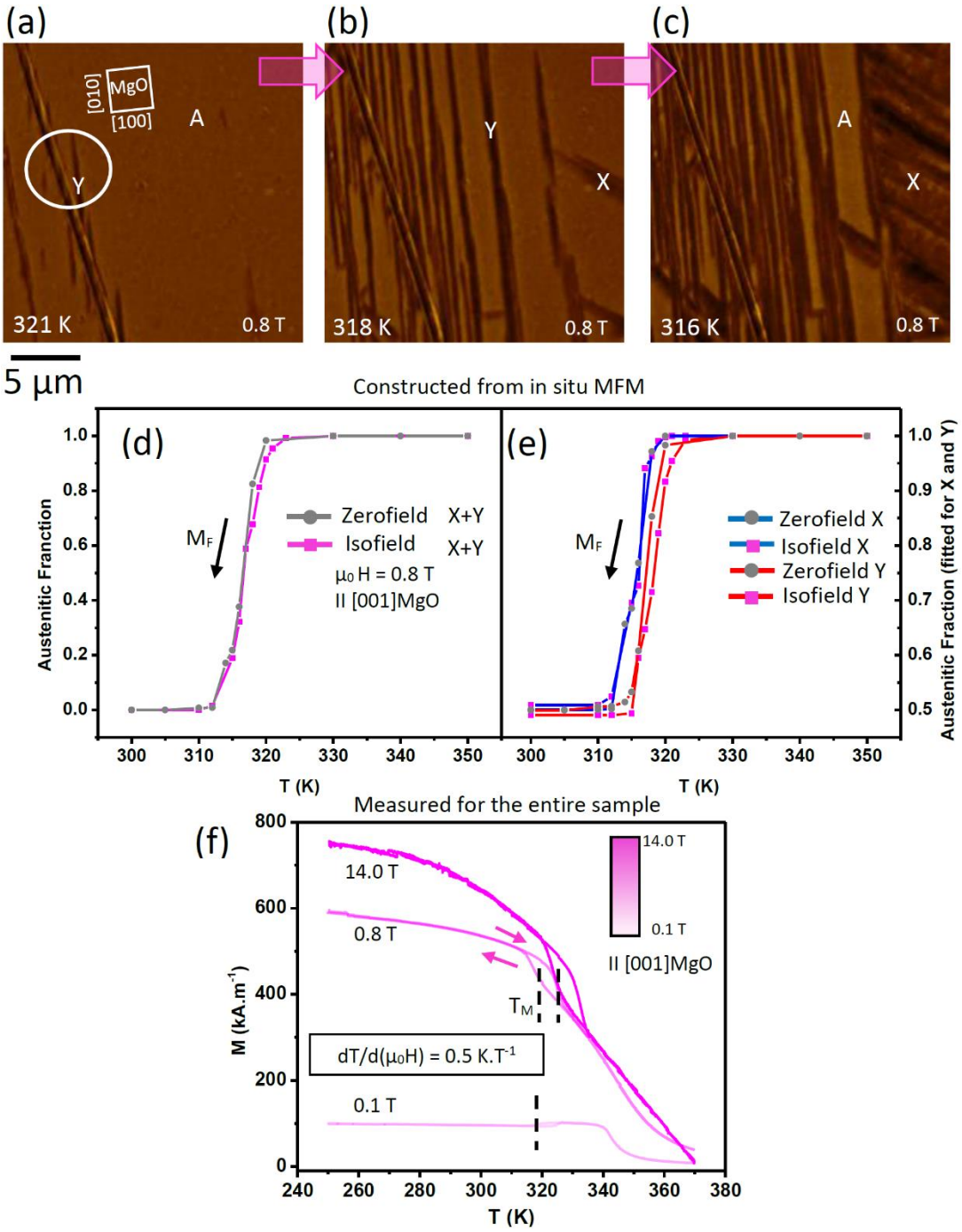

Figure 4.13: Isofield phase transition: a-c) in situ MFM images captured upon cooling in the presence of $\mu_0 H = 0.8$ T || [001] MgO, showing the formation and coalescence of the X- and Y-type twin boundaries, direction of the MgO substrate as a reference and temperatures at which the images were captured are reported. Some of the X- and Y-type regions as well as the austenitic areas (A) are highlighted as well. d) the phase transition curves constructed from the MFM images, showing the M_F for the X+Y (total transition) in the zerofield (grey) and isofield (pink). e) the hysteresis curves of the phase transition constructed from the MFM images separately for X-type (blue lines) and Y-type (red lines) in zerofield (grey circle) and isofield (pink squares). f) The isofield magnetization curves as a function of temperature measured for the same sample in $\mu_0 H = 0.1$ T, 0.8 T and 14.0 T along [001] MgO, the shift of the T_M vs. the applied magnetic field is highlighted.

4.4.3 Isothermal phase transition

In **Figure 4.14** we illustrate the isothermal phase transition at 323 K. As it was labeled in **Figure 4.12h** this temperature is close enough to the temperature, where the martensitic transition starts, therefore it could maximize the martensitic phase induced by the external magnetic field that we could provide (i.e. 14 T). Beyond that, the film is in the austenitic phase at this temperature, so that we could properly study the nucleation of each of the martensitic configurations in the magnetic field induced phase transition. **Figure 4.14a** shows the status of the film in the presence of 1 T; evidently, the tiny Y-type twin boundaries have started to nucleate; two of them are labeled. By increasing the magnetic field up to 7 T (**Figure 4.14b**), X-type twins also appear (labeled in the figure), while Y-type twins continue to nucleate and grow. The status of the film at 14 T is represented **Figure 4.14c**. It still shows the coexistence of phases; X-type twin areas, Y-type twin areas and the austenitic phase can be detected. This result can be interpreted if we consider a shift of the martensitic temperature of 0.5K/T, measured and shown in **Figure 4.13f**; this can be visualized by comparing **Figure 4.12c** and **Figure 4.14c**. The complete in situ MFM imaging including 20 images, showing the evolution of twin boundaries through the isothermal phase transition at 323 K is provided in the end of the chapter as **Figure 4.17**.

Figure 4.14d,**e** were constructed from the in situ imaging. It is clear that there is a kind of avalanche in the transition starting from 6 T. In order to compare the contribution of X-type and Y-type twin boundaries to the observed avalanche, we constructed the transition curves related to X (in blue) and Y (in red) separately, shown in **Figure 4.14e**. Evidentially, most of the contribution to the avalanche upon isothermal phase transition is attributed to Y-type twin boundaries. To compare the above results to the behavior of the entire sample, the magnetization of the sample was measured vs. applied magnetic field along [001] MgO at 323 K (**Figure 4.14f,g**). **Figure 4.14g** corresponds to the part of **Figure 4.14f**, selected by the rectangle. The curve related to the increasing $\mu_0 H$ shows a kink in the magnetization around 6.5 T (labeled by arrow). After this kink, upon further increasing the applied magnetic field, the curve shows only small fluctuation. By reducing the magnetic field however, no sudden drop of the magnetization is observed. Instead, the magnetization decreases gradually, causing the magnetic hysteresis between the two magnetization curves, as it is detectable in the figure.

As it was schematically shown in **Figure 1.16b**, the martensitic transition induced by external magnetic field crosses the phase borders, transforming the material from austenitic phase to the martensitic phase upon increasing the external magnetic field at a fixed temperature. Upon switching off the magnetic field, the material is ideally expected to regain it's thermodynamically zerofield stable state at 323 K, which is the fixed temperature in our experiment (**Figure 4.15** images 21,22 and **Figure 4.17** image 1). None of these imagines matches the obtained sate of the sample upon removing the external field, shown in **Figure 4.17** image 20. Comparing the latter image to the MFM image taken in the presence of 14 T of external magnetic field (**Figure 4.17** image 19) confirms that the material is in the field-induced state even after removing the external field. In other words, the material shown in **Figure 4.**17 image 20 presents a metastable state, which could arise from the nature of transitional behavior for the materials undergoing first order phase transition. This phenomenon is further supported by the absence of jump in the magnetization curve measured for reducing $\mu_0 H$ represented in **Figure 4.14g**. While it deserves further experimental investigations, this finding suggests the presence of metastability phenomenon for the martensitic phase transition induced by

magnetic field in Heusler compounds, which needs to be taken into account specifically for the applications requiring cyclic phase transition induced by magnetic field.

In the isothermal phase transition, in consistence with the other two transition paths discussed above, Y-type twin boundaries evidently contribute more, i.e., the position of the kink shown in **Figure 4.14g** is coherent with the positon of the avalanche$_{start}$ shown in **Figure 4.14d** and both are consistent with the position of the avalanche$_{start}$ highlighted for Y-type shown in **Figure 4.14e**.

It is also worth mentioning that, upon all the above-investigated paths of phase transition, the ratio between the area occupied by X-type twins and the area occupied by Y-type twins were measured to be around 1 in the scanned area. It was also measured that over the above-mentioned transition paths, X and Y typically occupy the same regions of the scanned area, therefore no variant selection was observed in the presence of the applied magnetic field.

For magnetic shape memory Heuslers, the recently reported avalanche criticality for the formation of twinning structures, promotes the concept of variant selection for a phase transition in the presence of an external stimuli [45,46]. It has been also evidenced in the literature that the martensitic transition in the presence of external magnetic field, could give rise to the selection of variants, or tuning the sequence of the transition by favoring the nucleation of some of the twin variants rather than the others [29]. Specifically, a considerable increase in the portion of the Y-type twin boundaries for 200 nm Ni-Mn-Ga films cooled down from the austenitic phase to the martensitic phase in the presence of an applied magnetic field of $\mu_0 H = 0.5$ T along [100] MgO and [010] MgO has been reported in Chapter 3.3. In the case of our film in this study however, throughout the three paths of the phase transition, the portion of the X and Y in the scanned area was almost stable. This could be due to the fact that in this study we have applied the magnetic field out of plane of the film ($\mu_0 H$ along [001] MgO). It is well known that magnetostatic energy in thin films favors in-plane magnetization orientation; this term in the magnetic energy of the system depends on the direction of the external field, opposes to the Zeeman term if the field is applied perpendicular to the film surface. Furthermore, in Ni-Mn-Ga films the balance between elastic, magnetic and magnetoelastic energy terms is complex and it deserves detailed theoretical studies and thermo/magnetomechanical simulations.

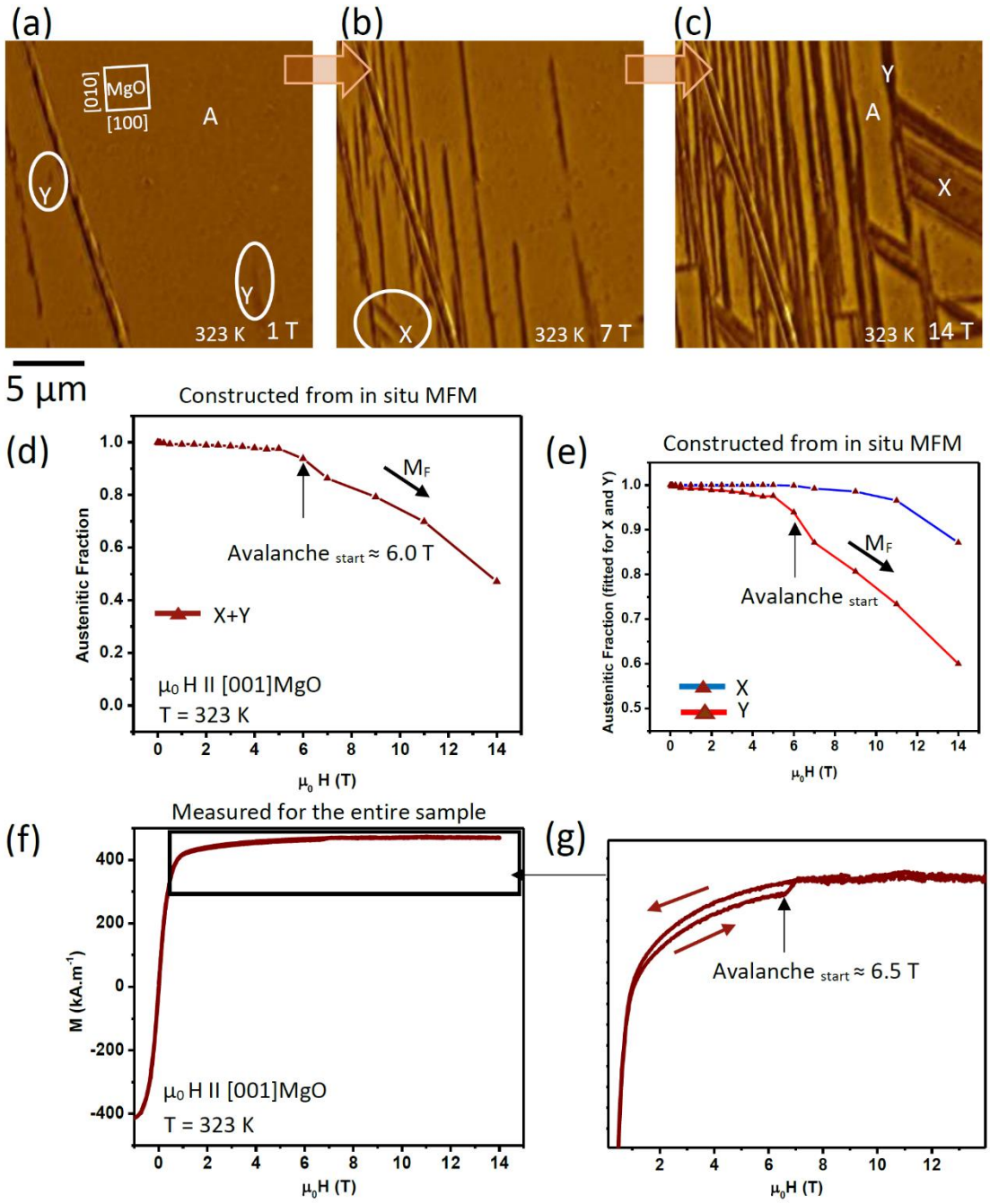

Figure 4.14: Isothermal phase transition: a-c) in situ MFM images captured upon applying $\mu_0 H$ = 0.0-14.0 T || [001] MgO at 323 K, showing the formation and coalescence of the X- and Y-type twin boundaries; direction of the MgO substrate as a reference, temperatures at which the images were captured and some of the X- and Y-type regions as well as the austenitic areas (A) are highlighted and reported; c) Phase transition curve constructed from the MFM images, showing the M_F for the X+Y (total transition) in brown, the starting point of the avalanche of the transition is highlighted; e) the hysteresis curves of the phase transition constructed from the MFM images separately for X-type (blue lines) and Y-type (red lines); f) the magnetization curve of the sample measured by applying $\mu_0 H$ = -1.0 to 14.0 T along [001] MgO at 323 K, g) magnified representation of the marked area in (f) showing the hysteric magnetization forward and reverse curves depicted for the phase transition induced by the applied magnetic field, the kink related to the starting point of the avalanche of the transition is highlighted.

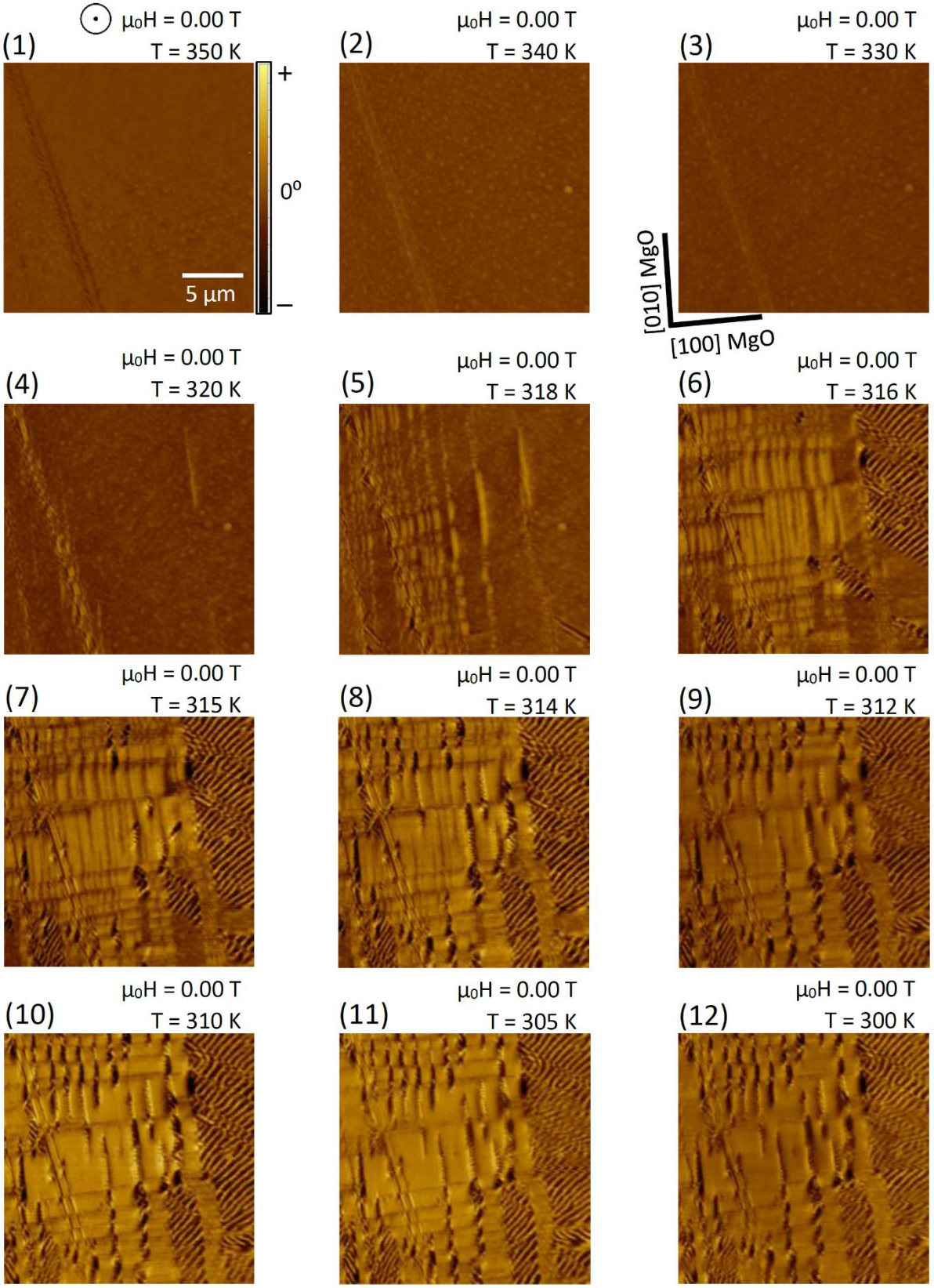
(1)
μ₀H = 0.00 T
T = 350 K
+
0°
–
5 μm
(2)
μ₀H = 0.00 T
T = 340 K
(3)
μ₀H = 0.00 T
T = 330 K
[010] MgO
[100] MgO
(4)
μ₀H = 0.00 T
T = 320 K
(5)
μ₀H = 0.00 T
T = 318 K
(6)
μ₀H = 0.00 T
T = 316 K
(7)
μ₀H = 0.00 T
T = 315 K
(8)
μ₀H = 0.00 T
T = 314 K
(9)
μ₀H = 0.00 T
T = 312 K
(10)
μ₀H = 0.00 T
T = 310 K
(11)
μ₀H = 0.00 T
T = 305 K
(12)
μ₀H = 0.00 T
T = 300 K

(13) $\mu_0 H$ = 0.00 T, T = 280 K

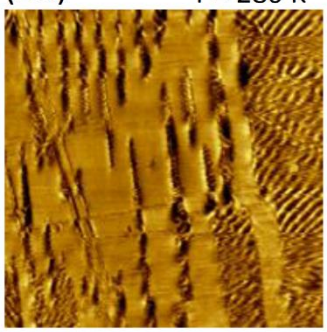

(14) $\mu_0 H$ = 0.00 T, T = 260 K

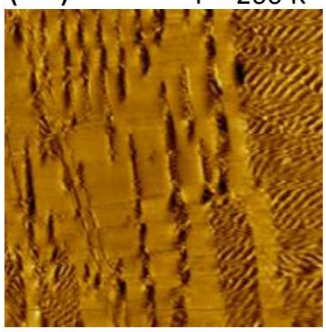

(15) $\mu_0 H$ = 0.00 T, T = 280 K

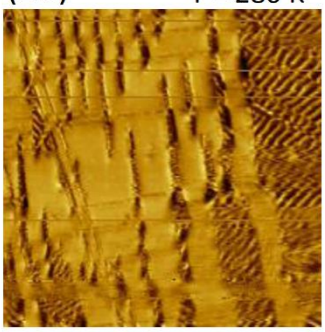

(16) $\mu_0 H$ = 0.00 T, T = 300 K

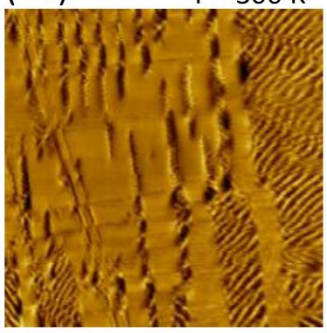

(17) $\mu_0 H$ = 0.00 T, T = 305 K

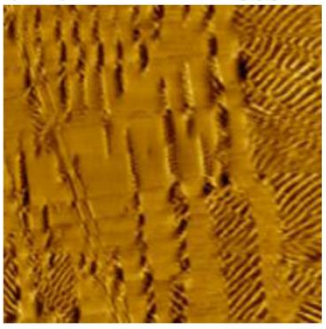

(18) $\mu_0 H$ = 0.00 T, T = 310 K

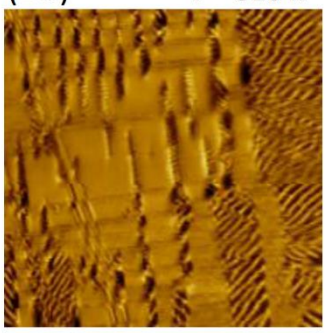

(19) $\mu_0 H$ = 0.00 T, T = 315 K

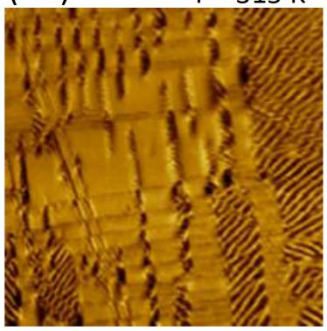

(20) $\mu_0 H$ = 0.00 T, T = 320 K

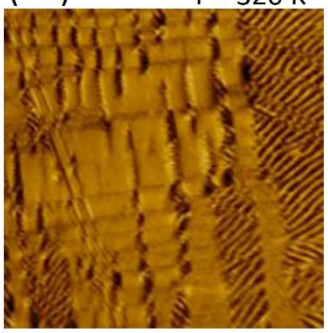

(21) $\mu_0 H$ = 0.00 T, T = 322 K

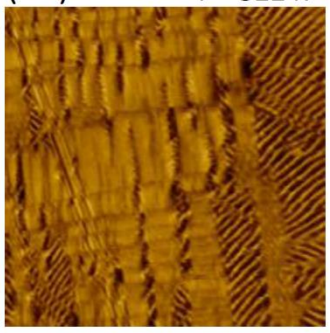

(22) $\mu_0 H$ = 0.00 T, T = 324 K

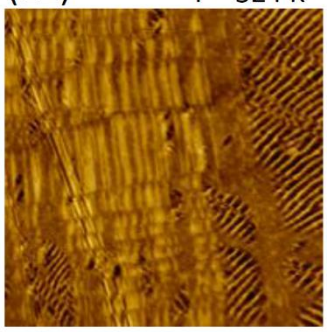

(23) $\mu_0 H$ = 0.00 T, T = 325 K

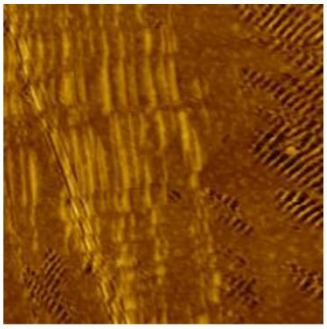

(24) $\mu_0 H$ = 0.00 T, T = 326 K

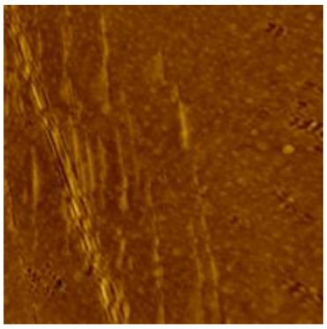

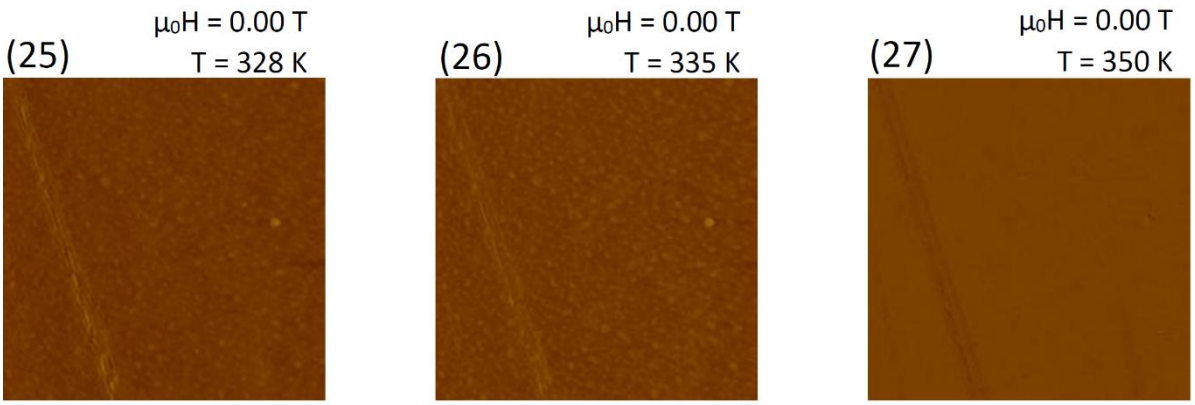

Figure 4.15: In situ MFM imaging for zerofield cooling and heating cycle (27 images).

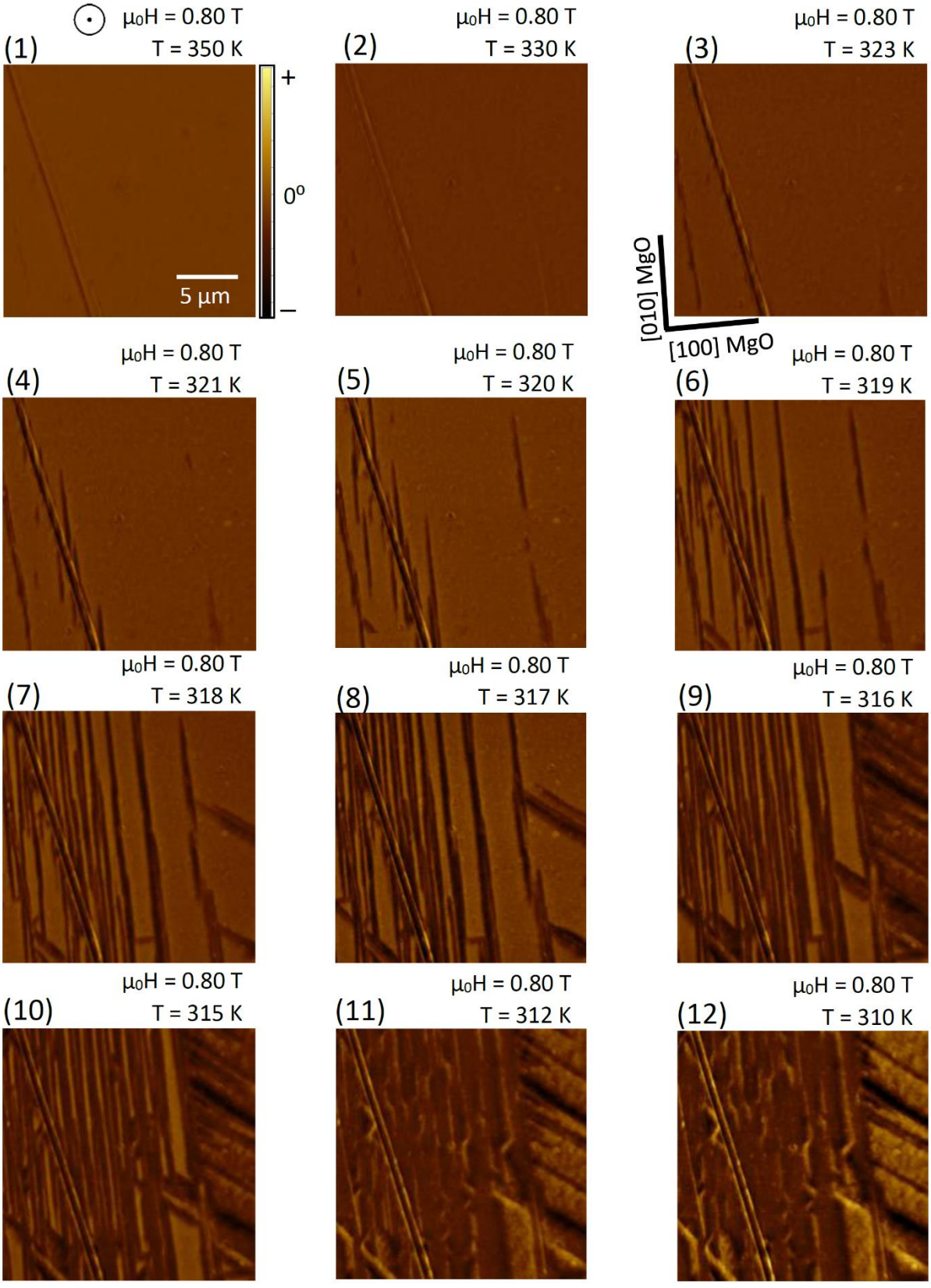
μ0H = 0.80 T
T = 350 K
(1)
+
0°
–
5 μm
μ0H = 0.80 T
T = 330 K
(2)
μ0H = 0.80 T
T = 323 K
(3)
[010] MgO
[100] MgO
μ0H = 0.80 T
T = 321 K
(4)
μ0H = 0.80 T
T = 320 K
(5)
μ0H = 0.80 T
T = 319 K
(6)
μ0H = 0.80 T
T = 318 K
(7)
μ0H = 0.80 T
T = 317 K
(8)
μ0H = 0.80 T
T = 316 K
(9)
μ0H = 0.80 T
T = 315 K
(10)
μ0H = 0.80 T
T = 312 K
(11)
μ0H = 0.80 T
T = 310 K
(12)

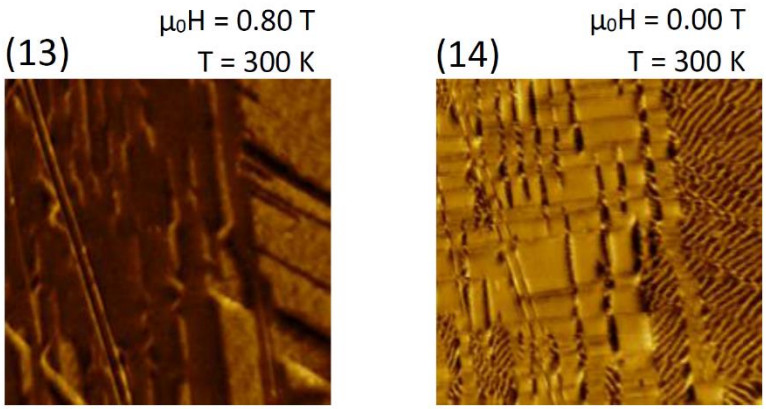

Figure 4.16: In situ MFM imaging for isofield cooling at $\mu_0 H = 0.8$ T perpendicular to the film plane (14 images).

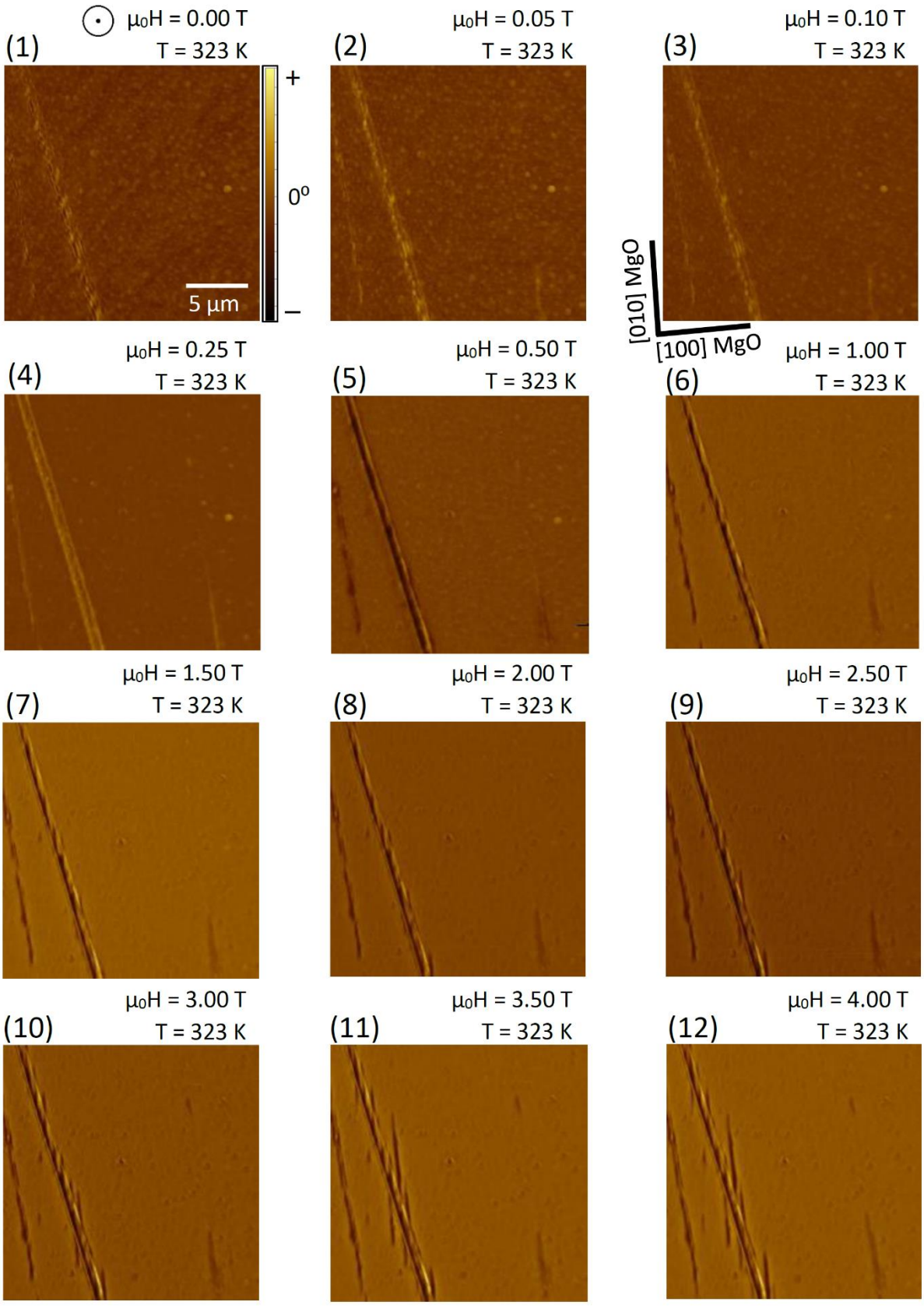
μ₀H = 0.00 T
T = 323 K
(1)
+
0°
–
5 μm
μ₀H = 0.05 T
T = 323 K
(2)
μ₀H = 0.10 T
T = 323 K
(3)
[010] MgO
[100] MgO
μ₀H = 0.25 T
T = 323 K
(4)
μ₀H = 0.50 T
T = 323 K
(5)
μ₀H = 1.00 T
T = 323 K
(6)
μ₀H = 1.50 T
T = 323 K
(7)
μ₀H = 2.00 T
T = 323 K
(8)
μ₀H = 2.50 T
T = 323 K
(9)
μ₀H = 3.00 T
T = 323 K
(10)
μ₀H = 3.50 T
T = 323 K
(11)
μ₀H = 4.00 T
T = 323 K
(12)

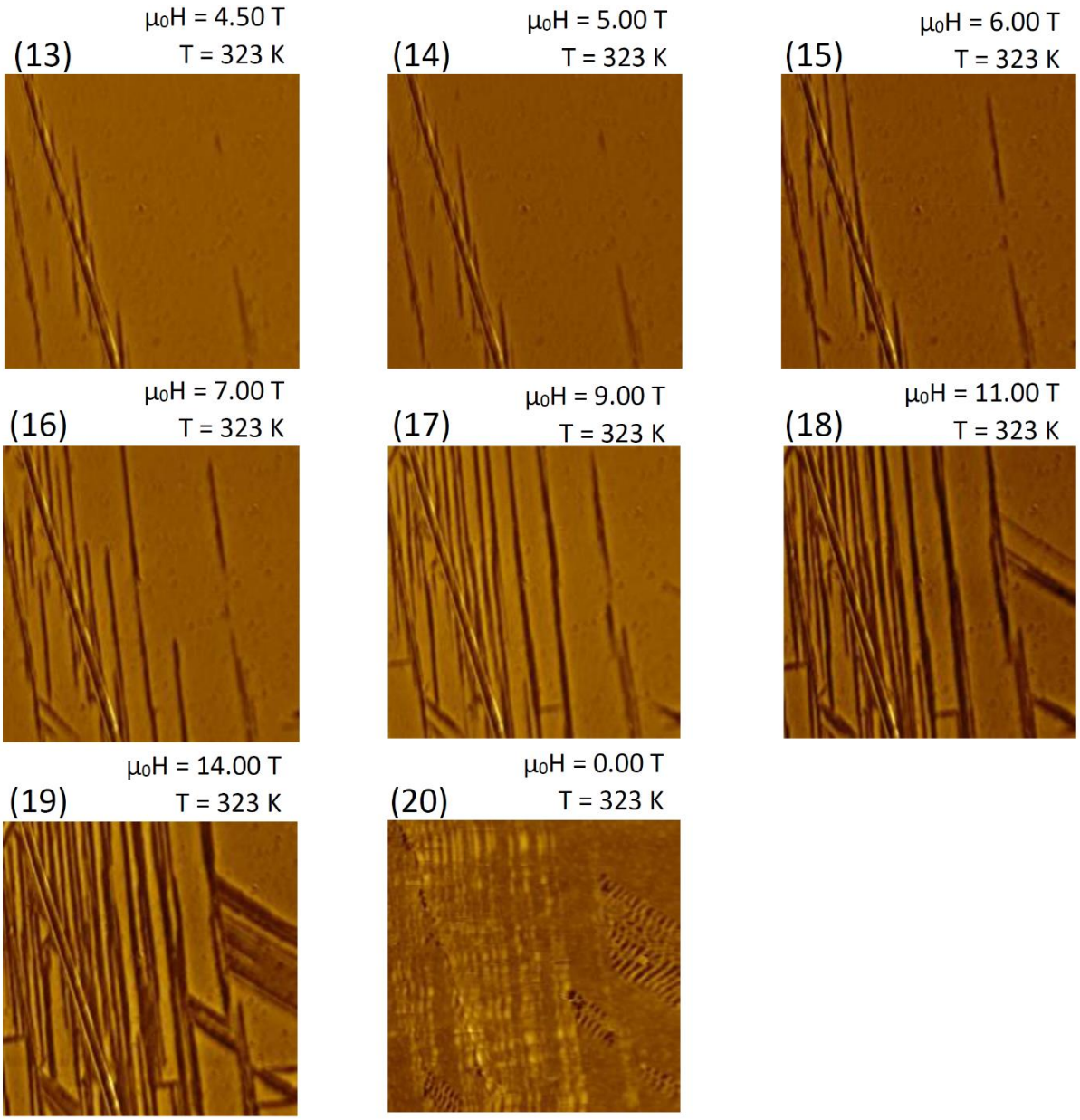

Figure 4.17: In situ MFM imaging for isothermal phase transition at T = 323 K (20 images).

4.5 Conclusions

We investigated the crystallographic relations between the twin boundaries and interfaces in Ni-Mn-Ga epitaxial films from the atomic scale to the microscale and accompanied this investigation with the direct observation of the evolution of the martensitic interfaces vs. temperature. Based on the symmetry relations between the twin variants, we identified the types of twin boundaries and the twinning interfaces, i.e., ridges, valleys, and non-conjugation interfaces. Using the change of modulation direction across the boundary observed by HAAFD and HR-TEM, in Y-type regions we were able to determine the presence of type I, type II, and modulation twin boundaries showing the dominant presence of type II. Beyond these findings, we proposed a transition route for the martensitic configurations, highlighting the major role played by the martensitic interfaces. The

forward transition starts with the heterogeneous formation of twin boundaries at the position of the ridges on the surface of the film and moves towards the substrate. The twin boundaries continue to nucleate and grow until they meet at the other kind of conjugation interfaces, i.e., valleys, or at non-conjugation interfaces, where the growth is hindered. In these regions, the elastic strain energy created during the transition is partially stored. This stored energy serves as the driving force for the reverse transition by initiating the nucleation of the austenitic phase.

We also investigated the influence of the density of the martensitic interfaces on the critical temperatures of the martensitic transition. It was found that the presence of imperfections could serve as the nucleation points, increasing the density of the martensitic interfaces, stored elastic energy and consequently they could give rise to the increase of the transition width. In contrast, the density of the martensitic interfaces as well as the sample roughness shows only a minor effect on the thermal hysteresis of the samples. Nevertheless, by the reduction of the imperfections, annealing plays the paradoxical role of reducing the transition width while increasing the thermal hysteresis.

In the third part of the chapter, the formation of the twin boundaries in Ni-Mn-Ga epitaxial films was investigated in situ in three different conditions, i.e. temperature induced phase transition (zerofield), temperature induced phase transition assisted by a constant external magnetic field (isofield) and the magnetic field induced phase transition in constant temperature (isothermal). The investigations highlight that Y-type twinning gives rise to a relatively sharper transition and lower hysteresis compared to the X-type configuration. Therefore, X and Y-type twins not only show different microstructural and magnetic characteristics, but they also display different characteristic nucleation and growth during the martensitic transition.

In conclusion, this chapter sheds light into the linkage between the martensitic configuration at the different length scales and the martensitic forward and reverse transitions. The results represent a step forward in the understanding of the transition processes and pave the way to the possibility of tuning the characteristics of the transition, e.g., hysteresis and transition width, by martensitic configuration engineering aimed at the full exploitation of martensitic Heuslers in applications requiring cyclic phase transition.

References

1. Müllner, P. & King, A.H. *Acta Mater.* **58**, 5242 (2010).
2. Christian, J.W. & Mahajan, S. *Prog. Mater. Sci.* **39**, 1 (1995).
3. Pitteri, M. & Zanzotto, G. Continuum Models for Phase Transitions and Twinning in Crystals; (CRC: Boca Raton, FL, USA, 2003).
4. Schwabe, S. et al. arXiv preprint arXiv:2004.09768, https://arxiv.org/abs/2004.09768 (Accessed: April 21, 2020).
5. Gutfleisch, O *et al. Philos. T. R. Soc. A* **374**, 20150308 (2016).
6. Cugini, F. *et al. Philos. T. R. Soc. A* **374**, 20150306 (2016).
7. Müllner, P. *Acta Mater.* **176**, 211 (2019).
8. Cui, J. *et al. Nature Mater.* **5**, 286 (2006).
9. Gottschall, T. *et al. Acta Mater.* **107**, 1 (2016).
10. Schwabe, S. et al. *Energy Technol.* **6** 1453 (2018).
11. Ranzieri, P. *et al. Acta Mater.* **61**, 263 (2013).

12. Ranzieri, P. *et al. Adv. Mater.* **27**, 4760 (2015).
13. Yang, B. *et al. Acta Mater.* **93**, 205 (2015).
14. Niemann, R. *et al. Acta Mater.* **132**, 327 (2017).
15. Diestel, A. *et al. J. Phys-Condens Mat.* **25**, 266002 (2013).
16. Takhsha Ghahfarokhi, M. *et al. Materials.* **13**, 2103 (2020).
17. Straka, L. *et al. Acta Mater.* **59**, 7450 (2011).
18. Straka, L. *et al. Scripta Mater.* ***67***, 25 (2012).
19. Szczerba, M.J. & R. Chulist. *Acta Mater.* **85**, 67 (2015).
20. Chulist, R. *et al. Int. J. Plasticity* **114**, 63 (2019**)**.
21. Muntifering, B. *et al. Acta Mater.* ***71***, 255 (2014).
22. Khachaturyan, A.G. Theory of structural transformations in solids, Courier Corporation; (Dover Publications INC.: Mineola, USA, 2008).
23. Diestel, A. *et al. Energy Technol.* **6**, 1463 (2018).
24. Orlandi, F. *et al.* Phys. Rev. B, **101**, 094105 (2020).
25. Reinhold, M. *et al. J. Appl. Phys.* **107**, 113501 (2010).
26. Buschbeck, J. *et al. Acta Mater.* **57**, 2516 (2009).
27. Waske, A. *et al. APL Mater.* **4**, 106101 (2016).
28. Wollants, J. *et al. Prog. Mater. Sci.* **37**, 227 (1993**)**.
29. Niemann, R. *et al. Phys. Rev. B* **89**, 214118 (2014).
30. Tong, H.C. & Wayman, C.M. *Acta Metall.* **22**, 887 (1974).
31. Pereira, M.J. *et al. Microsc. Microanal* **22**, 1270 (2016).
32. Fujita, A. *et al. Appl. Phys. Lett.* **102**, 041913 (2013).
33. Thornton, J.A. *Ann. Rev. Mater. Sci.* **7**, 239 (1977).
34. Niemann, R. *et al. APL Mater.* **4**, 064101 (2016).
35. Trassinelli, M. *et al. Appl. Phys. Lett.* 104 081906 (2014).
36. Zhou, N. *et al. Acta Mater.* **58**, 6685 (2010).
37. Basso, V. *et al. Phys. Rev. B* **85**, 014430 (2012).
38. Rao, W.F. *et al. Acta Mater.* **188**, 539 (2020)
39. Chernenko, V.A. *et al. Mater. Trans.* **47**, 635 (2006).
40. Heczko, O. *et al. Appl. Phys. Lett.* **94**, 152513 (2009).
41. Campanini, M. Advanced transmission electron microscopy on nanostructured magnetic materials, Ph.D. dissertation, Università degli Studi di Parma (2015).
42. Roitburd, A.L. *Phys. Status Solidi A* **37**, 329 (1976).
43. Pompe, W. *et al. J. Appl. Phys.* **74**, 6012 (1993).
44. Chernenko, V. A. *et al. Acta Mater.* **53**, 5071 (2005).
45. Planes, A. *et al. J. Alloys Compd.* **577**, S699 (2013).
46. Ludwig, B. *et al. Phys. Rev. B* **80** 144102 (2009).

Chapter 5

Geometry and size effects on the martensitic morphology and critical temperatures of Ni-Mn-Ga micro and nanostructures

5.1 Introduction

As it was extensively discussed in chapter 1, FSMA are a class of smart materials, well promising for being integrated into small-scale thermo/magnetomechanical devices, applicable in automotive, aerospace, biology and robotic fields of application. As a requirement for the applicability, in addition to the compactness and mechanical simplicity, it is crucial for the material to maintain its properties at small scales.

For around two decades, there have been a number of attempts for downscaling FSMA in the forms of powders, foils, ribbons, pillars, microwires, bridges, cantilevers and recently nanodisks (section 1.3), each of which introducing a method of fabrication and investigating particular aspects of the FSMA. However, the knowledge about the material properties, e.g., martensitic phase transition, critical temperatures and martensitic morphology as a function of size is still limited [1]. The complexity of the crystal structure, martensitic configuration, magnetic order and the dependence of the material characteristics onto several intrinsic and extrinsic parameters together with the complexity coming from the fabrication and the characterization sides, make the evaluation of the effect of size in FSMA a quite demanding task (section 1.3.3). Therefore, there are only few systematic investigations on the effects of the lateral confinement on the properties of FSMA [2-4]. The lack of extensive literature urges for further comprehensive investigations.

Considering the above-mentioned complexities, micro and nanofabricated epitaxial thin films can be considered the most homogenous platforms and the best candidate for such exploration. They enable not only the exploration of the characteristics of FSMA as a function of lateral size but also as a function of geometrical parameters, i.e., shape and orientation.

In this chapter, epitaxially grown Ni-Mn-Ga films (thickness = 200 nm for microfabrication and thickness = 75 nm for nanofabrication) were grown on (001) MgO following the conditions reported in **Table 2.1**. The films are used as a homogeneous platform to investigate the effects of lateral dimension, shape and geometry on the properties of FSMA. For this purpose, micro and nanostructures were fabricated using lithography technology:

First, arrays of microstructures with the lateral size of 3 μm 100 μm, having different shapes as well as various orientations with respect to the substrate edges are investigated. The stability of the material's properties is highlighted by reporting minor changes for the critical martensitic transition temperatures of the microstructures, scaled down to 3 μm. Notably, the shape and geometry of the

lithography-fabricated microstructures are reported to be as a tool to control the martensitic configuration. Combining the direct morphological characterizations and the direct observation of the critical transition temperatures sheds light into the links between the lateral size, geometry (i.e. shape and orientation), martensitic configuration and the martensitic transition of FSMA.

Second, arrays of nanostructures with the lateral size of 150 nm 800 nm, having different shapes as well as various orientations with respect to the substrate edges are investigated. Broadening of the martensitic transition as well as the shift of the transition to higher temperatures are highlighted as the major effect of lateral size reduction for the nanostripes, scaled down to 350 nm. Thermal hysteresis of the material shows a gradual decrease as a function of the lateral size. Similar to microstructures, the geometry of the lithography-fabricated nanostructures is found to be as efficient tool to control the martensitic configuration.

5.2 Continuous films

5.2.1 Ni-Mn-Ga films (200 nm of thickness)

Figure 5.1a shows the polarized light image of the sample at room temperature (RT). The bright and dark contrasts are referred to colonies of the X-type twin boundaries, which typically elongate along [110] MgO and [1$\bar{1}$0] MgO, schematically shown in the right side of the image (section 1.3.1). Since the twin boundaries having these two orientations interact differently with the polarized light, they appear in two different contrasts (section 2.3.1). The composition of the sample was measured as $Ni_{52.9}$-$Mn_{21.6}$-$Ga_{25.5}$ (uncertainty = 1 at. %).
In **Figure 5.1c**, we show a high-resolution back scattered electron (BSE) image of the selected region in **Figure 5.1a**. Inside the image, the X-type twin boundaries are shown as well as the corresponding inclined {110} cubic austenitic planes to each of the orientations of the twin boundaries (section 1.3.1). The width of the X-type twin variants in our films are in the nanometric range (≈ 10-30 nm). The regions where the twin boundaries along [110] MgO (in blue) and [1$\bar{1}$0] MgO (in yellow) intersect are known as non-conjugation interfaces (in green dash line, details can be found in section 4.2.1). The nucleation energy of the X-type twin boundaries along [110] MgO and [1$\bar{1}$0] MgO are typically equivalent for the continuous films, resulting in their equal distribution, forming a basket-like morphology (**Figure 5.1a**).

The magnetic characteristics of the microstructures at room temperature is provided by the MFM image shown in **Figure 5.1d**. It shows the typical out-of-plane magnetization for the X-type configuration showing alternating dark and bright stripe domains, due to magnetization components oriented perpendicularly to the film plane as typically observed for the X-type configuration. The stripe domains are approximately orthogonal to the X-type twin boundaries [5,6].

The isofield magnetization curves vs. temperature (**Figure 5.1b**) give us an overview of the phase transition of the film. As typically expected, upon cooling (blue curve), the sample crosses the Curie temperature (T_C) at 342.0 K, a sudden jump is observed in the magnetization as the material transforms to the ferromagnetic state, however the magnetization drops subsequently at 323.0 K as it reaches the forward martensitic transition temperature (T_M). For the heating curve (red curve), the material transforms back to the austenitic phase at 328.6 K (T_A) by another jump in the magnetization and a subsequent drop as it transforms to the paramagnetic phase (T_C). The critical temperatures are labeled by vertical lines. The thermal hysteresis (T gap between the T_M and T_A), is 5.6 K. Basic information about the phase transition can be found in section 1.2.4.

The epitaxial crystallographic relations between the MgO substrate and Ni-Mn-Ga cells were determined by X-ray reciprocal space mapping (RSM) as (001)[100]Ni-Mn-Ga//(001)[110]MgO. The crystallographic coordinates describing the martensitic cell are shown in **Figure 5.2d**. It represents the monoclinic cell in the standard martensitic setting (dark red) and the austenitic setting (black) with respect to the MgO substrate. The martensitic cells will be described only in the austenitic setting (i.e. a, b and c, c is the shortest axis and the magnetization easy axis) for the sake of simplicity and coherency of the description (section 1.2.1).

The microstructure of the film at room temperature presents a mixture of martensitic variants adopting different orientations on the MgO substrate. **Figure 5.2a** shows the out-of-plane and **Figure 5.2b** shows in-plane RSM, measured at 300 K and coherent with the (001) MgO plane, showing a variety of diffraction spots coming from the different variants as well as interference superstructure peaks arising from the modulation of martensitic variants. In **Figure 5.2a**, we find a central reflection centered at $Q_y = 0$, arising from the Ni-Mn-Ga planes parallel to (001) MgO. We cannot exclude a slight residual austenitic fraction leading to a $(004)_A$ reflection. However, as the martensitic nature of the film was confirmed via complementary techniques (**Figure 5.1**) and nanoscale characterization for similarly grown films (chapter 4). In addition, four strong reflection peaks are symmetrically placed around the central one, which we identify as the $(400)_M$ and $(004)_M$ peaks corresponding to the *a*- and *c*-axis reflections of the martensitic cells in differently oriented variants, tilted about 2.5° with respect to the sample plane (**Figure 5.2a**). Similar to the out-of-plane RMS, in the in-plane RMS (**Figure 5.2b**) the central peak is assigned to $(040)_M$ and the satellites are identified as the $(400)_M$ and $(004)_M$ planes of the martensitic cells.
Considering the out-of-plane and the in-plane RSM, the martensitic cell parameters are obtained as a = 6.094 Å, b = 5.810 Å and c = 5.528 Å.

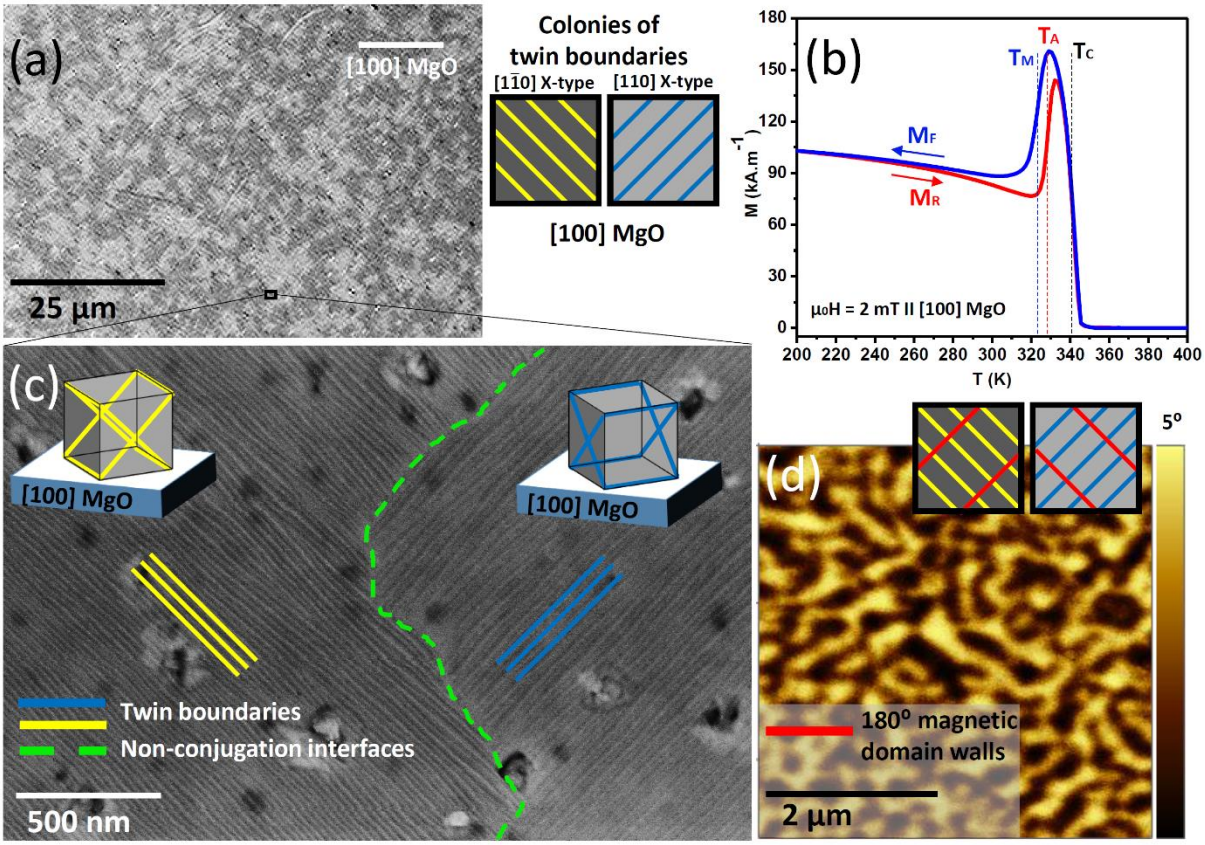

Figure 5.1: a) polarized light image at room temperature (left), simplified sketch of the colonies of the X-type twin boundaries (right). b) The isofield ($\mu_0 H$ = 2 mT along [100] MgO) magnetization curve as a function of temperature for the sample, showing the critical temperatures (martensitic transition temperature (T_M), austenitic transition temperature (T_A) and the Curie temperature (T_C)) in the martensitic forward (M_F in blue) and the martensitic reverse (M_R in red) transition. c) high-resolution BSE image of the marked region in (a), showing the twin boundaries in blue and yellow, non-conjugation interfaces in green dash line and the corresponding inclined {110} cubic planes for each of the represented orientations of the X-type twin boundaries. d) MFM image of the sample at room temperature, the inset sketches show a simplified relative orientation between the twin boundaries and the 180º magnetic domain walls.

Finally, the modulation period of the martensitic phase has been determined in the same fashion as in earlier works that analyzed thicker films on MgO substrates [7] and single-crystal Ni-Mn-Ga specimens [8]. The strategy consists of slightly reorienting the sample in the diffractometer reference frame to find the martensitic variant with the highest (400) reflection intensity in the out-of-plane diffraction configuration (in our case, we tilted the angle χ by about 3°). The φ sample azimuth is then adjusted such that the [001] orientation (*c*-axis) of the variant is aligned perpendicular to the x-ray plane of incidence. With a proper alignment routine, the (400) and (620) reflections of the chosen martensitic planes can then be detected in the wide-angle RSM, as in **Figure 5.2c**. The line in the RSM Q-plane connecting the (400) and (620) reflections is defined along the [110] orientation, which is the modulation direction in the martensite phase and in addition contains a full period of superstructure peaks between the aforementioned reflections. This is shown in the top panel of **Figure 5.2c**, where we have represented the intensity line scan along the [110] orientation as indicated in the RSM below. One can clearly observe that superstructure peaks are present in between the intense (400) and (620) reflections, evenly spaced by approximately 1/7th of the Q-distance in between the reflections, corresponding to $\Delta Q/7 = 0.0616$ Å^{-1}. This feature demonstrates the 7M (14M) microstructure modulation of the martensitic phase in the film (section 1.2.1). As in the case of thicker Ni-Mn-Ga films, the distance between superstructure peaks shows slight deviations from the expected

ΔQ/7 distance [7]. In the same way, only three superstructure peaks are visible to the right of the (400) reflection, and two to the left of the (620) reflection, often consisting of broad peaks. The origin of such irregularities has been attributed either to partially incommensurate modulation as well as the presence of stacking faults, which are ubiquitous in the case of epitaxially grown thin films [7].

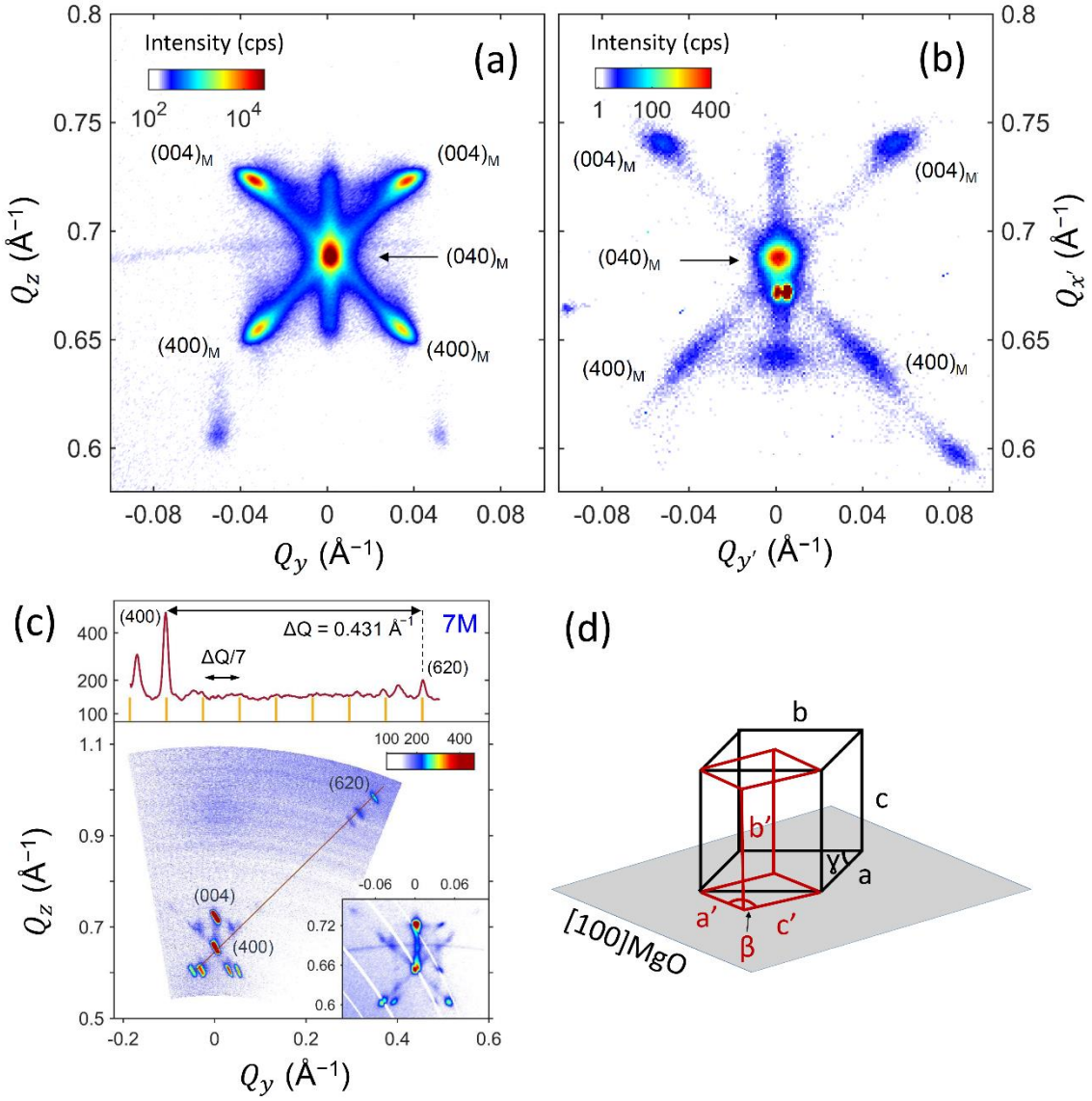

Figure 5.2: Room temperature XRD reciprocal space maps (RSM) measured on the as-prepared continuous film for a) out-of-plane and b) in-plane diffraction, respectively. These two maps are acquired for depicting diffractions that are coherent with the MgO substrate, c) Wide-range RSM after reorienting the sample to maximize the signal to the $(400)_M$ orientation of one of the martensitic planes. The series of equally Q-spaced peaks along the line connecting the (400) and (620) reflections (line scan above) confirms the 7M modulation of the martensitic phase. The inset shows a magnified area of the wide-angle RSM acquired with better resolution, where the $(400)_M$ and $(004)_M$ peaks are most prominent. d) Schematic representation of the relative orientations between the standard martensitic (dark red) and the austenitic setting (black) with respect to the MgO substrate directions. The indices show the three axes of the martensitic cell in the two represented settings. The martensitic seven modulation direction is along c', while it is along one of the (110) directions in the austenitic setting. The easy magnetization direction in the two settings is b' = c. The monoclinic non-right angle is β in the standard setting and ɣ in the austenitic setting.

5.2.2 Ni-Mn-Ga films (75 nm of thickness)

The films having 75 nm of thickness were selected for the nanofabrication mainly due to the fact that the lower thickness reduces the duration of the Argon etching process and consequently minimizes the re-deposition of etched material in the form the sidewalls. This aspect can be crucial for the fabrication of nanostructures with sizes below one micron, as relatively large amounts of re-deposited material may add up to the resulting patterns in a structurally disordered manner, thus negatively impacting the quality and sharpness of the martensitic transition (section 2.2.3). **Figure 5.3** provides a panel for the main characteristics of the as-grown 75 nm film. **Figure 5.3a** shows the thickness determination via XRR, measured by X-ray reflectivity technique (details can be found in section 2.3.5). The dots in the plot are referred to the experimental data and the plot in red is the simulated plot, obtained by fitting the experimental data. The fit reveals a 73.9 nm for the thickness of the Ni-Mn-Ga film on (001) MgO substrate. The composition of the sample was measured as $Ni_{53.6}$-$Mn_{19.9}$-$Ga_{26.5}$ (uncertainty = 1 at. %). **Figure 5.3b** shows the RSM, measured at room temperature on the as-prepared continuous film for out-of-plane diffraction configuration (section 2.3.5). Similar to 200 nm films described in 5.2.1, the central peak is ascribed to $(040)_M$. In addition, the four satellite peaks, which are symmetrically placed around the central peak are identify as the $(400)_M$ and $(004)_M$ peaks corresponding to the martensitic cells in differently oriented variants, tilted about 2.5° with respect to the sample plane. **Figure 5.3c** shows the high-resolution backscattered electron (BSE) image of the film, showing the morphological configuration of the twin boundaries (X-type). Some of boundaries are highlighted in blue and yellow, non-conjugation interfaces in green dash line and the corresponding inclined {110} cubic planes for each of the represented orientations of the X-type twin boundaries are schematized as well. **Figure 5.3d** show the MFM image of the sample at room temperature, the inset sketches show a simplified relative orientation between the twin boundaries and the 180º magnetic domains wall. The observed maze-like feature of the MFM image originates from the interference of the out-of-plane stray field of the intersected twin variants having basket-like morphology, as can be observed in **Figure 5.3c**.

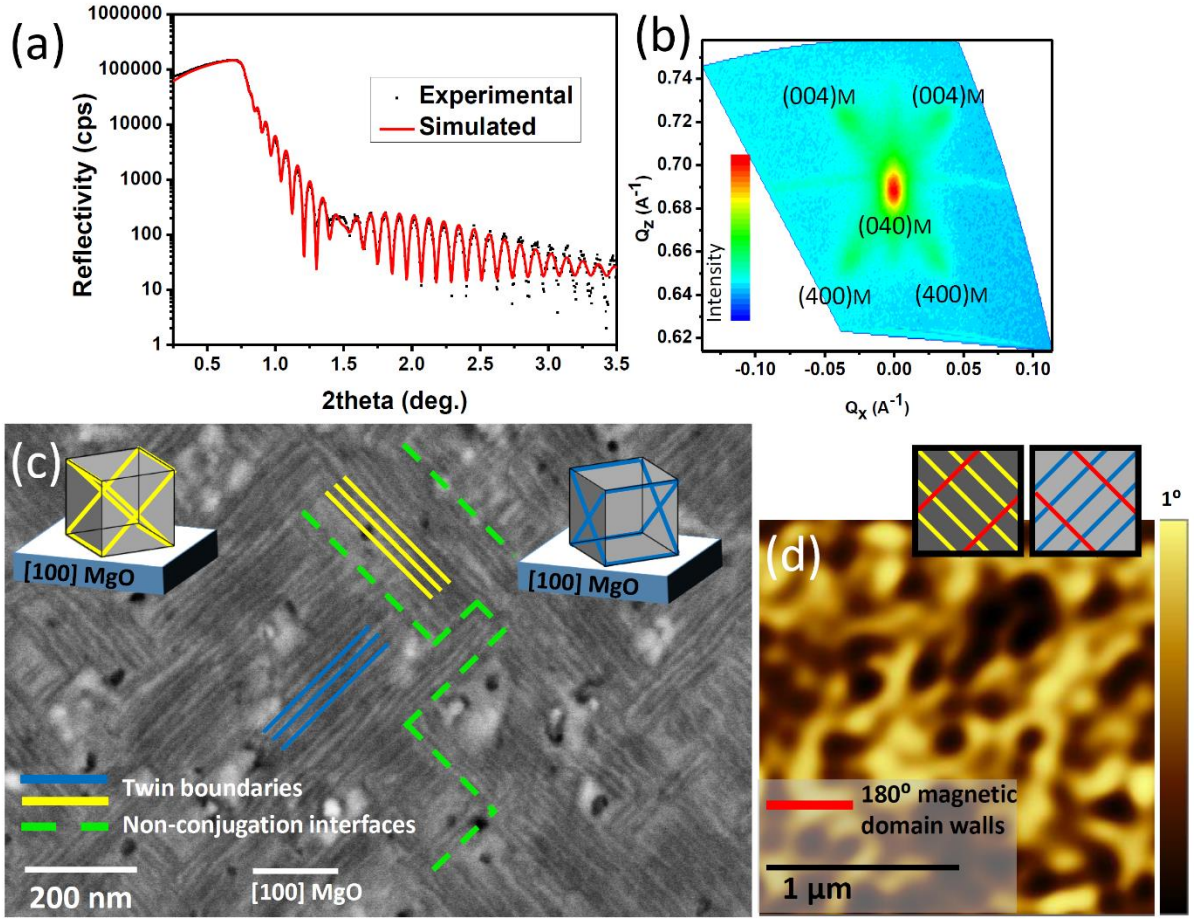

Figure 5.3: As-grown sample: a) XRR plot of the film, showing the experimental data in black dots and the simulated plot in red line. b) Room temperature RSM, measured on the as-prepared continuous film in out-of-plane configuration. c) High-resolution BSE image of the film, showing the twin boundaries in blue and yellow, non-conjugation interfaces in green dash line and the corresponding inclined {110} cubic planes for each of the represented orientations of the X-type twin boundaries. d) MFM image of the sample at room temperature, the inset sketches show a simplified relative orientation between the twin boundaries and the 180º magnetic domain walls.

5.3 Microstructures

As it was described in section 2.2, Ni-Mn-Ga epitaxial microstructures were fabricated using photolithography, followed by Ar ion etching. In order to investigate the effects of size, shape and the orientation on the martensitic morphology, different microstructures were fabricated with the lateral dimension range of 3-100 µm, in the forms of rings, fingers, square bands, L-shaped stripes, straight stripes, squares and disks. The martensitic morphology of the fabricated microstructures was investigated first in a large scale by polarized-light microscopy. An example of the polarized-light contrast images of the microstructures is represented in **Figure 5.4a**. This technique enables us to have an overview of the distribution of the X-type martensitic twin boundaries along [110] MgO and [1$\bar{1}$0] MgO for the different fabricated structures. As it is shown by the color-code in the image, bright grey represents the X-type arrays of the twin boundaries along [110] MgO while dark gray describes the X-type arrays of the twin boundaries along [1$\bar{1}$0] MgO. The borders between these two contrasts are described as the non-conjugation interfaces (section 4.2.1). The formation of the X-type twin

boundaries along [110] MgO and [1$\bar{1}$0] MgO is typically equivalent for a continuous film. As it is shown in the figure, we can observe both orientations of the X-type twin boundaries in almost all the fabricated microstructures. The evaluation of their distribution will be discussed below. A close look into the magnetic characteristics of the microstructures at room temperature is provided by the MFM images shown in **Figure 5.4b**. They show the typical out-of-plane magnetization expected for the X-type configuration showing alternating dark and bright stripe domains, as discussed above.

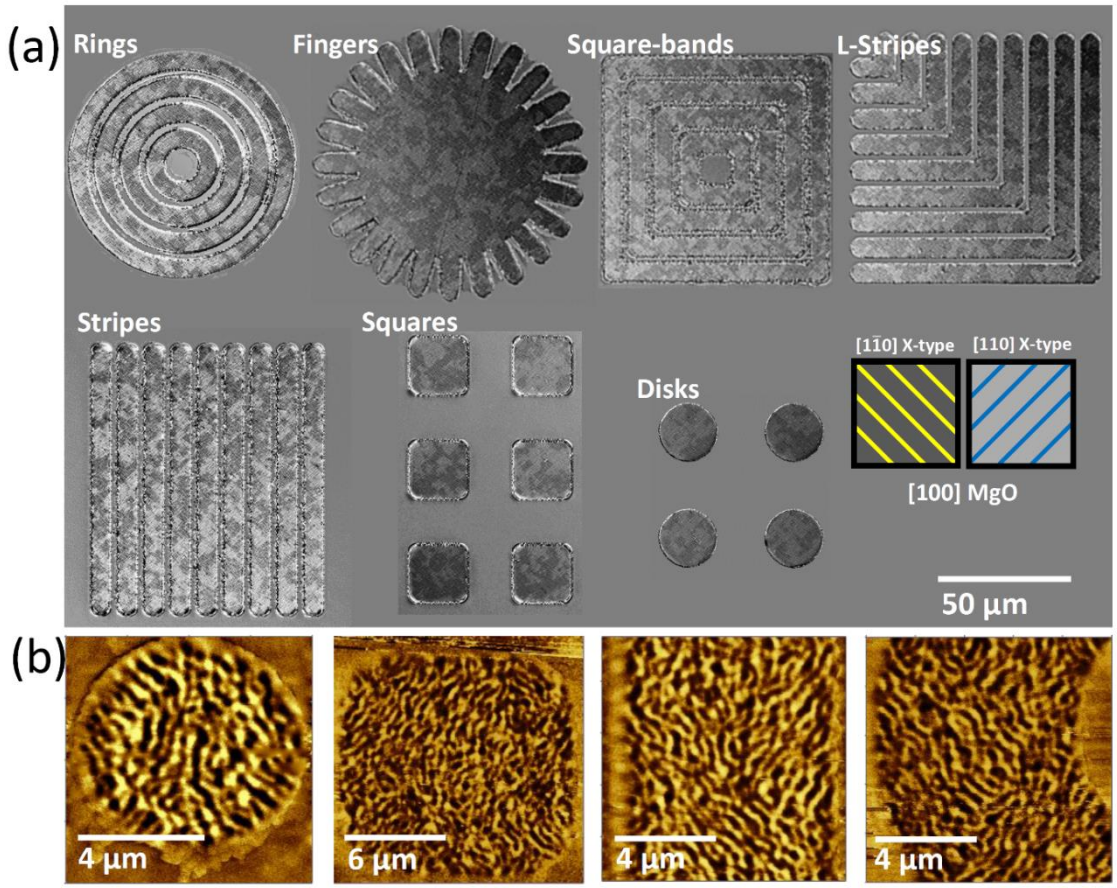

Figure 5.4: a) Polarized-light contrast microscopy images at RT, a panel showing different shapes of the fabricated microstructures (3-100 µm structures were fabricated), dark and bright contrasts show the two different orientations of the X-type twinning configuration, b) MFM images at RT showing the typical out-of-plane stripe domains of the X-type martensitic configuration in the fabricated microstructures**.**

5.3.1 Martensitic morphology vs. size and geometry

Microfabricated finger-shapes enable us to follow the distribution of the X-type configuration along [110] MgO and [1$\bar{1}$0] MgO as a function of different lateral dimensions as well as the different orientations of the fingers (with respect to the [100] MgO). **Figure 5.5** shows the backscattered electron (BSE) images of the 4 µm-wide fingers. The angular deviation between the fingers is 11.25º and they cover 360º (0º is defined along [100] MgO). In **Figure 5.5a** the microstructure is shown and the fingers with critical angles are marked and magnified in a way that the fingers, represented in **Figure 5.5b-d** are parallel to [110], [100], [1$\bar{1}$0] MgO, respectively. The two different orientations of the X-type twin boundaries in each of the fingers are highlighted by pink ([1$\bar{1}$0] X-type) or gray

([110] X-type) colors and the portion of the surface area occupied by the pink color is reported for each of the microfingers. It can be clearly observed that for the finger parallel to [100] MgO (**Figure 5.5c**), the distribution of the X-type twin boundaries is relatively equivalent (~60% along [1$\bar{1}$0] MgO vs. ~40% along [110] MgO), as we observe typically for a continuous film (**Figure 5.1a**). However, for the fingers fabricated along [110] MgO and [1$\bar{1}$0] MgO (**Figure 5.5b,d**), the twin boundaries parallel to the direction of the lithography are promoted remarkably, while the growth of the perpendicular twin boundaries is suppressed. This observation shows a kind of smart selection of the X-type twin boundaries with respect to the orientation of the fingers. A closer look into all of the microfingers from 315º-45º having the intermediate angles (**Table 5.1**) shows a trend for the fingers, i.e., selecting the twin boundaries that are relatively parallel to their orientations. The trend is proportional to the relative angle between the twin boundaries and the orientation of the fingers.

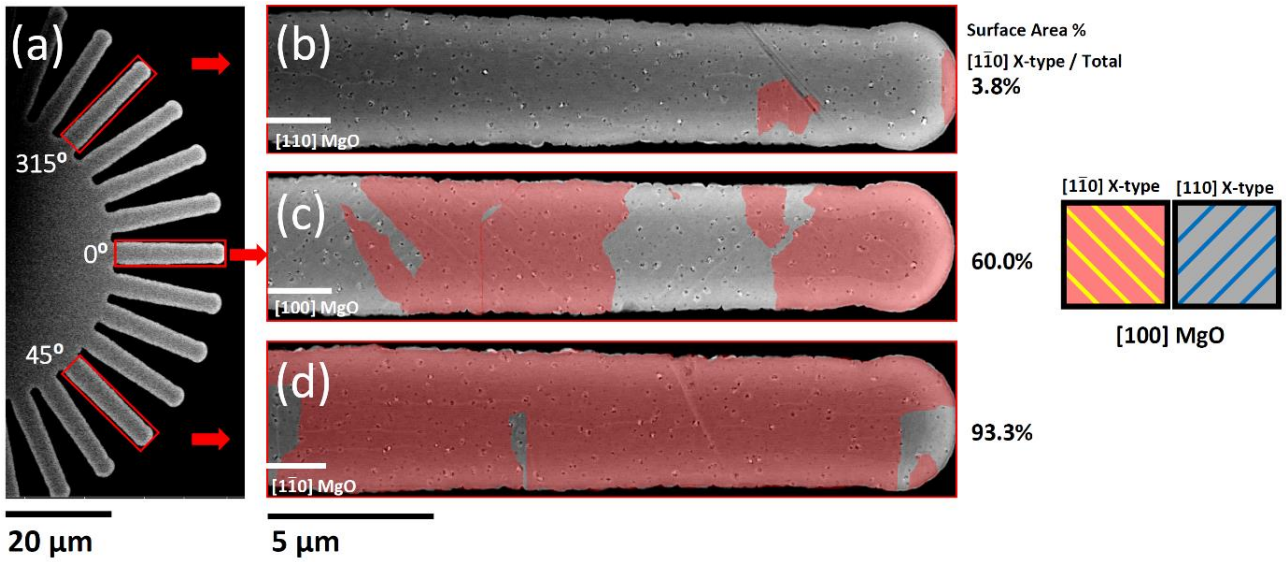

Figure 5.5: BSE images at RT, a) 4-µm width microfingers, b-d) magnified image of the marked regions in (a) showing the fingers orientated along [110], [100] and [1$\bar{1}$0] MgO, respectively. Different orientations of the X-type twinning configuration in the fingers are marked in red and grey, showing an evident dependence of the twinning orientations to the orientations of the fabricated fingers.

Starting from the finger along [110] MgO to the finger along [1$\bar{1}$0] MgO, shown in **Table 5.1**, the portion of the twin boundaries along [1$\bar{1}$0] MgO gradually increases (regardless of the two exceptions) until it reaches its maximum when the orientation of the finger is parallel to the orientation of the pink X-type configuration. The relative question is if the observed orientation dependent selection of the X-type twins applies also to the fingers with larger lateral size. Our measurements show that the phenomenon is mostly pronounced only for the microfingers smaller than 12 µm width. **Table 5.2** shows the portions of the surface area occupied by [1$\bar{1}$0] X-type twin boundaries for the three critical orientations, i.e. [100], [110] and [1$\bar{1}$0] MgO in the microfingers having the width range of 4-22 µm. The values were driven based on BSE and polarized light images of the fingers. Except for the values obtained for the 5 µm-wide microfingers, over upscaling, the rest of the fingers show a trend for equalizing the distribution of orientations of X-type configuration for the fingers fabricated along [100], [110] and [1$\bar{1}$0] MgO. For instance, the 22 µm fingers show almost an equal distribution of the X-type configurations in all the measured orientations, which is the condition we typically expect for a continuous film.

Table 5.1: Dependence of the twinning orientations to the orientations of the fabricated fingers (4 μm-wide fingers), (Uncertainty ≈ 5%).

Orientation of the 4 μm fingers (º)	**Surface area (%) [1$\bar{1}$0] X-type / Total**
315.00 ([110] MgO)	3.8
326.25	10.2
337.50	52.0
348.75	32.6
0.00º ([100] MgO)	60.0
11.25	70.6
22.50	71.0
33.75	41.0
45.00 ([1$\bar{1}$0] MgO)	93.3

Table 5.2: Dependence of the twinning orientations to the orientations of the fabricated fingers vs. finger-width, (Uncertainty ≈ 5%).

#	**Surface area (%) [1$\bar{1}$0] X-type / Total**		
Orientation of the microfingers	**315.00º ([110] MgO)**	**0.00º ([100] MgO)**	**45.00º ([1$\bar{1}$0] MgO)**
Width of the microfingers (μm)			
4	3.8	60.0	93.3
5	14.4	39.6	41.5
7	12.8	66.8	61.5
12	45.5	51.2	70.0
22	42.6	49.2	45.7

In epitaxial Ni-Mn-Ga thin films on MgO, the X-type twin boundaries along [110] and [1$\bar{1}$0] MgO (**Figure 5.1**) are energetically equivalent and hence nucleate simultaneously during the thermally driven transition, leading to their equal populations. (**Figure 5.1**, details can be found in chapter 4). However, when the martensitic transition is accompanied by an external force (i.e. mechanical stress, magnetic field), the equivalency of the twin boundaries breaks [9]. Similarly, in the case of microfingers, which are not aligned along the MgO crystal directions (i.e., [110] and [1$\bar{1}$0] MgO, **Figure 5.5b,d**), the different orientations of X-type twin boundaries are not equivalent anymore. The presence of the most favorable twin boundary orientation is promoted, which nucleates and extends predominantly throughout the structure, while the presence of the complementary twin boundary orientation is suppressed. On the other hand, both orientations of the X-type twin boundaries are 45º away from [100] MgO-oriented fingers. Therefore, there is no geometrical preference for the selection; the fingers keep the same equal multiplicity of the martensitic twin boundaries as observed for a continuous film.

For intermediate finger orientations (**Table 5.1**), the twin boundary orientations get gradually parallel and perpendicular to the long side of the fingers, where twin boundaries parallel to the long side form larger colonies than perpendicular ones. In agreement with the model reported in reference [9], larger structures of twin boundaries are less likely to collide during the self-accommodation. This leads to flatter and homogenized distribution of energy over the martensitic transition under external fields. Besides, larger twin boundary regions reduce the need for nucleation of further twin boundaries during the transition, such that the energy needed for the transformation is effectively reduced. Hence, these energetic considerations explain the observed predominance of specific twin boundaries upon controlling the system's geometry.

For microstripes' widths above 12 μm (**Table 5.2**), the same effect was not present and the microstructures resembled the continuous film behavior instead. Due to the constraint from the substrate and the large surface-to-thickness ratio, the mechanical coupling between different regions located far apart is lower in epitaxial films compared to the bulk samples. Therefore, the effects of size on the structural and magnetic properties is expected to be realized in far smaller length scales of films compared to bulk. [2,3,10].

The impact of external fields, i.e., mechanical stress [11] and magnetic field [12] have been previously analyzed in Ni-Mn-Ga single crystals by measuring the acoustic wave emission during the transition. It was found that these external fields have a relevant impact on the transition path by favoring some of the twins over the others. In the light of our investigation shown in **Figure 5.5** and **Table 5.1** and **Table 5.2**, we propose that lateral confinement, together with geometry constitute an additional relevant tool for controlling the multiplicity of twin boundaries in patterned epitaxial Ni-Mn-Ga films.

5.3.2 Martensitic morphology vs. size and shape

Another effect of the lateral confinement, which in this case is coupled to the shape of the microstructures rather than the orientation, was investigated by comparing the stripes and disks. In the case of the stripes, we have a significant difference between the lateral dimensions (aspect ratios are from 4 to 143) while for the disks the lateral dimension is constant and is equal to the diameter of the disks. Therefore, comparing the stripes to the disks, having the same lateral dimension (the match is between the disk diameter and the width of the stripe) implies a much lower volume of material for disks. **Figure 5.6** shows a panel of the BSE and the polarized light images of both the stripes and the disks with the lateral dimension range of 5-22 μm. Similar to the previous figure, different orientations of the X-type configuration are highlighted in the images with the same color code used above. **Figure 5.6a** shows the status of the stripes downscaling laterally from 22 to 5 μm. Evidentially, the material keeps the multiplicity of the X-type configurations as it scales down, keeping the equality of the distribution of the twin boundaries. However, the size of the X-type colonies reduces. In other words, the colonies of the twin boundaries break down to smaller pieces as the lateral size is reduced. This is not the case for the disks (**Figure 5.6b**) though. As the size is reduced for the disks, the material tends to select mostly one of the orientations of the X-type configuration. This phenomenon cannot be quantified as before simply by showing the relative portion of the surface area occupied by different orientations of the X-type twin boundaries in the microstructures. To obtain a quantifying factor, we measured the total length of the borders between the pink and the grey colored areas (i.e. perimeter of the pink color, edges of the microstructures were not included) for each of the microstructures and divided the obtained value by the total surface area of each structure. In other words, we obtained a representative number for the density of the non-conjugation martensitic interfaces (section 4.2) in each of the microstructures, so called α. These factors are provided close to each of the images in **Figure 5.6**. In addition, an inclusive report of the density of the interfaces is provide in **Table 5.3**, including the microstripes and microdisks with the lateral size of (5-42 μm). Looking at the density factors of the interfaces reported for the microstripes (**Table 5.3**), we observe an upward trend from 0.24 μm^{-1} for 42-μm-stripe to 0.43 μm^{-1} for 5-μm-stripe. While an opposite trend is observed for the microdisks, i.e., a reduction of the interface density factors as the lateral size is reduced. Similar to the microfingers, reported above, the effect almost disappears for the structures larger than 12 μm lateral size. For the larger disks the material turns back to the equal distribution of the X-type twin boundaries and for both the large stripes and the disks, α approaches the values we typically observe for the continuous film of the same sample (**Figure 5.1**). The two investigated shapes of the microstructures are the two ends of the spectrum. Other microstructures, i.e. rings, square bands, L-stripes and squares represent characteristics in between disks and straight stripes based on the geometrical similarities to each of them (**Figure 5.4a**).

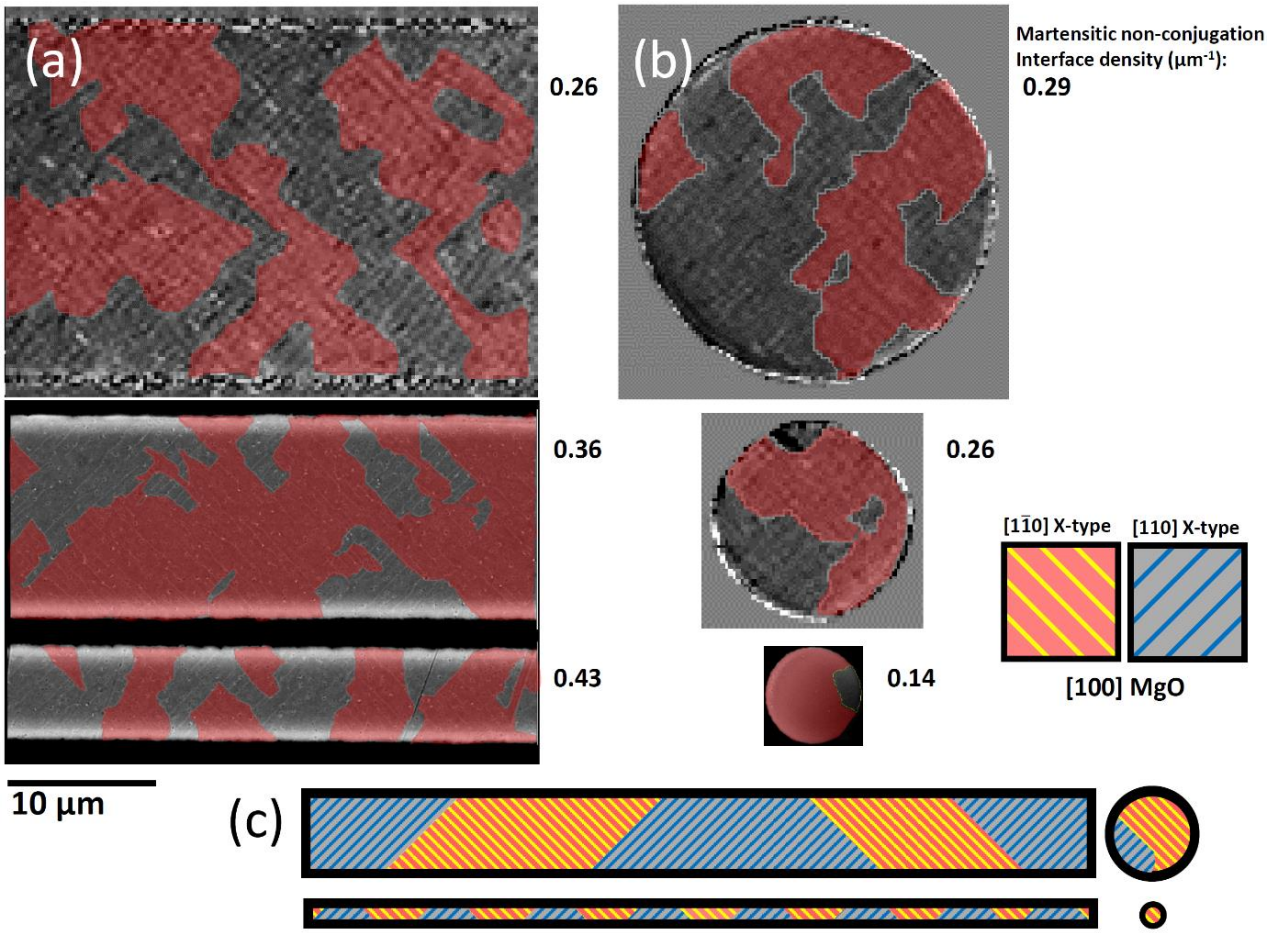

Figure 5.6: A combination of polarized light and BSE images of the stripes (along [100] MgO) and disks at RT: a) 5, 12 and 22 µm width stripes b) 6, 12 and 22 µm diameter disks. Different orientations of the X-type twinning configuration in the microstructures are marked in pink and grey. The length of the non-conjugation interfaces (borders between pink and grey) per total surface area are also provided, showing the influence of the shape and the lateral confinement on the distribution of the different orientations of the X-type twinning configuration. c) A simplified schematic representation of the distribution of the X-type twin boundaries for the stripes and the disks versus the lateral dimension.

Table 5.3: The influence of the shape and the lateral confinement on the distribution of the X-type twinning configuration by measuring the [1$\bar{1}$0] X-type relative surface area together with the interface density factor.

microstripes (μm)	**Surface area (%) [1$\bar{1}$0] X-type / Total**	**Interface density factor (α) (μm^{-1})**
5	47.1	0.43
7	48.1	0.31
12	68.6	0.36
22	49.9	0.26
42	47.0	0.24
Microdisks (μm)		
6	88.3	0.14
12	88.9	0.26
22	46.4	0.29
32	48.5	0.23

So far, we have described the distribution of the X-type twin boundaries and the impact of the lateral confinement, shape and the orientation of the lithography-fabricated microstructures on the smart selection of their orientations upon thermally induced martensitic transition. In **Figure 5.7** we represent the evolution of the aforementioned twin boundaries over the martensitic transition, directly measured for a 6 μm disk by in-situ MFM imaging vs. temperature. **Figure 5.7a** shows the configuration of the disk at room temperature, showing the stripe magnetic domains related to the X-type twin boundaries as discussed in **Figure 5.1**. As the disk is heated up to 326 K, it transforms to the austenitic phase, therefore the out-of-plane magnetic stripe domains disappear. While the disk is still undergoing the transition, the trace of annihilating twin boundaries is visible in the center of the disk (**Figure 5.7b**), which disappear after heating up to 329 K (**Figure 5.7c**). **Figure 5.7d** shows the microdisk, cooling back to 320 K, after heating to 343 K. It shows the martensitic nucleation points, approximately located in the central part of the disk. Evidently, they are four X-type martensitic twinning configurations nucleated individually in the matrix of the austenitic parent phase along [110] and [1$\bar{1}$0] MgO: they grow towards the edges of the disk and also towards each other, forming the non-conjugation interfaces. The growth directions are clearly visible in **Figure 5.7e**, showing the magnetic contrasts from the colliding and growing twin boundaries along [110] and [1$\bar{1}$0] MgO, reducing the austenitic matrix to small windows. Further cooling (**Figure 5.7f**) results in the further growth and colliding of the existing twin boundaries as well as the nucleation of new twin boundaries, which fill the untransformed regions till the edge of the disk also transforms to the martensitic phase (**Figure 5.7g**). The X-type twin boundaries close to the edge of the disk are shown in the high-resolution BSE image at room temperature (**Figure 5.7h**).

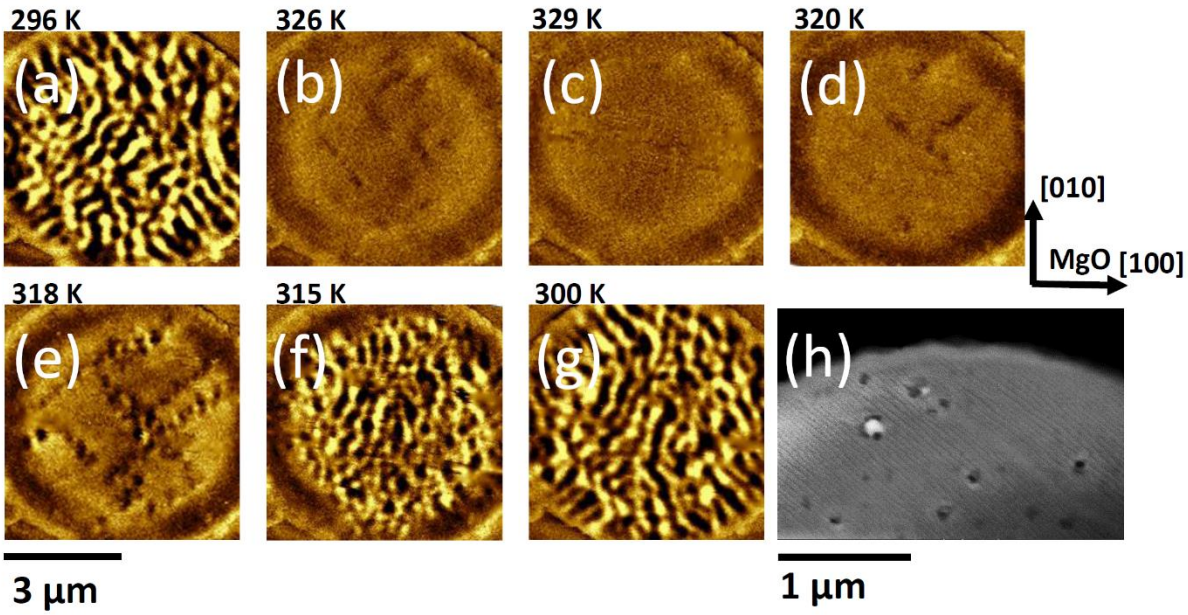

Figure 5.7: a-g) MFM images of a 6-µm disk vs. temperature showing the evolution of the X-type twinning configuration, h) BSE image of a 6-µm disk at RT showing the X-type twin boundaries at the edge of the disk.

The specific accommodation of the twin boundaries in microstructures of different shapes was also presented in **Figure 5.6** and **Table 5.**3. The lateral size of lithographically patterned structures influences the long-range elastic interactions as well as the kinetics of the martensitic phase, impacting the nucleation process and self-accommodation of the twin boundaries. While the relative orientation of the stripe's long side and the crystal axes can suppress or promote the growth of specifically oriented twin boundaries, the neutrality between the two different orientations is kept for disks upon downscaling their size. The interplay between elastic anisotropy and disorder (or pinning obstacles) has been investigated in the literature using simulations that determine the characteristics of the twinning patterns [13-15]. In the case the microstripes investigated here, the lateral edges of the structures can be considered as additional pinning obstacles, inhibiting further growth of twin boundaries. This additional obstacle is largest for the narrowest stripes and it could influence the kinetics of the transition. In these stripes the accommodation of twin boundaries is imposed via more frequent switching between the four different austenitic habit planes (**Figure 5.1c**) towards the long side of the stripes. This self-accommodation phenomenon provides an additional degree of freedom to compensate the long-range elastic strain of the material via diversifying the orientation of local transformation strains.

In addition, one needs to consider the substantial difference between the volume of the material in microstripes and microdisks of the same width. Therefore, the total number of nucleation sites for the martensitic transition is significantly lower in the disks, reducing twin boundary collision events (e.g., non-conjugation interfaces). A simplified representation of the orientations of the twin boundaries in the stripes compared to disks is provided in **Figure 5.6c**. These two factors explain the different evolution of the quantity α as stripes and disks are scaled down in size. For structures with widths above 12 µm, these confinement effects were absent.

5.3.3 Critical transition temperatures vs. size

Electrical transport measurements vs. temperature enabled us to directly measure and compare the critical transition temperatures and the thermal hysteresis of the microstripes (**Figure 5.8** and **Table 5.4**). Normalized resistance vs. temperature is represented in **Figure 5.8** for the stripes with the lateral dimension in the range of 3-100 μm, provided in different colors. The resistance of the material changes over the second order phase transition. In **Figure 5.8a**, a kink is observed around 342 K, which is assigned as the Curie temperature of the stripes. The resistance of the material also changes over the first order phase transition. The magnified image of the curves inside the marked square is shown in **Figure 5.8b**, representing the hysteretic martensitic transition with an evident slight shift towards higher temperatures as the lateral size of the stripes reduces from 100 μm to 3 μm. The martensitic forward and reverse transitions are marked with labels and arrows. The shift is evidently more consistent for the heating curves rather than the cooling curves. The shape of the curves also changes by changing the lateral size (**Figure 5.8**). Evidently, for the tiny stripes, i.e., 3 and 5 μm stripes, the transition has the so-called tails, meaning that after the transition avalanche, which is assigned by the sharp drop and raise of the resistance, the heating and the cooling curves do not overlap immediately. The tails maintain for about 10 K after the avalanches before the two curves overlap again. Having a closer look at the transition critical temperatures in **Table 5.4**, which were obtained by the tangent method, we observe no substantial change of the Curie temperature (Tc) of the stripes over downscaling. The measured value of ≈342 K is consistent to the Tc measured for the as-prepared continuous sample by isofield magnetization measurement vs. temperature (**Figure 5.1b**). The other aspect of interest is that the martensitic forward and reverse transition temperatures of the microstructures appear at ~5 K lower than the as-prepared sample. This is expected to be due to the annealing (the last step of microfabrication process). Similar to what has been reported in section 3.2, the post-growth annealing at 623 K temperature reduces the imperfections of the film, which typically serve as the martensitic nucleation points therefore, for the annealed films, typically the austenitic phase is stabilized and the transition temperatures shifts to lower temperatures by a few kelvin. The martensitic forward transition of the microstripes in **Table 5.4** shows a minor increase of the value over decreasing the lateral size of the stripes with the minimum number of 315.3 K belongs to 52 μm stripe and the maximum number of 317.6 K belongs to 3 μm stripe. While for the martensitic reverse transition, we measured a consistent minor increase of the value with decreasing the lateral size of the stripes, having a range of 321.6-323.7 K for 3-100 μm stripes. Finally, the thermal hysteresis also shows a non-consistent minor variation over the reduction of the lateral size. The range of the thermal hysteresis was measured as 5.6 to 7.6 K.

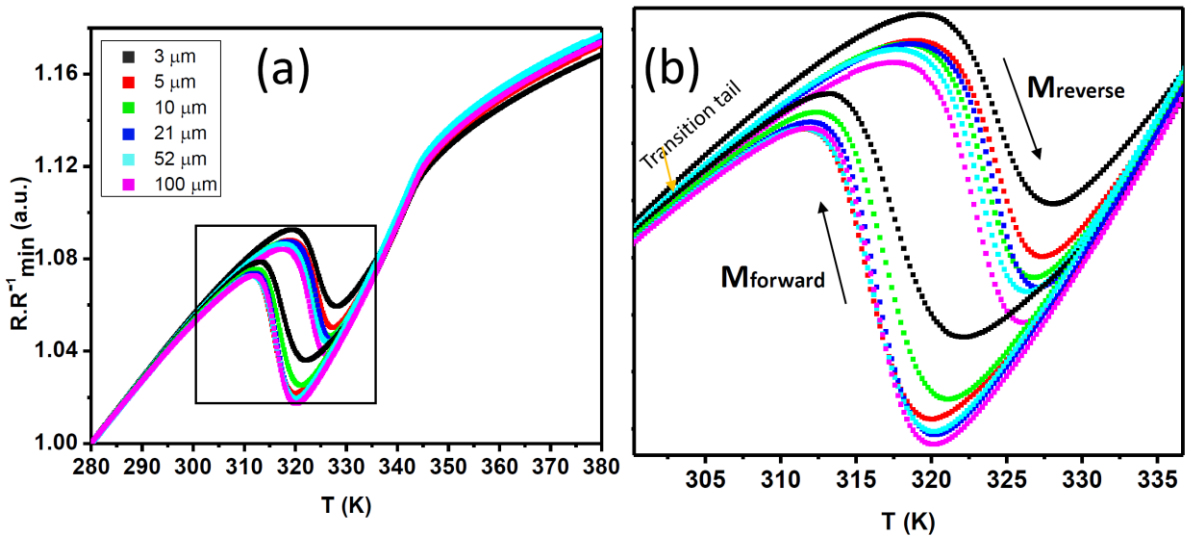

Figure 5.8: Size dependence of the critical temperatures and the thermal hysteresis: a) resistance of the 3-100 μm stripes vs. temperature, shown in different colors. b) magnified image of the marked area in (a). Cooling and heating curves are labeled by arrows.

Table 5.4: Size dependence of the critical temperatures and the thermal hysteresis for 3-100 μm fabricated microstripes. The transition values were obtained using tangent method.

Width (μm)	$T_{M\ start}$ (K)	$T_{M\ finish}$ (K)	$T_{M\ average}$ (K)	$T_{A\ start}$ (K)	$T_{A\ finish}$ (K)	$T_{A\ average}$ (K)	Hyst (K)	T_C (K)
3	322.0	313.1	317.6	319.4	328.0	323.7	6.2	341.8
5	319.9	311.4	315.6	318.9	327.7	323.3	7.6	342.2
10	321.3	312.4	316.8	318.1	326.8	322.4	5.6	341.8
21	320.1	311.7	315.9	318.8	327.2	323.0	7.1	342.0
52	320.3	311.3	315.3	317.7	326.3	322.0	6.2	341.8
100	320.3	311.8	316.0	317.3	326.0	321.6	5.6	342.4

During the martensitic transition, the elastic stress is partially stored in the martensitic phase [16] (detailed can be found in section 1.2.4). In a multivariant system, the stress is locally accumulated in the form of deformation at pining obstacles, e.g., non-conjugation interfaces, where the twin boundaries collide and their further growth is hindered (detailed can be found in section 4.2.3). Therefore, it is reasonable to assume that the stored elastic energy is proportional to α (the highest value of α (0.43 μm^{-1}) found for the narrowest stripes). The stored elastic energy also plays an important role in the broadening the transition [16] by regulating the formation and growth of the twin boundaries in the forward transition and annihilation of the twin boundaries in the reverse transition. In particular, higher stored elastic energy results in a broader transition (sections 1.2.4 and

4.3), thus explaining the observed elongated tails in the resistance vs temperature data before completion of the transition in the narrowest stripes.

Another characteristic of the material, shown in **Figure 5.8** and **Table 5.4** is referred to the slight shift of the transition temperatures to higher temperatures as a function of the reduction of the lateral size. The origin and behavior of stress induced shift of the transition temperature upon confinement are highly debated in the literature, in some cases even controversially:

Lambrecht et al. [4] have recently reported a shift of the transition temperatures of Ni-Mn-Ga/Si bimorph freestanding cantilevers to lower temperatures ($\Delta T \approx 40$ K) as the lateral size is reduced (200-2000 nm in width). In fact, the surface energy is increased by the reduction of the lateral size as a result of higher surface to volume ratio for the narrower structures. Since the surface energy of the martensitic phase is expected to be higher than the austenitic phase (due to negative volume change upon the transition) therefore, the surface energy contribution to the Gibbs free energy could be realized as the stabilization of the austenitic phase in lower lateral dimensions.

On the other hand, a couple of works from Prof. Schuh from Massachusetts Institute of Technology [10,17] report an increase of the transition temperatures of Cu-based shape memory microwires (20-500 μm of diameter) over downscaling. They have highlighted the effect of stored elastic energy for the observed increase of transition temperatures. In fact, for the microwires over downscaling, they reported decrease of the stored elastic energy and as a result of that, sharpening of the transition and a trend for the wires to go towards single domain martensitic morphology as well as the increase of the transition temperatures over downscaling.

Recently, Mashirov *et al.* [18] have reported a slight increase of the transition temperature in Ni-Mn-Ga-Cu wedge-like lamella by in situ TEM measurement. They referred the shift of the transition to the internal mechanical stress generated by a surface tension in the thinner region of the lamella.

The origin of slight increase (<3 K) of the transition temperatures upon downscaling our Ni-Mn-Ga microstripes could arise from the strain relaxation upon patterning. The residual stress in the cubic phase of Ni-Mn-Ga films attached to different substrates is typically high and exhibits nontrivial film thickness behavior depending on the substrate [19]. While the phase transition temperature variation upon lateral confinement is rather modest in our film, this finding suggests that the effect could be more prominent (> 10 K) for epitaxial Ni-Mn-Ga micro/nanostructures on different substrates rather than MgO as well as for lower thicknesses of films on MgO (section 5.4), where more significant values of the film's residual stress have been reported [19].

In our observation, the shift of the transition temperatures is more consistent for the reverse transition. Heterogeneous nucleation of the martensitic phase close to the defects and imperfections at the free surface, makes the forward transition more random and critical. However, for the reverse transition, the well-defined incompatible interfaces contribute to the transition (section 4.2.3), which is expected to make the reverse transition more regular; therefore, the shift is expected to be more visible for the reverse transition.

Recently, the stress-induced shift of the transition temperatures has quantified to be 0.096 $K.MPa^{-1}$ for $N_{54}Mn_{21}Ga_{25}$ bulk samples based on the Clausius-Clapeyron relation [20]. Taking this value as a reference, the shift of <3 K in the transition temperatures of our microstripes would require approximately a stress of 30 MPa.

5.4 Nanostructures

The investigation of the size effects on the morphology, magnetic characteristics and the critical transition temperatures of Ni-Mn-Ga films was continued by approaching nanometer lateral size. For this purpose, nanofabrication process was implemented as described in section 2.2. Different nanostructures were fabricated having the lateral dimension range of 150-800 nm, in the forms of stripes and squares. A close look into the magnetic characteristics of the nanostructures at room temperature is provided by the MFM images shown in **Figure 5.9**. They show the typical out-of-plane magnetization we expect for the X-type configuration, showing alternating dark and bright stripe domains, as discussed for the microstructures. The expected directions of the easy magnetization axis of the cells in the martensitic variants as well as the 180º magnetic domain walls in the stripes, causing the observed stray field contrast of the MFM images are demonstrated in **Figure 5.9b**, as an example.

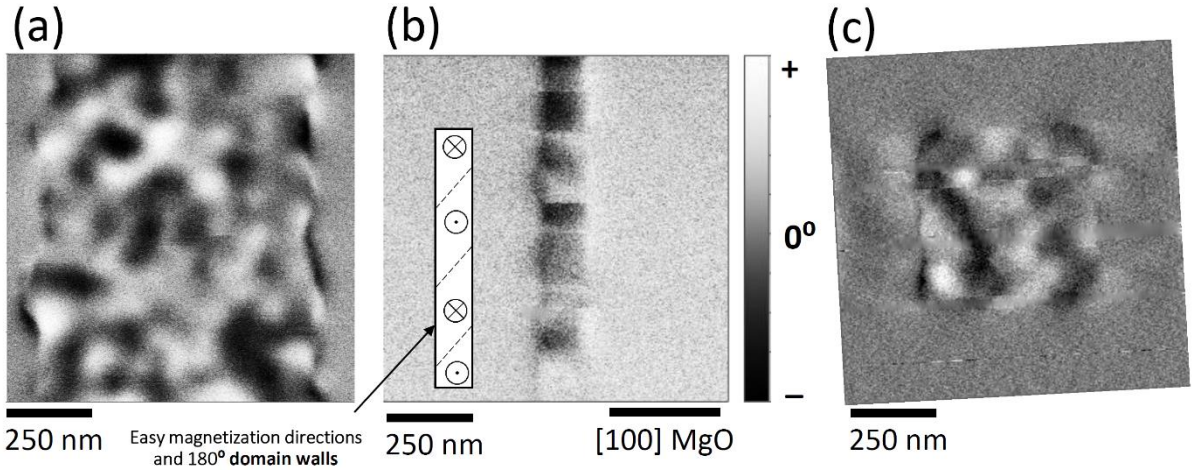

Figure 5.9: MFM images of the nanostructures at room temperature, showing the typical out-of-plane magnetic domains of the X-type martensitic configuration in a,b) 800 and 150 nm-wide nanostripes along [010] MgO and c) 500 nm-wide nanosquare. The inset in (b) shows the expected directions of the easy magnetization axis of the cells in the martensitic variants as well as the 180º magnetic domain walls in the stripe, causing the observed stray field contrast of the MFM images. The images are shown in black & white to maximize the contrast.

5.4.1 Martensitic morphology vs. geometry

Nanofabricated stripes enable us to follow the distribution of the X-type configuration along [110] MgO and [1$\bar{1}$0] MgO as a function of different lateral dimensions as well as the different geometry of the stripes (with respect to the [010] MgO, [110] MgO and [1$\bar{1}$0] MgO). **Figure 5.10** shows the MFM images of the stripes, having 550 nm to 300 nm of width. The nanostripes have been fabricated along the critical angles, i.e., [110], [010], [1$\bar{1}$0] MgO. As the size of the structures reduces, characterization becomes more sophisticated. Therefore, in the case of the nanostripes, the MFM images have been used both for gathering information about the magnetic stray field characteristics of the structures as well as the orientation of the X-type twin boundaries in the stripes, knowing that the 180º magnetic domain walls are approximately perpendicular to the twin boundary directions (section 1.3.1). Evidently, the effect of the orientation of the fabricated structures, discussed in details in section 5.3.1 applies for the nanostripes as well. For instance, the 300-nm-width stripe along [1$\bar{1}$0] MgO (**Figure 5.10c**) shows the main magnetic contrast change along the direction of its length. It

suggests that the orientation of the twin boundaries, accommodated in the stripe are along the length of the stripe, which is what was observed in the tiny microfingers of the same orientation as well (section 5.3.1).

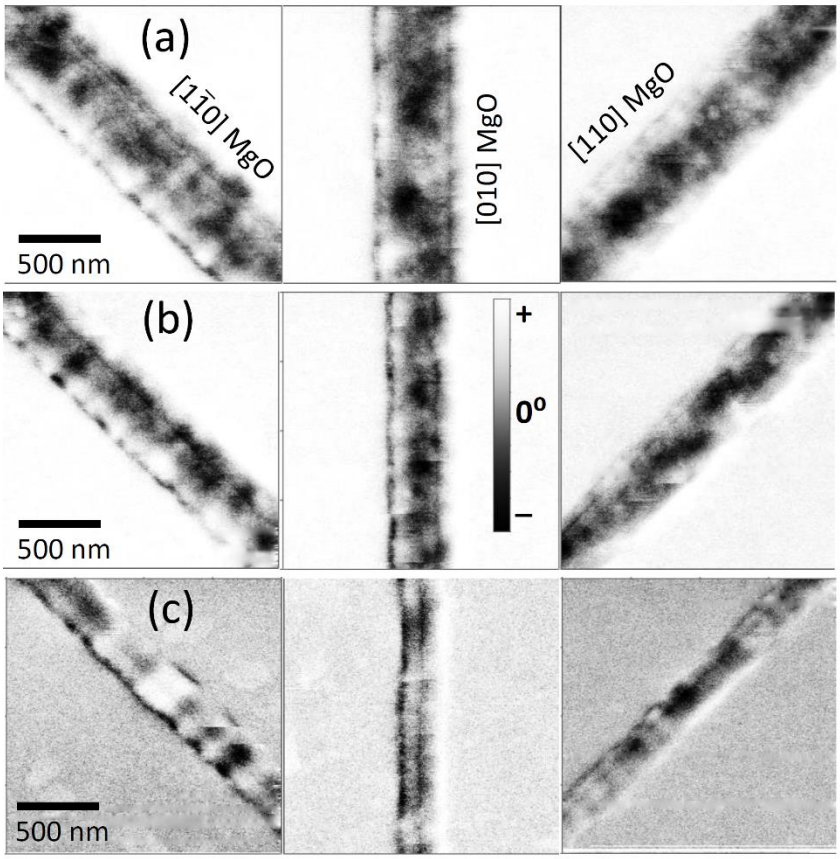

Figure 5.10: MFM images of the nanostripes along [1$\bar{1}$0] MgO, [010] MgO and [110] MgO at room temperature, showing the typical out-of-plane magnetic domains of the X-type martensitic configuration in a) 550-nm-width stripes, b) 350-nm-width stripes, c) 300-nm-width stripes. The images are shown in black & white to maximize the contrast.

5.4.2 Critical transition temperatures vs. size

Electrical transport measurements vs. temperature enabled us to directly measure and compare the critical transition temperatures and the thermal hysteresis of the nanostripes having different lateral sizes. The results are represented in **Figure 5.11b,c** and **Table 5.5**. In addition, the isofield magnetization curves of the as-prepared continuous film, from which the nanostripes were fabricated, has been provided in **Figure 5.11a** as a reference. Typically, by reducing the thickness of the films, the residual stress of the film increases [19], which in turn abstracts the martensitic transition temperature of our Ni-Mn-Ga films by stabilizing the austenitic phase. Broadening of the martensitic transition is also realized in 75-nm films as one of the consequences of the high stored elastic energy due to the substrate constraint. Therefore, in the systems in which the second order and the first order transition temperatures are close (as in our Ni-Mn-Ga films), they may overlap. This typically makes the characterization of the exact critical temperatures in 75 nm films more complex with respect to 200 nm films (compare **Figure 5.1b** and **Figure 5.11a**).

Figure 5.11a shows the isofield curves of the continuous sample vs. temperature (at an applied field of $\mu_0 H$ = 2mT along [100] MgO). The hysteretic behavior of magnetization curves suggests a broad martensitic transition temperature range from ~270 K to 334 K (Curie temperature), where the magnetization reduces to zero. Normalized resistance vs. temperature are represented in **Figure 5.11b,c** for the stripes with the lateral dimension in the range of 350-700 nm in different colors. The main characteristic of the curves, which can be recognized in a glimpse at **Figure 5.11b** is that the martensitic transition temperature range (transition width) has been increased as a function of lateral size reduction. Unfortunately, due to instrumental restrictions, measuring of the resistance of the nanostripes was bounded to the upper limit of 400 K therefore; major part of the curves in the austenitic phase is missing. This prevents us from measuring the exact value of transition width for 350 nm and 450 nm-width stripes however, the broadness of the transition as a function of lateral size is clearly observable. This increase of the transition width as a function of lateral size can be explained by referring to the stored elastic energy scenario as described for the microstripes in section 5.3.3:

Based on this scenario, the increase in the density of the colliding twin boundaries during the martensitic transition (which can be realized as the density of the martensitic interfaces in an epitaxial Ni-Mn-Ga film) increases the density of the stored elastic energy, in turn broadens the width of the martensitic transition. The evidences provided by high-resolution morphological characterizations as well as the high-resolution measurements vs. temperature suggest the validity of this scenario for both the continuous films (section 4.3) and lithography fabricated structures (section 5.3).

Another evidenced characteristic of the nanostripes, measured by the electrical transport measurements vs. temperature is the obtained gradual decrease of the hysteretic behavior of the transition curves as a function of the lateral confinement. The values are provided in **Table 5.5**. Commenting on the origin of the thermal hysteresis reduction, observed for the nanostripes as a function of the lateral size is a puzzling task, which requires detailed theoretical investigations. One needs to take into account the possibility of the contribution of the extrinsic parameters, discussed in chapter 1.2.4, including the effects of the nucleation points, surface energy, internal stress as well as the kinetics of the transition in the nanometer lateral dimensions. The strain relaxation caused by the nanofabrication process may also play a role. Ueland *et al*. [21] have recently reported a mechanism for the reduction of the hysteretic behavior of the Cu-based SMA as a function of size, which is worth taking into account while commenting on the possibilities. In the reported mechanism, the scarcity of the number of volumetric obstacles in the finite size of the material turns the typical role of the obstacles from being the phase boundary hindrance (dissipating energy, causing hysteresis) to serve as the nucleation points. This mechanism suggests a transition regime for sufficiently small volume of the martensitic materials, in which the nucleation sites' starvation rules out the transition path. This could lead to significant reduction of the hysteresis of the transition at the finite size of the material. For the samples below the finite size, the martensitic transition is suppressed.

Finally, as it was suggested in section 5.3.3, the transition temperatures increase as a function of lateral size reduction in the fabricated nanostripes due to the significant strain relaxation caused by the lateral confinement. As suggested in section 5.3.3, the shift of the transition temperatures as a functional of lateral size is more pronounced for nanostripes rather than the microstripes due to the nanometer lateral confinement as well as the relatively higher residual stress in 75-nm-thick film (used to fabricate nanostructures) compared to 200-nm-thick films (used to fabricate microstructures). The transport curves show the shift of more than 30 K from 700 nm stripe to 350 nm stripe (**Table 5.5**).

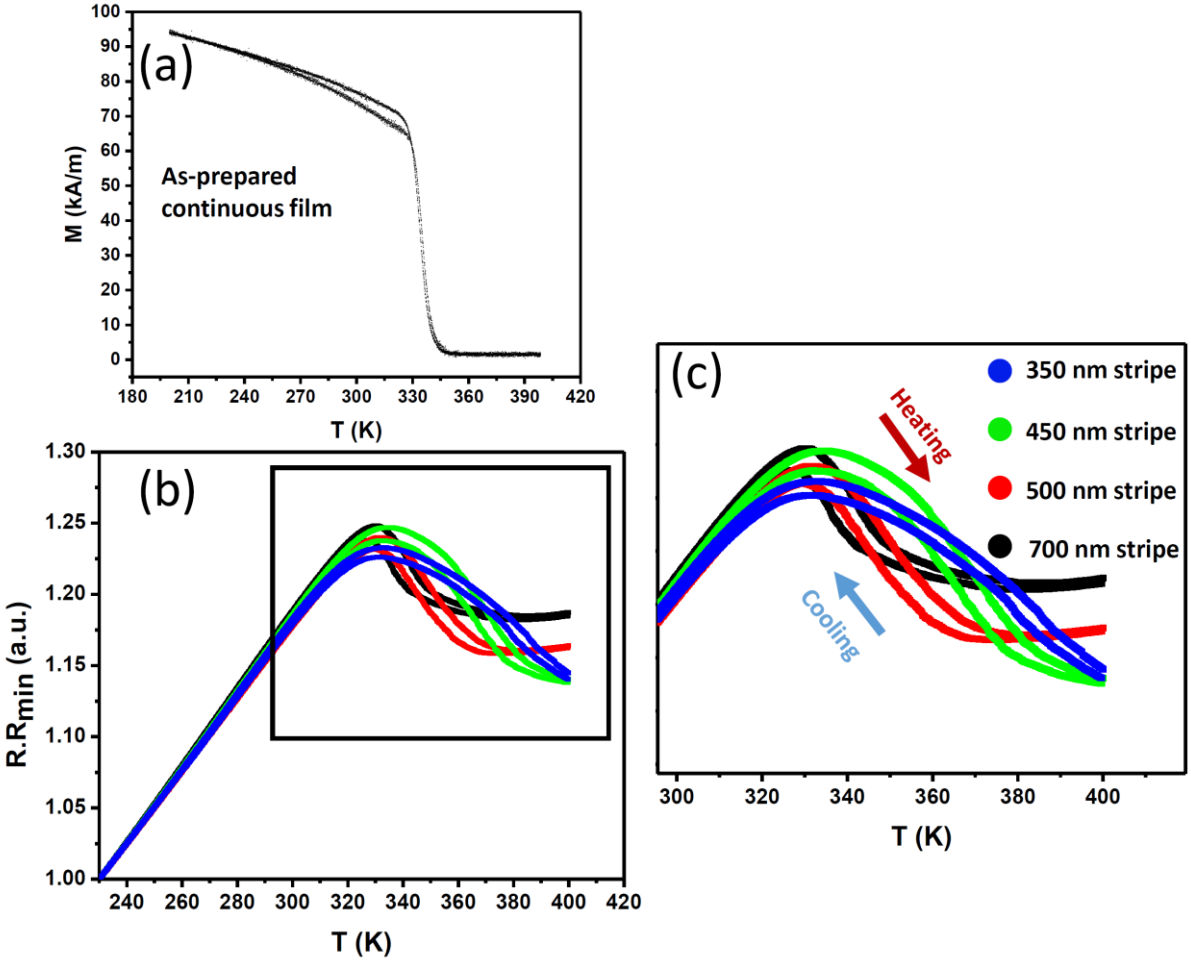

Figure 5.11: Size dependence of the critical transition temperatures and the thermal hysteresis: a) The isofield ($\mu_0 H$ = 2 mT along [100] MgO) magnetization curves as a function of temperature for the as-prepared sample, b) Normalized resistance of the 350-700 nm stripes along [100] MgO vs. temperature (shown in different colors), c) magnified image of the marked area in (b). Cooling and heating curves are labeled by arrows.

Table 5.5: Size dependence of the critical temperatures and the thermal hysteresis for 350-700 nm-width fabricated nanostripes obtained from the resistance measurement over temperature. ΔT_{Avg} shows the width of the transition. The transition values were obtained using inflection method.

Stripe-width (nm)	Hyst. (K)	T_M (K)	T_A (K)	ΔT_{Avg} (K)
700	7	335	342	43
500	6	347	353	49
450	6	~361	~367	~63
350	5	~368	~373	>70

5.5 Conclusions

Starting from 200 and 75 nm thickness of films, micro and nanostructures of epitaxially grown Ni-Mn-Ga were fabricated by means of lithography techniques and reactive ion etching. The microstructures represent the lateral size of 3 μm to 100 μm and the nanostructures have the lateral size range of 150 nm to 800 nm. The effects of the lateral size, shape and geometry were investigated on the martensitic configuration and the critical transition temperatures.

Microfingers with the lateral dimension of < 12 μm, fabricated along different orientations with respect to [100] MgO tend to break the equivalency of the X-type twin boundaries by selecting the boundaries, which are relatively parallel to the length of the fingers. This effect was also observed in the nanostripes having the lateral dimension range of 300-550 nm.

Shape of microstructures influences the self-accommodation of the X-type twin boundaries. Microstripes along [100] MgO keep the multiplicity of the X-type twin boundaries while alternate the orientation of the boundaries more frequently as function of size. Microdisks however, reduce the multiplicity of the X-type twin boundaries as a function of the lateral size.

The critical transition temperatures measured for microstripes show a minor shift (< 3 K) towards higher temperatures and the thermal hysteresis varies about 2 K upon downscaling. The critical transition temperatures measured for the nanostripes reveal the dominant effect of broadening of the transition width over down scaling. The thermal hysteresis also shows a gradual minor decrease (7 to 5 K) as function of the lateral size.

Overall, the observed effects are expected to be mainly due to the impact of lithography patterning in the number of the nucleation sites, growth and the self-accommodation of the martensitic twin boundaries as well as the strain relaxation as a result of the lateral confinement. To our knowledge, such a combinational study including the lateral size, shape and geometry has not been reported in the literature neither for FSMA nor for the broader class of conventional SMA. Our multiple approaches in this chapter can be considered as a step forward for investigating the links between lateral confinement, martensitic configuration and martensitic transition of FSMA.

References

1. Wang, C., *et al. J. Vac. Sci. Technol. B* **32**, 020802 (2014).
2. Ozdemir, N. *et al. Acta Mater.* **60**, 5670 (2012).
3. Gottschall, T. *et al. Adv. Funct. Mater.* **27**, 1606735 (2017).
4. Lambrecht, F. *et al. Shap. Mem. Superelasticity* **2**, 347 (2016).
5. Diestel, A. *et al. J. Phys.-Condens Mat.* **25**, 266002 (2013).
6. Ranzieri, P. *et al. Adv. Mater.* **27**, 4760 (2015).
7. Ge, Y. *et al. Acta Mater.* **58**, 6665 (2010).
8. Ge, Y. *et al. Mater. Sci. Forum* **635**, 63 (2010).
9. Niemann, R. *et al. Phys. Rev. B* **89**, 214118 (2014).
10. Tuncer, N. *et al. J. Mater. Sci.* **50**, 7473 (2015).
11. Niemann, R. *et al. Phys. Rev. B* **86**, 214101 (2012).
12. Ludwig, B. *et al. Phys. Rev. B* **80**, 144102 (2009).
13. Ball, J.M. *et al. MATEC Web of Conferences* **33**, 02008 (2015).
14. Porta, M. *et al. Phys. Rev. E* **98**, 032143 (2018).
15. Porta, M. *et al. Phys. Rev. E* **100**, 062115 (2019).
16. Wollants, J. *et al. Prog. Mater. Sci.* **37**, 227 (1993).
17. Chen, Y. & Schuh, C.A. *Acta Mater.* **59**, 537 (2011).
18. Mashirov, A.V. *et al. IEEE Magn. Lett.* **10**, 1 (2019).
19. S. Doyle, *et al. Eur. Phys. J. Spec. Top.* **158**, 99 (2008).
20. Kuchin, D.S. *et al. J. Magn. Magn. Mater.* **482**, 317 (2019).
21. Ueland, S.M. & Schuh, C.A. *Acta mater.* **61**, 5618 (2013).

Conclusions

The goal of investigation, reported in this thesis can be classified into three levels:

Level 1. Multiscale observation of the formation and self-accommodation of the twinning configurations in the martensitic phase of Ni-Mn-Ga epitaxial thin films, micro and nanostructures.

Level 2. Investigation of the possible relations between the formation and self-accommodation of the twins and the martensitic transformation processes.

Level 3. Looking for the possibilities of controlling the martensitic configurations and the martensitic transformation process in epitaxial films, micro and nanostructures.

We investigated the crystallographic relations between the twin boundaries and interfaces from the atomic scale to the microscale and accompanied this investigation with the direct observation of the evolution of the martensitic interfaces vs. temperature. Based on the symmetry relations between the twin variants, we identified the types of twin boundaries and the twinning interfaces, i.e., ridges, valleys, and non-conjugation interfaces. Using the change of modulation direction across the boundary, observed by transmission electron microscopy in Y-type regions, we were able to determine the presence of type I, type II, and modulation twin boundaries with a dominant presence of type II. Beyond these findings, we proposed a transition route by highlighting the major role of different martensitic interfaces. The forward transition starts with the heterogeneous formation of twin boundaries at the position of the ridges on the surface of the film and proceeds towards the substrate. The twin boundaries continue to nucleate and grow until they meet at the other kind of conjugation interfaces, i.e., valleys, or at non-conjugation interfaces, where the growth is hindered. In these regions, the elastic stress created during the transition is partially stored. This stored energy serves as the driving force for the reverse transition by initiating the nucleation of the austenitic phase.

We also investigated the influence of the density of the martensitic interfaces on the critical temperatures of the martensitic transition. It was found that imperfections could serve as the nucleation points, increasing the density of the martensitic interfaces and stored elastic energy and consequently leading to the increase of the transition width. In contrast, the density of the martensitic interfaces as well as the sample roughness shows only a minor effect on the thermal hysteresis of the samples. Nevertheless, by the reduction of the imperfections, annealing plays the paradoxical role of reducing the transition width while increasing the thermal hysteresis.

The formation of the twin boundaries in Ni-Mn-Ga epitaxial films was investigated in situ in three different conditions, i.e. temperature induced phase transition (zerofield), temperature induced phase transition assisted by a constant external magnetic field (isofield) and the magnetic field induced phase transition in constant temperature (isothermal). The observations highlight that Y-type twinning gives rise to a relatively sharper transition and lower hysteresis compared to the X-type configuration. Therefore, X and Y-type twins not only show different microstructural and magnetic

characteristics, but they also display different characteristics of nucleation and growth during the martensitic transition.

Starting from continuous epitaxially grown Ni-Mn-Ga films, micro and nanostructures were fabricated by means of lithography techniques and reactive ion etching. The critical transition temperatures measured for microstripes, having the lateral size of 3 μm to 100 μm show a minor shift (< 3 K) towards higher temperatures and the thermal hysteresis varies only 2 K upon downscaling. The critical transition temperatures measured for the nanostripes having the lateral size of 350 nm to 700 nm reveal the dominant effect of broadening of the transition width as well as the increase of the transition temperatures over down scaling. The thermal hysteresis also shows a gradual decrease (7 to 5 K) as function of the lateral size.

In addition to the effect of size on the critical transition temperatures, the self-accommodation of the martensitic configurations was found to be influenced by the lithography patterning. The fabricated finger-shaped microstructures having the width of < 12 μm, patterned along different orientations with respect to [100] MgO were found to break the equivalency of the X-type twin boundaries by selecting the boundaries, which are relatively parallel to the length of the fingers. This effect was also observed in the nanostripes having the lateral dimension range of 300-550 nm. The effect of shape on the self-accommodation of the martensitic configurations was realized by comparing microstripes and microdisks. The tiny stripes along [100] MgO were found to keep the multiplicity of the X-type twin boundaries while alternating the orientation of the boundaries more frequently as function of reduction of size. Microdisks however, were observed to reduce the multiplicity of the X-type twin boundaries as a function of the lateral size. The observed effects are expected to be mainly due to the impact of patterning on the strain relaxation, number of the nucleation sites, growth and the self-accommodation of the martensitic twin boundaries.

It was also reported that different simple post-growth treatments (i.e. post-annealing, magnetic field cooling and the application of a local mechanical stress) open up the possibility to tailor the twinning configuration of FSMA epitaxial thin films. Taking the advantage of growth temperature and post annealing treatment, twinning configuration can be easily tuned from full X-type to mixed X/Y-type with different geometrical distribution, in which controlling the defects and disorder affecting the martensitic transition path play an important role. Mixed X/Y-type configuration can be modified by applying an external magnetic field while crossing the martensitic transformation, exploiting the additional Zeeman energy term. In this case, with the field applied in the film plane, a predominant Y-type microstructure can be obtained. The application of post-growth stress is suitable for locally transforming X-type to Y-type configuration along the direction of the applied stress.

Overall, the multiple approaches used in this thesis shed light into the direct link between the martensitic configuration at the different length scales and the martensitic transition. The present results can be considered a step forward for understanding the transition processes as well as for tuning the characteristics of the transition such as hysteresis and transition width, by microstructure engineering. The tuning aims at the full exploitation of martensitic Heuslers for the applications requiring cyclic phase transition.

Publications

1. **08/2020**, Casoli, F., Varvaro, G., **Takhsha Ghahfarokhi, M.**, Fabbrici, S., Albertini, F. / Title: Insight into the magnetisation process of martensitic Ni-Mn-Ga films: a micromagnetic and vector magnetometry study, Journal of Physics: Materials, https://doi.org/10.1088/2515-7639/abb0ee
2. **05/2020**, **Takhsha Ghahfarokhi, M.**, Nasi, L., Casoli, F., Fabbrici, S., Trevisi, G., Cabassi, R., Albertini, F. / Title: Following the Martensitic Configuration Footprints in the Transition Route of Ni-Mn-Ga Magnetic Shape Memory Films: Insight into the Role of Twin Boundaries and Interfaces, Materials, 13(9), 2103, https://doi.org/10.3390/ma13092103
3. **02/2020**, **Takhsha Ghahfarokhi, M.**, Casoli, F., Fabbrici, S., Nasi, L., Celegato, F., Cabassi, R., Trevisi, G., Bertoni, G., Calestani, D., Tiberto, P., Albertini, F. / Title: Martensite-Enabled Magnetic Flexibility: the Effects of Post-Growth Treatments in Magnetic-Shape-Memory Heusler Thin Films, Acta Materialia, 187, 135-145, https://doi.org/10.1016/j.actamat.2020.01.049
4. **Submitted Manuscript**, **Takhsha Ghahfarokhi, M.**, Ander Arregi, J., Casoli, F., Horký, M., Cabassi, R., Uhlíř, V., Albertini, F. / Title: Ferromagnetic-Shape-Memory Heusler Microstructures: The Geometry and Size Effects
5. **Manuscript under preparation**, **Takhsha Ghahfarokhi, M.**, *et al.* / Title: Shape Memory Heusler Films: Martensitic Morphology Linkage to the Transition Width and Thermal Hysteresis.
6. **Manuscript under preparation**, **Takhsha Ghahfarokhi, M.**, *et al.* / Title: Influence of martensitic configuration on the transition of Heusler films: an advanced imaging in magnetic field and temperature

Acknowledgements

First of all, I would like to deliver my sincere thanks and respect to my supervisor; Franca Albertini, who provided the opportunity for me to grow my scientific character through this Ph.D. program, for which I will be grateful for the rest of my life. Her superior kindness together with her supportive attitude and generosity created a pleasant atmosphere to develop my academic character. Beyond the science, she has been one of the most inspiring people I have ever met.

Particularly, I would like to pay my thanks to my co-supervisor, Francesca Casoli, for her total and kind supports through my Ph.D. program. Her assertiveness and meticulosity helped me getting closer to the goals. Without her supports, I would definitely not be able to get through all the scientific as well as the non-scientific obstacles of the program.

Special thanks go to the IMEM-CNR staff; Lucia Nasi, Simone Fabbrici, Riccardo Cabassi, Giovanna Trevisi, Davide Calestani and Giovanni Bertoni, whose significant contribution enriched my scientific work.

I would also like to deliver my sincere thanks to our collaborators from other Italian institutions; Paola Tiberto and Federica Celegato at INRIM; Lara Righi at University of Parma; Elena Villa at ICMATE-CNR; and Alessandro di Bona at CNR-NANO for providing instrumental and technical support.

I am grateful for having the opportunity to visit Functional Materials group at Technical University of Darmstadt. I would like to thank Oliver Gutfleisch and his group members; Maija Laux, Alisa Chirkova, Semih Ener, Konstantin Skokov, Bahar Fayyazi, Fernando Maccari, Andreas Taubel as well as the collaborators of his group; Enrico Bruder and Christian Minnert for their kind hospitality and fruitful collaboration.

And the last but not least, my sincere gratitude goes to Vojtěch Uhlíř and his group members; Jon Ander Arregi, Michal Staňo, Michal Horký and Jan Hajduček at CEITEC, Brno University of technology, for their kind support and warm hospitality. They provided significant assistance as well as a full self-service access to the CEITEC NANO core-facilities, including 12-months access to clean rooms, micro- and nanofabrication facilities as well as the instruments, required for the characterization. On top of that, they shared their expertise in micro and nanofabrication techniques, to which I am utterly grateful.

CzechNanoLab project LM2018110 funded by MEYS CR is gratefully acknowledged for the financial support of the measurements/sample fabrication at CEITEC Nano Research Infrastructure.

***